The Phoenix Multiwavelength Deep Survey

Andrew Hopkins

A thesis
submitted for the degree of
Doctor of Philosophy
at the
University of Sydney

December, 1997

This thesis is printed on acid-free paper.

Abstract

This thesis describes the *Phoenix Deep Survey*, a multiwavelength survey of a two-degree diameter region. Observations at 1.4 GHz and 843 MHz in the radio continuum, at R-, V-, H-, and K-bands in the optical and near-infrared, and of galaxy spectra, are analysed to investigate the nature of the faintest observable radio sources. A catalogue of 1079 radio sources is compiled from these observations, and optical counterparts for 541 of these radio sources are identified. Radio and optical source counts are predicted from models for luminosity functions and are compared with the observational source counts. Radio luminosity evolution at a rate of $Q = 3.3 \pm 0.8$ for starburst galaxies, a rate consistent with other studies, is found to be required to match the observed radio source counts. The *bivariate* (radio/optical) luminosity function is also modelled and used to predict the bivariate source count distribution, for comparison with observation. The redshift distribution predicted from the bivariate luminosity function is investigated. It is established that, as anticipated from earlier studies, a larger proportion of sub-mJy radio sources are starburst galaxies than at higher flux densities, but there are still significant numbers of AGN sources present. The observational radio luminosity function is investigated, and several interesting sources are examined in more detail.

Preface

Acknowledgements

A large number of people have helped in various ways in the construction of this thesis. They include people who have provided both scientific and non-scientific help, support and advice, all of which have helped this production. I wish to thank first and foremost my supervisor, Lawrence Cram, and my wife, Toni Hopkins. They have both played a major role in making this thesis what it is, and I want to let them know how much their presence and efforts are appreciated.

I wish to thank Bahram Mobasher for extensive collaboration and the input of ideas and methods, and for hosting me at Imperial College for a time. My thanks go also to Rogier Windhorst for his help and advice, and for his approachability and hospitality.

I want to thank all the staff and students of the Astrophysics Department for continual support and camaraderie during the last four years. Students from other departments and institutions, too, also have my thanks in this area. In particular I want to give my thanks to Julia Bryant, Tanya Hill, Eileen O'Hely, Andrew Reid, Bryan Gaensler and Gene Davidson, for innumerable quantities of help and fun. Tom McDermott has my thanks for his incredibly helpful efforts in getting the radio images printed.

Others whose efforts deserved to be mentioned include Chris Pearson and Antonis Georgakakis from Imperial College, Chris Lidman from ESO, and all of the staff of the ATCA and of the AAT, in particular Bob Sault, Neil Killeen and Jeremy Bailey.

To all of you, Thank You.

The Australia Telescope is funded by the Commonwealth of Australia for operation as a National Facility managed by CSIRO. This research has used the NASA/IPAC Extragalactic Database (NED) which is operated by the Jet Propulsion Laboratory, California Institute of Technology, under contract with the National Aeronautics and Space Administration. The research has also used the NRAO VLA Sky Survey (NVSS) Database. The National Radio Astronomy Observatory is a facility of the National Science Foundation operated under cooperative agreement by Associated Universities, Inc.

Statement of Originality

This thesis describes work carried out in the Department of Astrophysics at the University of Sydney between 1994 and 1997. The sections of Chapters 2 and 3 relating to the radio observations, data reduction and source count analysis are the subject of a paper accepted for publication by Monthly Notices of the Royal Astronomical Society, on which I am first author. Except where acknowledged otherwise, the work presented in this thesis is my own. The major contributions from other people are as follows:

- Lawrence Cram performed the analysis described in Chapter 7,
- Antonis Georgakakis carried out the data reduction of the K-band data from IRAC2b,
- Chris Lidman performed the data reduction of the EFOSC spectral data.

Astronomical Units

For consistency with much of the published work in astronomy, the following non-SI units are used in this thesis:

- The Jansky (Jy):

$$1\,\mathrm{Jy} = 10^{-26}\,\mathrm{W\,Hz^{-1}\,m^{-2}} \tag{0.1}$$

- The Parsec (pc):

$$1\,\mathrm{pc} = 3.086 \times 10^{16}\,\mathrm{m} \tag{0.2}$$

- The Solar Mass ($\mathrm{M}_\odot$):

$$1\,\mathrm{M}_\odot = 1.989 \times 10^{30}\,\mathrm{kg} \tag{0.3}$$

Throughout this thesis the value of the Hubble constant, H_0, is taken to be $50\,\mathrm{kms^{-1}Mpc^{-1}}$, and the deceleration parameter $q_0 = 0.5$. All logarithms in this thesis are base 10 unless indicated by use of the natural logarithm symbol, "ln", or otherwise specified.

Contents

List of Tables

List of Figures

Chapter 1

Introduction

Studying the faintest observable galaxies has always been an interesting pursuit. They have the potential to test the accepted understanding of the nature of the Universe and to stimulate new ideas. Although the definition of "faint" continually changes as technology progresses, the faintest objects always provide an intrinsic fascination. In the past 15 years studies of the faintest galaxies at both radio and optical wavelengths have engendered one of the most fascinating enigmas in astrophysics. To provide a suitable context for the discussion of this puzzle, some background information is appropriate.

1.1 A brief history of radio astronomy

In the early 1930s Karl Jansky, a radio technician at Bell Labs, serendipitously detected radio noise from the sky. Working at 20.5 MHz, he was investigating the noise associated with trans-Atlantic radio signals using an antenna built to characterise the properties of "static". In early 1932 Jansky reported evidence of an unusual type of static, which "goes around the compass in 24 hours." Once he had established the static was extraterrestrial in origin he dubbed it "star static". He continued to monitor it until about 1936, although more sporadically as time went on. By 1934, after two papers on the topic, his further investigations had led to the conclusion that the static was originating from the Milky Way. In his third paper, in 1935, he speculates "Since it sounds so much like 'set noise' [intrinsic receiver noise], couldn't it be due to thermal agitation of charged particles?" (Sullivan, 1983). In the late 1930s Jansky had little opportunity to take the investigation further due to the other projects investigating radio static on which he was required to work. Further observations were made by Grote Reber in the early 1940s, but very little additional work on the "star static" was done until after the second world war, when advances in the technology of radar equipment set the stage for further astronomical investigation.

In 1949, Bolton, Stanley and Slee identified Centaurus A and Virgo A with the nearby optical galaxies NGC 5128 and NGC 4486 (M87) respectively. Also

in 1949, a third bright radio source was identified with the the Crab Nebula, a galactic supernova remnant. The Large Magellanic Cloud was detected in the radio by Mills and Little in 1953. However, the two strongest radio sources, Cygnus and Cassiopeia, were still unidentified at this time. It wasn't until 1954 that Baade and Minkowski identified Cygnus A optically as a distant galaxy.

At that point in time radio sources were categorised as Class I or Class II sources, the former being concentrated in the galactic plane, the latter isotropically distributed. By 1954 it had been proposed that Class I sources, which boasted large angular sizes (typically > 1 degree), were the radio counterparts of optical supernova remnants. This conclusion was reached by analogy with the Crab Nebula, after other Class I sources were established as having large angular sizes and were identified with low optical surface brightness nebulosities in the Galactic Plane. Also by this time, Class II sources, typified by Cen A, Vir A and Cyg A, were identified as being extragalactic. This was the discovery of a new class of object, "radio galaxies".

Early investigations of radio sources concentrated on obtaining accurate positions, for the purpose of identifying their optical counterparts. The goal of obtaining accurate radio source positions required further development in radio telescope technology. Two large single dish instruments which had a profound impact through their early observations were the 76 m antenna at Jodrell Bank, commissioned in 1958, and the 64 m antenna at Parkes, commissioned in 1961. The development of radio interferometry, too, had been occurring during the early 1950s, introducing accurate measurements of radio source angular diameters and positions. Aperture synthesis techniques, developed by Martin Ryle at Cambridge, played a fundamental role in radio astronomy by enabling radio telescopes to attain the resolution necessary to distinguish both fainter and more compact sources than could be achieved with even the largest single dish instruments. A contemporary description of radio telescopes and the advantages and disadvantages of single dish versus interferometric instruments is given by Christiansen (1963). This account is also an interesting overview of the technology which had developed by that time.

When Class II sources were being observed with the Jodrell Bank radio intensity interferometer in the 1950s, it was found that a number remained unresolved, even as interferometer baselines were significantly increased. Those that were resolved were mostly identified optically as galaxies, in the same fashion as Cyg A, Cen A and Vir A. By 1961 a maximum baseline of about 115 km had been used for measuring angular sizes of sources by the Jodrell Bank group. Further observations of the 384 sources from the Cambridge survey using such long baselines found that seven sources were still unresolved (Hanbury Brown, 1983). These sources, including 3C 48, had angular sizes less than one or two arcseconds. By 1960 radio source position measurements were so accurate that optical identifications even with relatively innocuous stars could be considered likely. However, spectra of such "stars" showed either a featureless continuum or broad, unrecognised emission lines in the red part of the spectrum. The identification of the emission lines was not a trivial problem, and it wasn't until 1963 that Martin Schmidt, working on the spectrum of 3C 273, realised the emission lines could be identified if a redshift of 0.16 was invoked. Once

this step was taken, Greenstein and Matthews re-examined the spectrum for 3C 48, which had been obtained by Thomas Matthews in 1961, and discovered it to have a redshift of 0.37, much greater than the most distant galaxies known at the time (Hazard et al., 1963; Schmidt, 1963; Oke, 1963; Greenstein & Matthews, 1963). These new objects were called "quasi-stellar radio sources" – quasars.

By the end of the 1960s radio astronomy had come a long way. Many different types of celestial radio phenomena had been identified: Supernova remnants, radio galaxies, H II regions, "normal galaxies", quasars, and pulsars. The discovery of the 21 cm line of neutral hydrogen had been made in 1951 almost simultaneously by researchers in Australia, the US, and the Netherlands. Polarisation of extended radio sources had been discovered (Mayer et al., 1962), and variability in the intensity of radio sources had been confirmed (Hunstead, 1972). The technology for large dishes, interferometers and aperture synthesis was well established, and several all sky surveys were already completed. An enlightening description of the stage radio astronomy had reached by 1967 is given in an article on radio source populations by Wall (1994).

Systematic deep radio surveys began in the early 1970s with the Westerbork Synthesis Radio Telescope (WSRT). A summary of these surveys prior to 1984 was given in the first paper presenting results from the *Leiden Berkeley Deep Survey* (LBDS) (Windhorst et al., 1984b), and this summary is repeated here, for convenience and completeness. The following surveys were made with the WSRT, mainly at 1.4 GHz, and with a maximum baseline of 1.5 km: The 1st Westerbork survey (Katgert et al., 1973) covered ~18 deg^2 down to ~10 mJy, the 2nd Westerbork survey (Katgert & Spinrad, 1974) covered ~4.5 deg^2 down to ~7 mJy, the 3rd Westerbork survey (Katgert, 1975) covered ~18 deg^2 down to ~6 mJy, the *Background Survey* (BGS) (Willis et al., 1976) was constructed from the WSRT database and covered ~90 deg^2 down to 4-10 mJy.

With the improvement in receiver technology through the development of cooled front-ends in 1980, detections of sub-mJy radio sources with the WSRT became feasible (Windhorst et al., 1984b). Making its appearance in the early 1980s, the Very Large Array (VLA) entered the faint radio survey scene with two "snapshot" surveys (Condon et al., 1982b; Mitchell, 1983). Following this work came the LBDS (Windhorst et al., 1984b) and the first of the sub-mJy surveys with the VLA (Condon & Mitchell, 1984). By then the enigma surrounding sub-mJy radio sources had emerged.

1.2 Sub-mJy radio surveys

Over the past two decades the sensitivity of deep radio surveys of small areas has reached flux densities well below 1 mJy at 1.4 GHz, as summarised in Table 1.1 (after Table 1 in Benn et al., 1993). The Table lists the galactic latitude of the survey, the instrument used for the observations, the frequency of the observations, the limiting flux density at that frequency, the number of radio sources detected and the number

of optical identifications claimed in the reference given.

Table 1.1 : Sub-mJy radio surveys.

Reference	b °	Telescope	ν GHz	S mJy	N	N_{ID}
Condon & Mitchell (1984)	35	VLA(C)	1.4	0.08	159	45
Mitchell & Condon (1985)	86	VLA(C)	1.4	0.07	145	49
Windhorst et al (1985)	38	VLA(C)	1.4	0.25	124	41
Partridge et al (1986)	19/38	VLA(C/D)	5.0	0.1	32	9
Weistrop et al (1987)	−47	VLA(D)	1.4	0.1	13	10
Oort (1987)	39	WSRT	1.4	0.09	349	66
Windhorst et al (1987)	35	WSRT	1.4	0.5	116	116
Fomalont et al (1991)	60	VLA(B/C/D)	5.0	0.016	62	
Windhorst et al (1993)	19/38	VLA(D)	8.4	0.014	82	
Windhorst et al (1995)	74	VLA(C/D)	8.4	0.009	24	15
Fomalont et al (1997)	55	VLA(C)	8.4	0.012	18	14
This thesis (1997)	−71	ATCA(6A)	1.4	0.1	1079	541

It can be seen that from the early 1990s the trend in most deep surveys has been towards observations at higher frequencies. Observations at higher frequencies have a limiting flux density much lower than those at lower frequencies for comparable times of observation. However this increase in sensitivity comes at the expense of survey area. This is due to the smaller area of high primary beam response in antennae at the higher frequencies. The spectral index of $\alpha \sim -0.8$ ($S \propto \nu^{\alpha}$) for many radio sources implies that the population being observed at tens of microjanskys at 8.4 is similar to that at hundreds of microjanskys at 1.4 GHz. There will be differences, however, since fainter 1.4 GHz sources do tend to have flatter spectra (Windhorst et al., 1993), but the smaller primary beam at the higher frequencies restricts those surveys to smaller areas, leading to smaller samples less suited to a statistical analysis of the populations observed.

1.3 Source counts

When the surface density of galaxies (the number per unit area of sky) observed at a given wavelength is plotted as a function of their apparent brightness, the resulting graph is called the source counts. If the Universe had a Euclidean geometry, such a graph would have a shape proportional to $S^{-2.5}$, taking S to be the flux density of the sources. This is not the case, but it is not only the Universe's non-Euclidean nature which causes the observed source counts to differ from this result. If the luminosity or density of galaxies evolves with time, the observed source counts will also show a non-Euclidean shape. Example source count graphs, both radio and optical, are shown in Figure 1.1.

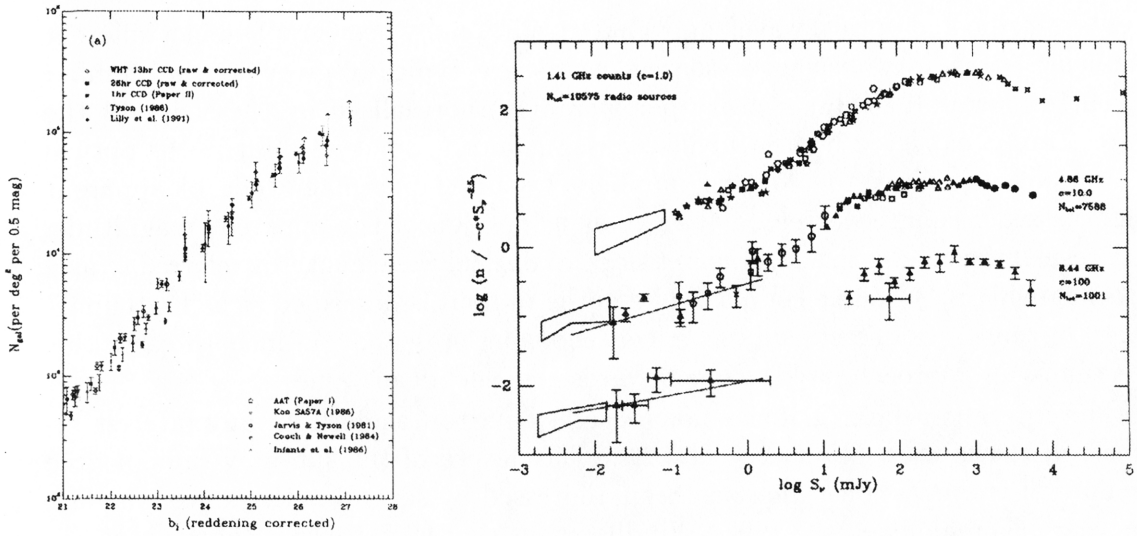

Figure 1.1 Example source count graphs. Left: Differential optical source counts in B_J band (Figure 5 from Metcalfe et al., 1995). The vertical axis runs from 10^2 to 10^6 galaxies/deg^2/0.5 mag. Right: Normalised differential radio source counts at three frequencies (Figure 3 from Windhorst et al., 1993).

The shape of the radio source counts (Windhorst et al., 1993; Condon, 1989, for example) shows a Euclidean distribution for the most apparently bright sources. Below a flux density of about 10 Jy the curve begins to steepen above the Euclidean slope. It flattens back to Euclidean at about 1 Jy, and then turns over, dropping away below 100 mJy with a slope much less than that expected from the Euclidean example as flux densities continue to decrease. The shape of the source counts to this level is well modelled by invoking luminosity evolution, at different rates, for flat- and steep-spectrum radio sources (Dunlop & Peacock, 1990). Below a few millijanskys, though, there is a "resteepening" of the curve back towards the Euclidean slope (Windhorst et al., 1984b; Windhorst et al., 1985; Oort, 1987; Katgert et al., 1988), which cannot be predicted by models of luminosity or density evolution of these populations.

Optical source counts, however, are well modelled without needing to invoke evolution at all, at least for the brighter apparent magnitudes. This doesn't produce a Euclidean shape for the source counts, though, due to the non-Euclidean geometry of the Universe. At the faint end of the optical source counts there is an increase in the slope, which doesn't match the predictions of no-evolution (NE) models. This is most pronounced in the B_J-band (440 nm), the excess in the observed counts with respect to the NE model predictions being of the order of $\sim$4 to 5 at $B_J = 24$ and $\sim$5 to 10 at $B_J = 26$ (Maddox et al., 1990; Guiderdoni & Rocca-Volmerange, 1991). The evidence for evolution of faint galaxies has been reviewed by Koo and Kron (1992).

One potentially confusing aspect of the change in source count slope arises from the terminology used to describe it. This comes from the fact that the source

counts at radio and optical wavelengths have traditionally been graphed in a different manner. At radio wavelengths source counts are typically given as the number of sources per unit of flux density per steradian, normalised by the shape of the source counts expected if the Universe was Euclidean in nature. But in the optical it is standard simply to plot the number of sources per magnitude of apparent brightness per square degree on the sky as a function of the apparent magnitude. As a result, the change in source count slope at optical wavelengths is referred to as a "steepening" of the source counts, while in the radio it is described as a "flattening" or an "upturn", or occasionally as a "resteepening" (as above). In both cases this is actually an approach of the slope towards the Euclidean value.

The interest in faint galaxies now becomes clearer, aside from any interest intrinsic in the faintest observable objects. The nature of the sub-mJy radio source population is a question which has been addressed by several authors over the last ten years (Fomalont et al., 1997; Windhorst et al., 1995; Rowan-Robinson et al., 1993; Benn et al., 1993, for example), but one around which a certain level of controversy remains.

1.4 Starburst and AGN galaxies

Bright radio sources are predominantly comprised of objects such as pulsars, supernovae remnants, and H II regions in our own galaxy, and quasars and giant elliptical galaxies with strong radio jets outside the Milky Way. The extragalactic radio-loud objects, quasars and radio galaxies, are classified as having an active galactic nucleus (AGN). But what type of objects make up the sub-mJy radio source population? Are they the same objects which cause the upturn in the faint optical source counts? And what is the cause of the "resteepening" of the radio source count slope at about a millijansky? In studies to date, it has been shown that the majority of faint radio sources are identified optically with galaxies having magnitudes much brighter than B$\approx$ 25, at which the change in optical source count slope occurs (Windhorst et al., 1985; Benn et al., 1993; Hammer et al., 1995; Fomalont et al., 1997). This indicates that different galaxies are responsible for the effects in the radio and optical source counts. Suggestions for the cause of the change in the radio source count slope include an evolving population of blue radio galaxies with a stronger radio power than normal spirals (Windhorst et al., 1985), evolving spiral galaxies (Condon, 1984a; Condon, 1984b) and a population of starbursts (Danese et al., 1987; Rowan-Robinson et al., 1993).

AGN galaxies have enhanced levels of emission at radio, X-ray and FIR as well as optical wavelengths. Seyfert galaxies, quasars, BL-Lac objects and radio galaxies are all examples of AGN galaxies. (The term "radio galaxy" historically describes galaxies detected initially through their prodigious radio emission, which is a result of the activity present in the nucleus. However, it is currently believed that all galaxies have some level of emission at radio wavelengths. Hence, the term "radio galaxy" to refer solely to that class of AGN can be quite misleading.) The enhanced

emission from an AGN is due to the presence of a highly energetic, very compact nuclear object, which many current theories interpret to be a super-massive black hole with a mass ranging between 10^6 and $10^{10}\,M_\odot$. Work on the Broad-Line Region (BLR) in active galaxies and quasars (Heckman et al., 1980; Heckman, 1980a; Heckman, 1980b) established that there were no obvious differences between the BLRs associated with strong compact radio sources and those selected optically. The ramifications are that it is probable the BLR of every galaxy has associated with it a radio source of some strength, merely distinguished by intensity. The acronym LINER (Low Ionisation Nuclear Emission-line Region) to describe a category of low-powered AGN was coined (Heckman, 1980b). This was one of the earliest hints that the phenomena now referred to collectively as AGN galaxies are all manifestations of the same physical process on different scales. It also illustrates the fact that not all AGN are radio-loud objects – even some of the most powerful AGN, such as radio-quiet quasars, can have very little radio emission – but all radio-loud galaxies are AGN.

A starburst galaxy is a galaxy which is experiencing a rapid burst of star formation at rates unsustainable over the lifetime of the galaxy. A typical galaxy forms stars at a rate of $\sim 0.1\,M_\odot yr^{-1}$ or less. In starburst galaxies, star formation rates range from $\sim 10\,M_\odot yr^{-1}$ in a typical case up to a few$\times 100\,M_\odot yr^{-1}$ in more extreme cases. Such a starburst can last for only 10^7 to 10^8 yr before running out of fuel, compared to 10^9 or 10^{10} yr for the age of a galaxy at the present epoch. The observational indications that a galaxy is experiencing a starburst are enhanced far-infrared (FIR) radiation and blue colour-indices, with strong, narrow recombination lines in emission in their spectra.

The name "starburst" developed in the late 1970s. It was foreshadowed by the phrase "flashing galaxies" (Searle et al., 1973) used to denote a flash of light due to enhanced massive star formation. Bierman (1976) required a "burst of star formation" to account for both the observed radio emission and the blue colours for some galaxies in his model of the radio emission from spiral galaxies. An "outburst of star formation" was proposed (Ulrich, 1978) as a trigger of the outflow observed in NGC 253. "Star-burst nuclei" were introduced as a distinct morphological galaxy type by Balzano (1983). "Starburst galaxies" became common terminology after results from the IRAS (Infrared Astronomical Satellite) observations demonstrated the cosmological significance of the starburst phenomenon.

For spiral galaxies there is a surprisingly strong correlation between emission in the FIR and the radio regions of the spectrum (Dickey & Salpeter, 1984; Helou et al., 1985). The flux density observed at $60\,\mu$m in the FIR is about one hundred times that observed at 1.4 GHz in the radio: $S_{60\,\mu m} \simeq 100\,S_{1.4\,GHz}$ (Helou et al., 1985), and there are similar correlations between flux densities at other FIR and radio wavelengths (Knapp et al., 1990). (The correlation for optically bright spiral galaxies has been re-examined and more precisely defined by Devereux & Eales (1989)). This very tight correlation appears to be valid for all types of spiral galaxies, from dwarf galaxies right through to the most luminous starburst systems. The source of this correlation is believed to be related to the formation and evolution

of massive stars. The ultraviolet (UV) radiation from these stars is absorbed by interstellar dust and re-emitted in the FIR, while the rapid evolution of the same massive stars results in many supernovae producing radio emission through shock-accelerated, relativistic electrons. For AGN galaxies, though, there doesn't appear to be any similar radio/FIR correlation.

Condon (1989), Benn et al. (1993) and others have concluded that the 1.4 GHz source count distribution requires two populations of radio sources for its explanation. Condon (1989) describes these populations as "starbursts" and "monsters". With these descriptions he draws a distinction between the energy sources powering the radio galaxies, "starbursts" deriving their radio emission from disk stars and related nebulae (supernova remnants, H II regions, etc), and "monsters" from nuclear super-massive compact objects (e.g., black holes). He comments that in this terminology even low-luminosity disks in normal spiral galaxies are called "starbursts". He also notes that most "starburst" galaxies are spiral galaxies and most "monsters" are elliptical or lenticular galaxies, although the morphological correspondence is not perfect. Wall (1994) gives an interesting review of extragalactic radio source populations.

From spectroscopic studies, Hammer et al. (1995) assert that the faint radio galaxies are comprised about equally of high-redshift AGN and low- to intermediate-redshift blue emission line objects. The latter are either starburst or post-starburst galaxies, or possibly low-power AGN, such as LINERs. Benn et al. (1993) claim that while galaxies brighter than 1 mJy at 1.4 GHz are dominated by elliptical galaxies, indistinguishable in their optical properties from the giant elliptical, weak radio galaxies found in higher flux-density limited surveys, the majority of sub-mJy radio sources are identified with star-forming galaxies and Seyfert galaxies. Windhorst et al. (1985) and Kron et al. (1985) provide the relative fraction of red (giant elliptical) and blue (starburst) galaxies as a function of 1.4 GHz flux density in the range 0.1 to 100 mJy, indicating an increasing fraction of the starburst population as flux density decreases. In addition to these results, 8.4 GHz observations of the Hubble Deep Field have established that the optical identifications for microjansky radio sources are preferentially with red elliptical galaxies and blue early-type spiral galaxies (Fomalont et al., 1997). It is becoming more firmly established that the fraction of sub-mJy radio sources identified with actively star-forming galaxies (at least half) is much greater than at higher radio flux densities (only a few percent). These results, combined with the evidence that the radio (1.4 GHz) and far-infrared (60 μm) flux densities of galaxies are correlated (Helou et al., 1985), imply that the faint radio population contains a significant proportion of starburst galaxies, unlike the brighter radio sources.

1.5 This thesis

The goal of this thesis is to further investigate the sub-mJy radio source population, by carrying out a deep, large area, multiwavelength survey. Are deep radio

surveys, combined with multi-object spectroscopy, good methods for detecting starburst galaxies? Do they provide a good cosmological probe of the phenomenon, or are only local events detected? What types of galaxies comprise the sub-mJy radio population? What part, if any, does evolution play in these galaxies, and to what degree?

The multiwavelength survey, called the *Phoenix Deep Survey* (PDS), covers a two-degree diameter region of sky. The PDS (named for the constellation in which it lies) includes observations at two optical passbands, near-infrared observations, 843 MHz radio observations with the Molonglo Observatory Synthesis Telescope (MOST), spectroscopy of selected sources, and 1.4 GHz radio observations with the Australia Telescope Compact Array (ATCA). The study covers a larger area than previous work, motivated in part by the requirement to avoid the small sizes of earlier 1.4 GHz radio surveys (Windhorst et al., 1985; Windhorst et al., 1987; Oort, 1987), and also by the desire to exploit the multi-object spectroscopy capability of the 2dF fibre spectrograph on the Anglo-Australian Telescope (AAT). As a result of the field's size it will be less subject to field-to-field variations in the source counts as induced by high-redshift clustering (Windhorst et al., 1990; Windhorst et al., 1993) compared to earlier surveys of smaller areas. Chapter 2 describes the details of the observations and data reduction.

The analysis begins with the compilation of a catalogue of radio sources from the ATCA observations, and the determination of their optical counterparts. The radio and optical source counts are constructed from the observations, following established methods. Models for radio and optical luminosity functions are investigated, along with various types of evolution. These are used to predict the source counts and are compared with the observational results. This work is detailed in Chapter 3.

In Chapter 4 the *bivariate* (radio/optical) luminosity function is modelled, and used to make predictions of the bivariate source count distribution. The observed source count distribution is constructed and compared with the model predictions. This comparison is used to investigate the use of the bivariate luminosity function as a predictor of expected optical identification rates for radio surveys, and vice versa. The redshift distribution for galaxies is predicted from the model bivariate luminosity function, and discussed.

Results from the spectroscopic observations are presented in Chapter 5. Classification of galaxies by spectral properties is carried out, and an analysis of spectral line ratios is made using various diagnostic diagrams to distinguish between galaxies whose predominant energy source arises from starburst or AGN activity. A preliminary calculation of the observational radio galaxy luminosity function is also presented, and it is compared with model luminosity functions used in earlier chapters.

Chapter 6 discusses some interesting sources from the sample, and the conclusions of the thesis are presented in Chapter 8.

Chapter 2

Field selection, observations and data reduction

2.1 Field selection

The following criteria were used to select the *Phoenix Deep Survey* (PDS) field:

1. absence of strong radio sources to reduce confusion which might complicate detection of faint sources. This was done by searching the Parkes-MIT-NRAO survey (Griffith & Wright, 1993) for a suitably large area containing no source brighter than 100 mJy at 4.85 GHz,
2. high galactic latitude to avoid confusion by stellar objects, when making optical identifications,
3. low 100 μm cirrus to ease the task of optical/infrared identification. This was established by investigation of IRAS 100 μm maps (Mobasher, private communication),
4. a field size and limiting radio flux density providing the maximum number of candidates for optical spectroscopy using the 2-degree Field (2dF) spectroscopic facility at the Anglo-Australian Telescope (AAT).

The selected field has a diameter of 2°, centred at RA(2000) = $01^{h}\ 14^{m}\ 12\overset{s}{.}16$, Dec.(2000) = $-45°\ 44'\ 8\overset{''}{.}0$.

Observations of the entire field have been made with the Australia Telescope Compact Array (ATCA) at 1.4 GHz, and the Anglo-Australian Telescope (AAT) in R-band. Half the field was also observed with the AAT in V-band. In addition, observations of selected sub-fields have been performed in H-band and K-band. The ESO 3.6 m telescope was used with EFOSC to obtain spectra of a selected number of sources, and the 2dF instrument at the AAT was also used to obtain spectra of a selection of galaxies. These observations are summarised in Table 2.1.

Table 2.1 : Observations made as part of the *Phoenix Deep Survey.*

Instrument	Time spent observing	Target
ATNF (1.4 GHz)	8 × 12 hours	PDF
ATNF (1.4 GHz)	4 × 12 hours	PDFS
AAT (R-band)	3 nights	PDF
AAT (V-band)[1]	2 nights	PDF
MSSSO 2.3 m (CASPIR: H-band)	3 nights	42 selected fields
ESO 2.3 m (IRAC2b: K-band)	5 nights	21 selected fields
ESO 3.6 m (EFOSC)[2]	2 nights	23 selected sources
AAT (2dF)[3]	3.5 hours	158 selected sources

Notes:
1. Only two thirds of the field observed due to poor weather
2. 15 redshifts obtained, plus one object identified as an M-star
3. 126 redshifts obtained, plus one object identified as an M-star

2.2 The ATCA observations

The 1.4 GHz data were acquired in 12 sessions of 12 hours each, using the 6A configuration of the ATCA. The observations were carried out in mosaic mode using two frequencies, 1.380 GHz and 1.472 GHz, each with a bandwidth of 128 MHz comprised of 32 × 4 MHz channels.

Of these 12 sessions, a total of 8 were used to observe 30 pointing centres covering the whole 2° diameter field in a hexagonal pattern designed to provide uniform sensitivity over the full area of the field. The other four 12 hour observations were made with a single pointing, centred at RA(2000) = $01^h\ 11^m\ 13\overset{s}{.}0$, Dec.(2000) = $-45°\ 45'\ 0\overset{''}{.}0$. This field, lying within the uniformly sensitive coverage of the PDF, was selected to investigate fainter sources than would otherwise be detected, and to extend the radio source counts to $S_{1.4} \sim 0.1$ mJy. This field is called the Phoenix Deep Field Sub-region (PDFS). The Primary calibrator (1934-638, RA(2000) = $19^h\ 39^m\ 25\overset{s}{.}026$, Dec.(2000) = $-63°\ 42'\ 45\overset{''}{.}63$) was observed at the start and end of each 12 hours, and a phase calibrator (0153-410, RA(2000) = $01^h\ 55^m\ 37\overset{s}{.}059$, Dec.(2000) = $-40°\ 48'\ 42\overset{''}{.}36$) was observed for ten minutes every hour.

2.2.1 Radio data reduction

The data were reduced in two independent ways, using the AIPS and MIRIAD (Multi-channel Image Reconstruction, Image Analysis and Display) packages. The MIRIAD procedures were found to produce images with better sensitivity than those from AIPS. This was mostly as a result of more efficient flagging of interference (sim-

ply due to ease of use). The MIRIAD images were used as the basis for all further analysis.

External artificial interference from a transmitter located at Mt Dowe affected the shortest baseline in all observations quite severely, and most of the short baseline data were rejected. Weak self-interference from the sampler clocks was sufficiently strong to produce an artificial source at the phase centre of each image at the very low noise levels of the dataset, and this was removed by discarding data at every second channel. Since adjacent channels are not independent with respect to noise (the effective bandwidth of a single channel is twice the channel separation – a characteristic of the ATCA correlator in continuum mode) this resulted in essentially no loss of sensitivity. The first few data points recorded after returning from observations of the primary or secondary calibrators were also rejected, as it was found that the telescope had started integrating before it was stably pointed at the field centre. This resulted in spurious "ghost sources" if these data were not excluded. The flux density calibration was based on 1934-638 having flux densities of 14.9477 Jy and 14.7305 Jy at frequencies of 1380 MHz and 1472 MHz respectively [i.e., the post-1994 ATNF flux scale, which is consistent with current northern hemisphere scales (Baars et al., 1977) at the 1-2 percent level (Reynolds, 1994)].

At 1.4 GHz the primary beam FWHM of the ATCA is 30 arcmin and with the 6A configuration the synthesised beam is nominally 6 arcsec. An imaging cell size of 2 arcsec per pixel was used, providing approximately 9 pixels per synthesised beam area. The radio images for each pointing were made 2000 pixels (67 arcmin) square, to ensure that bright sources far from the centre of each field would be CLEANed correctly. This was necessary to prevent sidelobes from bright, out-of-field sources degrading the high-sensitivity image. After considerable experimentation, uniform weighting was used, as it was found that images made this way had better sensitivity than those with natural weighting. Normally it would be expected that the naturally weighted image would show lower noise characteristics, so this empirical result is unusual. The differences were minor, however, and little emphasis was placed on this aspect of the imaging. The final synthesised beam size for each of the PDF pointing centres (in the RA×Dec sense) was $\sim$ 8 arcsec $\times$ 10 arcsec and for the PDFS was 5.5 arcsec $\times$ 6.9 arcsec.

The images for each pointing were then CLEANed individually. To this point in the imaging procedure, the methods were the same for both the PDF and the PDFS. For the PDFS the final step involved correction for the response of the primary beam as a function of distance from the field centre. For the PDF the final step involved both correction for the primary beam response, and construction of a mosaic of the images (Sault et al., 1996). A contour map of the sensitivity of the resulting mosaic is exhibited in Figure 2.1. The asymmetry visible in this figure principally reflects the different levels of external interference experienced during the 8 observing sessions contributing to the final image.

The distribution of the pixel values in the two degree diameter region of the PDF can be seen in Figure 2.2. This is a histogram of the number of pixels in the PDF as a function of their flux density value. A similar figure for the PDFS is shown in

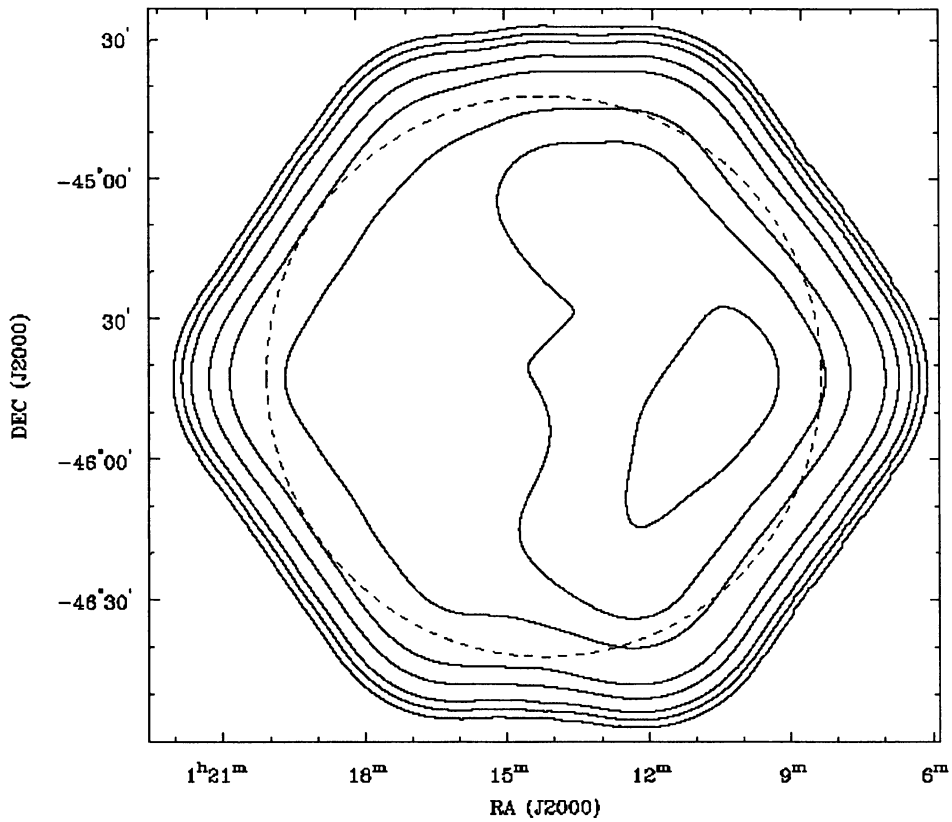

Figure 2.1 Contour map showing the RMS noise level in the ATNF mosaic. The dashed circle is the 2 degree diameter region defining the PDF. The contour levels are 50, 70, 100, 200, 300, 500, 700, 1000 μJy.

Figure 2.3. The slightly non-gaussian tail below about -4σ in both Figures is an indication of the limited dynamic range of the images. In particular, the north-east quadrant of the PDF suffers from more limited dynamic range than the rest of the mosaic (Figure 2.1), which will contribute to this tail.

The images of the PDF and the PDFS are presented at the end of this thesis. The mosaic of the PDF is shown as a contour map, with contour levels of 0.17, 0.2, 0.3, 0.4, 0.5, 0.7, 1, 2, 3, 5, and 10 mJy. The two degree diameter region encompassing the PDF is marked by a solid circle. The regions outside this area where few or no individual images from the mosaic overlap have been removed from this image. The PDFS image is shown as a grey-scale having extremes of -0.2 mJy (white) and 0.2 mJy (black).

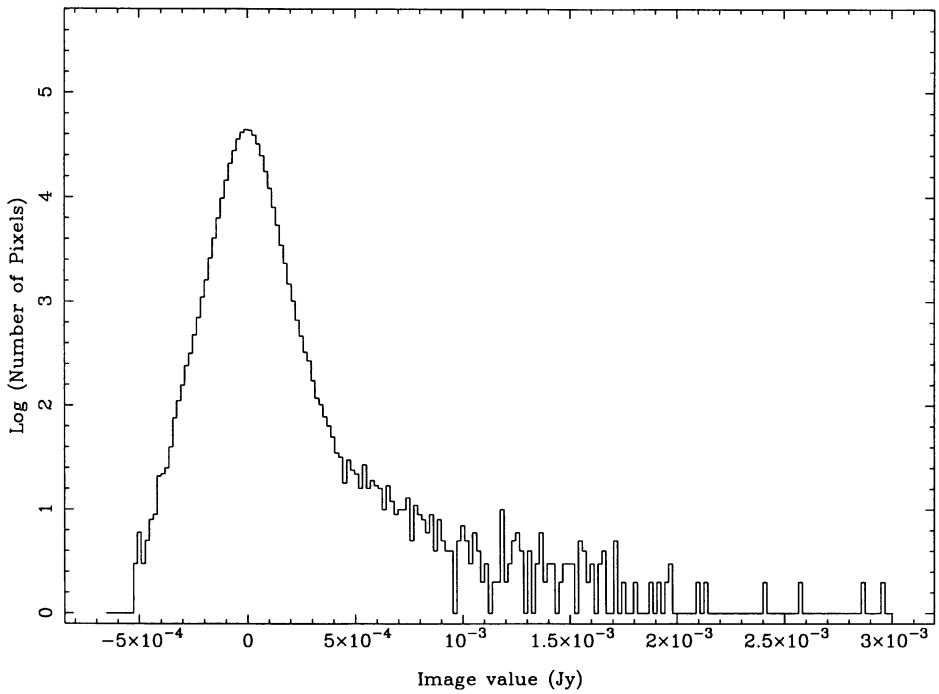

Figure 2.2 Histogram showing the number of pixels in the PDF versus their flux density. Around zero flux density, the histogram describes the characteristics of the noise in the image, and is commonly approximated by a gaussian. Above about 0.3 mJy the flux density in the image is no longer dominated by noise, but by radio sources. This explains the change in the slope of the histogram at this point.

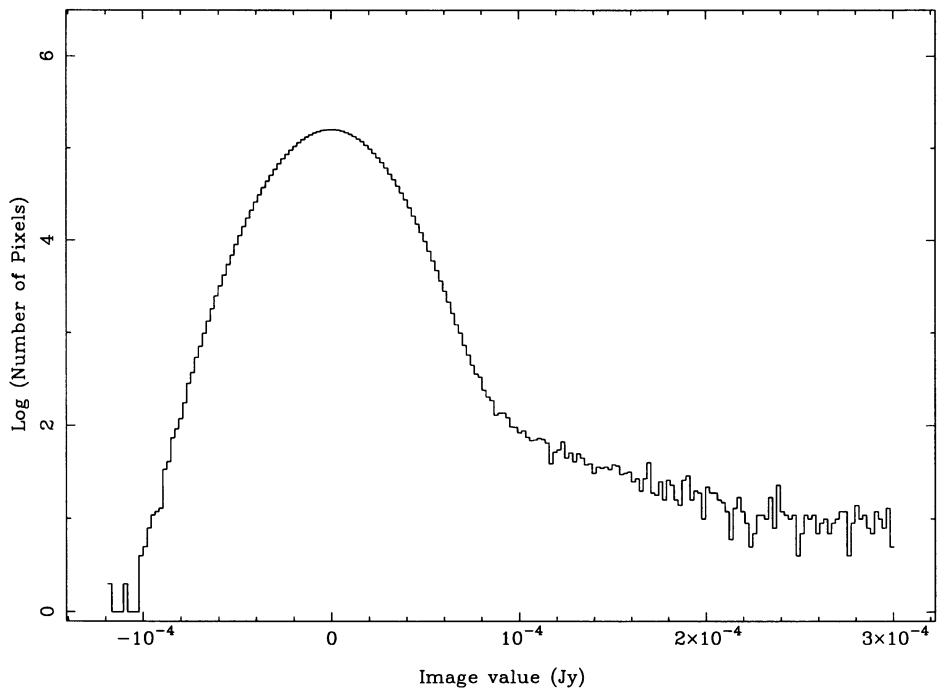

Figure 2.3 As for Figure 2.2 but for the PDFS.

2.3 The MOST observations

Prior to the ATCA observations, observations of the PDF had also been carried out using the Molonglo Observatory Synthesis Telescope (MOST) (Robertson, 1991) over a 3 MHz bandwidth in the radio continuum at 843 MHz. The MOST observations consist of a mosaic of 17 fields covering a much larger area than the PDF, reaching a (1σ) sensitivity of approximately 0.5 mJy in regions unaffected by sidelobes of strong sources.

The MOST data were used to confirm the absence of very strong sources in the field prior to the ATCA observations. Combined with the ATCA observations, the MOST data were used to provide consistency checks, confirming the validity of the brighter sources in both sets of observations. They were also used to obtain information on the relative flux density scales in the images. This knowledge will be of benefit to the upcoming SUMSS (Sydney University Molonglo Sky Survey) observations, which will utilise the new wide-field imaging capability of the MOST (Large et al., 1994). The combination of MOST and ATCA data for the PDS will be useful in linking the low density of actively star forming galaxies detected in the SUMSS to the same population investigated in greater depth in this thesis.

2.4 The AAT observations

The PDF was observed with the AAT over a total of 5 nights using the CCD prime focus (f/3.3) imaging system. The first three nights observations (made in September 1994) used an R-band filter to survey the full PDF, and began the survey of the PDF with a V-band filter The properties of these filters are given in Table 2.2, and more details on can be found on the web[1]. The conditions for these observations were photometric, with the seeing varying between 1 and 2 arcsec. The remaining two nights observations (made in October 1995) continued the V-band survey but was affected by poor weather conditions, and only slightly more than half the field was surveyed with this filter. The seeing for these nights was periodically as good as 2 arcsec, but more commonly 3 or 4 arcsec or worse. Figures 2.4 and 2.5 show the positions of the observed CCD frames relative to the region of the PDF. The detector used was the Tektronix 1024×1024 pixel CCD. Details of the properties of this detector can be found on the web[2]. This CCD at f/3.3 has a pixel scale of 0.39″/pixel, giving a field of view of 6.656 × 6.656 arcmin.

Each frame had an integration time of 60 seconds for the R-band survey, and 120 seconds for the V-band survey. The photometric standards used were the stars TPhe A, TPhe C and TPhe D, from the Landolt catalogue of photometric standards (Landolt, 1992).

[1] http://www.aao.gov.au/local/www/cgt/ccdimguide/ccd_app1.html
[2] http://www.aao.gov.au/local/www/cgt/ccdimguide/ccd_chap2.html

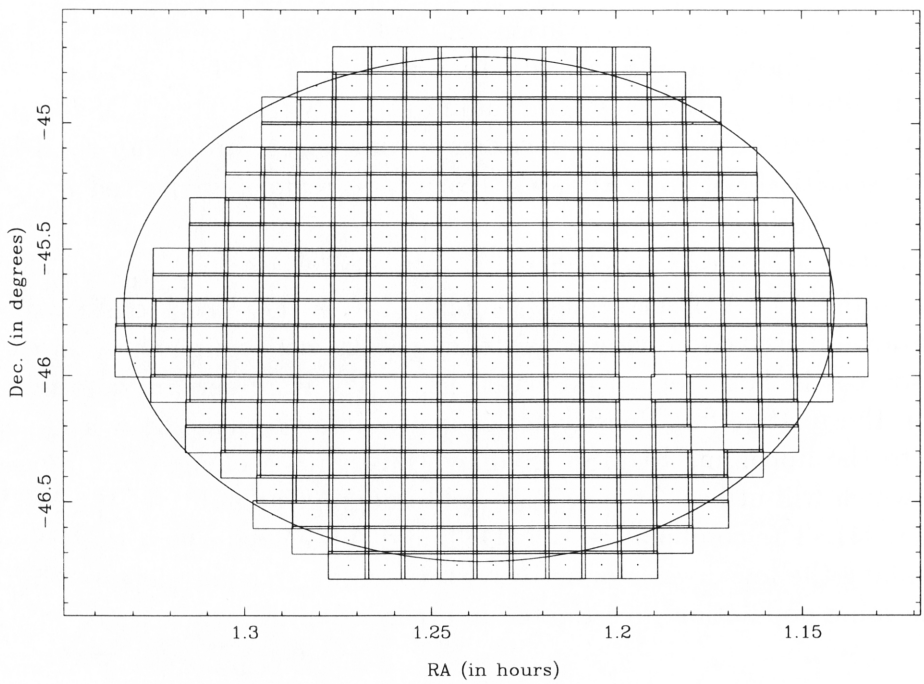

Figure 2.4 Region of the PDF (ellipse) observed in R-band. Each rectangle containing a point corresponds to a single CCD frame observation.

2.4.1 Optical data reduction

The IRAF package (Image Reduction and Analysis Facility) was used for all optical, infrared and spectral data reduction. The standard CCD data reduction procedures were followed, using the CCDPROC task. These are briefly outlined below. The flat fields used were twilight sky flats, as it was found that these produced better quality images than those made using dome flats. The CCD data reduction steps outlined here are not an exhaustive description of the specific methods and tools used, as these are dependent on the choice of software, but rather a general description of the purpose of each of the steps involved:

1. Fixing bad lines and columns. CCD detectors are not perfect, and suffer from defects in the form of groups or lines of "hot" pixels. These are removed by replacing these pixels' values with values interpolated from surrounding pixels.
2. Applying overscan strip correction. The section of the CCD which is not exposed is called the overscan strip. This region gives a measure of the response of the CCD to zero signal, and this is subtracted from the image.
3. Trimming the image. The image is trimmed to remove the overscan strip.
4. Applying flat field correction. This corrects for the relative detector pixel to pixel variation. A flat field image is obtained by making an observation of a

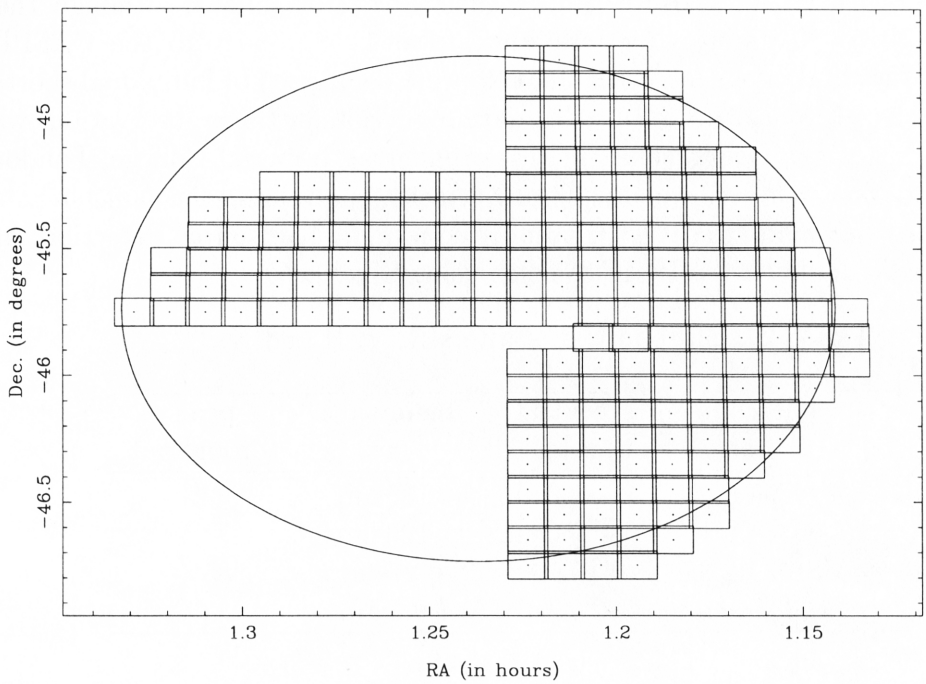

Figure 2.5 Region of the PDF (ellipse) observed in V-band. Each rectangle containing a point corresponds to a single CCD frame observation.

spatially uniform source of light, such as the twilight sky. The target image is divided by the scaled flat field image to make the correction.

The resulting images were then processed with the FOCAS2 (Faint Object Classification and Analysis System) package (Valdes, 1982) to compile the optical source catalogues. This is detailed in Chapter 3.

2.5 Infrared observations and data reduction

These observations were made in two parts. Firstly there are the H-band (1.7 μm) observations of 42 selected fields carried out using CASPIR (Cryogenic Array Spectrometer and Imager) on the MSSSO 2.3 m telescope over 3 nights. The targets were chosen from the list of radio sources with optical counterparts (see Section 3.6 for details on identifying optical counterparts to the radio sources). The observations were designed to maximise the number of targets in the field of view at each pointing. With 0.″5 pixels the CASPIR field of view is 2.′1 and, by selecting sources with appropriate configurations, between 2 and 5 objects per pointing were targeted. The integration on each target field was a total of about 5 minutes, comprised of individual 5 second integrations.

There are also the K-band (2.2 μm) observations made using IRAC2b (Infrared

Array Camera) on the ESO 2.3 m telescope. A total of 21 fields were observed over 5 nights, with most exposure times being a total of 1 hour, although they ranged from 10 to 80 minutes for individual frames. Similarly to the CASPIR observations, the total exposures with IRAC2b were comprised of individual shorter exposures, each of 1 minute duration. The data reduction for these observations was carried out by Antonis Georgakakis, a PhD student at Imperial College, London. This data reduction was performed using IRAF tasks, and follows the same steps as those described below for the CASPIR data reduction. The source detection and photometry were made on the IRAC2b fields using SExtractor.

Table 2.2 : Properties of filters R, V, H and K.

filter	telescope	central wavelength	bandwidth	peak throughput
R	AAT	~ 660 nm	135 nm	92%
V	AAT	~ 550 nm	120 nm	77%
H	MSSSO 2.3 m	1.672 μm	0.274 μm	85%
K	ESO 2.2 m	2.2 μm	0.4 μm	84%

The CASPIR observations were reduced using software written specifically for this purpose. This software is designed to run within IRAF. The steps outlined below are again not meant to be an exhaustive description of infrared data reduction, but instead a brief summary of each step in the process.

1. Linearity correction. The CASPIR detector's response to illumination has a quadratic form, which this step corrects for. The processes performed in this stage are the BIAS frame correction (similar to the overscan correction in the optical CCD process), the quadratic correction (which corrects for the detectors response, as described above), and subtraction of a linearized DARK frame (an exposure with the shutter closed; this corrects for signal detected by the CCD when it is not illuminated).
2. Flatfielding. Dome flats, rather than twilight skys, are used. The flat field is constructed by subtracting a "lamp off" frame from a "lamp on" frame. That is, an exposure of the uniformly illuminated dome minus an exposure with no illumination. This is done to eliminate the thermal emission from the telescope itself. The image is divided by the resulting flatfield.
3. Sky subtraction. Because the sky is very bright at infrared wavelengths, this is a very important step. Sky frames are made by combining the object frames with a median filter to remove the objects. To ensure that the objects can be removed by median filtering, the successive observations must be made at slightly differing positions on the sky. Also, the frames comprising the sky frame should ideally be close in time to the frame from which the resulting sky will be subtracted, due to the fact that the sky emission varies on a reasonably short timescale.

4. Fixing bad pixels. A similar procedure to that used for optical CCD data reduction.
5. Mosaicing. Due to the brightness of the infrared sky, individual exposures need to be quite short to prevent the CCD detector from saturating. To make a longer integration on an object many observations need to be combined, and are commonly made at slightly different positions around the source to facilitate sky subtraction. To combine the series of offset observations one of three mosaicing methods can be used. Blind mosaicing simply combines all the images at the nominal telescope offsets from the specified pointing. Manual mosaicing allows the user to interactively select the reference point in each image as the images are combined. Automatic mosaicing allows the user to select a position at which a centroiding procedure will be calculated to define the reference position in each image to be combined.

The photometric standards used were the stars HD1274, HD7644 and HD15911.

Photometry of the resulting images was performed using the PHOT task within IRAF. This was hindered by smeared images in several cases due to poor mosaicing which was, however, unpreventable. The only mosaicing option open in these cases was the blind mosaic, as there were no visible objects in the individual short exposure observations to use as references for the other two mosaicing methods. As a result of this the errors in m_H are quite large, possibly as much as 1 mag in many cases and occasionally larger. Both m_H and m_K are recorded in Table B.3.

2.6 Spectral observations and data reduction

The spectral observations were made again using two instruments, EFOSC (ESO Faint Object Spectrograph and Camera) on the 3.6 m ESO telescope at La Silla, and the 2dF (2 degree field fibre-fed spectrograph) on the AAT. The EFOSC data were reduced by Dr Chris Lidman from ESO, using the SPECRED tasks within IRAF. The 2dF data were reduced first using the version of the 2dF data-reduction pipeline software current in March 1997, and independently using the DOFIBERS routine within IRAF. The redshifts obtained from these methods were consistent in both cases.

The EFOSC observations resulted in redshift measurements of 15 objects. The 2dF observations resulted in redshift measurements of 126 objects. As 8 of the objects with measured redshifts were common to both samples, a total of 133 objects from the radio selected sample have had redshift measurements made. These are recorded in Table B.3.

2.7 COSMOS data

In addition to observations made specifically of the PDF, some existing observations were also exploited. The COSMOS database is constructed from digitally scanned

UKST plates subject to star/galaxy separation. COSMOS contains positions, B_J magnitudes, and a morphological classification for all objects in the database. In the region of the PDF, there are 17609 objects listed in the COSMOS database, and these were included in the analysis. The B_J magnitude of PDS objects identified as having a COSMOS counterpart are presented in Table B.3.

Chapter 3

Source detection and catalogues

3.1 Radio source detection and parameters

In a field the size of the PDF it is expected that almost one thousand sources down to the expected 5σ flux density cut-off of 0.3 mJy would be found, based on previous 1.4 GHz source counts (Windhorst et al., 1985; Oort, 1987; Katgert et al., 1988; Windhorst et al., 1993). The large number of sources, as well as the need to have an objective identification criterion made it desirable to have an automated source detection algorithm. However, the complexity of radio sources and the background noise made it beneficial to have an interactive yet still automated procedure for source identification and fitting. The task used for this purpose was a procedure, SFIND, written by the author for use within MIRIAD.

SFIND begins by detecting pixels brighter than the surrounding 24. It then performs a bi-parabolic fit to provide a first estimate of the peak flux density and then determines whether this is brighter than a user defined multiple of the RMS of the background noise around the source. If so, a two-dimensional elliptical gaussian is fit to the source. The algorithm identifies automatically all possibly sources, and moves the cursor to the position of each displayed source, as well as showing the parameters associated with each source. This aids the user in determining the reality or otherwise of each potential source. Although the user-confirmation of sources is subjective, the identifications are being made "blindly" in the sense that there is no *a priori* reason to accept or reject a particular proposed source. The method is especially useful for maximising the reliability of the faintest sources. Source splitting is not formally addressed by this version of SFIND. Once a peak pixel is detected, pixel values in the surrounding regions are tested to ensure they are decreasing monotonically away from the peak pixel value, and if so are included in the gaussian fitting procedure, otherwise they are ignored. (The procedure which performs the gaussian fitting uses the same algorithm invoked by the task IMFIT in both AIPS and MIRIAD.) Very few sources in the catalogue were subject to this effect, however.

Using SFIND two source lists were compiled, one for the PDF, containing 938

sources within the 2° diameter field, and one for the PDFS, containing 232 sources within a 36 arcmin diameter region. The two source lists were combined into a single catalogue of radio sources in the PDS, using the source parameters from the PDFS source list where an object was identified as being present in both lists. This catalogue of PDS radio sources is presented in Appendix A.

The formal relative errors reported for the gaussian fits used by SFIND to estimate flux density and position are usually of the order of $10^{-3} - 10^{-4}$. These are, however, not good indications of the true errors, as factors other than those used by SFIND in its error analysis produce a greater effect. Deviations of a source from a gaussian profile is one example, and another is the slightly differing synthesised beam size for each pointing centre in the mosaic comprising the PDF.

More realistic estimates of the errors in position and flux density of the radio sources were obtained by Monte Carlo methods. The RMS noise of the PDF over source free areas of about 10 square arcmin varies from about 45 μJy up to almost 200 μJy, with the mean and median both around 75 μJy. For the the PDFS the RMS noise is about 25 μJy at the centre of the field, increasing to about 40 μJy at the edge. For the PDF, artificial sources with flux densities of 2, 1, 0.5 and 0.3 mJy were placed in positions of varying background RMS noise, then recovered with SFIND to compare the detected positions and flux densities with the intrinsic values. The procedure was repeated for the PDFS, using artificial sources with flux densities of 1, 0.5, 0.3 and 0.15 mJy. It was found that for the 1 and 2 mJy sources, the positions had typical errors of only a few tenths of an arcsec in both the PDF and the PDFS. For the fainter sources, the positional errors were occasionally as large as 2 arcsec, especially in the more noisy regions of the images, but were more typically between 0.5 and 1 arcsec, for both the PDF and the PDFS. Flux density measurements returned typical errors of about 10 per cent for all sources, except for the faintest sources in regions of higher than average background noise, where differences of up to 50 per cent were found between measured and intrinsic flux densities. An alternative method for characterising position and flux density errors is described in Windhorst et al. (1984).

The criterion for including a source in the sample was that its peak flux density should be greater than four times the locally calculated value of σ, the background RMS, and that it was not obviously an artifact or noise spike. The cutoff level of 4σ was chosen to maximise the value of the interactive method of source detection. Although levels or 5σ or even higher are often preferred to minimise the number of spurious sources detected, Monte Carlo simulations with SFIND indicate that less than 1 spurious source over the whole two-degree field (assuming gaussian noise) is expected when running interactively with a 4σ cut-off. This figure is significantly less than the 20.5 spurious sources expected above 4σ due simply to gaussian noise over a two-degree diameter field, given the synthesised beam size. The Monte Carlo simulations were performed by taking a field of gaussian noise the same size as the PDF and using SFIND to detect sources above 4σ. In ten simulations an average of 4 source candidates were detected each time by SFIND and, on average, 3 of these were rejected by inspection, having features deemed unlikely to be associated

with a real source. In practice, the non-gaussian nature of the background noise in the image (due to artifacts and confusion) will act to raise the number of spurious sources. If this effect causes an order of magnitude increase in the number of spurious sources (a reasonable estimate given the low number predicted from simple gaussian statistics), the sample reliability will still be better than 99%, with fewer than 10 spurious sources expected.

Also there is another issue to be mentioned here. When trying to establish the reality of a radio source, such precautions as outlined above are required to minimise the number of spurious detections. However, many of the 3σ, 2σ and even 1σ radio sources will be real, although the fraction of spurious detections grows significantly as this factor decreases. But if radio emission is detected at the location of a known optical source, then it is almost certainly real even if the detection limit for the emission is very low. This strategy has not been used in the analysis described in this thesis, but will be investigated in future work on the PDS.

3.2 Optical source detection and classification

The FOCAS2 (Faint Object Classification and Analysis System) package (Valdes, 1982) was used to detect and classify objects in both the V-band and R-band surveys. The FOCAS2 software runs either from within IRAF or as a stand-alone program. For this analysis it was used exclusively from within IRAF. The classification procedure used by FOCAS2 to distinguish stars and galaxies is based on two parameters, "scale" and "frac", as well as the magnitudes of the objects. Both "scale" and "frac" are parameters calculated for each detected source, related to the point spread function of the image. The star-galaxy separation is carried out by selecting suitable ranges for each parameter. The "frac" parameter was not used in the final star-galaxy separation performed, as it was found that reliable classifications could be obtained even in its absence (R. Webster, private communication). Table 3.1 shows the ranges in "scale" and magnitude which were used in the definitions of object class when compiling the object catalogue.

The resulting parameters calculated by FOCAS2 include a total magnitude and an isophotal magnitude. These are very similar for bright objects, but begin to differ for objects close to the background noise level of the observations. This can be seen in Figure 3.1. All further analysis has been carried out using the total magnitude for each object.

There were a total of 95241 objects detected in R-band (excluding objects classified as noise), of which 32160 were classified as "galaxies", 14994 were classified as "stars", and 47203 were classified as "too faint". The remaining 884 fell into a category called "long", which is defined internally by FOCAS2 in terms of an asymmetry parameter. These objects are likely to be collections of bad pixels, satellite or meteor trails, but may also be edge-on galaxies. In V-band there were a total of 50556 objects detected, of which 14426 were "galaxies", 6823 were "stars", 28728 were "too faint", and 579 were "long".

Table 3.1 Ranges of parameters used in object classification.

classification	"scale"	magnitude
stars (s)	$0.7 < s \leq 1.2$	$\lesssim 22$
galaxies (g)	$1.2 < s \leq 10$	$\lesssim 22$
too faint (f)	all	$\gtrsim 22$
noise (n)	$0.1 < s \leq 0.7$	all

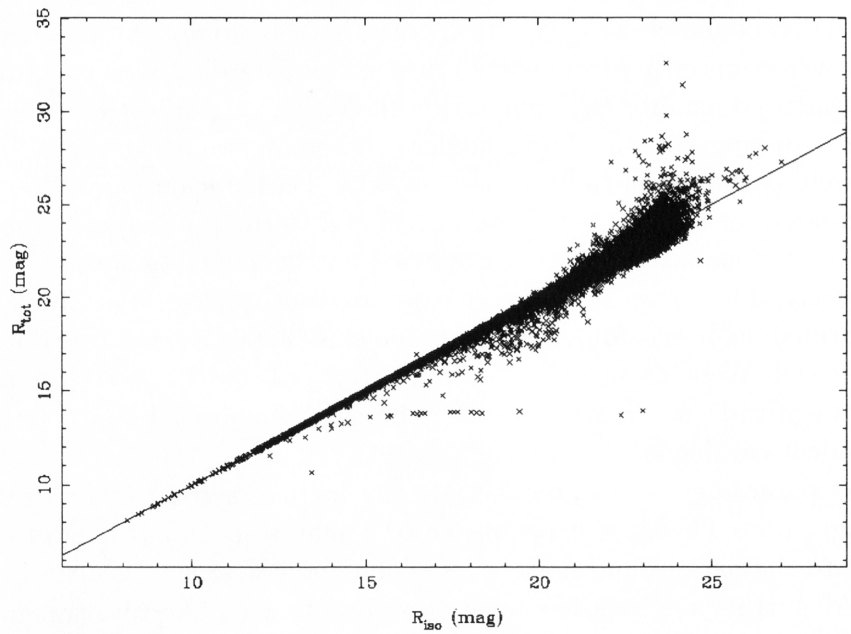

Figure 3.1 Comparison of FOCAS2 total and isophotal magnitudes. The diagonal line indicates where these quantities are equal. There are about 13 objects branching off this line at a roughly constant $R_{tot} \sim 14$. These objects are not real – they are some of a very few artifacts, such as diffraction spikes from bright stars, which were incorrectly identified as objects. They have been excluded from any analysis.

Astrometry for the CCD objects was performed in an automated fashion using Cambridge APM (Automatic Plate-measuring Machine) objects as positional references. Only stars from the APM were used in this fashion, as star positions can be measured much more accurately than those of galaxies. The position of each CCD frame is recorded in the FITS header, so using the pixel positions and the known CCD frame orientation very rough coordinates for the brightest 5 objects in each frame could be calculated. These objects were then identified with APM stars of comparable location, and a "plate solution" calculated for each frame using FOCAS2 routines. The "plate solution" is simply a matrix relating the pixel coordinates of the CCD objects to the coordinates of the corresponding APM stars. The coordinate transformation (from pixels to right ascension and declination) for each frame was then applied to each object in the CCD frame to produce the final optical catalogue.

3.3 The radio source counts

3.3.1 Sample completeness and corrections

In determining the differential source counts close to the survey limits it was necessary to apply so-called "weighting" and "resolution" corrections (Oosterbaan, 1978; Windhorst et al., 1985; Oort, 1987; Windhorst et al., 1993). The weighting correction accounts for incompleteness due to the increasing attenuation of the beam with increasing distance from the field centre, i.e. the observations are less sensitive closer to the edges of each field. The correction for a given flux density is calculated by dividing the total area of the field by the area over which a source of that flux density could be detected. This, multiplied by the number of detected sources of that flux density, represents the total number of sources with that flux density in the entire area implied by the presence of the detected sources. Tables 3.2 and 3.3 show the total correction applied along with the other details of the radio source counts.

The resolution correction accounts for the fact that extended objects with a total flux density above the survey limit can be missed by a search procedure which initially selects candidates based on the peak flux density. The source catalogues from the PDF and the PDFS are derived in terms of peak flux density limits, 0.3 mJy for the PDF and 0.1 mJy for the PDFS, and so such a correction was necessary. Given a flux density S, there will be an angular size ($\Psi_{\mathbf{max}}$, say) beyond which that source will no longer be detected because its peak flux density *in the data* drops below the source detection cut-off. The distributions of angular size as a function of flux density for the PDF and PDFS are shown in Figures 3.2 and 3.3. The angular sizes on the ordinate are the geometric mean of the major and minor axis of the source (after deconvolution with the synthesised beam size) in arcseconds. To correct for this "resolution" effect, a knowledge of the intrinsic angular size distribution as a function of flux density is required.

An exponential form for the integral angular size distribution, $h(\Psi)$, has been

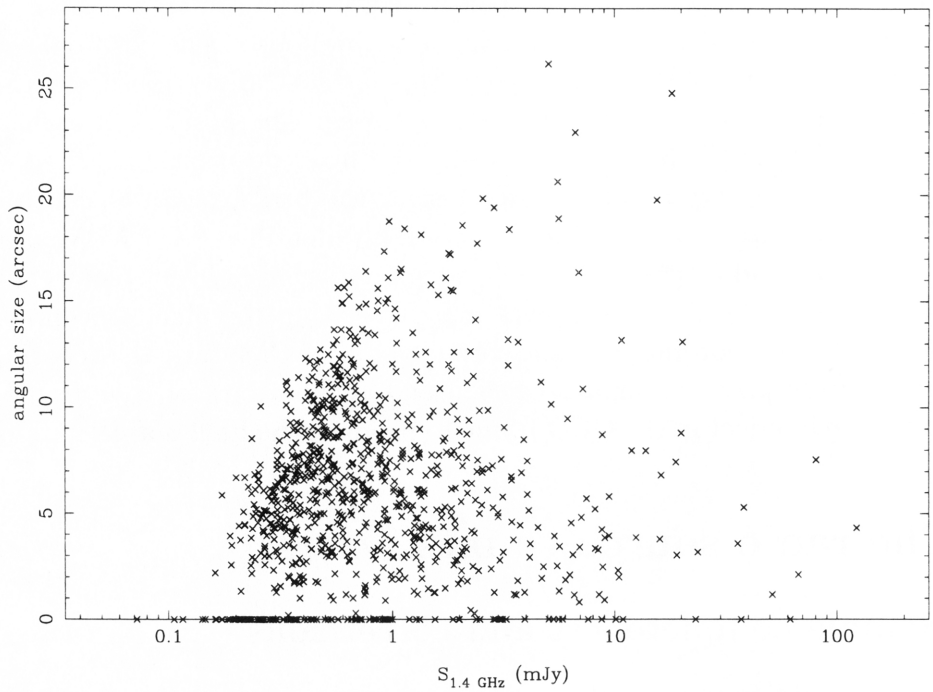

Figure 3.2 Angular sizes, after deconvolution with the synthesised beam size, for sources in the PDF. The maximum angular size detectable at a given flux density is apparent from this diagram. Sources with measured sizes equal to or smaller than the synthesised beam were assigned a deconvolved size of zero, indicating a "point-source" object.

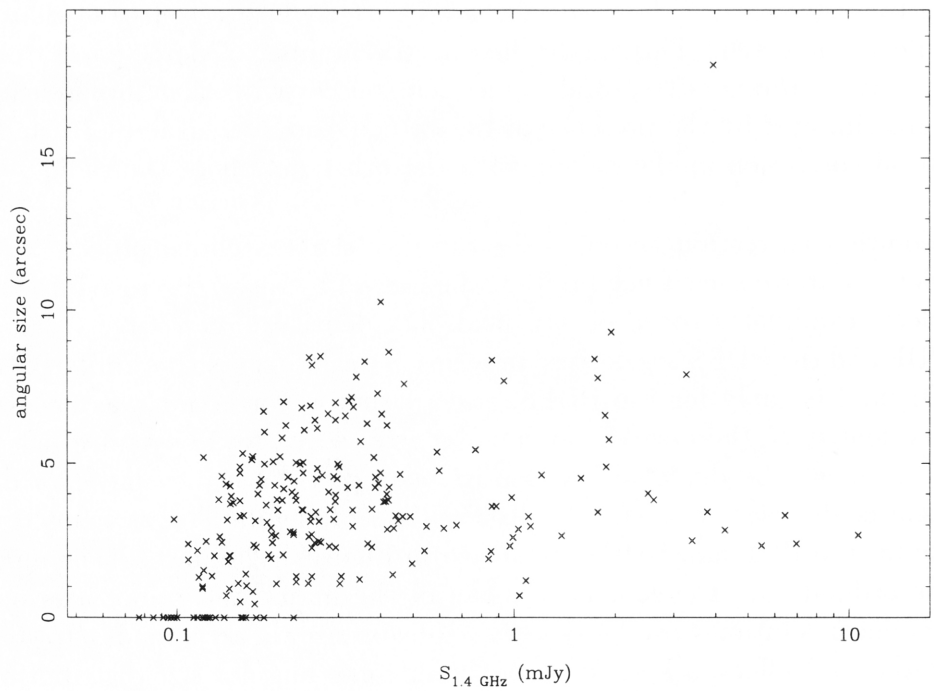

Figure 3.3 As in Figure 3.2, but for sources from the PDFS.

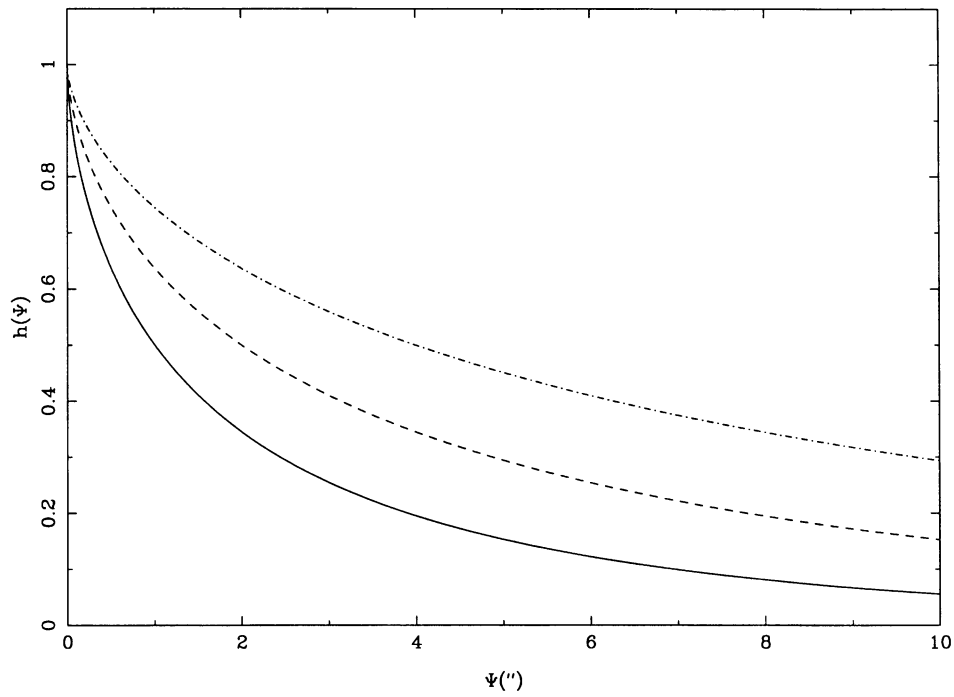

Figure 3.4 The integral angular size distribution for radio sources, $h(\Psi)$. Solid line: $S_{1.4} = 0.1\,\mathrm{mJy}$; Dashed line: $S_{1.4} = 1\,\mathrm{mJy}$; Dot-dashed line: $S_{1.4} = 10\,\mathrm{mJy}$.

adopted (Windhorst et al., 1990):

$$h(\Psi) = e^{-\ln 2\,(\Psi/\Psi_{\mathrm{med}})^{0.62}} \tag{3.1}$$

with

$$\Psi_{\mathrm{med}} = 2.0''\, S_{1.4}^{0.30} \tag{3.2}$$

where $S_{1.4}$ is in mJy, and Ψ is in arc-seconds. Here Ψ is the apparent angular size for a radio source. The shape of $h(\Psi)$ is shown in Figure 3.4 for three values of $S_{1.4}$. The correction factor, c, is then simply calculated from h, given an angular size cut-off from the sample:

$$c = \frac{1}{1 - h(\Psi_{\mathrm{max}})} \tag{3.3}$$

where Ψ_{max} is the maximum detectable angular size at the given flux density. The quantity Ψ_{max} was calculated from the data by deconvolving the observed angular size with the beam. This calculation was hampered by the different synthesised beam sizes for each pointing centre field within the PDF mosaic. However, while this made it difficult to estimate individual angular source sizes with any great accuracy, it was found that it did not significantly affect the value of Ψ_{max}. An average synthesised beam size of 8 arcsec $\times$ 10 arcsec for the whole mosaic was used.

An indication of the validity of $h(\Psi)$ is presented in Figure 3.5. This Figure shows a comparison of the observed differential angular size distribution (for the

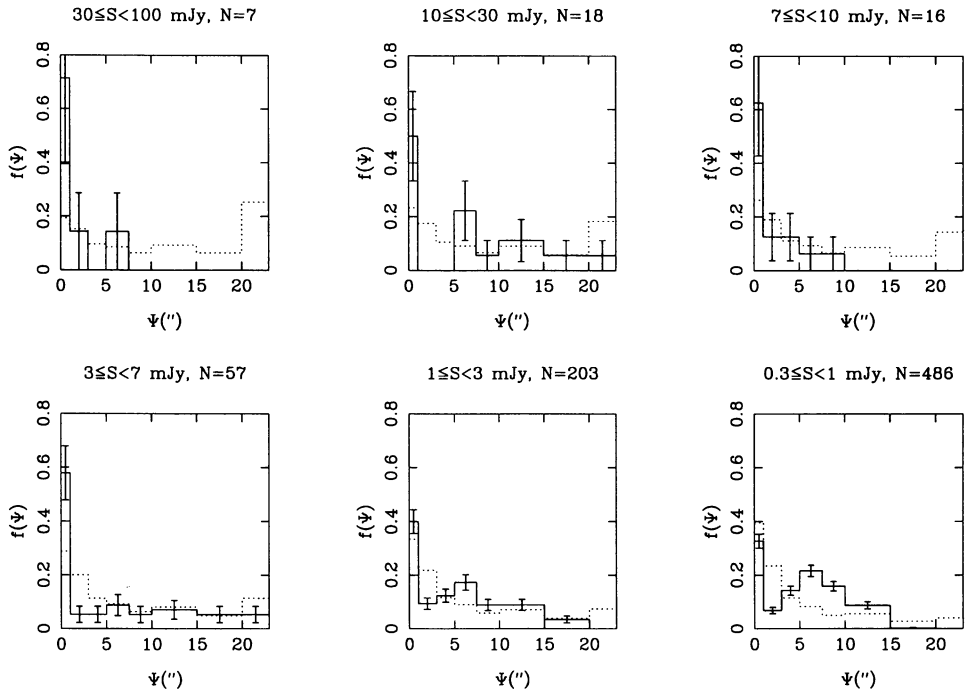

Figure 3.5 The observed differential angular size distribution, $f(\Psi)$, from the PDF (solid line) compared with the predicted distribution calculated from $h(\Psi)$ (dotted line). The error bars shown assume Poisson statistics ($\sqrt{N}$). The flux density ranges and angular size bin widths are taken from Figure 2 in Windhorst et al. (1990), to aid in comparison. The only exception is their faintest flux density bin ($0.4< S_{1.4} <1.0$ mJy), which is replaced here by $0.3< S_{1.4} <1.0$ mJy.

PDF sources only) with that predicted from $h(\Psi)$. (The PDFS sources were not included, as a complete sample with a uniform synthesised beam size was desirable to minimise possible bias in the analysis.) The format of this Figure is the same as that of Figure 2 from Windhorst et al. (1990) to allow direct comparison of the two. One small difference is the extent of the faintest flux density bin between the two Figures, the values encompassed here extending down to 0.3 mJy compared to their 0.4 mJy limit. Aside from the faintest and brightest flux density bins shown here, the predictions from $h(\Psi)$ compare well with the observations, and are within the Poisson errors for all but a few angular size bins. For the brightest flux density bin there are too few sources in the PDF to put much weight behind the differences, however the differences in the faintest flux density bin could be an indication that $h(\Psi)$ is no longer valid for those flux densities. There are only 13 objects contributing to this bin in Figure 2 of Windhorst et al. (1990), which shows reasonable consistency with the predictions, but almost 500 objects here from the PDF The true angular size estimation for the faintest objects in the PDF is quite coarse, though, especially since this estimate was made using only an average synthesised beam size for the whole mosaic. Hence, a more detailed analysis of the true angular sizes of this sample is needed to confirm whether the assumed $h(\Psi)$ is indeed less accurate at

sub-mJy flux densities.

3.3.2 Constructing the radio source counts

The radio source count distributions were constructed by counting the number of radio sources in specified flux density bins. The number of sources in each bin was then divided by the area of the survey and the bin width (in janskys) to produce the number of sources per steradian per jansky. The flux density bins were defined by starting with a lowest flux density boundary of $S_{\rm min}$, the lowest measured source flux density, and incrementing bin boundaries by a factor of $\sqrt[4]{2}$. This factor was chosen to provide good resolution while also retaining a large number of sources per bin. It also produces bin widths which are logarithmically equal in size. At higher flux densities, however, the factor was increased to $\sqrt{2}$ or 2 for those bins which would otherwise have less than 30 sources (c.f. Windhorst et al., 1993). The mean flux density for each bin was calculated using Equations (19) and (20) from Windhorst et al. (1984). This turns out to be equal to the geometric mean of the bin delimiters (to within 1%), except in the case of the brightest two bins of the PDF. The counts are normalised to those expected in a Euclidean geometry by dividing by $S^{-2.5}$. Numerical values are given in Tables 3.2 and 3.3.

The radio source counts, constructed for the PDF and PDFS, are presented in Figure 3.6. The MOST source counts are overlayed, after being shifted to 1.4 GHz from 843 MHz, using a flux density dependent spectral index taken from Figure 5(a) of Windhorst et al. (1993). Points from other surveys (Windhorst et al., 1993) are also plotted, as a comparison, and the PDS counts are in good agreement with these. The error bars illustrate the uncertainties due simply to counting statistics, assuming a Poisson process ($\sqrt{N}$).

The striking feature in Figure 3.6 is the flattening of the counts below $S_{1.4} =$ 1 mJy. The shape of the observed counts at this faint level is in agreement with the previous studies (Windhorst et al., 1993; Rowan-Robinson et al., 1993, and references therein). The PDFS counts in the overlap region, between about 0.2–0.4 mJy, are notably higher than those from the PDF. This difference may be partially explained by discrepancies in the resolution corrections to the two samples. This comes about since SFIND may detect sources in the PDFS with peak flux densities below the level detectable in the PDF, but with total integrated flux densities in the overlap region. The PDFS, being a smaller sample, is more strongly affected by the resolution correction when trying to account for this effect, hence resulting in the higher source count.

3.3.3 Radio source count models

The PDF radio source counts shown in Figure 3.6 represent the largest 1.4 GHz sample so far obtained to such faint flux density limits. Galaxy population and evolution models predicting radio source counts (Rowan-Robinson et al., 1993) can be

Table 3.2 The PDF radio source counts. $N_0 = S^{-2.5}$. See Table 3.3 for column descriptions.

S (mJy)	<S> (mJy)	N	N(S) (ster^{-1})	dN/dS (ster^{-1}Jy^{-1})	N/N$_0$
0.219					
	0.239	51	5.33×10^4	5.37×10^9	4.75
0.261					
	0.284	63	6.58×10^4	3.20×10^9	4.37
0.31					
	0.338	78	8.15×10^4	1.93×10^9	4.05
0.369					
	0.402	78	8.15×10^4	1.39×10^9	4.50
0.438					
	0.478	82	8.57×10^4	1.10×10^9	5.47
0.521					
	0.569	69	7.21×10^4	7.60×10^8	5.85
0.62					
	0.676	67	7.00×10^4	6.15×10^8	7.31
0.737					
	0.804	53	5.54×10^4	4.09×10^8	7.49
0.877					
	0.956	53	5.54×10^4	3.34×10^8	9.43
1.043					
	1.137	40	4.18×10^4	2.12×10^8	9.25
1.24					
	1.352	43	4.49×10^4	1.92×10^8	12.87
1.475					
	1.608	30	3.13×10^4	1.12×10^8	11.66
1.754					
	1.912	34	3.55×10^4	1.07×10^8	17.12
2.085					
	2.480	45	4.70×10^4	5.44×10^7	16.67
2.949					
	3.507	31	3.24×10^4	2.65×10^7	19.31
4.171					
	5.892	35	3.66×10^4	8.77×10^6	23.40
8.342					
	31.528	40	4.18×10^4	3.34×10^5	67.95
133.467					

Table 3.3 The PDFS radio source counts.

S (mJy)	<S> (mJy)	N	N(S) ($ster^{-1}$)	dN/dS ($ster^{-1}Jy^{-1}$)	N/N_0
0.096					
	0.124	54	1.86×10^{10}	6.27×10^{5}	3.22
0.161					
	0.192	51	9.39×10^{9}	5.92×10^{5}	4.79
0.228					
	0.272	46	5.99×10^{9}	5.34×10^{5}	7.27
0.323					
	0.384	34	2.95×10^{9}	3.95×10^{5}	8.53
0.457					
	2.369	47	4.61×10^{7}	5.46×10^{5}	12.60
12.288					

Notes
Column 1: Flux density bounds on each source count bin.
Column 2: Mean flux density of each bin.
Column 3: Number of sources per bin.
Column 4: Number of sources per steradian in each bin.
Column 5: The differential source count corrected by weighting factor and for resolution effects.
Column 6: The normalised source count.

compared with this new sample to investigate how different populations contribute to the count, and what role galaxy evolution plays.

Following the discussion in Section 1.4 the two-population model described by Condon will be adopted in the analysis of the radio source counts herein, and Condon's nomenclature adopted when referring to "starburst" galaxies, but using "AGN" rather than "monster" to describe galaxies powered by a compact nuclear object. One effect of adopting this two-population model is the fact that it predicts some flux density above which one population dominates and below which the other does. Kron et al. (1985) claim this cross-over point from one population to the other happens at 9 mJy. Benn et al. (1993) imply that 1 mJy is this dividing flux density. The question of precisely where the change between the observed galaxy populations occurs as 1.4 GHz flux density decreases forms an important aspect of the predictions of model radio galaxy luminosity functions and their evolution.

The 60 μm luminosity function of field galaxies has been reliably determined following the IRAS mission (Saunders et al., 1990). As a result of the strong correlation between 60 μm and 1.4 GHz luminosities and flux densities, these FIR luminosity functions can be transformed into a radio luminosity function model. This model

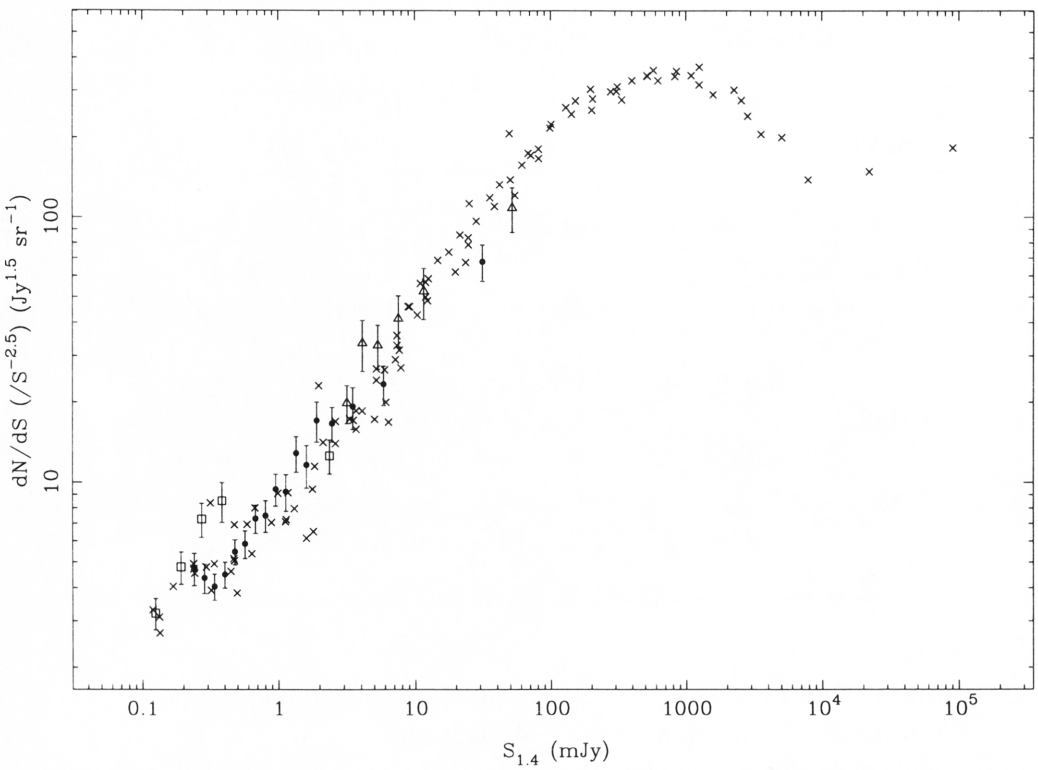

Figure 3.6 Circles – 1.4 GHz source counts for the PDF; Boxes – 1.4 GHz source counts for the PDFS; Triangles – 843 MHz source counts (shifted to 1.4 GHz as explained in the text) for the PDF from the MOST; Crosses – Example comparison source counts (Windhorst et al., 1993).

can be combined with luminosity functions for "normal" radio galaxies to form a model luminosity function for all radio galaxies. However, when source counts are predicted from this model, it is found that the observed source counts fainter than ~ 5 mJy lie distinctly above the prediction. To improve the predictions, evolution of the starburst galaxy luminosity function models can be invoked. These luminosity and density evolutions can be described by $L(z) \propto (1+z)^Q$ and $\phi(z) \propto (1+z)^P$ respectively. Saunders (1990) established that the FIR source counts could be well predicted by invoking either a density evolution (with $P = 6.7 \pm 2.3$) or a luminosity evolution (with $Q = 3.1 \pm 1.0$). Rowan-Robinson et al. (1993) showed that the density evolution model was inconsistent with faint radio source counts at 1.4 GHz, but that luminosity evolution was consistent with the observations.

The PDS radio source counts have been modelled using luminosity functions described by Rowan-Robinson et al. (1993). The luminosity function for the starburst galaxy component is derived from that of the IRAS 60 μm population, and is of the form (after Saunders et al. 1990)

$$\phi(L) = C \left(\frac{L}{L^*}\right)^{1-\alpha} \exp\left[-\frac{1}{2\sigma^2} \log_{10}^2 \left(1 + \frac{L}{L^*}\right)\right], \tag{3.4}$$

with parameters (assumed the same at 60 μm and 1.4 GHz) ($\alpha = 1.27$, $\sigma = 0.626$, $C = 3.25 \times 10^{-2}$). At 60 μm, $L^*_{60} = 10^{23.9}\,\mathrm{W\,Hz^{-1}}$, so correspondingly, from the radio/far-infrared correlation, $L^*_{1.4} = 10^{21.9}\,\mathrm{W\,Hz^{-1}}$. These values correspond to the "warm" IRAS galaxy component [Saunders et al. 1990, solution no. 25, Table 3(a)]. For AGN galaxies, both flat and steep spectrum sources, the luminosity functions of Dunlop & Peacock (1990) have been used, with K-corrections calculated assuming $S_\nu \propto \nu^\alpha$, with $\alpha = -0.8$. These luminosity functions have the form

$$\phi = \phi_0 \left\{ \left(\frac{L_{1.4}}{L_c(z)} \right)^\alpha + \left(\frac{L_{1.4}}{L_c(z)} \right)^\beta \right\}^{-1}, \tag{3.5}$$

with parameters

$$\begin{aligned} \phi_0 &= 10^{-6.91}, \\ \alpha &= 0.69, \\ \beta &= 2.17, \\ P_c(z) &= 26.22 + 1.26z - 0.26z^2, \end{aligned}$$

for steep spectrum AGN, and

$$\begin{aligned} \phi_0 &= 10^{-8.15}, \\ \alpha &= 0.83, \\ \beta &= 1.96, \\ P_c(z) &= 26.36 + 1.18z - 0.28z^2, \end{aligned}$$

for flat spectrum AGN. The luminosity evolution of this population is included in the redshift dependence of $P_c(z)$.

The source count models are compared with observations in Figure 3.7. Several models for the counts of the starburst population are shown, with different rates of density or luminosity evolution, including no evolution (NE). From this study, firstly, it is confirmed that both the starburst and AGN populations are required to explain the radio source counts across the whole flux density range. Secondly, a modest amount of luminosity evolution is required to fit the observed counts at the faint end. The counts, based on different values of the luminosity evolution, are predicted and compared with the observed data in Figure 3.8. A rate of $Q = 3.3 \pm 0.8$ for the luminosity evolution best fits the data, in agreement with $Q = 3.1 \pm 1.0$ from model fits to other radio surveys (Rowan-Robinson et al., 1993), and the IRAS observations (Saunders et al., 1990).

It can be concluded that the sub-mJy radio population is well modelled by a population of "starburst" or spiral galaxies undergoing luminosity evolution. The question of what happens to the *optical* luminosity of a galaxy undergoing *radio* luminosity evolution is an interesting one, deserving closer attention. This will be addressed in Chapter 4. An important point here is, although pure luminosity evolution seems to be a good model for predicting the observed source counts, there

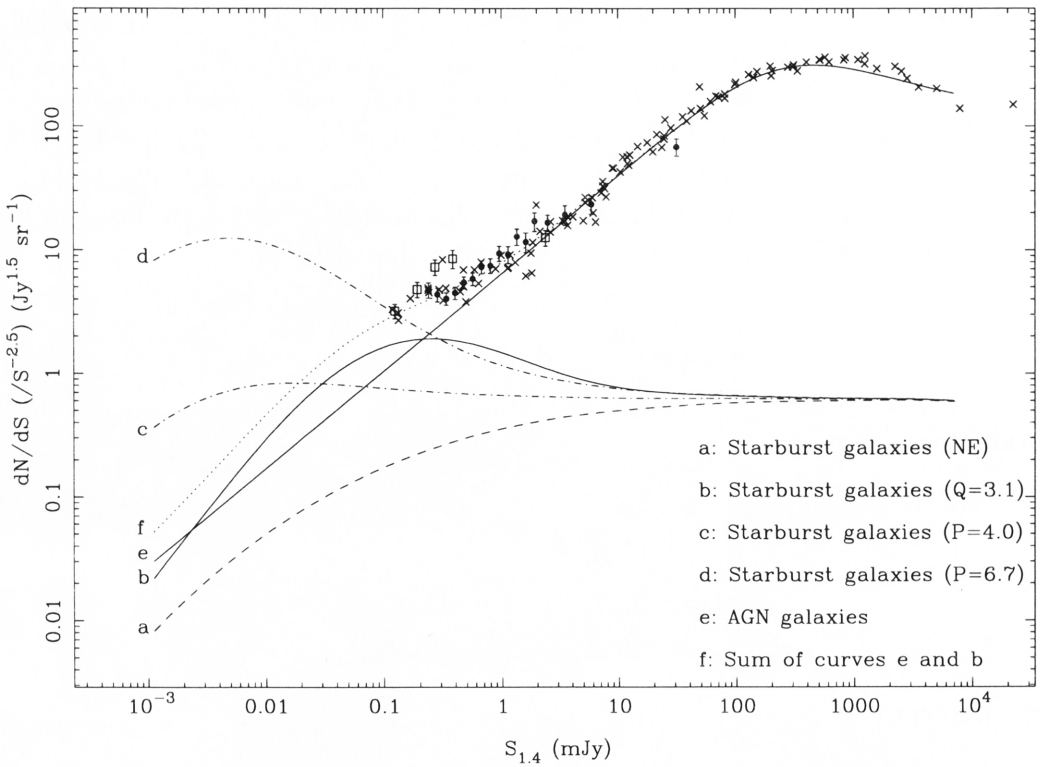

Figure 3.7 Radio source count models with observational data overlayed.

is evidence that density evolution should not be neglected. Burkey et al. (1994) provide evidence that the galaxy merger rate between $z = 0.6$ and the present evolves with redshift as $(1+z)^{2.5\pm0.5}$, speculating that this may be related to quasar and faint radio source evolution. However, it has already been shown that density evolution alone cannot reproduce the observed sub-mJy radio source counts (Rowan-Robinson et al., 1993), so perhaps the best model should really include contributions from both luminosity *and* density evolution. Although such an analysis is beyond the scope of this thesis, combinations of luminosity and density evolution models will be examined at a later stage in the analysis of PDS data. The radio source catalogues from the PDS combined with the 2dF spectroscopy provide a valuable resource for this investigation, and this will be significantly enhanced when spectral observations for all the optical counterparts (see Section 3.6) have been completed. Additional tools which will be useful in establishing the extent of each form of evolution are the redshift and luminosity distributions for the two galaxy populations. The different evolution models affect the predictions for these distributions in different ways, but a valid model must accurately predict both, as well as the source counts (Rowan-Robinson et al., 1993).

Figure 3.9 illustrates the redshift distribution corresponding to the two populations of radio sources being considered. Note how the redshift distribution changes as the limiting radio flux density is reduced. For relatively high limiting flux densities, the contribution to the radio galaxy population from starbursts is small and

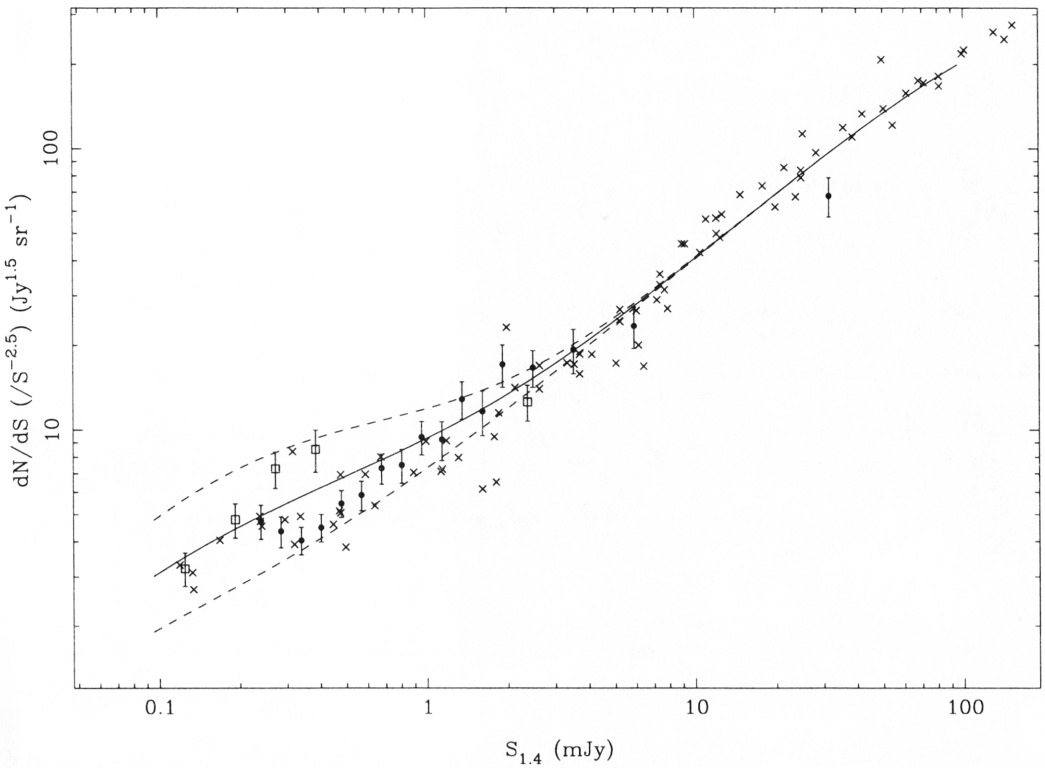

Figure 3.8 Radio source count models for differing rates of luminosity evolution with observational data overlayed. Solid line – sum of elliptical galaxy source counts and luminosity evolved spiral galaxy source counts with $Q = 3.3$; dashed lines – as for the solid line, but with $Q = 4.1$ (upper) and $Q = 2.5$ (lower).

restricted to nearby objects. As the limiting flux density is lowered the number of starbursts detected in the radio increases, as does their median redshift. With a flux density limit of 0.1 mJy the proportion of starburst galaxies detected should be about half the sample, and they should have a redshift range comparable to the AGN galaxies. Of course, without knowing the optical selection effects (since one requires an optical ID to get a redshift) these curves do not tell the whole story. The redshift distributions for various optical magnitude limited samples are predicted in Chapter 4.

3.4 Integral source counts

The *integral* radio source count distribution, while having been shown to be inferior to the differential counts for analyses of evolution and cosmology (Crawford et al., 1970), is still of interest inasmuch as it readily provides the number of sources expected to be observed brighter than a given flux density limit. The integral radio source counts are shown in Figure 3.10 for both the PDF and the PDFS. See Figure 2(b) from Becker et al. (1995) for a comparison, (but note the different units).

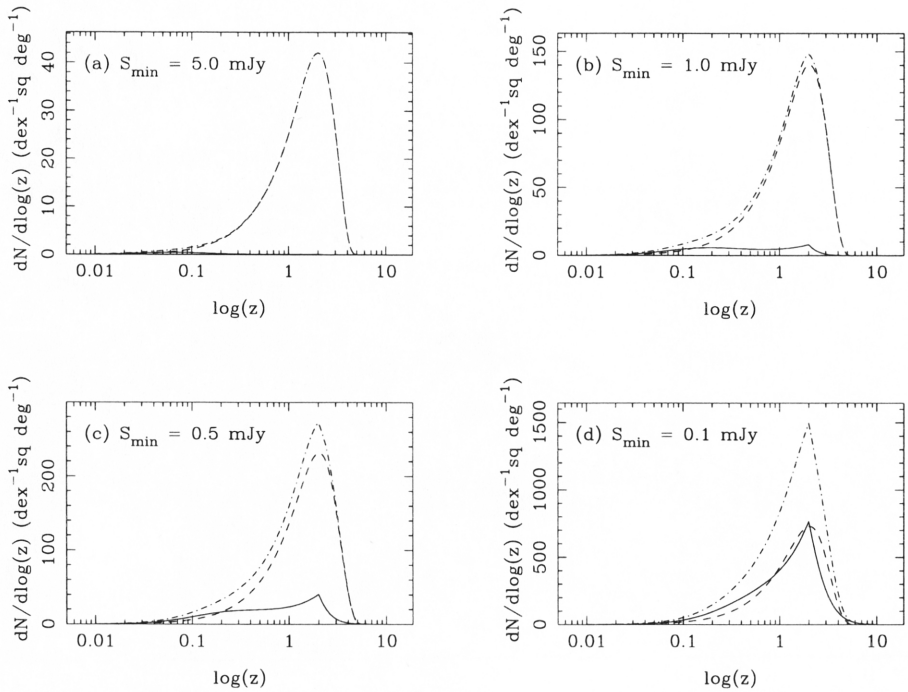

Figure 3.9 Predicted redshift distributions from the luminosity evolution model ($Q = 3.3$) showing how the distribution changes for successively lower flux density cutoffs. The solid line is the disk galaxies, the dashed is the elliptical galaxies, and the dot-dashed line is both combined.

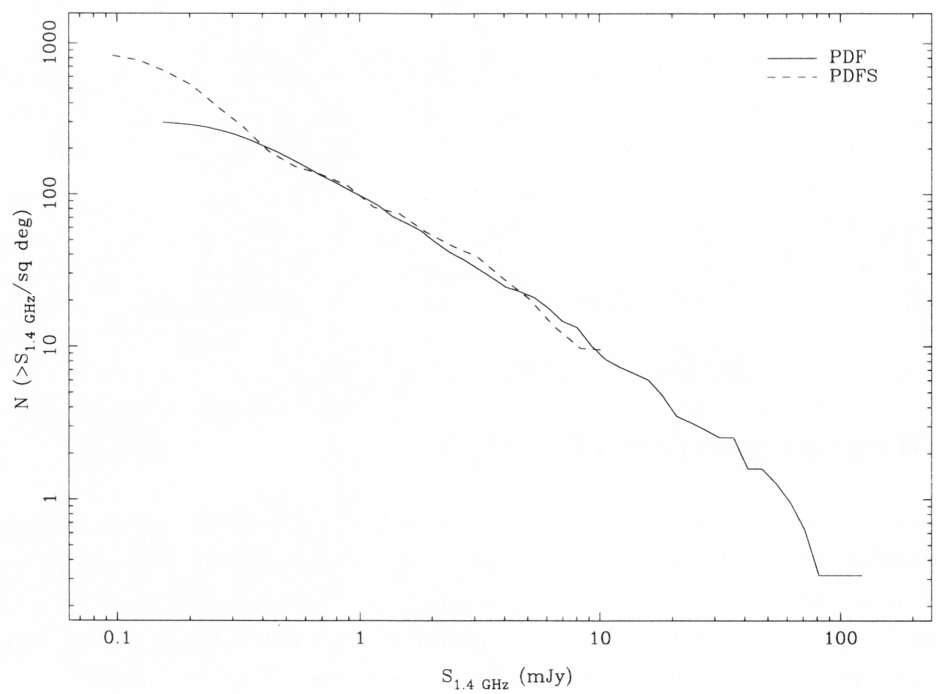

Figure 3.10 The integral source counts for the PDF and the PDFS.

The completeness level of the PDF is apparent from this diagram, and occurs where the integral source count from the PDFS rises above that from the PDF. The construction of this figure did not invoke the weighting and resolution corrections used in the construction of the differential source counts, so the counts at the faint ends are distorted by the primary beam sensitivity over the field and the bias against detecting low surface brightness extended sources with the source detection software.

3.5 Optical source counts

The optical source counts can be used as a guide to the development of models for galaxy luminosity functions and evolution in the same manner as the radio source counts. The optical source counts are constructed in the same fashion as the radio source counts, although the weighting and resolution corrections made in the radio case are not relevant here. The sensitivity of the CCD detector is quite uniform once the appropriate data reduction procedures have been performed, and so no further correction for the detector response is required. No resolution correction is made, since there is no clear distribution of angular sizes with optical flux density as there is in the radio. The bins in apparent magnitude were chosen to be 0.2 magnitudes in width, as that resulted in sufficient numbers of galaxies per bin to provide statistical robustness, while still providing good resolution. Since the magnitude scale is logarithmic in nature, a constant bin width in magnitudes is analogous to the constant logarithmic bin sizes in radio flux density chosen for the radio source counts. Unlike the radio source counts, the optical source counts have not been normalised by the Euclidean counts, for ease of comparison with other published work. Also unlike the radio source counts, the optical counts are presented here in units of number per magnitude per square degree, as opposed to number per unit flux density per steradian, for the same reason.

The COSMOS objects in the PDF were used to construct optical source counts at B_J-band (~450 nm), and these are shown in Figure 3.11 along with data points from Metcalfe et al. (1991), for reference purposes. The R-band source counts were constructed from the observational data, and are shown in Figure 3.12. Again, counts from Metcalfe et al. (1991), now in R-band, are shown for comparison purposes. Details of the optical source counts are given in Table 3.5.

In both these Figures, there is a significant excess at the brighter magnitude end. While this may be partially due to poor star-galaxy separation (by the COSMOS classifier in one case and FOCAS2 in the other) it is more likely a result of an Abell cluster which is present in the southwest region of the PDS field. Since the counts themselves are only used as a reference with which to compare model predictions, this does not affect any of the analysis in this thesis.

Both Figure 3.11 and Figure 3.12 show total source count predictions as solid lines, with the two individual populations shown separately as dashed (E/S0) and dot-dashed (disk galaxies) lines. Table 3.4 gives the Schechter function parameters defining the luminosity function used in making these predictions (Metcalfe et al.,

1991). No evolution was invoked in the calculation of the source count model from the luminosity function, and this leads to a prediction noticeably lower than the observations at $m_{B_J} > 22$. In the R-band, this can also be seen, to a lesser extent. However, given the good predictions over the range of R-band magnitudes included in the PDS sample, this function should be appropriate to examine these data provided the caveat that it is not valid at the fainter magnitudes is kept in mind. It should also be noted that the luminosity function parameters given in Table 3.4 are not necessarily unique. Other sets of parameters may also model a luminosity function which adequately predicts the source counts.

Table 3.4 Schechter function parameters used in modelling the optical source counts.

galaxy types	$\log(L^*)$ (WHz^{-1})	$\Leftrightarrow$ $\Leftrightarrow$	M* (mag)	α	$C = \phi^* \ln(10)$ Mpc^{-3}
B_J-band ellipticals	21.38	$\Leftrightarrow$	−19.6	-0.7	0.0226
B_J-band spirals	21.50	$\Leftrightarrow$	−19.9	-1.1	0.0101
R-band ellipticals	21.96	$\Leftrightarrow$	−21.05	-0.7	0.0226
R-band spirals	21.87	$\Leftrightarrow$	−20.84	-1.1	0.0168

3.6 Identification of optical counterparts to radio sources

The optical counterparts for the radio sources in the PDS were chosen preferentially from the R-band CCD observations, those being the deepest, most complete observations made. Since the R-band observations did not completely cover the PDF (see Figure 2.4) there were a small fraction of radio objects for which optical IDs had to be found from another source. The COSMOS and APM databases were used for this task. The radio sources lying outside the region of the R-band observations (see Figure 2.4) are listed in Table B.2. This table also indicates whether the radio source was identified with a counterpart from the COSMOS or APM databases.

Since the APM source positions are more accurate than those from COSMOS, the optical counterparts for the radio sources not observed in R-band are quoted with the APM position where possible. The plates measured with the APM in which the PDF lies do not however have a calibrated magnitude scale. The B_J magnitude, where given for optical IDs, comes from the COSMOS ID for these objects.

The procedure for choosing whether any given radio source had an optical counterpart is described below. Alternative methods for compiling catalogues of optical counterparts exist (Windhorst et al., 1984a, for example), and should be compared with the method presented here.

For each radio source position the optical source list was searched for objects within a given cut-off radius. Each object within that radius, and its distance

Table 3.5 The optical source counts.

<m> (mag)	N(B_J)	N(R)	dN/dm (B_J) ($deg^{-2}mag^{-1}$)	dN/dm (R)
15.10		11.00		17.51
15.30		15.00		23.87
15.50		23.00		36.61
15.70		18.00		28.65
15.90		39.00		62.07
16.10		34.00		54.11
16.30	4.00	43.00	6.37	68.44
16.50	11.00	41.00	17.51	65.25
16.70	5.00	46.00	7.96	73.21
16.90	17.00	70.00	27.06	111.41
17.10	19.00	93.00	30.24	148.01
17.30	30.00	88.00	47.75	140.06
17.50	31.00	151.00	49.34	240.32
17.70	30.00	139.00	47.75	221.23
17.90	34.00	174.00	54.11	276.93
18.10	37.00	242.00	58.89	385.15
18.30	51.00	293.00	81.17	466.32
18.50	74.00	284.00	117.77	452.00
18.70	88.00	382.00	140.06	607.97
18.90	97.00	474.00	154.38	754.39
19.10	122.00	561.00	194.17	892.86
19.30	154.00	767.00	245.10	1220.72
19.50	158.00	843.00	251.46	1341.68
19.70	191.00	1033.00	303.99	1644.07
19.90	242.00	1191.00	385.15	1895.54
20.10	255.00	1409.00	405.85	2242.49
20.30		1723.00		2742.24
20.50		1852.00		2947.55
20.70		2214.00		3523.69
20.90		2684.00		4271.72
21.10		3061.00		4871.73
21.30		3709.00		5903.06
21.50		4287.00		6822.97
21.70		5020.00		7989.58
21.90		6046.00		9622.51
22.10		7131.00		11349.34
22.30		7950.00		12652.82
22.50		7528.00		11981.18

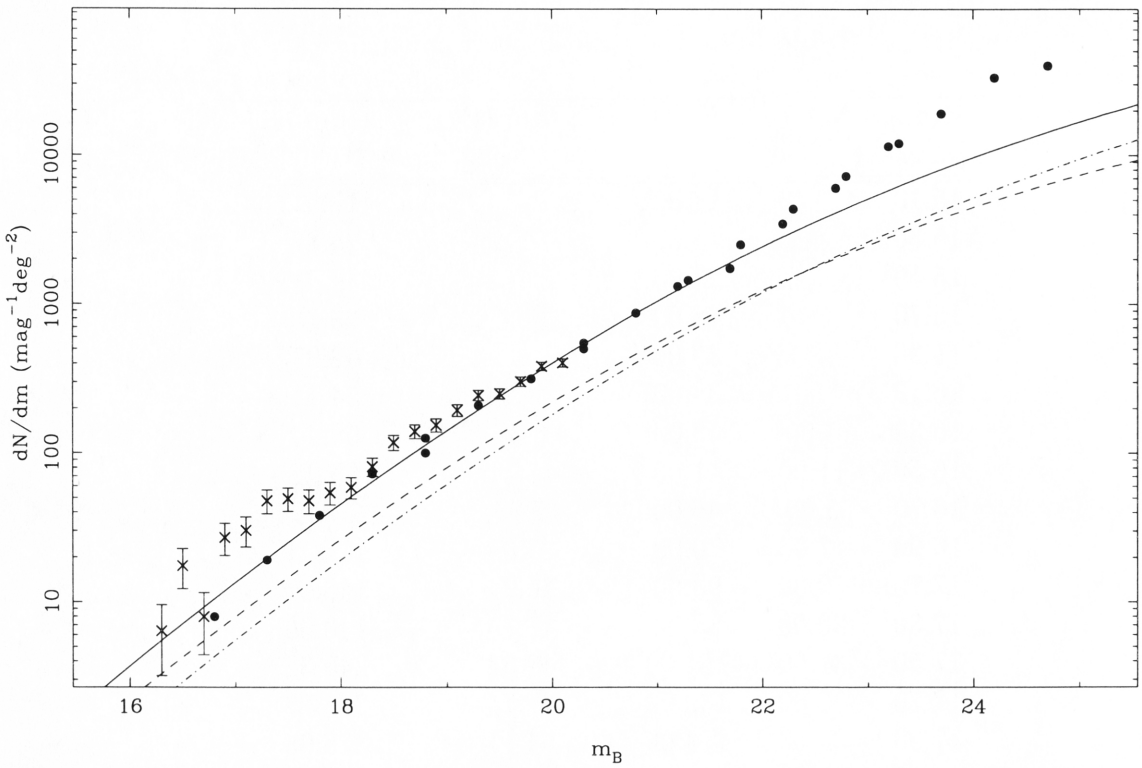

Figure 3.11 B_J-band source counts. Error bars are $\sqrt{N}$ errors. The solid line is the source count prediction from the luminosity function model (see text).

from the radio source, was recorded. Then, for each of these, a calculation of the probability of finding a source of that magnitude by chance at the observed distance from the radio source was made. For each radio source with optical sources within the cutoff radius, the most likely counterpart is the one with the lowest chance of appearing that close by coincidence. The fractional chance that a given alignment is coincidental is $F = \sigma\pi r^2$, where σ is the observed number density of optical sources brighter than the given magnitude, and r is the distance between the radio source position and the potential optical counterpart position. The number density, σ, can be calculated independently from the optical sample, and in fact a graph of σ as a function of magnitude is just the integral source count for the sample. A cut-off in the values of F can be applied, to limit optical IDs only to those least likely to be chance alignments.

This process does not take into consideration the clustering of optical galaxies on the sky. Rather, it assumes that the galaxies are uniformly distributed. It is well known that galaxies *do* cluster, however, and the resulting values obtained for F using the assumption of a uniform distribution will hence be lower limits to the true values.

In compiling the catalogue of optical counterparts, presented in Table B.1, a cut-off radius of 10 arcsec and a cut-off in F of 0.05 was chosen. The limit of $F < 0.05$ was chosen as it provides a 95% confidence level sample, minimising the

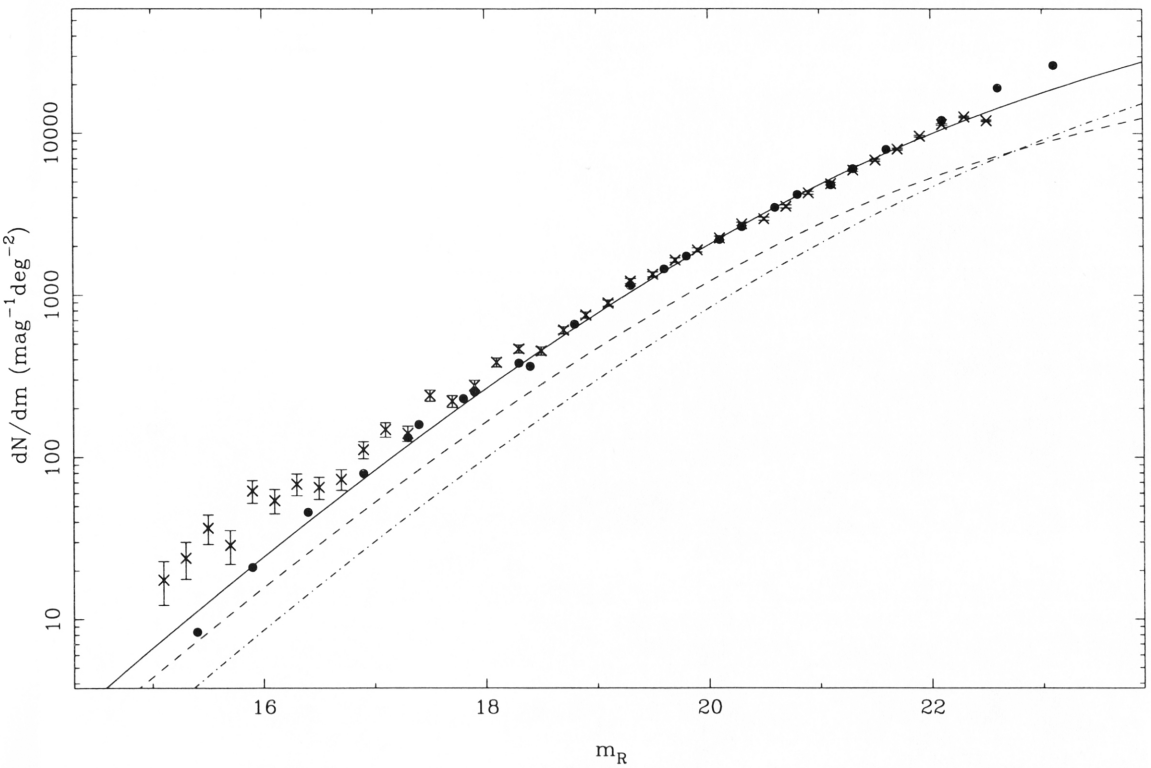

Figure 3.12 R-band source counts. Crosses are the counts in the PDS with Poisson ($\sqrt{N}$) errors shown. Filled circles are the R-band counts taken from Metcalfe et al. (1991) for comparison. The solid line is the source count prediction from the luminosity function model (see text).

chance of including a spurious ID. This also results in a sample which excludes some real IDs, but the number of these is small, and the exclusion of these few is preferable to the inclusion of a large number of questionable optical counterparts for the further analysis of the sample. A histogram of the values of F for all the identified counterparts is shown in Figure 3.13.

The cut-off radius of 10 arcsec was chosen after a consideration of Figure 3.14. Cut-offs larger than this produce very few additional optical IDs while greatly increasing the distance between optical and radio sources, making their validity harder to accept despite the calculated value of F still being less than 0.05. Since 10 arcsec approximately matches the synthesised beam size in the radio images, choosing a cut-off smaller than this would obviously exclude many valid optical IDs. Also, it seems likely that the size of the radio image synthesised beam governs the shape of curves such as those in Figure 3.14. That is, the "knee" of such a curve will appear at the distance equal to the size of the radio synthesised beam.

The radio sources identified as having optical counterparts will be investigated further at the end of the next Chapter, when they are compared with predictions of the expected number of identifications, and with the distribution in flux density of those identifications.

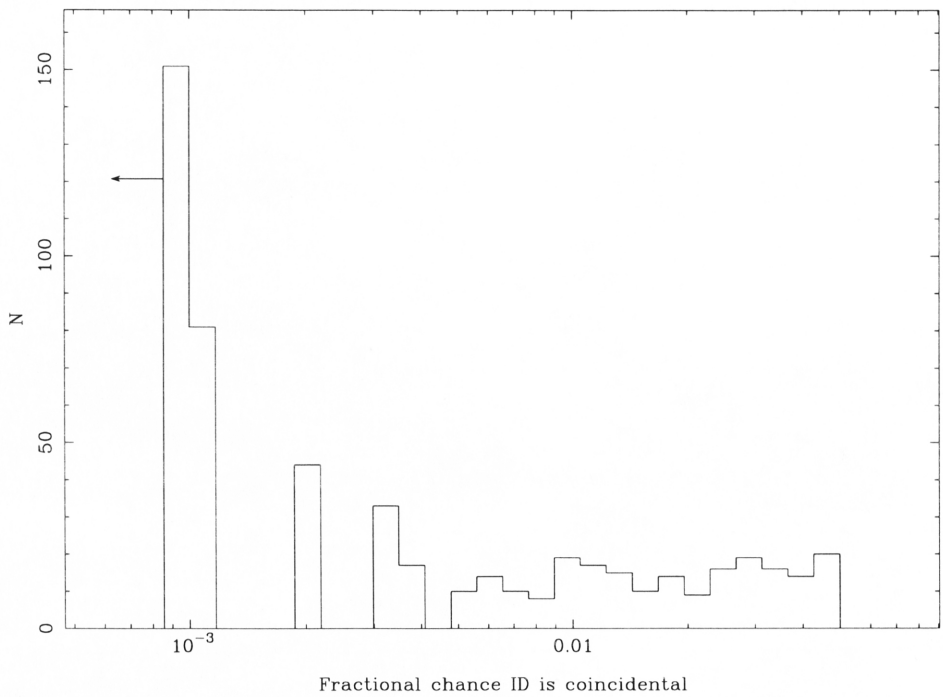

Figure 3.13 Histogram of fractional chance optical IDs are coincidental. The leftmost bin is an upper limit - the chance these objects are coincidental IDs is less than 0.1%.

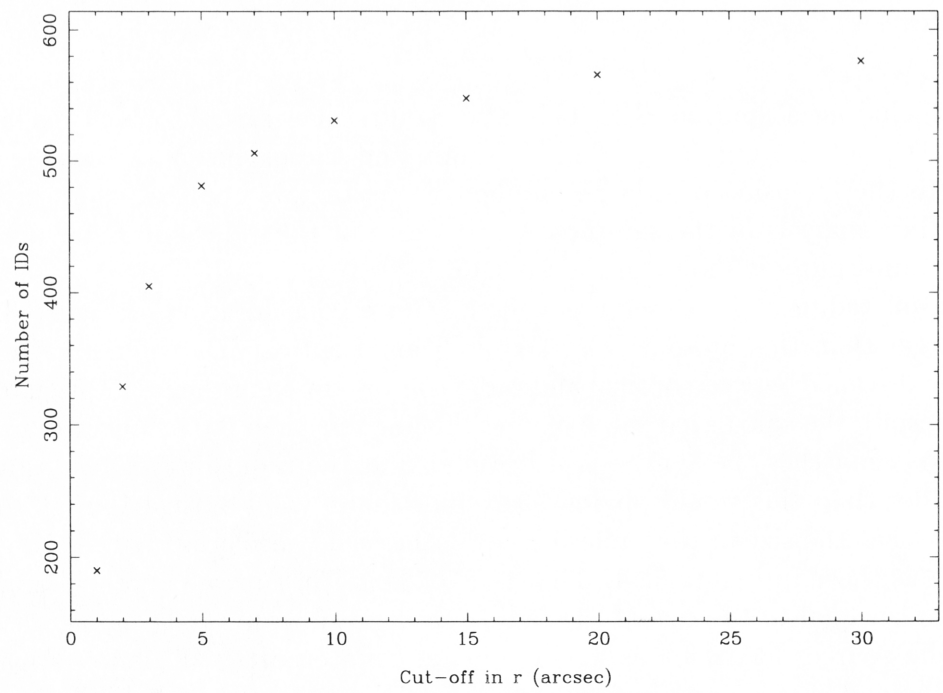

Figure 3.14 Number of optical IDs with $F < 0.05$ plotted as a function of the cut-off radius used.

Chapter 4

The bivariate luminosity function of galaxies

The PDS is a multiwavelength survey aimed at characterising the population of sub-mJy radio sources through multicolour photometry, and a significant step in this process is identifying the optical counterparts to the radio sources. To be able to predict how many optical IDs are likely to be found, and what range in magnitudes they will cover, something about the way the optical luminosity function is linked with the radio luminosity function needs to be known. This "linking" construct is the bivariate luminosity function (BLF), for radio and optical luminosities in this instance. If a model for the BLF can be constructed, a joint radio-optical source count distribution can be predicted. This bivariate source count (BSC) distribution can then be used directly to predict the expected rates for optical identifications of radio sources. Since this has been observationally established in the previous Chapter, the predictions of such a model can be compared with the observations to test the model's accuracy.

For this purpose a model bivariate (radio-optical) luminosity function and its method of construction are presented below, as well as the predicted BSC and the numbers and magnitudes of optical IDs expected from the PDS.

4.1 The bivariate luminosity function

The bivariate luminosity function (BLF) of galaxies, $\Phi(L_1, L_2, z)$, is defined as the volume density of galaxies per unit of luminosity squared at redshift z with luminosities in the intervals $[L_1, L_1 + \mathrm{d}L_1]$ and $[L_2, L_2 + \mathrm{d}L_2]$. The BLF has the property that it must integrate over each of the luminosity variables to reproduce the luminosity function of the other variable, i.e.,

$$\int_{L_1} \Phi(L_1, L_2, z)\, \mathrm{d}L_1 = \Phi(L_2, z), \tag{4.1}$$

$$\int_{L_2} \Phi(L_1, L_2, z)\, \mathrm{d}L_2 = \Phi(L_1, z). \tag{4.2}$$

As explained in Chapter 3, univariate luminosity functions can be used to predict the differential source counts at the corresponding wavelength, $n(S_\nu) = \frac{\mathrm{d}N}{\mathrm{d}S_\nu}$, (where N is the integral source count distribution). The BLF can, in the same manner, be used to generate a *bivariate* source count distribution, $n(S_1, S_2) = \frac{\partial^2 N}{\partial S_1 \partial S_2}$. This distribution is the number of galaxies per unit area of sky with flux densities in the range $[S_1, S_1 + \mathrm{d}S_1]$ and $[S_2, S_2 + \mathrm{d}S_2]$. In a similar fashion to the BLF, the BSC integrates over each flux density variable to reproduce the source counts of the other flux density variable, i.e.,

$$\int_{S_1} n(S_1, S_2)\, \mathrm{d}S_1 = \frac{\mathrm{d}N}{\mathrm{d}S_2}, \tag{4.3}$$

$$\int_{S_2} n(S_1, S_2)\, \mathrm{d}S_2 = \frac{\mathrm{d}N}{\mathrm{d}S_1}. \tag{4.4}$$

Now consider the function

$$\Psi(L_1, L_2, z) = \frac{\Phi(L_1, L_2, z)}{\Phi(L_2, z)}. \tag{4.5}$$

With this definition, some properties of $\Psi(L_1, L_2, z)$ can be examined. $\Psi(L_1, L_2, z)$ is normalised in the sense that its integral over L_1 is unity:

$$\begin{aligned} \int_{L_1} \Psi(L_1, L_2, z)\, \mathrm{d}L_1 &= \int_{L_1} \frac{\Phi(L_1, L_2, z)}{\Phi(L_2, z)}\, \mathrm{d}L_1 \\ &= \frac{1}{\Phi(L_2, z)} \int_{L_1} \Phi(L_1, L_2, z)\, \mathrm{d}L_1 \\ &= 1, \end{aligned}$$

by Equation (4.1). If both $\Phi(L_2, z)$ and $\Psi(L_1, L_2, z)$ are known, the BLF could be constructed simply by rearranging Equation (4.5):

$$\Phi(L_1, L_2, z) = \Phi(L_2, z)\Psi(L_1, L_2, z). \tag{4.6}$$

Thus knowledge of $\Psi(L_1, L_2, z)$ and $\Phi(L_2, z)$ allow $\Phi(L_1, z)$ to be calculated from Equations (4.6) and (4.2):

$$\Phi(L_1, z) = \int_{L_2} \Psi(L_1, L_2, z)\Phi(L_2, z)\, \mathrm{d}L_2. \tag{4.7}$$

This method for constructing a BLF is not new, and has been used in a similar fashion by earlier authors working on bivariate luminosity function problems (Corbelli et al., 1991; Toffolatti et al., 1987; Meurs & Wilson, 1984; Elvis et al., 1978, for example). Also, if it is believed that galaxy characteristics should be modelled by dealing separately with different galaxy populations, then this method can be used for each population, the final BLF simply being the sum of those from each population. (It should be noted that this is not the case if the populations in question

evolve from one to the other over the periods of time encompassed by the above integrals over redshift. This is a scenario which has not yet been ruled out.)

Now, a dimensional simplification of the problem is possible if $\Psi(L_1, L_2)$ (at every redshift, z) depends only on the ratio L_1/L_2. This is a useful step as luminosity ratios are used in many astrophysical analyses, providing information about the relative emission at different wavelengths. It is straightforward to make a coordinate change $L_1 \Rightarrow L_1/L_2 (= r$, say), so that $\Psi(L_1, L_2) \Rightarrow \Psi(r, L_2)$. It can now be postulated that there are some functions $\Psi(r, L_2)$ which do not depend explicitly on L_2 and which can therefore be written simply as $\Psi(r)$, or more generally $\Psi(r, z)$. Now, $\Psi(r, z)$ has the properties $\int_r \Psi(r, z)\, \mathrm{d}r = 1$ and $\Phi(L_2, z)\Psi(r, z) = \Phi(L_1, L_2, z)$. The goal of constructing a model radio-optical BLF, $\Phi(L_1, L_2, z)$, now becomes one of choosing suitable functions for $\Psi(r)$ (or $\Psi(r, L_2, z)$ in general) and $\Phi(L_2, z)$. At this point in the discussion it will become appropriate to start referring to a frequency-specific BLF, the radio-optical (1.4 GHz/R-band) BLF. This shall be denoted by using the independent variables $(L_{1.4}, L_{\mathrm{R}})$ rather than (L_1, L_2).

4.2 The model

The optical luminosity function, $\Phi(L_{\mathrm{R}}, z)$, and the distribution $\Psi(r, z)$ chosen to construct $\Phi(L_{1.4}, L_{\mathrm{R}}, z)$ must be consistent with observational results. In addition the $\Phi(L_{1.4})$ predicted from Equation (4.7) should be within observational errors of the known radio luminosity function. As an example, and a test of the method, the 60 μm FIR luminosity function was predicted from the distribution of $r = L_{\mathrm{FIR}}/L_{\mathrm{B}}$ and the B-band optical luminosity function of Rowan-Robinson et al. (1987), and compared with their observed 60 μm luminosity function. The results are shown in Figure 4.1. There are discrepancies between the two curves, particularly at $\log(L_{60}) \simeq 24.9$. However, this example shows the validity of the method itself, and even suggests that there may perhaps be some inconsistency between the three functions described in Rowan-Robinson et al. (1987). This is supported by the fact that, if the BLF is calculated using Ψ derived from the distribution of $r_{\mathrm{FIR}} = L_{\mathrm{FIR}}/L_{\mathrm{B}}$ given by Corbelli et al. (1991), a more consistent 60 μm luminosity function is produced. This is shown as a dot-dashed line in Figure 4.1.

The two population model consisting of starbursts and AGN discussed in Sections 1.4 and 3.3.3 has again been adopted. To construct the BLF with the two populations indicated, the functions $\Phi_{\mathrm{SB}}(L_{\mathrm{R}}, z)$, $\Phi_{\mathrm{AGN}}(L_{\mathrm{R}}, z)$, $\Psi_{\mathrm{SB}}(r)$ and $\Psi_{\mathrm{AGN}}(r)$ need to be determined. It should be emphasised here that a number of assumptions will be made in the modelling of the BLF. This is an initial attempt at constructing $\Phi(L_{1.4}, L_{\mathrm{R}}, z)$ and it is recognised that some of the early assumptions will require refinement in future modelling. However, a basic model is useful for providing insight into how effective the method is likely to be at making the required predictions, and into how the included assumptions affect the result.

After the two population model assumption, the next assumptions made are that starbursts occur predominantly in spiral galaxies and AGN in ellipticals. This

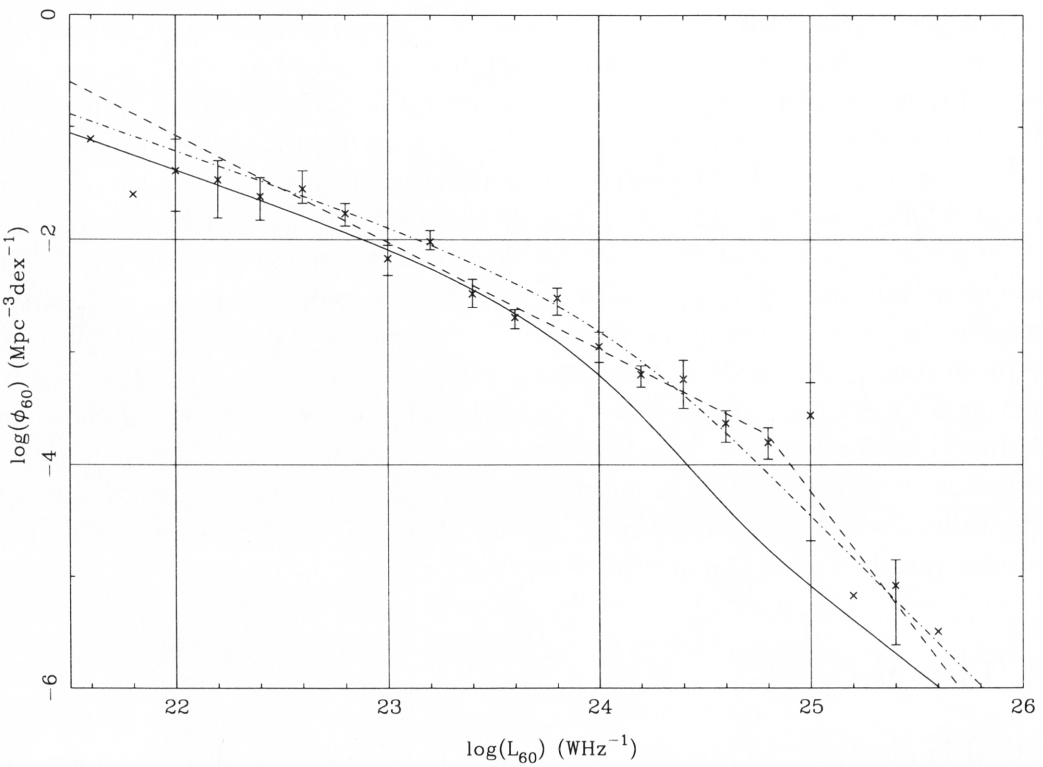

Figure 4.1 Predicted and observed 60 μm luminosity functions. The solid line is the luminosity function predicted from a BLF. The dashed line is the observed 60 μm luminosity function taken from Rowan-Robinson et al. (1987). The dot-dashed line is the 60 μm luminosity function predicted from a BLF constructed with a different Ψ, taken from Corbelli et al. (1991).

assumption implies that *all optical galaxies have radio emission at some level,* although that level may fall well below any given detection limit. This is a reasonable assumption, but it still leaves room for refinement. It does, however, allow the $\Phi(L_{\rm R}, z)$ chosen for the starburst and AGN populations to be the optical luminosity functions for the corresponding morphological types. Schechter functions were used for the $\Phi(L_{\rm R}, z)$ in both cases:

$$\Phi(L) = C\left(\frac{L}{L^*}\right)^{1+\alpha} e^{\frac{-L}{L^*}}, \tag{4.8}$$

($C = \ln(10)\Phi^*$). It was also assumed that these functions had no redshift dependence, as the R-band luminosity functions for these populations adequately predict the optical source counts down to the PDS magnitude limit of $R = 22$, without invoking any evolution (Section 3.5). For the purposes of an initial attempt at modelling the BLF this assumption is reasonable. Obviously, though, the model will require further refinements in which evolution of the optical luminosity functions will need to be taken into account. The parameters used in the construction of the BLF are those for R-band spirals and ellipticals (Metcalfe et al., 1991), and are given

in Table 3.4. It should be noted that all the luminosity functions quoted are in units of Mpc^{-3} per *decade* of luminosity, rather than Mpc^{-3} per *unit* of luminosity. This accounts for an extra factor of $\ln(10)L/L^*$ in the Schechter function above compared with Schechter's original formulation (Schechter, 1976).

There is potential for confusion to arise over the units in which luminosities are expressed, as a result of inconsistent notation. Luminosities can be expressed as a power, denoted herein as P_ν and having units of watts, commonly used when describing a broadband luminosity (one measured over a large range of frequencies, ν). They can also be expressed in units of $\mathrm{W\,Hz}^{-1}$, commonly used for monochromatic luminosities and symbolised herein as L_ν. These quantities are related by $P_\nu = \int_\nu R_\nu L_\nu \mathrm{d}\nu$ where R_ν is the frequency response of the detector used to measure L_ν. This is more commonly approximated by $P_\nu = \nu L_\nu$ at radio wavelengths, and by $P_\nu = \Delta\nu L_\nu$ for optical luminosities.

Now that $\Phi_{\mathrm{SB}}(L_{\mathrm{R}}, z)$ and $\Phi_{\mathrm{AGN}}(L_{\mathrm{R}}, z)$ are chosen, $\Psi_{\mathrm{SB}}(r)$ and $\Psi_{\mathrm{AGN}}(r)$ remain to be determined. For starburst galaxies the distribution of $r_{\mathrm{FIR}} = L_{\mathrm{FIR}}/L_{\mathrm{B}}$, the ratio of the far-infrared to B-band optical luminosities, is well determined (Corbelli et al., 1991; Rowan-Robinson et al., 1987). This distribution, $\psi(L_{\mathrm{FIR}}, L_{\mathrm{B}})$, appears to be independent of L_{B}, (although Corbelli et al. (1991) find a very weak dependence), and so can be written $\psi(r = L_{\mathrm{FIR}}/L_{\mathrm{B}})$, say. By making use of the radio/far-infrared correlation ($L_{60\,\mu\mathrm{m}} = 100\,L_{1.4}$), and invoking $m_{\mathrm{B}} - m_{\mathrm{R}} = 1$ as a typical colour for spiral galaxies, the variable can be changed to $r = L_{1.4}/L_{\mathrm{R}}$. (The assumption of a constant colour index is reasonably coarse, and variations of up to a few tenths of a magnitude could be expected for individual objects. However, it still provides reasonable basis for the analysis presented here.) This distribution, $\psi(r)$, can be used to construct $\Psi_{\mathrm{SB}}(r)$ by normalising the distribution so that its integral over all $\log(r)$ is unity:

$$\Psi_{\mathrm{SB}}(r) = \frac{\psi(r)}{\int_{-\infty}^{+\infty} \psi(r)\mathrm{d}r}. \tag{4.9}$$

Figure 4.2(a) shows $\Psi_{\mathrm{SB}}(r)$ together with the (normalised) observational results for late-type galaxies, derived by Corbelli et al. (1991), after conversion as described above. The model form for $\Psi_{\mathrm{SB}}(r)$ fitted to the observational distribution is described as:

$$\log(\Psi_{\mathrm{SB}}(r)) = \begin{cases} 0.13 - \frac{\gamma}{\ln(10)}(\log(r) - a)^2 & \log(r) < 0.09 \\ 0.13 - \frac{\gamma}{\ln(10)}(0.09 - a)^2 - 1.9(\log(r) - 0.09) & \log(r) > 0.09 \end{cases} \tag{4.10}$$

where $a = -0.27$, and $\gamma = 6.2$ for $r = L_{1.4}/L_{\mathrm{R}}$.

For AGN galaxies $\Psi_{\mathrm{AGN}}(r)$ was also fit to existing data taken from Sadler et al. (1989). These data (at 5 GHz in the radio and B-band in the optical) were converted to 1.4 GHz and R-band using a spectral index of $\alpha = -0.7$ in the radio, and $m_{\mathrm{B}} - m_{\mathrm{R}} = 1.55$ in the optical, and the distribution $\psi(r = L_{1.4}/L_{\mathrm{R}})$ formed. (The assumption of constant radio spectral index is justified here, since the objects in question have high flux densities.) This distribution was then normalised as described above for disk galaxies. It is a recognised result from Sadler et al. (1989) and

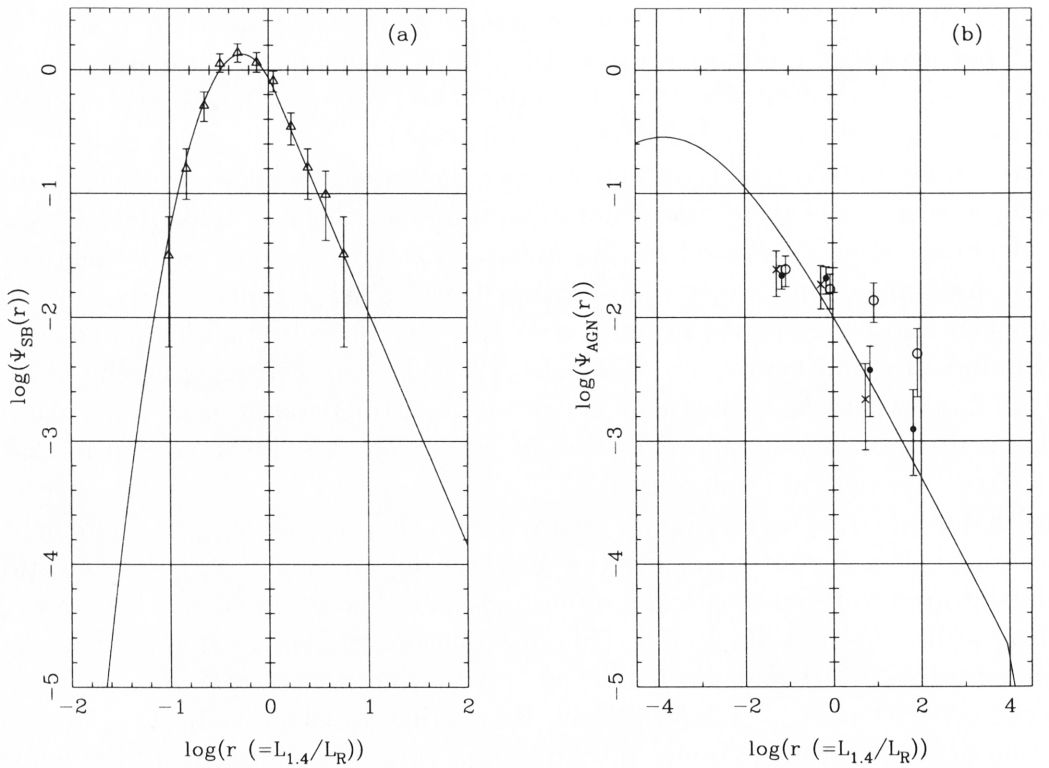

Figure 4.2 Models of $\Psi_{\rm SB}(r)$ and $\Psi_{\rm AGN}(r)$ with observational data overlayed. (a) shows $\Psi_{\rm SB}(r)$, triangles are data from Figure 3(a) of Corbelli et al. (1991). (b) shows $\Psi_{\rm AGN}(r)$ and data from Sadler et al. (1989), which are classified by optical magnitude range. Crosses: $21.23 < \log(L_{\rm R}) < 21.63$; Solid circles: $21.63 < \log(L_{\rm R}) < 22.03$; Open circles: $22.03 < \log(L_{\rm R}) < 22.43$.

other authors that this distribution is actually dependent on the optical luminosity of the galaxies, i.e. $\Psi_{\rm AGN}(r)$ should be $\Psi_{\rm AGN}(r, L_{\rm R})$. This is an important result which should be included in any detailed model of the BLF, although it was decided to neglect it in this initial treatment of the problem in favour of simplicity. This is recognised as being a serious oversimplification, and indeed the poorness of the fit of the assumed $\Psi_{\rm AGN}(r)$ to the observational data can be seen in Figure 4.2(b). However, it should still provide a useful starting point for the model BLF. The details of the assumed model for $\Psi_{\rm AGN}(r)$ are given as:

$$\log(\Psi_{\rm AGN}(r)) = \begin{cases} 1.76 - b(1 - \frac{(\log(r)-a)^2}{c^2})^{0.5} & \log(r) < 3.94 \\ 2.90 - \frac{\gamma}{\ln(10)}(\log(r) - a)^2 & \log(r) > 3.94 \end{cases} \tag{4.11}$$

where $a = -3.86$, $b = 2.3$, $c = 3.0$, and $\gamma = 0.286$ for $r = L_{1.4}/L_{\rm R}$.

The BLF itself (calculated for $z = 0.01$) is shown in Figure 4.3. The horizontal axes are $\log(L_{1.4})$ and $\log(L_{\rm R})$ in $\rm WHz^{-1}$, and the vertical axis is $\log(\Phi(L_{1.4}, L_{\rm R}))$. The unit of $\Phi(L_{1.4}, L_{\rm R})$ is $\rm Mpc^{-3}dex^{-2}$ (i.e., $\rm Mpc^{-3}$(decade of radio luminosity)$^{-1}$ (decade of optical luminosity)$^{-1}$).

Figure 4.4 shows the radio luminosity functions predicted for each population

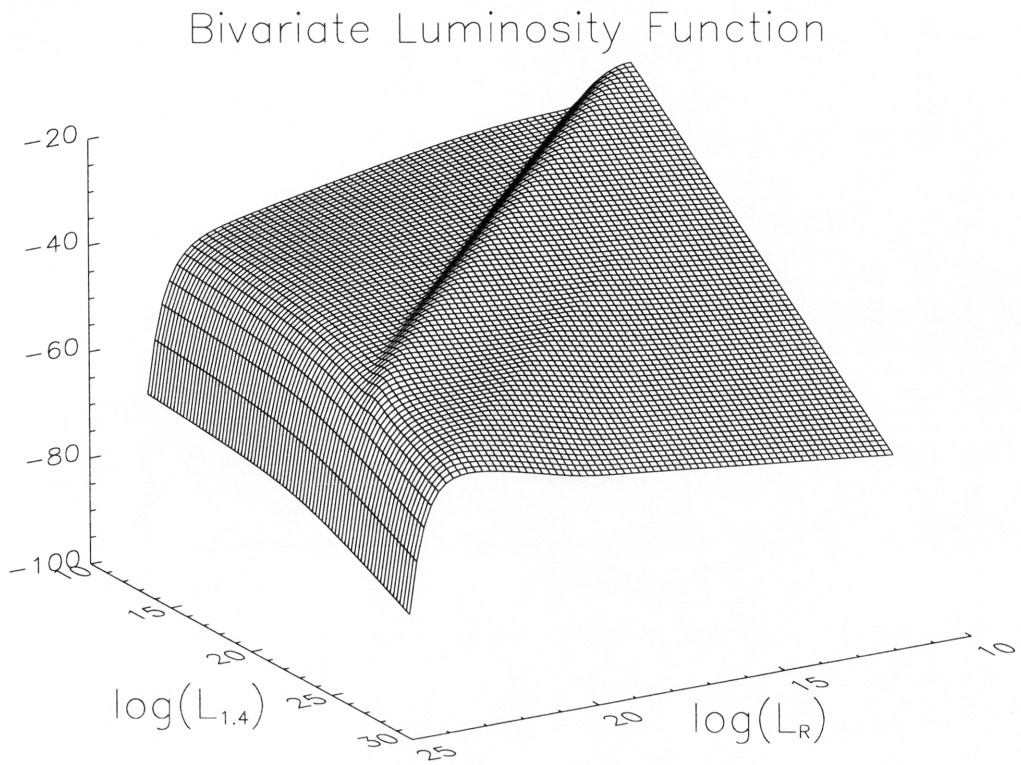

Figure 4.3 Model BLF constructed as described in text.

from the model BLF. Figure 4.4(a) shows luminosity functions for starburst galaxies, and Figure 4.4(b) those for AGN. The solid lines in both Figures are the radio luminosity functions predicted from the model BLF. In Figure 4.4(a) the dashed line is the starburst galaxy luminosity function from Condon (1989), and the data points are his. The dot-dashed line is the far-infrared luminosity function of Saunders et al. (1990) which has been shifted to radio frequencies using the radio/far-infrared correlation. In Figure 4.4(b) the dashed line is the luminosity function for AGN galaxies described by Condon (1989), and again the filled circles are his data. The dot-dashed line is the luminosity function at $z = 0$ described by Dunlop & Peacock (1990) with their two-population model (flat- and steep-spectrum sources). The open circles are data from Sadler et al. (1989), and the crosses are from Franceschini et al. (1988).

It is well established that the predicted radio source counts don't match observations unless the radio luminosity function is evolving (Dunlop & Peacock, 1990; Rowan-Robinson et al., 1993, for example), and so such evolution must be incorporated into the BLF. Luminosity evolution for radio luminosities only was used. (As described above, no evolution in the optical dimension was needed to accurately predict the source counts over the range of apparent magnitudes considered). This evolution in the BLF can be expressed as a redshift dependence of $\Psi(r)$, since no evolution of $\Phi(L_{\rm R}, z)$ is required. The amount of the luminosity evolution ($L^*_{1.4} \propto (1+z)^Q$) required to ensure the radio source counts were accurately predicted by the BLF

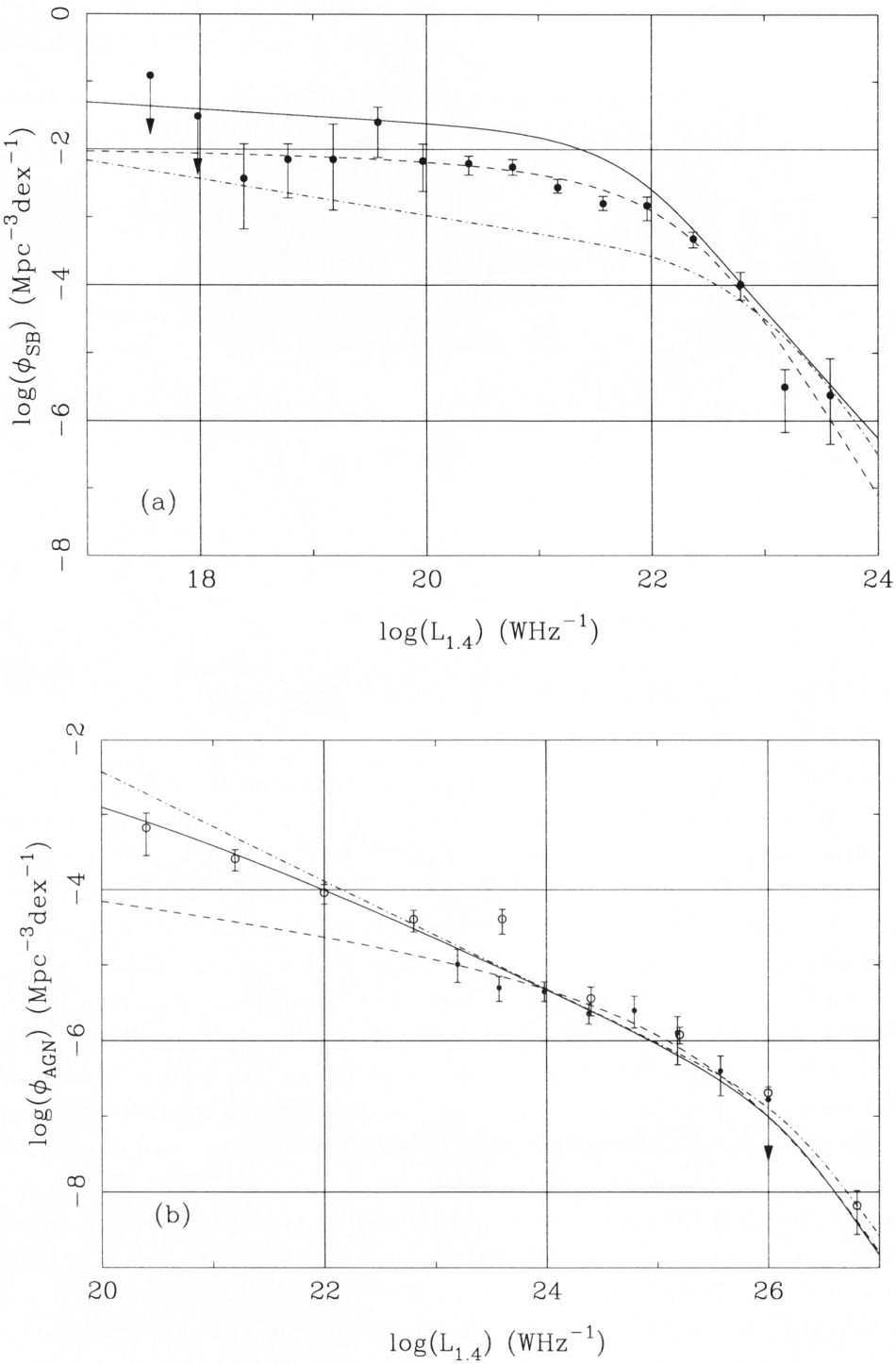

Figure 4.4 Predicted and observed radio luminosity functions. See the text for full description.

was $Q = 2.3$ for starburst galaxies, $Q = 3.5$ for AGN brighter than $\log(L_{1.4}) = 26$, and $Q = 2.0$ for AGN fainter than $\log(L_{1.4}) = 26$. The evolution chosen affects the predictions of the source counts from the model $\Phi(L_{1.4}, L_{\rm R}, z)$. The BSC predicted from the model BLF shown in Figure 4.3 is presented in Section 4.8, but first the method for predicting the BSC from the BLF is described.

4.3 Bivariate source counts

The procedure for calculating the source counts from a luminosity function (as described by Pearson & Rowan-Robinson (1996) for example) is revised here. The procedure is then generalised to the case of the BLF. The *integral* source counts can be calculated from the formula

$$N(S) = \int_{L_l}^{L_u} \mathrm{d}L \int_0^{z_f} \phi(L, z) \frac{\mathrm{d}V}{\mathrm{d}z} \mathrm{d}z, \tag{4.12}$$

where $N(S)$ is the integral source count and

$$S = \frac{L}{4\pi D_L^2} (1+z)^{1-\alpha},$$

the flux density corresponding to a source of luminosity L and spectral index α,

$$D_L = \frac{c}{H_0 q_0^2} (q_0 z + (q_0 - 1)(\sqrt{1 + 2q_0 z} - 1)),$$

the luminosity distance, and

$$\frac{\mathrm{d}V}{\mathrm{d}z} = \frac{4\pi c D(z)^2}{H_0 (1+z)^3 \sqrt{1+2q_0 z}},$$

the comoving volume element per redshift element. z_f is the redshift of formation of galaxies, which was assumed to be $z_f = 10$ in the modelling performed. By experimentation, it was established that values of z_f as low as about 3 could be assumed without producing a significant change in the predicted source counts. L_l and L_u are the lower and upper limits of galaxy luminosities for the wavelengths in question. The differential source counts are then obtained simply by differentiating the integral source counts.

For the case of the BLF this procedure was generalised using

$$N(S_{1.4}, S_{\rm R}) = \int_{L_{1.4}} \mathrm{d}L_{1.4} \int_{L_{\rm R}} \mathrm{d}L_{\rm R} \int_0^{z_f} \Phi(L_{1.4}, L_{\rm R}, z) \frac{\mathrm{d}V}{\mathrm{d}z} \mathrm{d}z. \tag{4.13}$$

The bivariate differential source counts are obtained from the equation

$$n(S_{1.4}, S_{\rm R}) = \frac{\partial^2 N(S_{1.4}, S_{\rm R})}{\partial S_{1.4} \partial S_{\rm R}}. \tag{4.14}$$

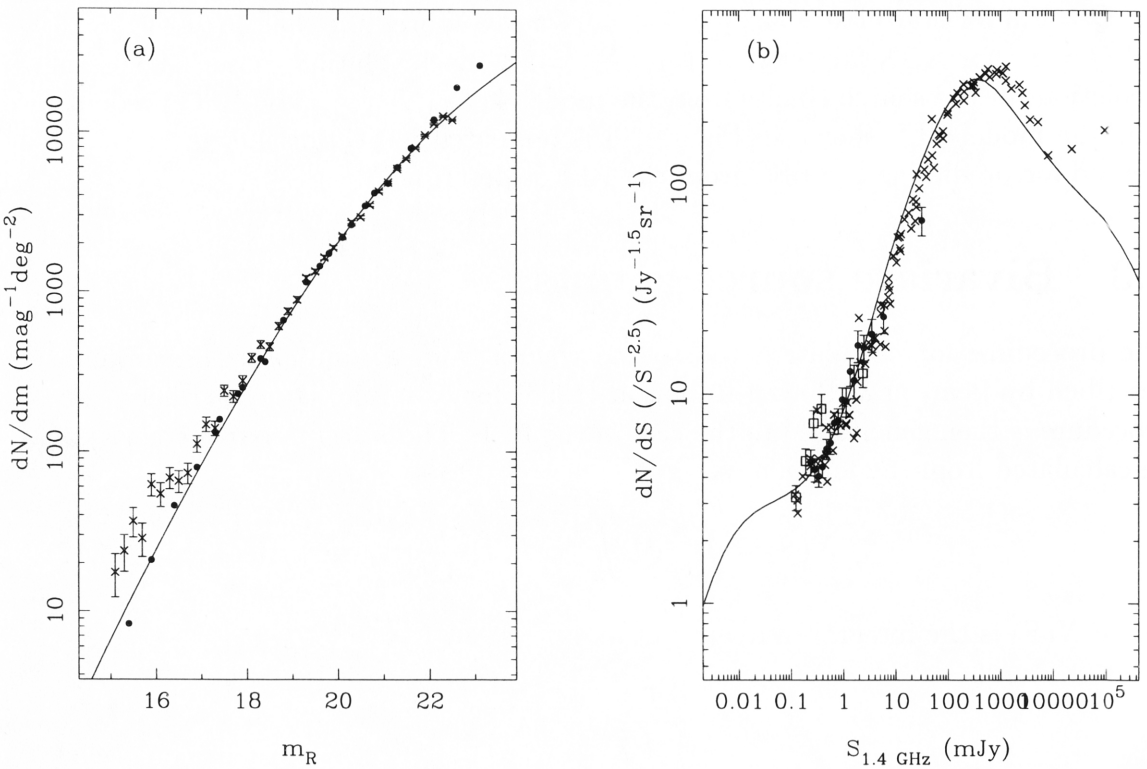

Figure 4.5 Predicted optical and radio source counts compared with observational data from the PDS. Windhorst's radio source counts are also shown (as crosses) for comparison with the high flux-density prediction.

An alternative to this procedure, and the method actually used in practice when predicting bivariate source counts from the BLF, is to calculate the differential bivariate source counts directly from the BLF:

$$n(S_{1.4}, S_{\rm R}) = \int_0^{z_f} \Phi(L_{1.4}, L_{\rm R}, z) \Delta L_{1.4}(S_{1.4}, z) \Delta L_{\rm R}(S_{\rm R}, z) \frac{{\rm d}V}{{\rm d}z} {\rm d}z, \qquad (4.15)$$

where $\Delta L_\nu(S_\nu, z)$ is the luminosity range calculated between the L_ν determined from S_ν and z, and that determined from $S_\nu + {\rm d}S_\nu$ and $z + {\rm d}z$.

4.4 Predicted optical ID rates

A model for the differential bivariate source counts was predicted from the model BLF, and is shown in Figure 4.6. The horizontal axes are both in units of mJy, and the vertical axis has units of galaxies steradian^{-1}Jy^{-2}. The separate radio and optical source counts, obtained by integrating over the appropriate axis of the model BSC, are presented along with the observational data for comparison, in Figure 4.5. The observational BSC was also constructed for comparison with the model, but for the PDF only. The PDFS radio sources, even with over a hundred optical counterparts, suffered too strongly from having small numbers of sources in each

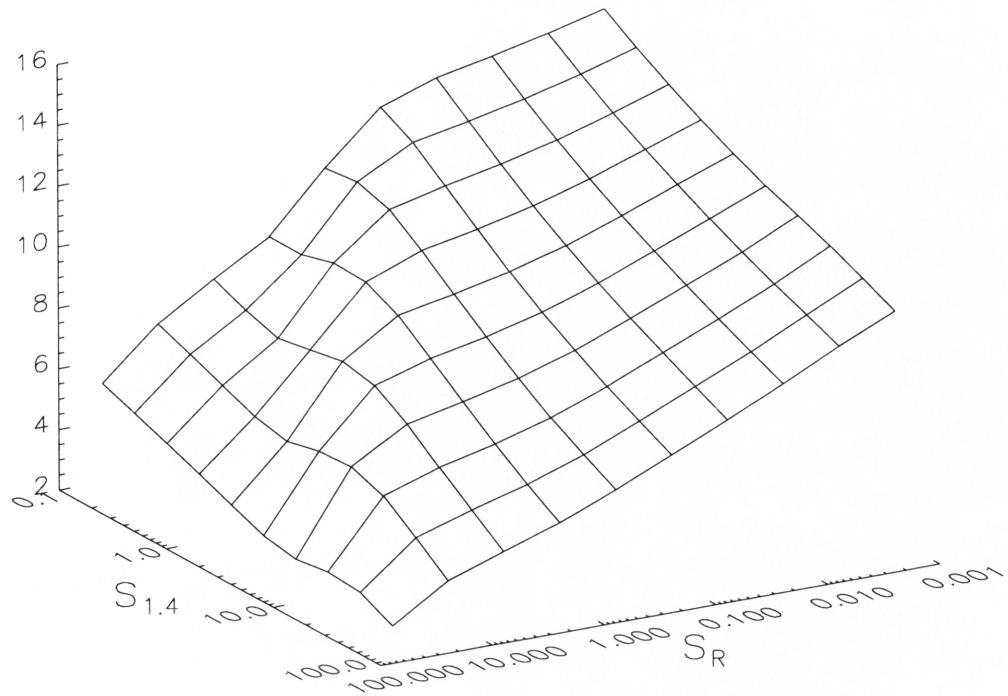

Figure 4.6 Model BSC predicted from model BLF. All three axes are logarithmic, and the two flux density axes are in units of mJy.

two-dimensional flux density bin. Consider, for example, five flux density bins in each wavelength. This gives a total of 25 bins, which would have only about 4 objects in each if they happened to be uniformly distributed in flux density. In reality there are more faint sources than bright ones, so most of the brighter bins are empty, with many more containing one source, and only a few of the faintest bins contain ten or twenty objects. The alternative, taking still fewer bins, provides too little resolution to make a satisfactory comparison with the predictions, as well as still retaining a majority of empty bins.

Given a list of objects for which both the radio and optical flux densities are known, the BSC is constructed by counting the numbers of objects in each bin of a two-dimensional array (for which the axes are the radio and optical flux densities). That number is divided by the size of the bin (being the product of $\mathrm{d}S_{1.4}$ and $\mathrm{d}S_{\mathrm{R}}$), and the area of sky (in steradians) over which the given source list was compiled. The resulting $n(S_{1.4}, S_{\mathrm{R}})$ has units of galaxies steradian^{-1}Jy^{-2}. The observational BSC for the PDF is shown in Figure 4.7. The axes in both Figures 4.6 and 4.7 are to the same scale and cover the same range, to aid comparison. Note that, as a result of this, bins in Figure 4.7 which actually contain no sources appear to have $\log(n(S_{1.4}, S_{\mathrm{R}})) = 2$.

From the model BSC, the numbers of optically identified radio sources were predicted to test the accuracy of the model BLF. These are shown, along with the

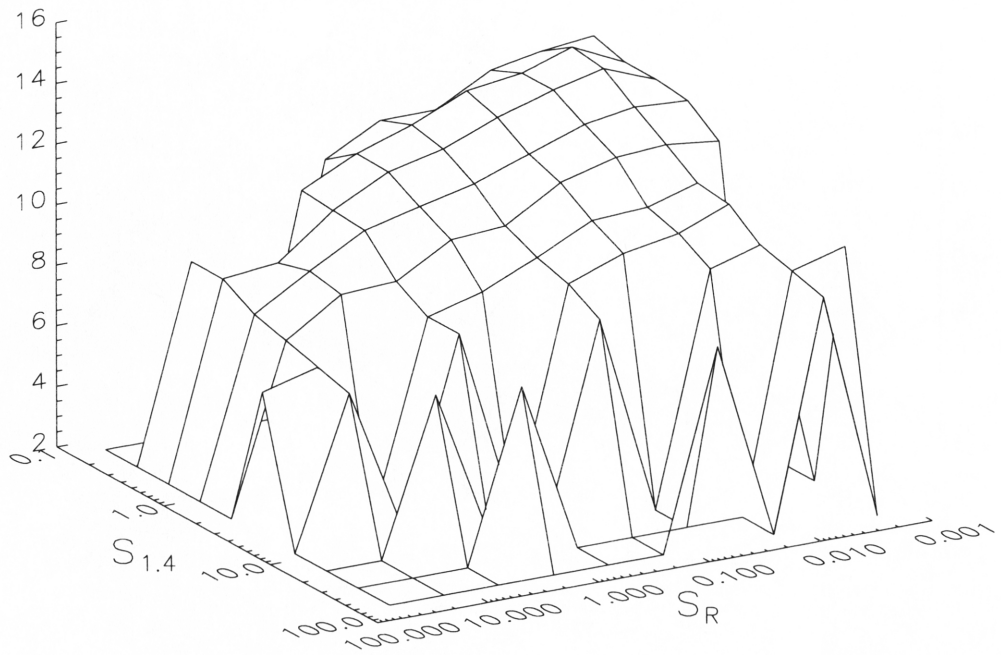

Figure 4.7 Observational BSC constructed from PDS data. Axes are as for Figure 4.6.

observed values for the PDF, in Table 4.1. The corresponding ID rate, expressed as percentages, is given in Table 4.2. (This Table should be interpreted very carefully. The predictions show the dominant fraction of sources in the faintest flux density bin, while the real data suffers from incompleteness at those levels. The result of this is that the ID rate distribution is skewed. Hence, this Table is not particularly useful for making direct comparisons between prediction and observation, and so should perhaps not be presented in this fashion. It is useful for showing what the observed ID rate looks like, which is why it has been included.) Table 4.1 shows that the predictions are actually quite different to the observations in many bins. However, much of the discrepancy in the model can be explained by the fact that the faintest two rows and columns both suffer from incompleteness in the data, the radio catalogue for the PDF being complete to 0.3 mJy, and the optical to $R = 22$ mag. At the brightest flux densities in the observational BSC small number statistics dominate, with only one or two sources in each bin. The values in the intermediate bins, however, are in reasonable agreement with the observations, although there are certainly still discrepancies. This serves to show that even this initial model, with all the assumptions included, can still make reasonable predictions. To push these further, the model BLF has been used to predict the BSC over a much greater range of flux densities, to be used as a comparison with later observations as their sensitivities increase, and surveys cover larger areas of the sky. This prediction for this BSC is shown in Figure 4.8.

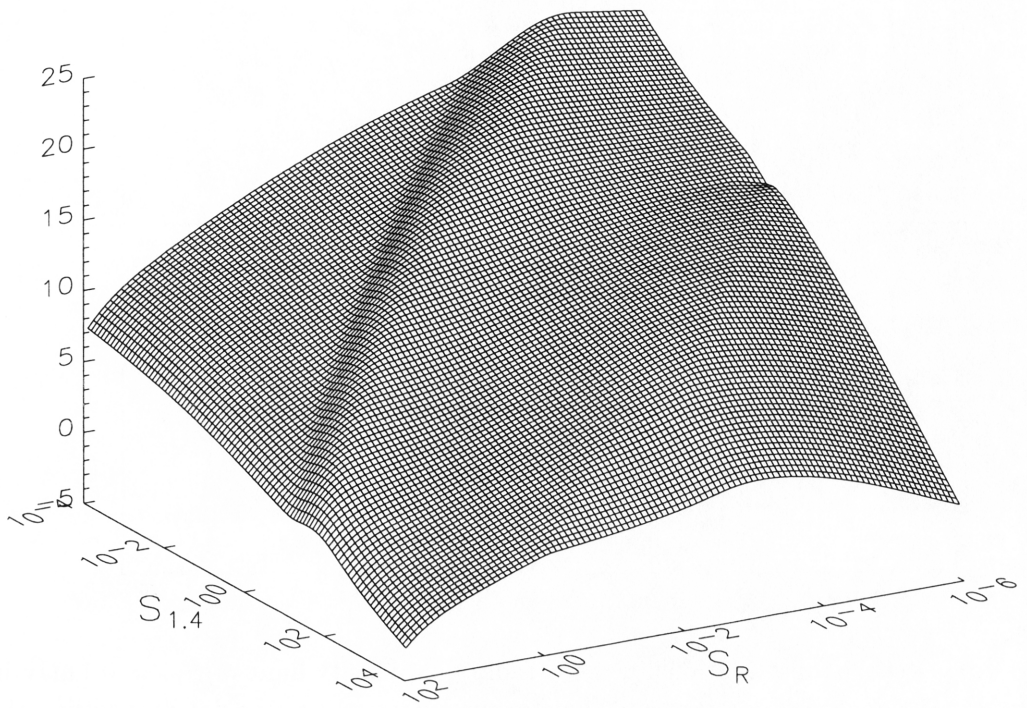

Figure 4.8 Prediction of the BSC for greater range of flux densities.

4.5 Redshift distribution

The redshift distribution for these two galaxy populations can also be predicted given the model for the BLF. It is particularly interesting to investigate how the redshift distribution changes as the limiting flux densities in the radio and the optical are varied. The redshift distribution for galaxies, $\mathrm{d}N/\mathrm{d}\log(z)$, is calculated from $\mathrm{d}N(z)$, the number of sources at a given redshift brighter than given bivariate flux density limits:

$$\mathrm{d}N(z) = \int_{L_{1.4}(S_{1.4},z)>S_{1.4_{\min}}} \int_{L_R(S_R,z)>S_{R_{\min}}} \mathrm{d}L_{1.4}\mathrm{d}L_R\Phi(L_{1.4}, L_{\mathrm{R}}, z)\frac{\mathrm{d}V}{\mathrm{d}z}\mathrm{d}z. \quad (4.16)$$

The model BLF used to predict the BSC has also been used to predict the redshift distribution for a range of flux density cutoffs. The results are shown in Figures 4.9 and 4.10.

Figure 4.9 shows how the redshift distribution changes for a constant radio flux density limit (of $S_{1.4} = 0.1$ mJy) as the optical limit is lowered (from $R = 18$ through to $R = 24$). The separate populations, starburst and AGN galaxies, are shown individually so their contribution to the sum can be seen. The median redshift of the starburst population changes from $z \sim 0.1$ to $z \sim 0.3$ as the optical limit imposed becomes fainter. The median redshift of the AGN population moves from $z \sim 0.3$ to $z \sim 2$ over this same range of optical magnitude limits. This is the trend

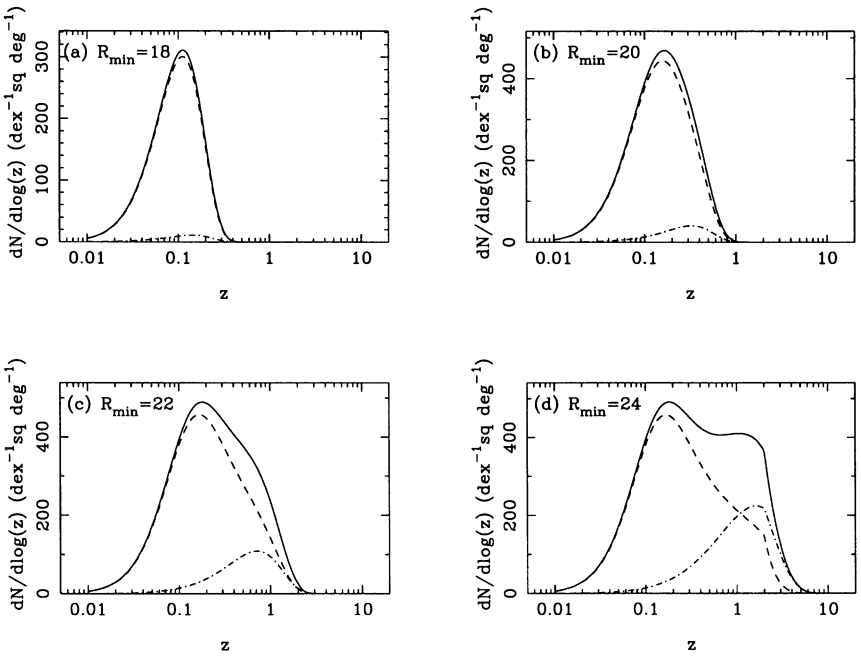

Figure 4.9 Redshift distributions, using a radio flux density limit of $S_{1.4} = 0.1\,\mathrm{mJy}$ in each graph. The dashed line represents the starburst population, the dot-dashed line the AGN population, and the solid line is the sum of the two. The optical R-band magnitude limits are shown for each graph.

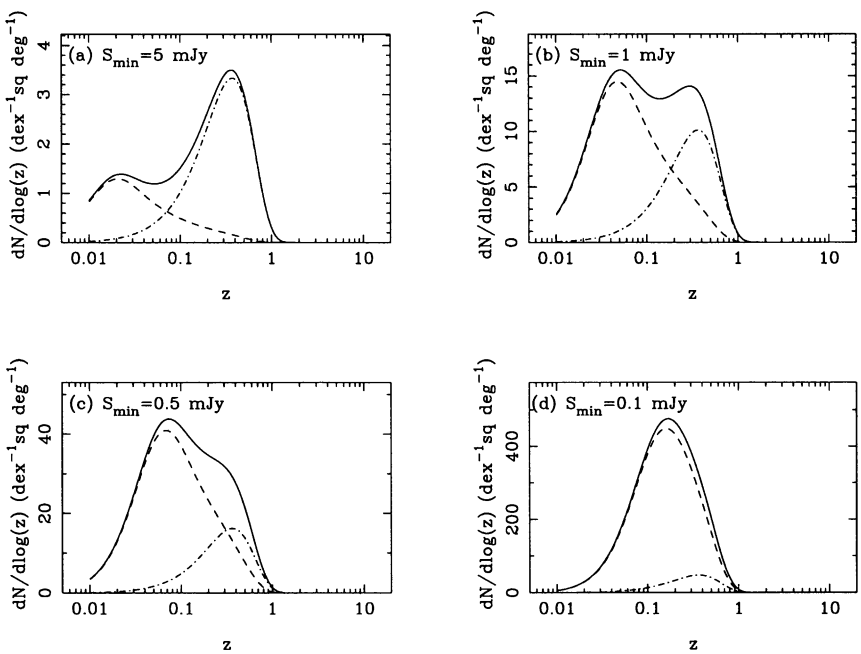

Figure 4.10 Redshift distributions, using an R-band optical magnitude limit of $R = 22$ in each graph. The lines are as for previous figure. The radio flux density limits are shown for each graph.

Table 4.1 Predicted number of optical IDs for the radio sources in the PDS (upper values) compared with the observed numbers (lower values).

$S_{1.4}$ (mJy)	Optical (R-band) magnitude									
	23.8	22.6	21.3	20.1	18.8	17.6	16.3	15.1	13.8	12.6
0.14	163.0	171.8	204.8	276.3	206.4	13.8	0.5	0.2	0.0	0.0
	2	3	1	2	2	0	0	0	0	0
0.28	63.9	58.7	61.9	77.6	108.4	37.2	1.0	0.1	0.0	0.0
	12	21	30	25	11	5	1	1	0	0
0.56	29.7	23.6	20.9	23.0	30.5	35.5	4.3	0.1	0.0	0.0
	19	43	32	18	28	10	5	2	0	0
1.1	15.7	11.3	8.3	7.5	8.8	12.3	7.8	0.3	0.0	0.0
	8	20	11	14	12	10	9	1	0	1
2.2	9.1	6.1	3.9	2.8	2.7	3.5	4.8	1.0	0.0	0.0
	2	7	14	8	6	2	4	1	0	0
4.5	6.1	3.5	2.1	1.3	1.0	1.0	1.4	1.2	0.1	0.0
	1	2	3	4	2	1	0	1	1	0
8.9	5.0	2.1	1.2	0.7	0.4	0.3	0.4	0.5	0.1	0.0
	2	3	2	2	0	0	2	1	0	0
17.8	3.8	1.5	0.7	0.4	0.2	0.1	0.1	0.1	0.1	0.0
	1	0	1	1	0	0	2	0	0	0
35.5	2.6	1.1	0.4	0.2	0.1	0.1	0.0	0.0	0.0	0.0
	1	1	0	0	0	0	1	0	0	0
70.8	1.6	0.8	0.3	0.1	0.1	0.0	0.0	0.0	0.0	0.0
	1	0	1	0	0	0	0	0	0	0

predicted by the BLF model for progressively deeper optical observations taken of a flux density limited radio catalogue. Figure 4.10 is the analogous situation for a constant optical magnitude limit (of $R = 22$). It is interesting to note the radically different shape of the distribution at the brighter radio flux density limit, clearly showing the predominance of the AGN population at high radio flux densities. The real situation would show this effect even more markedly, the discrepancy here probably due to the assumptions about the shape of $\Psi_{\rm AGN}$ and the evolution invoked. This Figure also shows how the starburst galaxy population emerges, at moderate redshifts, as the radio flux density limit is decreased. This is the trend the BLF model predicts when progressively deeper radio observations are taken of a given magnitude limited optical catalogue.

These predictions are valuable indicators of what the next generation of deep multiwavelength and redshift surveys can expect to see. In the next Chapter, redshifts for some of the PDS objects are presented and a preliminary comparison with these predictions is offered.

Table 4.2 Predicted optical ID rates (as percentages of the total number in these flux density ranges) for the radio sources in the PDS (upper values) compared with the observed rates (lower values).

$S_{1.4}$ (mJy)	Optical (R-band) magnitude									
	23.8	22.6	21.3	20.1	18.8	17.6	16.3	15.1	13.8	12.6
0.14	9.25	9.75	11.62	15.68	11.71	0.79	0.03	0.01	0.00	0.00
	0.46	0.68	0.23	0.46	0.46	0.00	0.00	0.00	0.00	0.00
0.28	3.62	3.33	3.51	4.41	6.15	2.11	0.06	0.01	0.00	0.00
	2.73	4.77	6.82	5.68	2.50	1.14	0.23	0.23	0.00	0.00
0.56	1.68	1.34	1.19	1.30	1.73	2.01	0.24	0.01	0.00	0.00
	4.32	9.77	7.27	4.09	6.36	2.27	1.14	0.46	0.00	0.00
1.1	0.89	0.64	0.47	0.43	0.50	0.70	0.44	0.02	0.00	0.00
	1.82	4.55	2.50	3.18	2.73	2.27	2.05	0.23	0.00	0.23
2.2	0.52	0.34	0.22	0.16	0.16	0.20	0.27	0.06	0.00	0.00
	0.46	1.59	3.18	1.82	1.36	0.46	0.91	0.23	0.00	0.00
4.5	0.35	0.20	0.20	0.07	0.06	0.06	0.08	0.07	0.00	0.00
	0.23	0.46	0.68	0.91	0.46	0.23	0.00	0.23	0.23	0.00
8.9	0.28	0.12	0.07	0.04	0.02	0.02	0.02	0.03	0.01	0.00
	0.46	0.68	0.46	0.46	0.00	0.00	0.46	0.23	0.00	0.00
17.8	0.22	0.08	0.04	0.02	0.01	0.01	0.01	0.01	0.01	0.00
	0.23	0.00	0.23	0.23	0.00	0.00	0.46	0.00	0.00	0.00
35.5	0.15	0.06	0.03	0.01	0.01	0.00	0.00	0.00	0.00	0.00
	0.23	0.23	0.00	0.00	0.00	0.00	0.23	0.00	0.00	0.00
70.8	0.09	0.04	0.02	0.01	0.00	0.00	0.00	0.00	0.00	0.00
	0.23	0.00	0.23	0.00	0.00	0.00	0.00	0.00	0.00	0.00

Chapter 5

Spectral analysis of sub-mJy radio sources

5.1 Observations and data reduction

The 2dF observations were carried out in December 1996 by the 2dF commissioning team during time allocated for the scientific verification of the instrument. The list of targets was chosen from the catalogue of PDS radio sources with optical counterparts brighter than $R = 21$. Objects which had radio emission fainter than 1 mJy were preferentially selected from this group, although a number of sources brighter than this were included for comparison purposes. All targets were identified with sources in the APM catalogue and the APM positions (measured from UKST plates, and with positional errors of the order of 0.″2 to 0.″3) were used when making the observations. The optical magnitude limit was chosen to ensure APM positions would be available for the targets, although this results in a sample which is biased away from the faint optical counterparts of faint radio sources. This bias should be kept in mind in the following discussion.

The fibre configuration was done using the custom software CONFIG. 27 sky positions were included in the configuration, along with 4 fiducial stars for positional reference. The 270R grating was used, having a 90% throughput over the wavelength range $560 < \lambda < 760$ nm, with a dispersion of 199.9 Å/mm onto a 24 mm detector (Bailey & Glazebrook, 1996). The spectral resolution was $\lambda/\Delta\lambda \approx 600$ with a pixel scale of ≈ 4.7 Å/pixel. A single 3.5 hour integration was made with the resulting fibre configuration, producing signal-to-noise (S/N) ratios ranging from about 5 for the faintest objects up to 200 or so for the brightest.

The spectral data reduction was performed twice, once using standard techniques and software in the IRAF data reduction package, and once using the custom 2DFDR software for reducing 2dF data. The results from the separate analyses were almost identical, and although much effort was directed at correcting the poor sky-subtraction, it was unable to be significantly improved from the results initially obtained. Despite this drawback, individual emission features were still able to be

identified and redshifts measured for many objects.

The redshifts were measured using a program called ZPLOT written by Chris Lidman, in IRAF. Each redshift measured was assigned a "qualifier," (Q), a number from 1 to 3 indicating the confidence with which the redshift was established. A redshift with Q=1 has been firmly established through the presence of two or more clearly identified lines. Q=2 indicates that the redshift has been established through one line only where the identity of the line is reasonably clear, or through two lines whose identities are less clear. Q=3 indicates a possible redshift only, based on a single line of uncertain identity. The values of Q are presented along with the redshifts in Table B.3.

In addition to providing redshifts (and hence enable comparisons with the predictions described in the previous Chapter) the spectra from the 2dF and EFOSC observations provide information about the emission processes of some of the sub-mJy radio sources in the PDS. By measuring emission line strengths for these galaxies, a quantitative estimate can be made of the process causing the emission, resulting in a delineation between AGN and starburst galaxies.

5.2 Spectral classification

The 2dF observations of 158 objects produced 126 spectra for which redshifts were able to be measured. The spectra measured using EFOSC are not included in the following initial analysis to ensure the uniformity of the sample, although they will be included in future investigations. Redshifts could not be obtained for 32 of the 2dF targets for two main reasons. First, the poor sky subtraction resulted in forests of emission lines from atmospheric processes, which mask faint emission lines from a target galaxy. Second, the galaxies may have simply been too faint to detect any emission line with significant S/N.

The 126 2dF spectra are classified using 4 categories, in the same manner as Tresse et al (1996). Class (A) consists of spectra with Hα and Hβ in emission. Class (B) consists of spectra with Hα in emission and Hβ in absorption. Class (C) consists of spectra with Hα and Hβ in absorption. Class (D) consists of spectra at redshifts high enough that neither Hα nor Hβ are visible, but displaying broad emission lines enabling the redshift to be established. The physical processes at the origin of the observed emission or absorption lines are quite different. Stellar atmospheres give rise to Balmer absorption lines, while Balmer emission lines are produced by hot gas surrounding stars. So the two features trace different processes, absorption lines the stellar populations in a galaxy, emission lines more violent phenomena. Processes such as star formation, supernovae, or even harder radiation sources such as active nuclei, are typical sources of emission lines.

Spectra of class (A) are galaxies with strong emission lines and a blue continuum. They exhibit strong forbidden lines such as [O III]λ4959, [O III]λ5007, [O II]λ3727 and [S II]λ6725 in addition to Hα. Several spectra were classified as class (A) despite being at too high a redshift for Hα to be observable ($z > 0.35$). This was done on the

basis of strong Hβ emission, and for some objects on the presence of other emission lines as well or instead. Spectra of class (B) exhibit moderate to strong Hα emission, indicating galaxies with star formation activity. But absorption features such as Hβ, the 4000 Åbreak, the G-band (λ4304) and MgI (λ5183) which are also present, trace the underlying stellar population. Tresse et al. (1996) describe these objects as looking "like starbursts occurring in early type galaxies." However, the number of objects in class (B) are likely to be under-counted. This is because spectra with $z > 0.35$ do not have the Hα emission observable, and in this case the object is most likely to be put into class (C) as the other, shorter wavelength, absorption features are present. Class (D) objects are all quasars at moderate to high redshifts. This is evidenced by their broad emission line characteristics.

Some spectra with Hα in emission do not exhibit either Hβ in emission, like those in class (A), or in absorption, like those in class(B). Again following Tresse et al. (1996), these spectra are included in a subclass, (AB), which forms a subset of class (A). Class (A) is chosen rather than (B), as class (AB) spectra show spectral features typical of strong emission line spectra such as [O II]λ3727, [O III]λ4959, [O III]λ5007, [S II]λ6725. In these cases the Hβ emission must be hidden by significant stellar absorption. The resolution of the 2dF spectra cannot resolve these competing effects, so no accurate measurement of this effect can be made.

The number of spectra by spectral class are given in Table 5.1. Composite redshift-corrected spectra of classes (A), (B) and (C) are shown in Figures 5.1, 5.2 and 5.3, providing an example of the features prominent in these classes.

Table 5.1 : Distribution of the 126 2dF spectra by spectral classes as described in the text.

class	number	percentage
A	68	54.0%
(AB)	(32)	(25.4%)
B	6	4.8%
C	43	34.1%
D	9	7.1%
Total	126	100%

The different spectral types can be roughly collected into the two populations, starbursts and AGN, being used to describe radio galaxies in this thesis. The distribution with flux density of emission (starburst) and absorption (AGN) type galaxies is shown in Figure 5.4. Types A and AB are typically starburst-type objects, while types C and D are definitely of the AGN class. Type B galaxies are slightly harder to classify. The relatively few of this type found have been tentatively grouped with the AGN. The important feature of Figure 5.4 is the fact that emission line objects dominate the population at fainter flux densities. Admittedly the sample for which spectra exist is not complete, and can not be considered to be representative, but even so it is interesting to note the trend. The prediction from the model radio

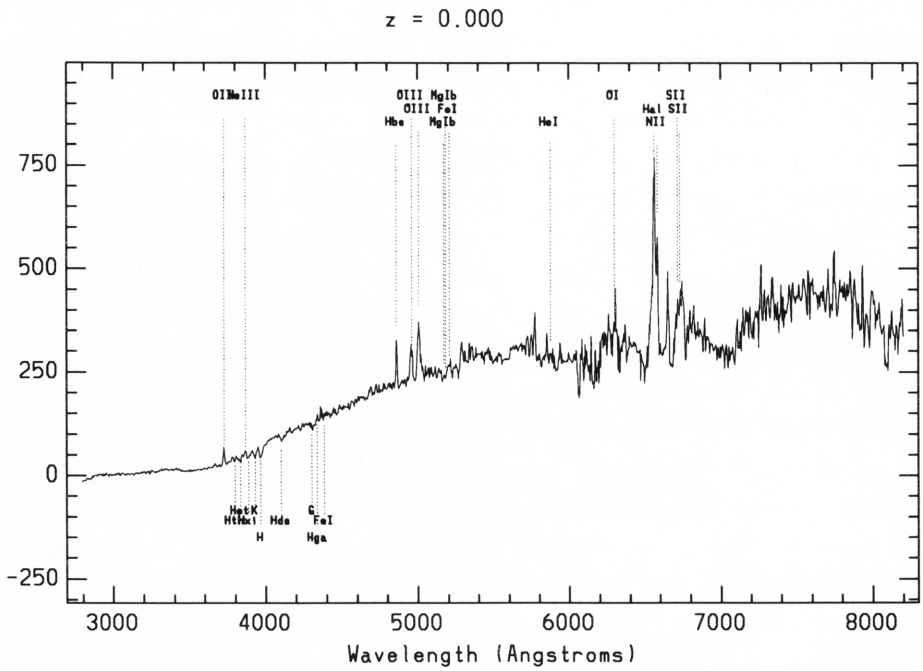

Figure 5.1 Compilation of emission line object spectra, showing location of major emission and absorption lines.

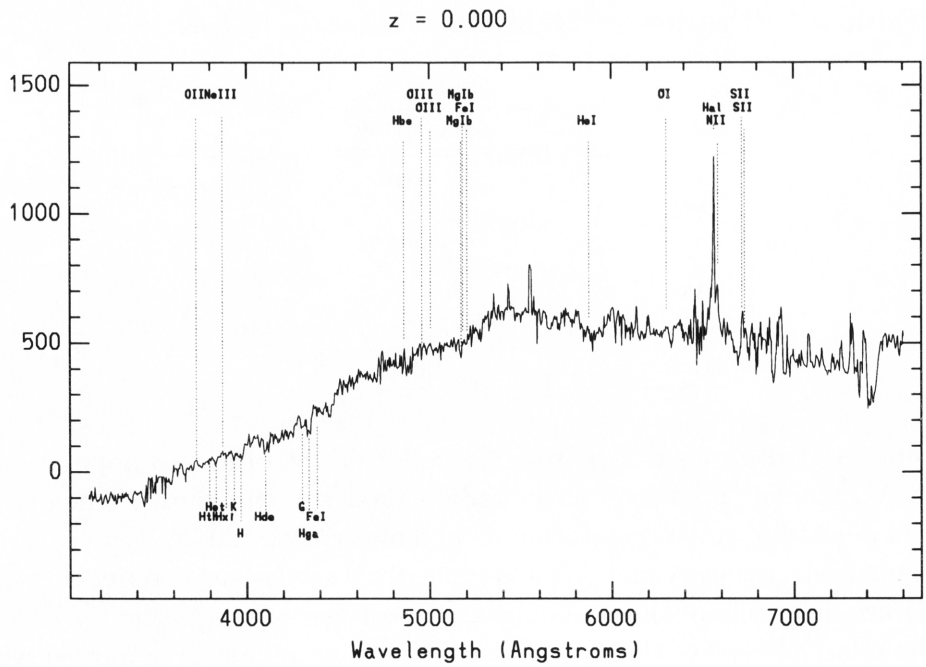

Figure 5.2 Compilation of class (B) spectra, with location of major lines indicated, although only Hα really appears in emission.

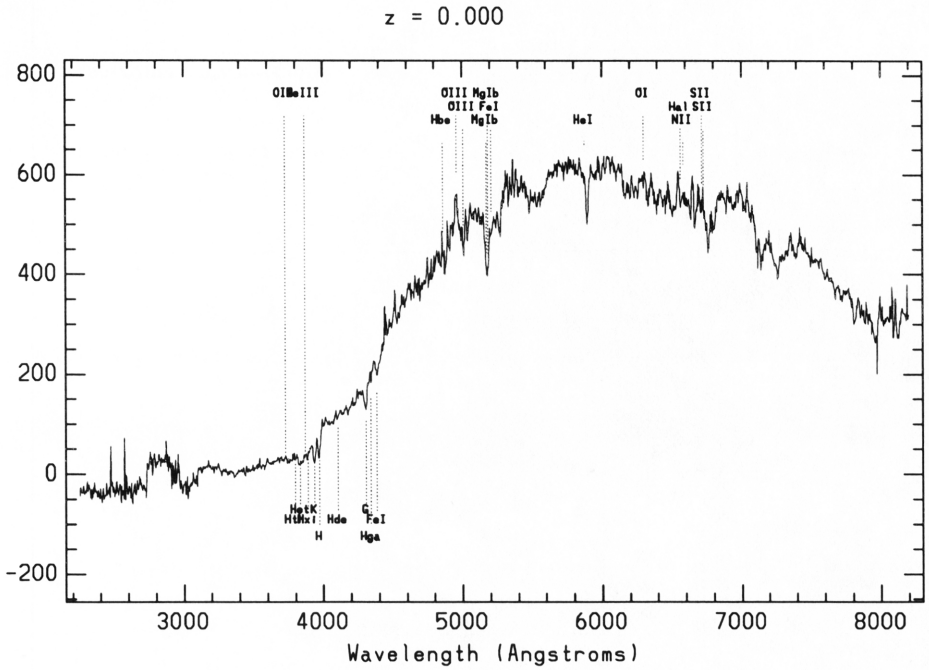

Figure 5.3 Compilation of absorption line object spectra, showing location of major emission and absorption lines.

luminosity functions of the two populations is for roughly equal numbers of starbursts and AGN to occur at about 0.2 mJy, with AGN dominating above that value, and starbursts below. Once further spectra are available, it will be an interesting exercise to reproduce this diagram to see how well the model predictions compare with the observations. This will also provide a useful test of the claims of Benn et al. (1993), Kron et al. (1985) and others regarding the location of the flux density at which the "crossover" between the two populations occurs.

5.3 Diagnostic diagrams

A series of diagnostic tools based on optical emission line ratios for distinguishing AGN and starbursts are well established (Baldwin et al., 1981; Veilleux & Osterbrock, 1987). Line ratios commonly used in such diagnostic diagrams are [O III]λ5007/Hβ, [N II]λ6583/Hα, [S II]λ6716 + λ6731/Hα, and [O I]λ6300/Hα. Another diagnostic diagram also uses the [O II]λ3727/Hβ ratio.

The spectral line ratio diagnostic diagrams are shown in Figure 5.5. Each diagram shows the ratios of the observed emission line flux densities for every PDS source which had all the necessary lines for that diagram present. The spectra have not been flux calibrated, (this doesn't change the emission line ratio since the lines are situated closely in wavelength, and the detector response, which is quite uniform,

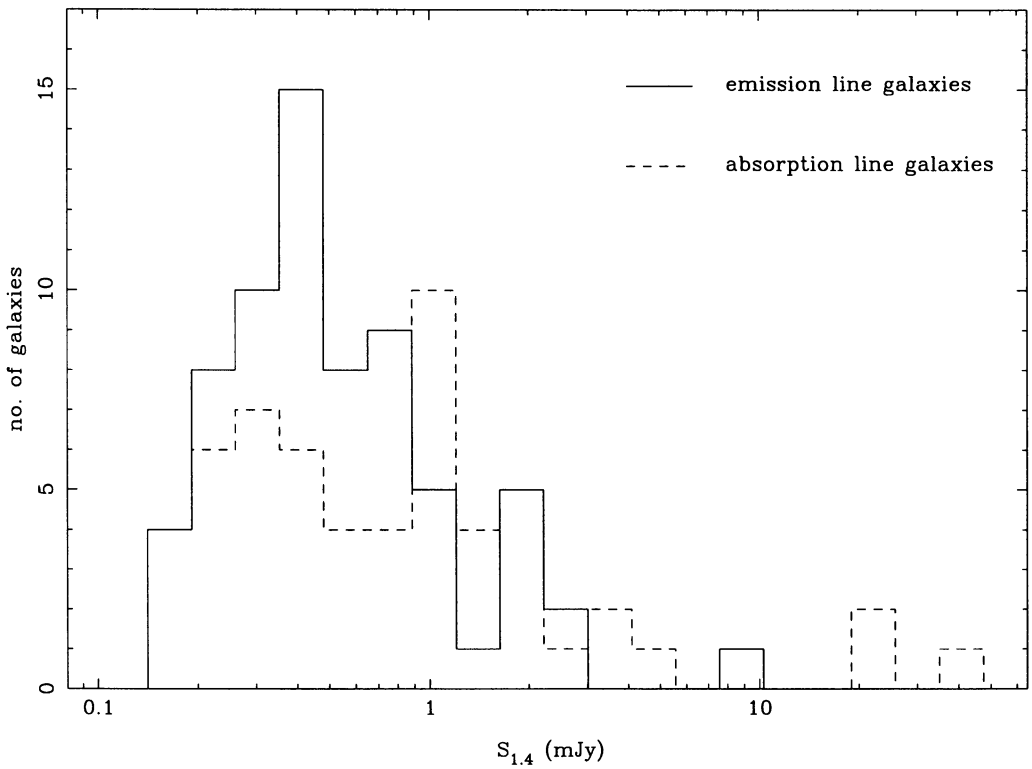

Figure 5.4 The radio flux density distribution of the emission and absorption line galaxies.

doesn't change significantly over the small wavelength range), and it is important to emphasise that obtaining accurate photometry from 2dF is difficult. It is hindered by tiny uncertainties in the fibre placement: errors as small as 0.″1 will produce a significant reduction in the amount of light entering the fibre from the target. This combined with other effects make spectrophotometry with the instrument impractical.

The solid and dotted lines shown on the diagnostic diagrams separate galaxies which have characteristics of H II regions, starbursts for example, from those whose emission lines show AGN properties. The lines are predictions from photoionisation models for stars at 50000 K (dotted line) and 60000 K (solid line) (Rola et al., 1997). Objects to the lower left in these diagrams have the properties of H II-like regions, starbursts for example, while objects to the upper right tend to be AGN, in particular Seyfert 2 galaxies. LINERs would appear to the lower right in these diagrams. Following the description in Baldwin et al. (1981), a reddening correction to the emission line ratios has been applied before constructing the final diagnostic diagrams. This has been carried out using parameters for the reddening curve presented by Miller & Matthews (1972), with the assumption that the unreddened $H\alpha/H\beta$ ratio is 2.86 for H II-like objects, and 3.1 for AGN-like objects. Since it is not known before applying the reddening correction which objects show what characteristics, the application of the reddening correction followed an iterative pro-

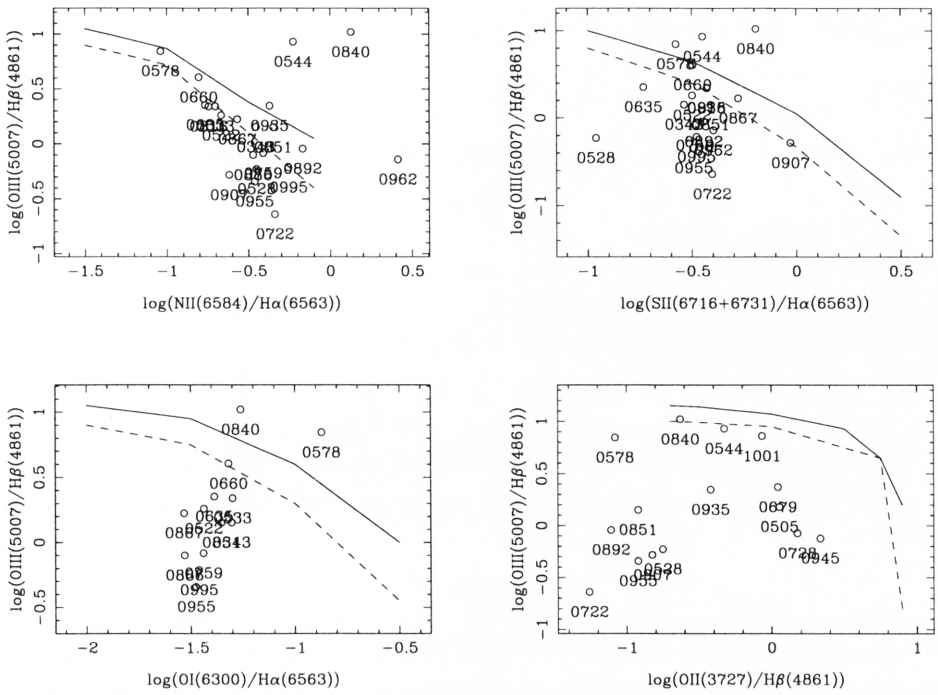

Figure 5.5 Diagnostic diagrams for narrow emission line galaxies. Objects are indicated by their catalogue number just below the circle showing their location in the diagram. This enables individual galaxies to be traced through each of the diagrams. Lines are photoionisation models for stars at 50000 K (dotted line) and 60000 K (solid line).

cess. Initially no reddening correction was applied, and then an appropriate choice of value for the Hα/Hβ ratio was used according to where the unreddened ratios appeared in the diagnostic diagrams. In all cases, though, the reddening correction was small, and made no significant changes to the way individual sources would be classified from each diagram.

The distributions shown in Figure 5.5 indicate that of the 36 objects for which at least one pair of emission lines can be measured the majority appear to be starburst galaxies. They also all fall into class (A) or (AB), and this is consistent with the assertion above that galaxies in those classes are typically starburst galaxies. Only two objects, PDS0544 and PDS0840, consistently appear to be Seyfert 2 galaxies.

A small number of galaxies in Figure 5.5 occupy the region between the lines, or even inconsistently straddle the starburst and Seyfert regions. It is possible that these galaxies may host both an AGN and a starburst, although further research needs to be undertaken to investigate this hypothesis.

5.4 Photometric redshifts

There are established methods for calculating photometric redshifts from multiwavelength observations of galaxies, which rely on having observations at many optical

or near-infrared wavelengths (Brunner et al., 1997; Sawicki et al., 1997; Subbarao et al., 1996; Connolly et al., 1995). While the PDS observations do not include sufficient data at present to make accurate calculations of photometric redshifts for the sample, it is instructive to investigate the trivial case for photometric redshift calculation. A very coarse approximation for a galaxy's redshift can be made using observations at a single wavelength. This is the original idea used by Hubble, and it requires galaxies to be "standard candles" for its success. Figure 5.6 shows the trend with redshift of the apparent R-band magnitude for galaxies in the PDS which have had their redshift established through 2dF observations. The galaxies are marked by the spectral class (A, B, C or D) to which they have been assigned. Galaxies of class 'AB' are marked as class 'A'. Galaxies marked with a '*' are those whose redshifts were measured using EFOSC and hence weren't assigned a spectral class in the fashion of the 2dF targets. Although in the absence of any defining selection procedure galaxies do not have a single, clearly defined absolute magnitude, those of class 'C', (likely to be elliptical galaxies), are clustered more closely around a constant value of M_R. They are therefore better for use as "standard candles" than the other classes in establishing photometric redshifts. If, however, any galaxy is assumed to be a "standard candle", a resulting increase in the error of the estimated redshift will result. The error in such a calculation is easy to investigate. Since the PDS galaxies typically have apparent R-band magnitudes between about 16 and 22, expected distance moduli assuming $M_R = -22$ would lie between about 38 and 44. Table 5.2 shows calculations of redshift from a given distance modulus. A 2 magnitude error in the distance modulus can be seen to produce very large differences in the predicted redshift, especially for the more distant galaxies.

Table 5.2 : Redshift as a function of distance modulus.

$\Delta(= m_R - M_R)$	38	40	42	44	46
z	0.065	0.16	0.38	0.91	4.15

In Figure 5.6 there are several objects which lie well outside the region bordered by the dashed lines. These are objects which are either intrinsically very bright (above the trend), corresponding to QSOs as shown by their spectral class (D), or objects which are intrinsically very faint (below the trend), which are likely to be either dwarf galaxies or galaxies exhibiting a lot of obscuration due to dust. The relevant properties of the five latter objects are listed in Table 5.3. The redshifts for two of these are uncertain, which may contribute to their location in this diagram.

5.5 Redshift distribution

Figure 5.7 shows the observational redshift distribution from the PDS compared with the predictions from the BLF with appropriate flux-density limits at both optical and radio wavelengths. The observational distribution has been separated

Table 5.3 Objects lying below the trend in Figure 5.6. The first column is the PDS catalogue number of the object.

	m_R	class	z	Q	type
270	20.919	s	0.126	1	C
343	18.587	g	0.025	1	A
553	21.342	g	0.032	2	AB
621	19.586	g	0.070	1	A
681	19.558	g	0.047	3	C

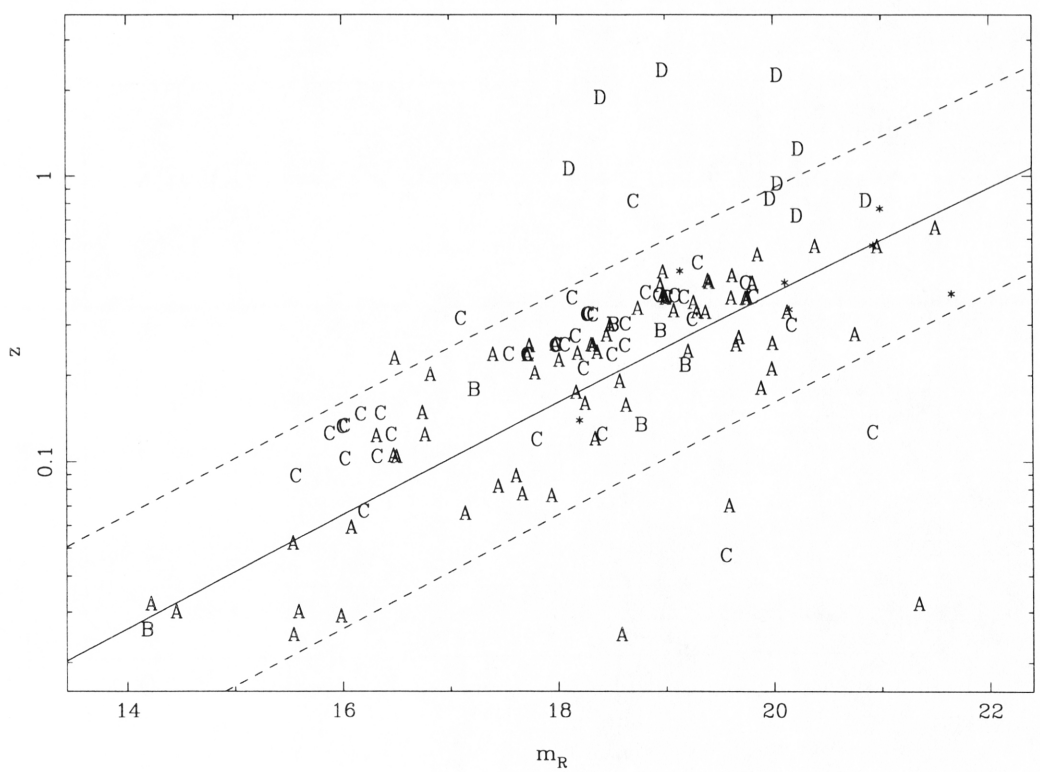

Figure 5.6 Redshift as a function of m_R. The lines are of constant M_R. Solid line: $M_R = -22$ mag; Upper dashed line: $M_R = -24$ mag; Lower dashed line: $M_R = -20$ mag.

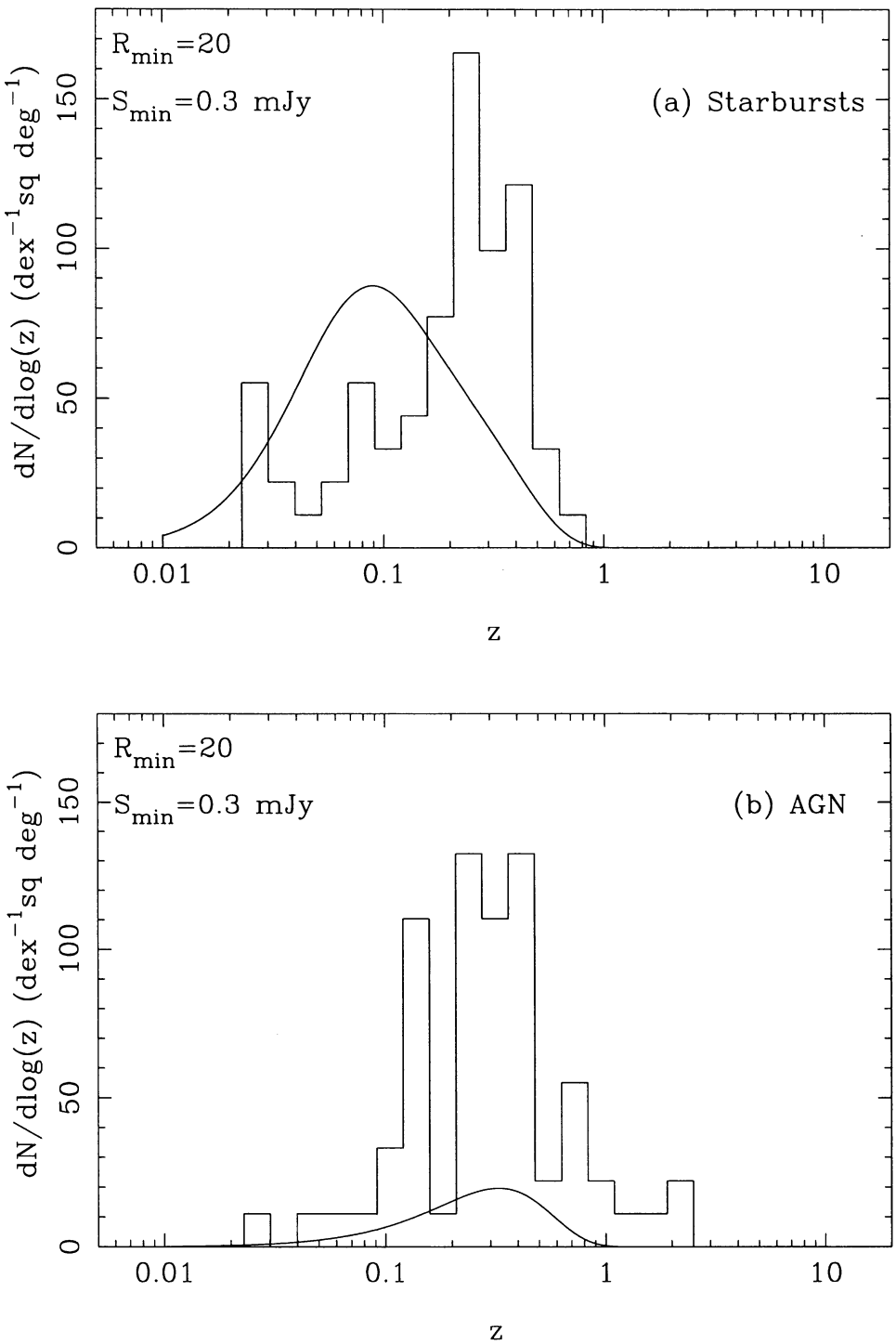

Figure 5.7 Observed redshift distribution shown with predictions from the BLF overlayed. The predicted curves are for flux-density limits corresponding to $m_{\mathrm{R_{min}}} = 20$ and $S_{1.4\mathrm{min}} = 0.3\,\mathrm{mJy}$. (a) shows the distribution for starburst galaxies, (b) shows that for AGN galaxies.

into starbursts (spectral classes A and AB) and AGN (classes B, C and D), for comparison with the predictions. Since not all optically identified radio sources have their redshifts measured at present, the comparison with predictions must not be taken at face value. They have been multiplied by N_{ID}/N_z before plotting (where N_{ID} is the number of optical IDs of radio sources, and N_z is the number of those with measured redshifts). Those with measured redshifts can be considered to be a roughly representative sample of sources brighter than about $R = 20$ and $S_{1.4} = 0.3\,\mathrm{mJy}$ ($R = 20$ was chosen as the limiting magnitude for the predictions, since, although the 2dF target list was chosen from objects as faint as $R = 21$, only 17 objects fainter than $R = 20$ had redshifts measured). Qualitatively, at least, the predictions have similar properties to the observational distributions: There are more starburst galaxies at the nearby redshifts, and more AGN at the distant redshifts; the shapes of the observed distributions – a long tail at lower redshifts with a sharper drop-off at higher redshifts – mimic the predictions, although the median redshift (for AGN) and the normalisation (for both populations) doesn't. The differences, however, are quite pronounced. There is a large spike in the observed redshift distribution for starbursts above the predictions at $z \sim 0.2$, and the AGN population has a significantly greater amplitude than the model predicts. These are discrepancies which need to be investigated as the model BLF is refined.

5.6 Radio galaxy luminosity function

The luminosity function for the radio galaxies can now be calculated using the flux density and redshift data from the PDS. The method used to construct the luminosity function is the standard method for flux density limited surveys (Condon, 1989). Every radio source having an optical counterpart and a measured redshift is treated individually. First, the intrinsic luminosities, both radio and optical, are calculated. These are then used together with the flux density limits from both the radio and optical surveys to calculate the maximum redshift at which this galaxy would still have been detected in *both* surveys. The volume, V_{max}, corresponding to this maximum redshift is calculated, and $1/V_{\mathrm{max}}$ is added to the luminosity function in the appropriate radio luminosity bin. The result of this process is the radio luminosity function, $\Phi(L_{1.4})$, with units of $\mathrm{Mpc}^{-3}(\mathrm{WHz}^{-1})^{-1}$.

A volume V is calculated from a redshift using $V = \frac{4}{3}\pi r^3$ with r defined in terms of z according to the cosmological model adopted. Now, the luminosity distance of an object at a redshift of z is defined as

$$D_L = \frac{c}{H_0 q_0^2}(q_0 z + (q_0 - 1)(\sqrt{1 + 2q_0 z} - 1)), \tag{5.1}$$

in Mpc when c, is in units of kms^{-1} and the Hubble constant, H_0, is in units of $\mathrm{kms}^{-1}\mathrm{Mpc}^{-1}$. The value of $q0$ has been assumed to be 0.5 throughout this thesis, giving

$$D_L = 2\frac{c}{H_0}(1 + z)(1 - \frac{1}{\sqrt{1 + z}}). \tag{5.2}$$

Then, since $r = D_L/(1+z)$,

$$r = 2\frac{c}{H_0}(1 - \frac{1}{\sqrt{1+z}}), \tag{5.3}$$

and so

$$V = \frac{32\pi c^3}{H_0^3}\left(\frac{1}{1+z} - \frac{1}{(1+z)^{0.5}} - \frac{1}{3(1+z)^{1.5}} + \frac{1}{3}\right). \tag{5.4}$$

In a pencil-beam survey only a certain solid angle, Ω, is observed, so the actual volume sampled is $V_\Omega = (\Omega/4\pi)V$. Now $V_{\max}$ can be calculated directly from known quantities for each source, and the luminosity function constructed.

5.7 Construction of the luminosity function

There are 133 sources in the PDS which have measured redshifts. There are 5 sources which have redshifts greater than $z = 1$ and these were excluded from the luminosity function construction to reduce any strong effect due to luminosity evolution. The flux density limits used in the calculations were $m_R = 22$ mag and $S_{1.4} = 0.1$ mJy. There are no sources fainter than these limits which have measured redshifts. If there had been they would have been excluded from the analysis. It was necessary to correct for the fact that not all the radio sources had their redshifts measured, and this was done simply by using a constant correction factor equal to the total number of radio sources divided by the number having observed redshifts. This is a very crude way of dealing with the fact that not all the sources have had their redshifts measured, and will undoubtedly be biased when comparing starburst and AGN populations. This arises since emission line galaxies are easier to obtain redshifts for than ellipticals. As a result, the calculated luminosity functions may disproportionately reflect the starburst galaxy population in favour of the AGNs. Also as a result of this, no attempt has been made to divide luminosity evolution out of the observationally derived LF. Rather, comparison radio LF models have been graphed at the redshift which best matches the derived observational LF. If the sample with measured redshifts is characteristic of the whole sample, then this redshift would be, in some sense, a median value for the whole sample.

The radio luminosity function calculated is presented in Figure 5.8. Errors were calculated by the method described in Condon (1989), except that for luminosity bins containing only 1 source, error bars are not shown. The model radio luminosity functions for AGN and starbursts are shown overlayed for comparison. The dashed line is the luminosity function for starburst galaxies from Equation (3.4), the dot-dashed line is the luminosity function for AGN galaxies from Equation (3.5), and the solid line is the sum of the two populations. These models, which are redshift dependent when the luminosity evolution required to model the source counts is included, have been calculated at $z = 0.2$. This is a reasonable value to take, given the range of the observed redshifts (see Figure 5.7).

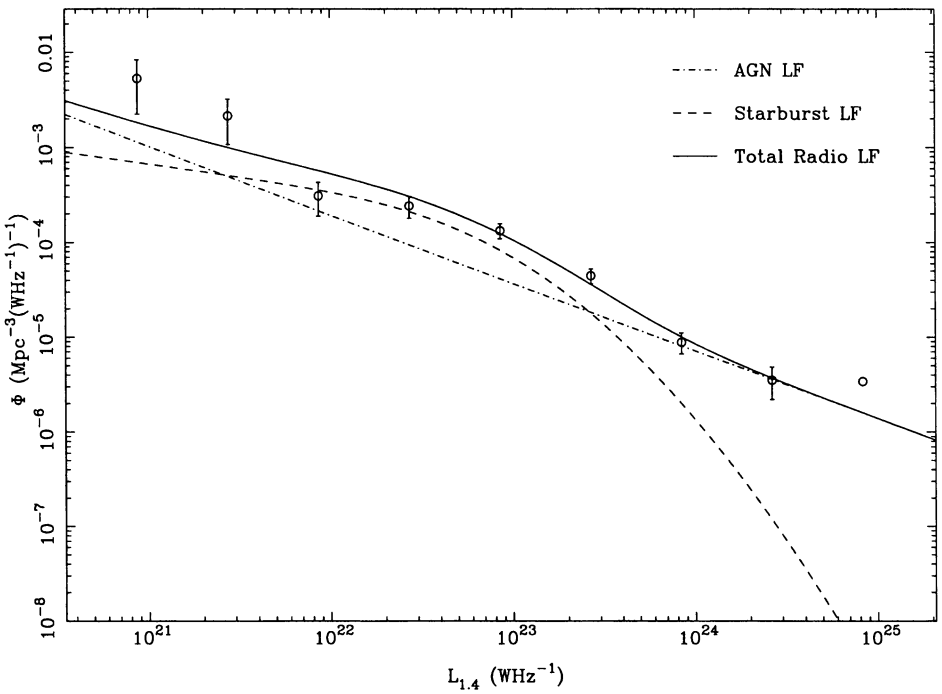

Figure 5.8 $\Phi(L_{\rm rad})$ compared with radio luminosity function models at $z = 0.2$ (see text).

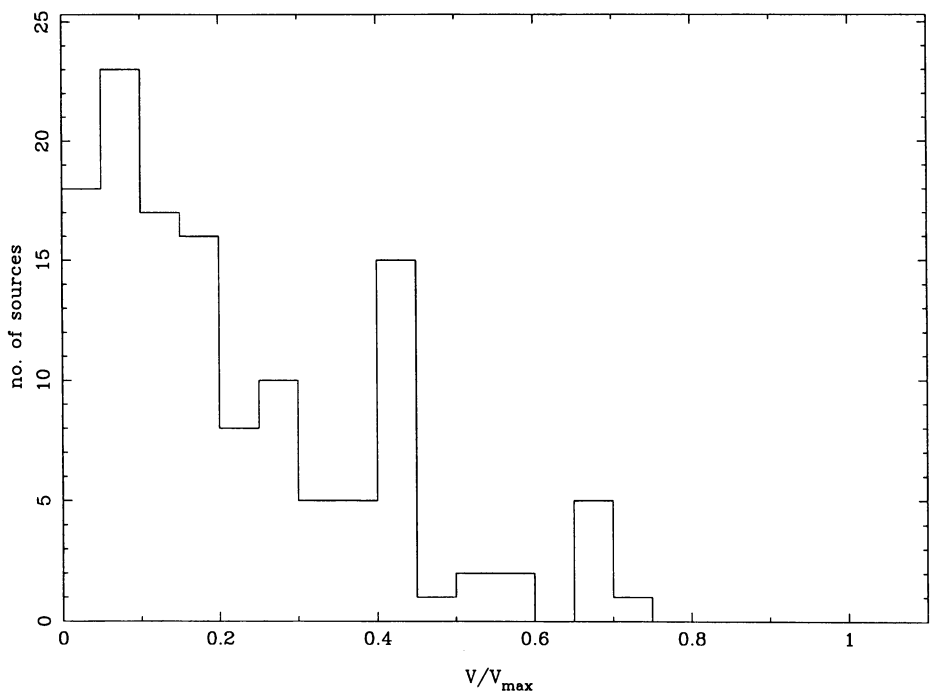

Figure 5.9 Distribution of $V/V_{\rm max}$ for luminosity function shown in Figure 5.8.

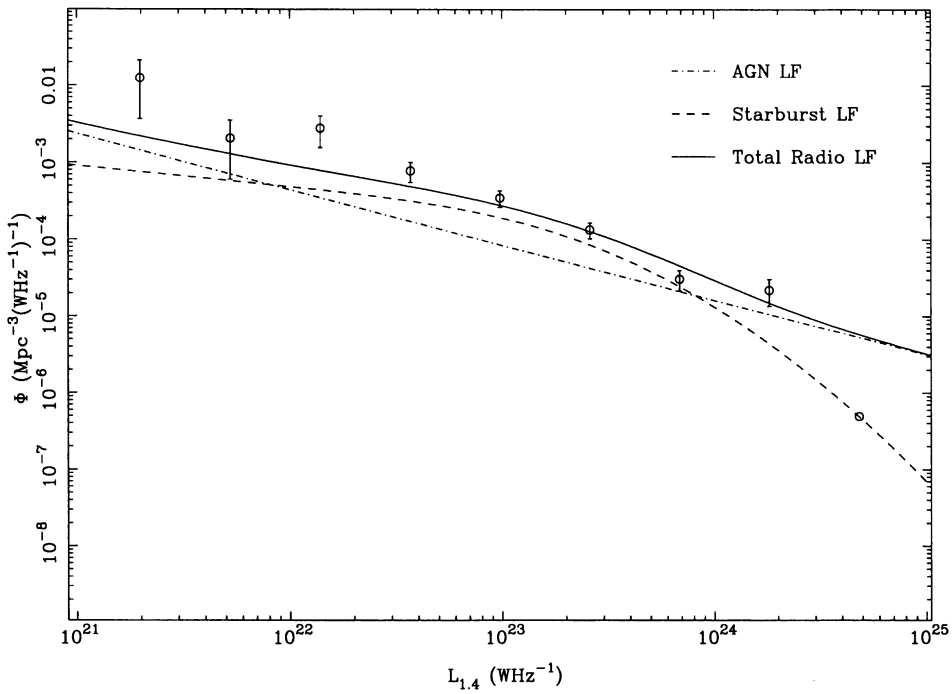

Figure 5.10 $\Phi(L_{\rm rad})$ calculated using higher flux density limits. The comparison luminosity functions are now at $z = 0.7$.

The distribution of $V/V_{\rm max}$ (the volume out to the actual redshift of each object divided by $V_{\rm max}$ for that object) (Schmidt, 1968) is a measure of galaxy clustering when the sample being investigated is complete. However, since the sample under investigation here is not complete, in the sense that redshifts for all radio sources have not been measured, this quantity instead gives an indication of the nature of the incompleteness. For a complete sample which doesn't show any clustering, $V/V_{\rm max}$ should have a uniform distribution between 0 and 1. If this is true, then $< V/V_{\rm max} >= 0.5$. For the radio sources from the PDS with known redshifts, the distribution of $V/V_{\rm max}$ is shown in Figure 5.9, and $< V/V_{\rm max} >= 0.220$. This low value is a reflection of the fact that of the sources with measured redshifts, there are more which are apparently much brighter than the assumed flux density limits, than there are close to those limits. This is highlighted if the flux density limits assumed are raised, say to $m_{\rm R} = 20$ mag and $S_{1.4} = 0.3$ mJy. There are only 90 of the sources with measured redshifts which are brighter than these limits, and the luminosity function calculated using these objects and these limiting flux densities is shown in Figure 5.10. Figure 5.11 is the accompanying distribution of $V/V_{\rm max}$, and now $< V/V_{\rm max} >= 0.463$. The comparison luminosity functions have been calculated this time at $z = 0.7$.

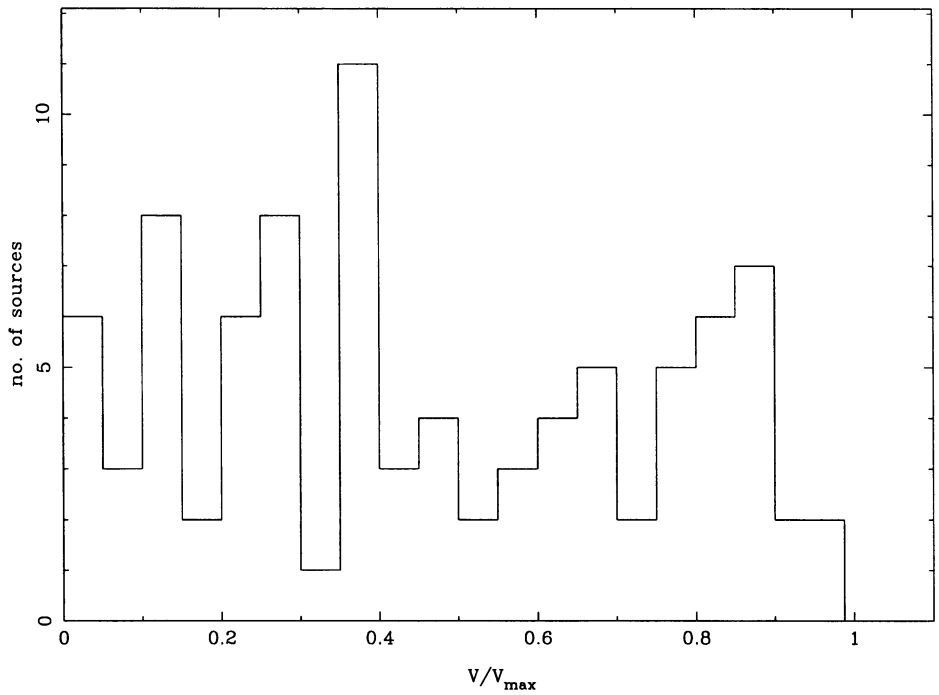

Figure 5.11 Distribution of $V/V_{\rm max}$ for luminosity function shown in Figure 5.10.

5.8 Summary

The 2dF spectra obtained have been analysed with the aim of providing a feel for the redshift range and object type comprising the radio sources in the PDS. The distribution of redshifts for the flux densities and magnitudes involved is comparable to that expected from earlier work (Fomalont et al., 1997; Hammer et al., 1995; Benn et al., 1993), although without a complete sample, preferably to at least as faint as $R = 21$, no definite conclusions can be drawn. Using the existing spectra, however, the redshift distribution has been investigated, showing qualitative similarities with model predictions. Significant quantitative differences are also evident, though, requiring further investigation using a complete spectroscopic sample. Diagnostic line-ratio diagrams have been used to attempt to distinguish between starburst and Seyfert 2 galaxies in the narrow emission line sample. Only two of the 36 objects able to be graphed in such diagrams consistently showed ratios indicative of Seyfert 2 processes. The remaining objects are likely to be either starbursts or hybrid objects with both Seyfert 2 and starburst processes present. An attempt at constructing the observed radio luminosity function has been made, although this is hampered by the lack of redshifts.

The main conclusion here is that while the BLF model predictions don't agree quantitatively with the population and redshift distribution of the subsample of the PDS measured, a complete sample is required before any firm conclusion about the validity of the model can be drawn.

Chapter 6

Some interesting galaxies

6.1 The most luminous starburst galaxies

It is now well established that star formation appears to be the dominant energy source in most (70%-80%) luminous infrared galaxies (Genzel et al., 1998; Colina et al., 1997; Crawford et al., 1996, for example), while the remaining cases would require implausibly luminous radio supernovae to explain the emission through a starburst model (Smith et al., 1998b), and are most likely to be powered by an AGN source instead. Indeed, as many as 50% of such galaxies may contain both AGN and circumnuclear starburst sources (Genzel et al., 1998). Highly radio luminous starburst galaxies are also likely to be interacting systems, the interaction triggering the burst of star formation (Smith et al., 1998a). A commonly invoked mechanism for explaining this scenario is angular momentum loss during galaxy interactions which drives gas towards the nucleus, there concentrating and compressing it to initiate a circumnuclear starburst (Barnes & Hernquist, 1996). This is followed by further gas transport into the region of the accretion disk of a central massive black hole, to power an AGN (Norman & Scoville, 1988; Scoville & Norman, 1988).

To identify new objects for further study into this relationship and other details of the luminous starburst phenomenon, the most luminous PDS galaxies identified as being possible starbursts were investigated.

6.2 Luminous starbursts in the PDS

From the sample of radio sources with known redshifts, the galaxies with radio luminosities greater than $10^{23.5}\,\mathrm{WHz}^{-1}$ were examined more closely. For galaxies whose source of radio luminosity is a result solely of a starburst, a radio luminosity this high is extremely bright. There are 44 galaxies (out of the 133 with measured redshifts) with $L_{1.4} > 10^{23.5}\,\mathrm{WHz}^{-1}$. The majority of these, unsurprisingly, are either quasars (in fact all 9 objects established to be quasars are in this group) or absorption line galaxies (giant ellipticals), and hence their radio luminosity is most likely derived from an AGN. Only 13 of these 44 galaxies show narrow emission

lines, indicating the presence of a starburst or Seyfert 2 activity. These are listed in Table 6.1.

A selection of five of these thirteen emission line galaxies are shown (in decreasing order of radio luminosity) in Figures 6.1 to 6.5. These Figures are radio contour images, the contour levels being given in the Figure captions, overlayed on grey-scale optical CCD frames. In each case the coordinates of the relevant object are given in the Figure title, and the PDS catalogue number (see Table A) in the caption.

The spectra for these galaxies are presented in Figures 6.6 to 6.10. The Figures indicate the redshift of the object and also the location of some emission lines. Night sky lines, still present after poor sky subtraction, are indicated by "NS". Note the presence of [O II] and [O III] emission, which are strong indicators of star formation. All five of these objects show [O II] emission, and three show [O III] lines as well. This alone does not confirm the objects are starbursts, as AGNs may show narrow emission lines from ionised oxygen. In fact, the radio morphology indicates that perhaps at least two of these may have their radio emission derived from AGN processes. PDS1001 shows an extended radio tail, typical of an AGN. There is a nearby galaxy within the radio contours of this object, possibly an interacting system. PDS1018 also shows extended radio emission, the warping visible possibly due to radio jets distorted by the passage of the galaxy through the intergalactic medium. However, PDS0946, PDS0729 and PDS0679 all show fairly compact radio sources and nearby optical galaxies. Where there is any distortion of the radio contours it is in the direction of these companions, indicating a possible interaction between the galaxies (Condon et al., 1982a). Such interactions are associated with initiating starbursts (Hopkins & Cram, 1997) and AGN phenomena in galaxies, so it is possible that this is the situation here. The prodigious radio emission may be due either to the combination of emission from starbursts in both objects, or to an AGN together with a starburst (Sopp & Alexander, 1991). initiated by the interaction. PDS0679 and PDS1001 are the only two of these five galaxies which appear in the line-ratio diagnostic diagrams, (Figure 5.5). Their line ratios indicate that PDS0679 is possibly a starburst object, while PDS1001 is probably an AGN (since it lies close to PDS0840 and PDS0544 which are likely to be AGNs by virtue of their line ratios presented in the other graphs in this Figure). It is possible that the other compact radio sources are starbursts involved in interactions, but more detailed observations and analysis of the individual systems are required to confirm this hypothesis.

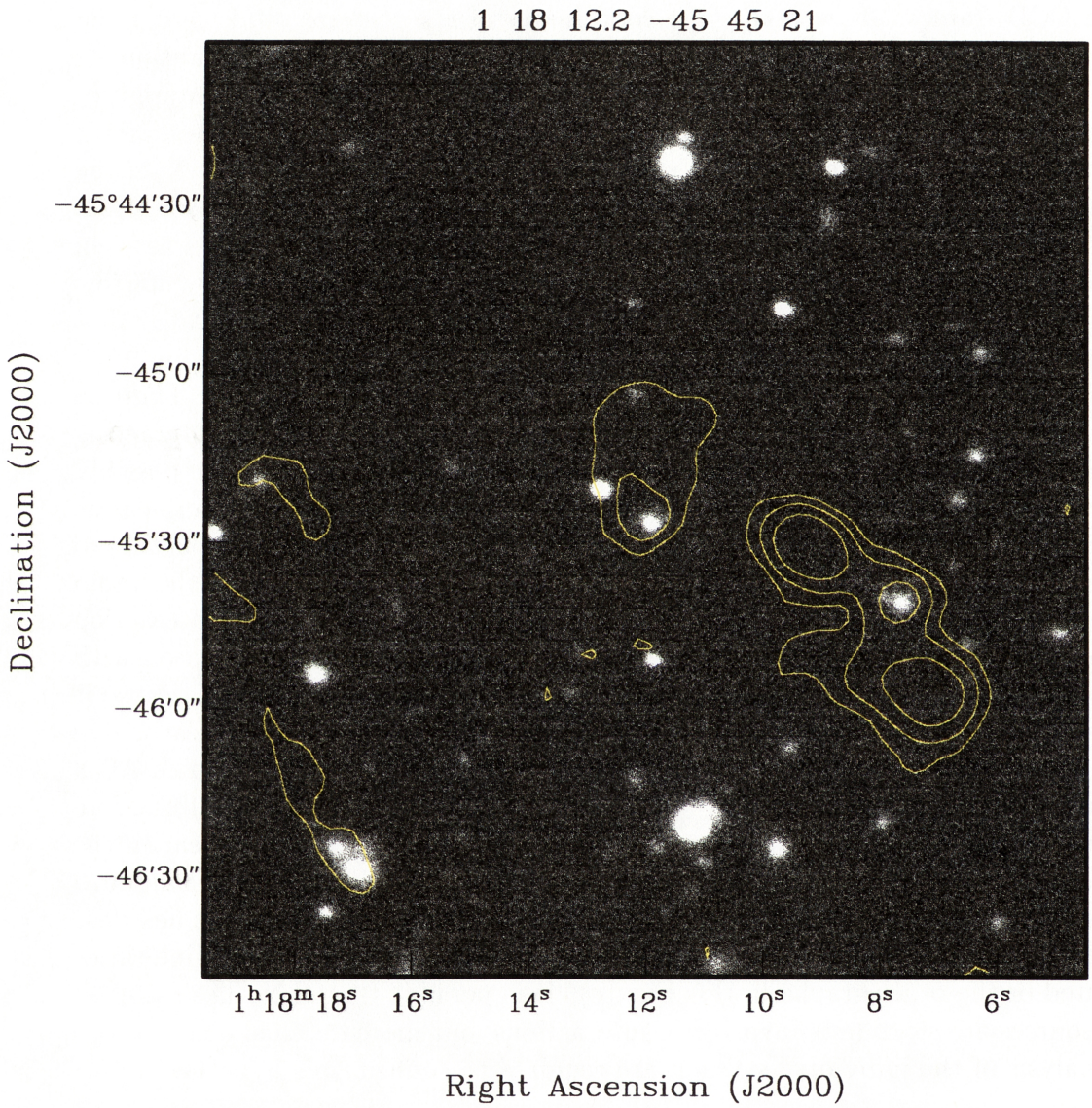

Figure 6.1 Catalogue number 1001. Contour levels are 0.20, 0.50 and 1.00 mJy.

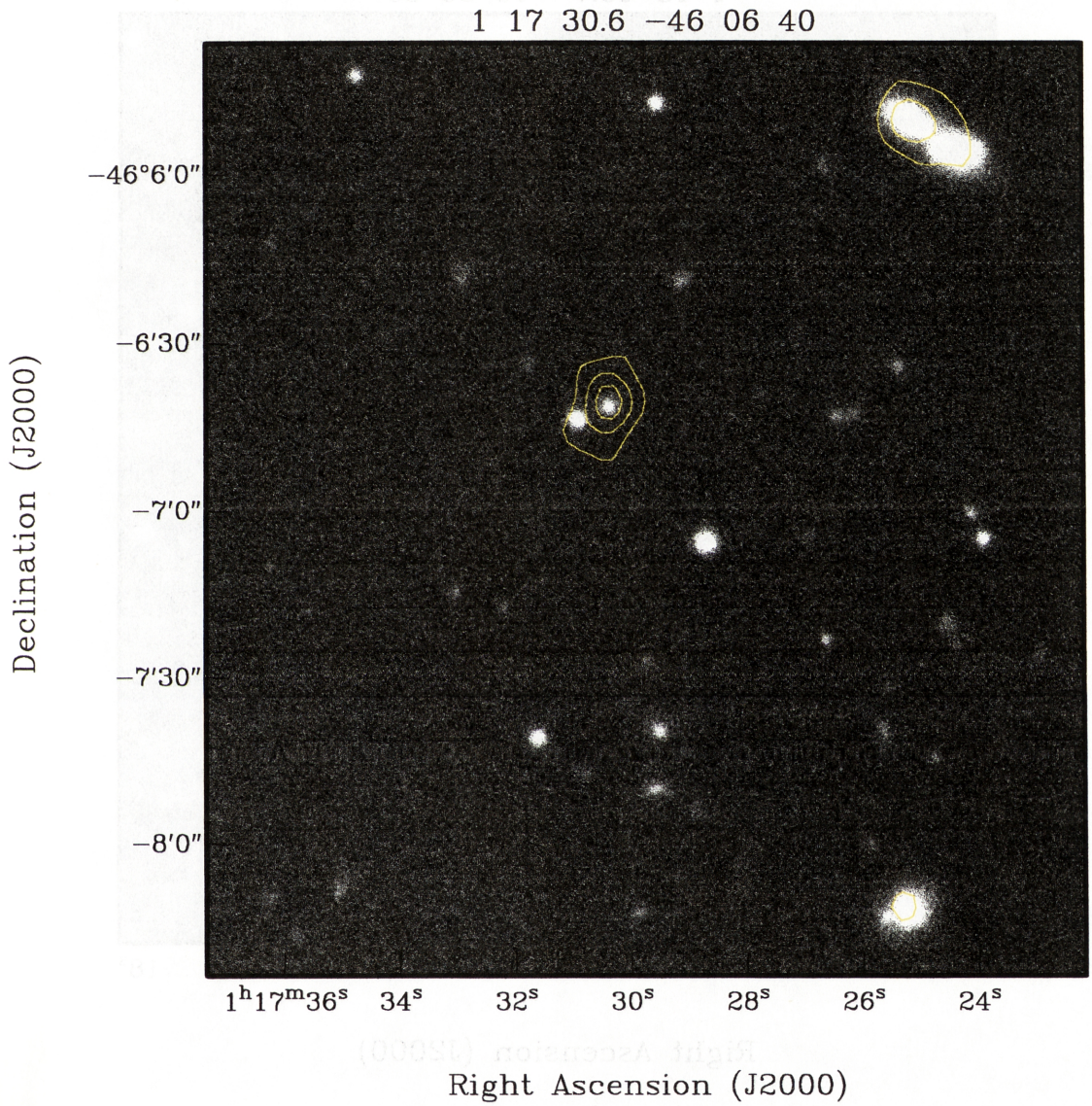

Figure 6.2 Catalogue number 0946. Contour levels are 0.20, 0.45 and 0.70 mJy.

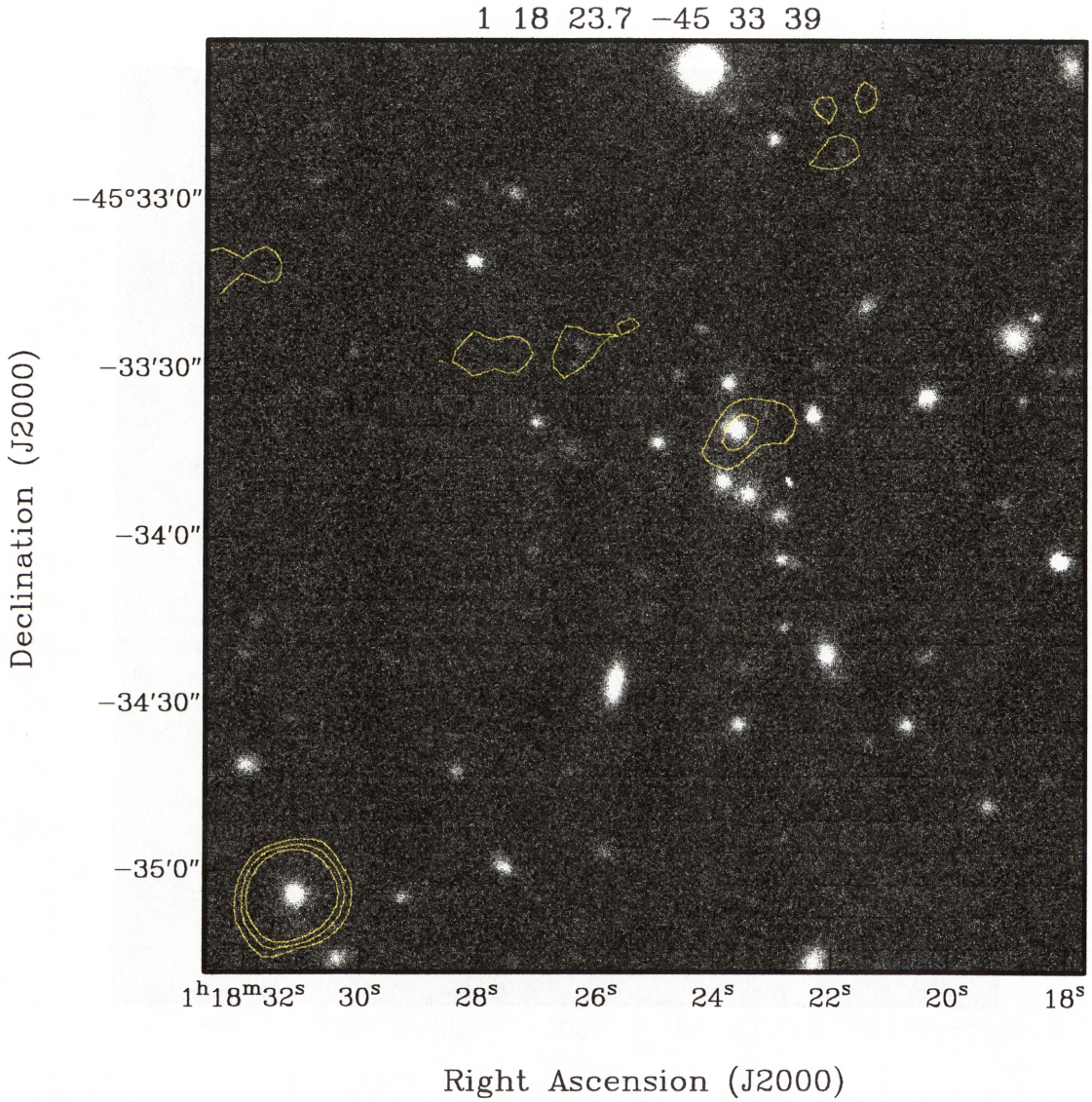

Figure 6.3 Catalogue number 1018. Contour levels are 0.20, 0.40 and 0.70 mJy.

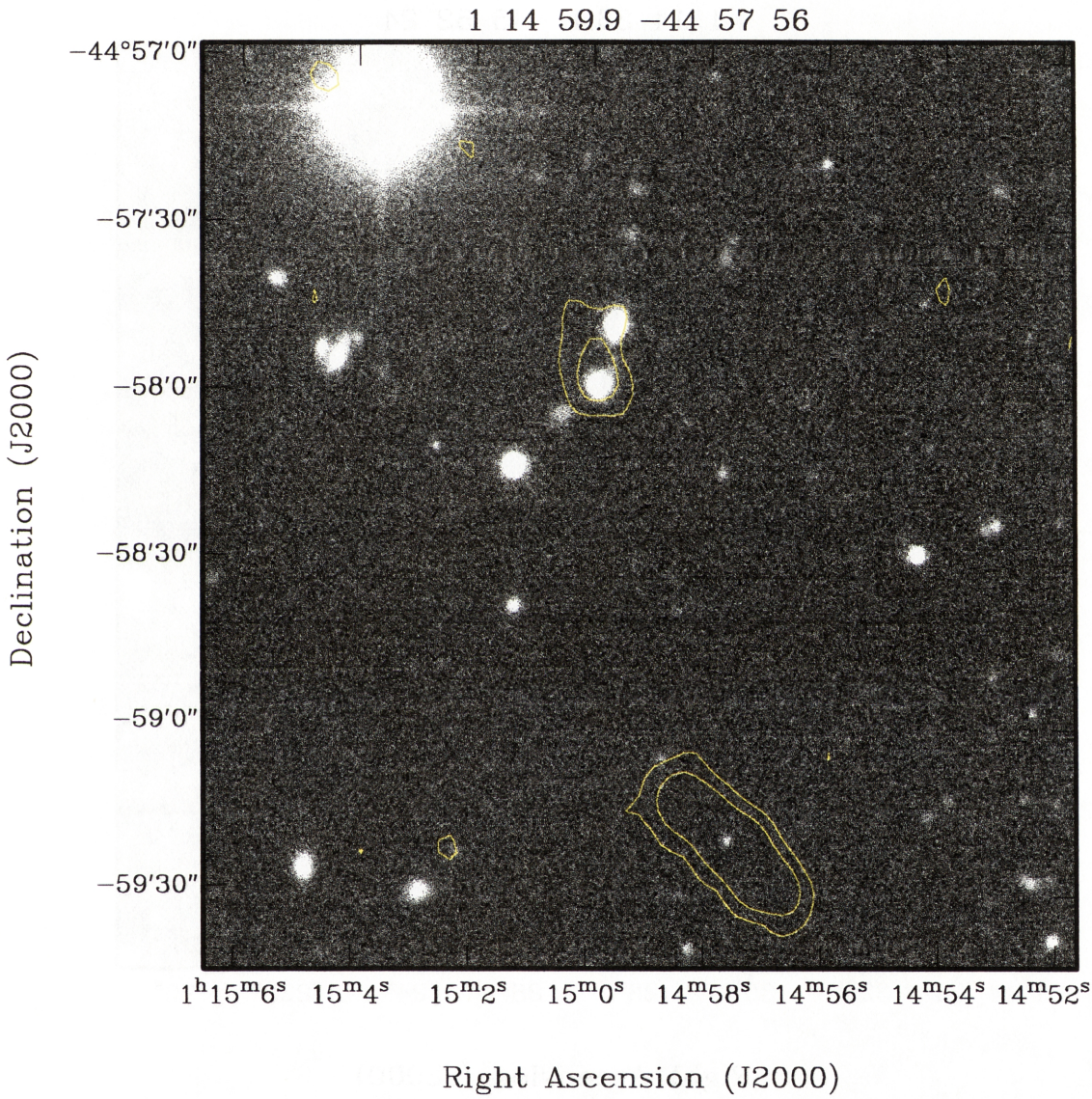

Figure 6.4 Catalogue number 0729. Contour levels are 0.20 and 0.50 mJy.

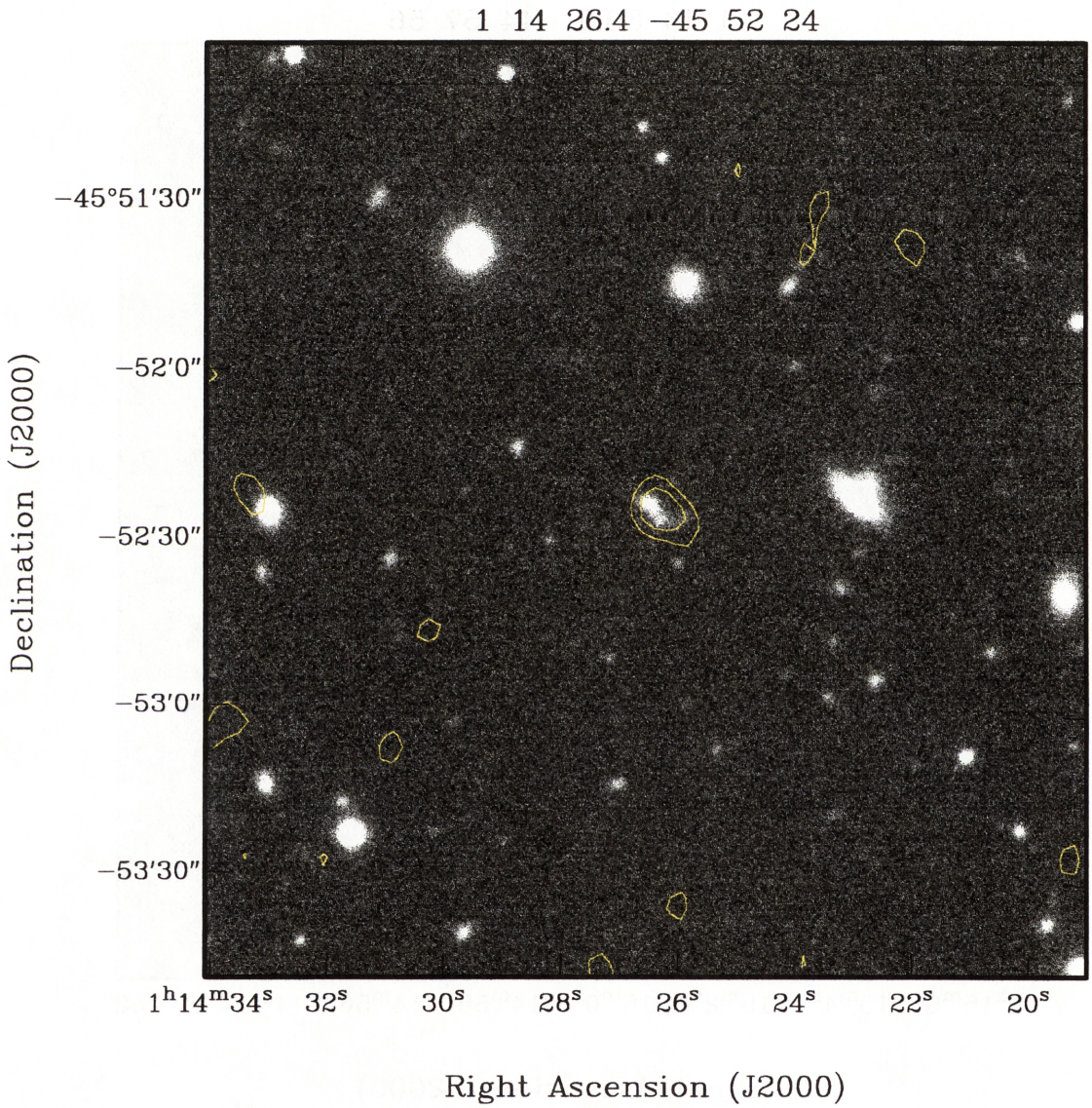

Figure 6.5 Catalogue number 0679. Contour levels are 0.12 and 0.20 mJy.

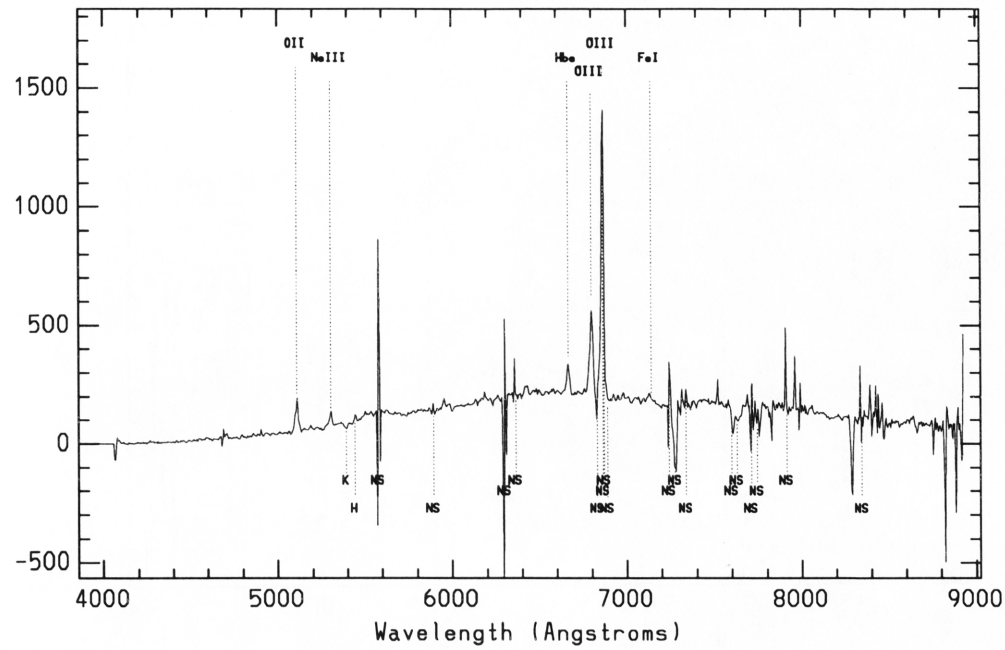

Figure 6.6 Spectrum of PDS1001.

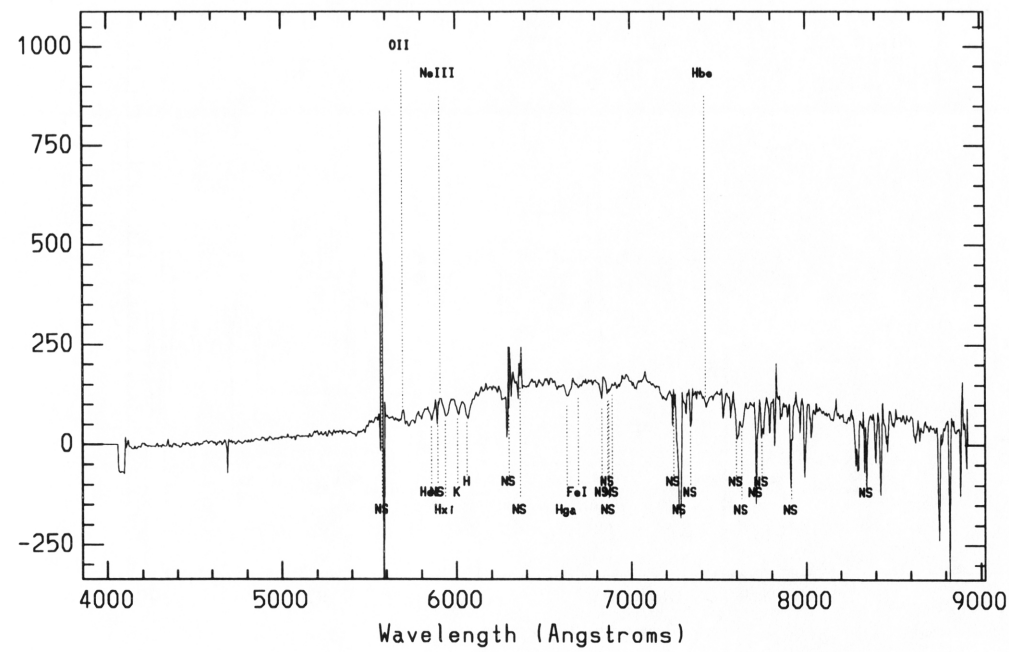

Figure 6.7 Spectrum of PDS0946.

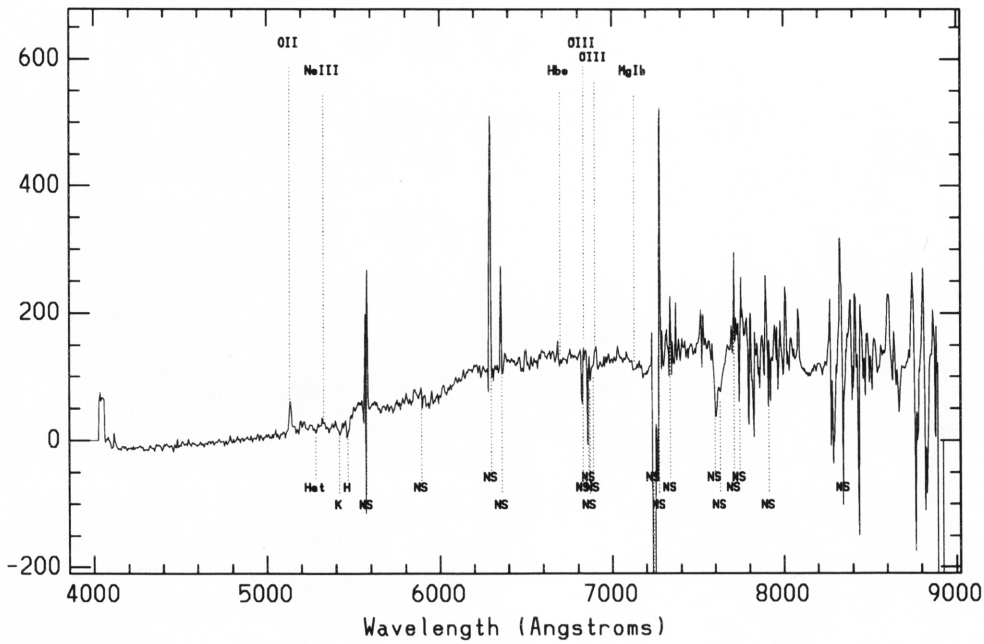

Figure 6.8 Spectrum of PDS1018.

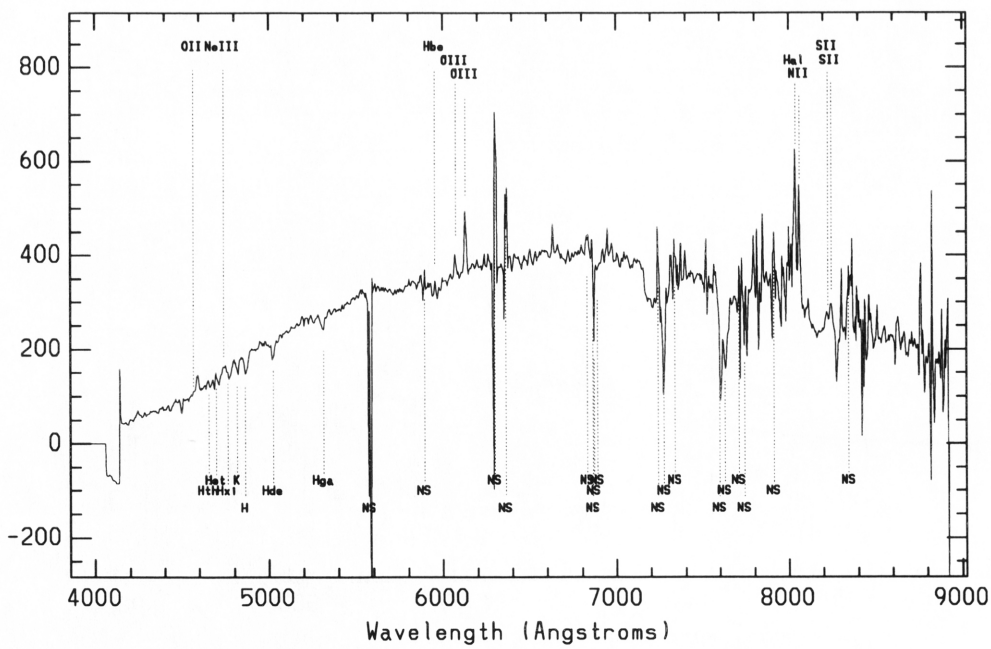

Figure 6.9 Spectrum of PDS0729.

Table 6.1 The 13 narrow-line objects with $L_{1.4} > 10^{23.5}\,\mathrm{WHz}^{-1}$. These objects are the brightest radio sources whose radio emission may derive solely from starburst mechanisms. The first column is the PDS catalogue number (see Appendix A). The last column gives all (uncorrected) measured line ratios.

	$\log(L_{1.4})$	M_R	M_V	M_{B_J}	class	z	Q	type	
0409	23.51	-22.83	-20.80	-21.43	g	0.427	1	A	[O II]/Hβ = 1.65
0505	23.55	-22.70	-21.80	-20.93	g	0.445	1	A	[O II]/Hβ = 1.13
									[O III]/Hβ = 1.52
0672	24.55	-21.73	-20.54	-20.22	s	0.655	3	AB	
0679	23.52	-23.42		-23.05	g	0.459	1	A	[O II]/Hβ = 1.11
									[O III]/Hβ = 2.35
0728	23.56	-22.36		-21.69	g	0.333	1	A	[O II]/Hβ = 1.50
									[O III]/Hβ = 0.84
0729	23.66	-22.75		-22.80	g	0.225	1	AB	[N II]/Hα = 0.48
									[S II]/Hα = 0.39
0847	23.56	-22.49		-26.29	g	0.564	1	AB	
0856	24.00	-22.38		-19.55	g	0.419	1	AB	
0895	24.15	-22.15			g	0.370	2	AB	
0946	24.13	-22.86		-22.01	s	0.527	1	AB	
1001	24.27	-22.90		-21.16	g	0.371	1	A	[O II]/Hβ = 0.50
									[O III]/Hβ = 7.24
1018	23.77	-22.97	-22.00	-20.97	g	0.378	1	AB	
1019	23.90	-21.91		-19.83	g	0.563	2	AB	

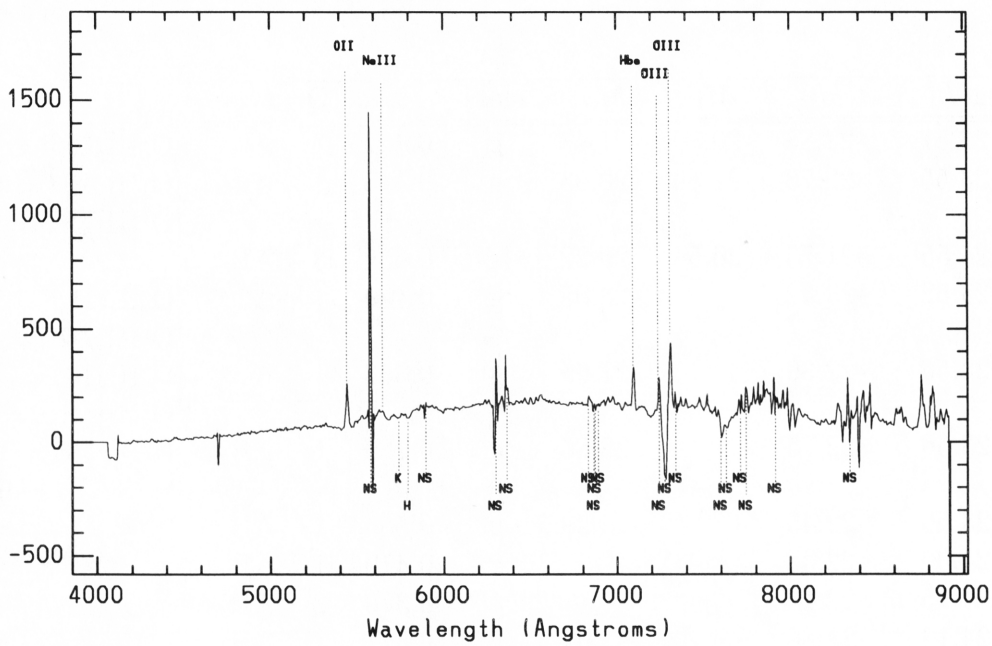

Figure 6.10 Spectrum of PDS0679.

Chapter 7

Star formation rates

The work presented in this Chapter is not independent research, but is a project led by Lawrence Cram which is closely related to the work described in this thesis. It follows on from results presented in Chapter 5 and it is particularly relevant to suggestions posed at the end of the previous Chapter.

7.1 Radio source populations

In the vast majority of extragalactic radio sources with 1.4 GHz flux density $S_{1.4} \gtrsim 1\,\mathrm{mJy}$ the radio emission is produced by a "monster" emitting a spectral power density $P_{1.4} \gtrsim 10^{23}\,\mathrm{WHz^{-1}}$ (e.g. Condon 1989, especially his Fig. 12; Wall & Jackson 1997). These sources are members of the class of powerful radio galaxies. Their optical hosts are intrinsically bright elliptical galaxies with red colours and optical luminosities of the order of $5 \times 10^{37}\,\mathrm{W}$ (Kron et al., 1985). While the monster may stimulate some nuclear star formation, or vice versa, there is not a tight relationship between the radio power and either the number of stars or the current rate of star formation in the host galaxy.

Many of the remaining extragalactic radio sources with $S_{1.4} \gtrsim 1\,\mathrm{mJy}$, as well as a large fraction of fainter sources, belong to a different population. These have optical counterparts that are spiral (if $V \lesssim 18.5$) or blue peculiar (if $V \gtrsim 18.5$) galaxies with a wide range of optical luminosities, often displaying evidence of current star formation (Kron et al., 1985; Benn et al., 1993). For the brighter members of this population it is known that there is a tight correlation between the far-infrared (FIR) luminosity and the 1.4 GHz radio power (reviewed by Condon 1992). Astrophysical interpretations of this correlation usually identify both the FIR and the radio emission as the consequence of ongoing star formation. As a corollary, the opportunity exists to determine the current rate of star formation from measurements of the FIR or radio luminosity.

The astrophysical significance of this is heightened by the fact that very sensitive radio surveys can reveal large numbers of star-forming galaxies at redshifts well beyond $z \sim 0.1$, at an epoch where there is growing evidence that some classes of

galaxies experience star formation at a rate higher than in the local Universe. In this paper we calibrate the relationship between radio luminosity and star formation rate using local star-forming radio galaxies, and apply the calibration to determine the current star formation rate in a sample of galaxies at $0.1 \lesssim z \lesssim 0.5$.

7.2 Estimators of star formation rates

There are several measures of the current star formation rate in galaxies, including the U-band magnitude, the strength of Balmer line emission, the power radiated in the FIR, and the radio luminosity. Here we check empirically the utility of these indicators by using a sample of nearby galaxies for which the radio flux density and several other indicators are available.

Radio continuum emission at 1.4 GHz from star-forming galaxies is mainly synchrotron radiation produced by relativistic electrons. It has long been acknowledged that supernovas could play a role in accelerating these electrons (Biermann, 1976; Kirk, 1994). This view has been reinforced by the discovery of the tight correlation between radio continuum and FIR emission (reviewed by Condon 1992). Explanations of the correlation usually suggest that massive stars dominate both radiation mechanisms, and imply that the supernova rate determines the non-thermal radio luminosity. At first sight there is a serious problem with this interpretation, since the total radio luminosity of a galaxy divided by the typical luminosity of a supernova remnant implies supernova rates that are far too high (Biermann, 1976; Gehrtz et al., 1983). The problem can be resolved consistently with the current understanding of supernova shock acceleration mechanisms by supposing that accelerated electrons, and perhaps the acceleration process itself, endure beyond the $\sim 2 \times 10^4$ yr lifetime of detectable remnants (Condon & Yin, 1990). The relationship between the radio luminosity and the supernova rate can then be calibrated using the Galactic values of $L_{1.4} \sim 2.3 \times 10^{22}\,\mathrm{WHz^{-1}}$ and $\nu_{SN} \sim 1/43\,\mathrm{yr^{-1}}$. From this Condon (1992) estimates the star formation rate (SFR) for stars massive enough to form supernovas (i.e., $M \geq 8\,\mathrm{M_\odot}$) and then adjusts this using a model for the initial mass function (IMF) with $\Psi(M) \sim M^{-5/2}$ to obtain

$$SFR_{1.4}(M \geq 5\,\mathrm{M_\odot}) = \frac{L_{1.4}}{4.0 \times 10^{21}\,\mathrm{WHz^{-1}}}\,\mathrm{M_\odot\,yr^{-1}}. \qquad (7.1)$$

An alternative account of the relationship between the SFR and the radio luminosity rests on the possibility that the major contributors to the non-thermal emission are radio supernovae (with lifetimes of 100 yr or so) rather than remnants (with lifetimes of 20000 yr) (Colina & Pérez-Olea, 1995). This model predicts a value of SFR within a factor of ~ 2 of that given by Equation 7.1.

The use of the U-band luminosity to infer a current star formation rate rests on the idea that the emission arises mainly from the photospheres of young, massive stars (Cowie et al., 1997; Mobasher & Mazzei, 1997). Cowie et al. (their Equation 1)

give an expression involving the UV luminosity $L(2500\text{Å})$ which corresponds to

$$SFR_U(M \geq 5\,\mathrm{M}_\odot) = \frac{L_U}{5.9 \times 10^{21}\,\mathrm{WHz}^{-1}}\,\mathrm{M}_\odot\,\mathrm{yr}^{-1}. \tag{7.2}$$

Balmer line emission from star formation in galaxies is the recombination radiation formed in the H II regions excited by early-type stars. Kennicutt (1983) has determined the theoretical relationship between the Hα luminosity and the current star formation rate in a galaxy in a form corresponding to

$$SFR_{H\alpha}(M \geq 5\,\mathrm{M}_\odot) = \frac{L(H\alpha)}{1.5 \times 10^{34}\,\mathrm{W}}\,\mathrm{M}_\odot\,\mathrm{yr}^{-1}. \tag{7.3}$$

An average correction for extinction of 1.1 magnitude has been applied as suggested by Kennicutt (1983), who also emphasises that variations in extinction imply that *individual* measurements of Hα luminosity must be treated with caution (this point applies also the U-band measurements). Kennicutt points out that the statistical properties of a sample will be considerably more accurate.

FIR emission from star-forming regions is due to the absorption of stellar photospheric radiation by grains, with subsequent re-radiation as thermal continuum in the far infrared. A simple theory relating the FIR power of a galaxy to its current star formation rate can be based on the proposition that essentially all of the UV and much of the blue radiation from massive stars is absorbed by grains, with the associated thermal re-radiation appearing as emission in the $40 - 120\,\mu$m band. From these ideas Condon (1992) derives a star formation rate equivalent to

$$SFR_{\mathrm{FIR}}(M \geq 5\,\mathrm{M}_\odot) = \frac{L_{60\mu\mathrm{m}}}{5.1 \times 10^{23}\,\mathrm{WHz}^{-1}}\,\mathrm{M}_\odot\,\mathrm{yr}^{-1}, \tag{7.4}$$

Thronson & Telesco (1986) derive a rate that is ~ 2.3 times larger than this, the difference being a fair indication of the unavoidable uncertainty in such theories.

A comparison of the rates predicted by Equations 7.1 to 7.4 for a sample of local galaxies is illustrated by crosses and open symbols in Figure 7.1, which plots the SFR deduced from U-band, FIR and Hα luminosities against the SFR deduced from the 1.4 GHz luminosity. Four "reference" samples have been used to test the relations, as listed in Table 7.1. The data of Kennicutt & Kent (1983) and Lehnert & Heckman (1996) were chosen because these authors tabulate a relatively large number of integrated Hα luminosities. Eales et al. (1988) and Condon et al. (1991) were chosen to give good coverage of IRAS galaxies. Values of the Hα equivalent widths or luminosities have been taken from the original papers. The NASA Extragalactic Database (NED) has been consulted to obtain U-band and FIR photometry and most of the necessary redshifts, as well as the V-band photometry needed to convert Hα equivalent widths to flux densities. Values of the 1.4 GHz flux densities are taken from the original papers where available, using a spectral index of $\alpha = -0.8$ ($S_\nu \propto \nu^\alpha$) to convert from other frequencies where necessary. The on-line NVSS database (Condon et al., 1997) was used in the other cases. A

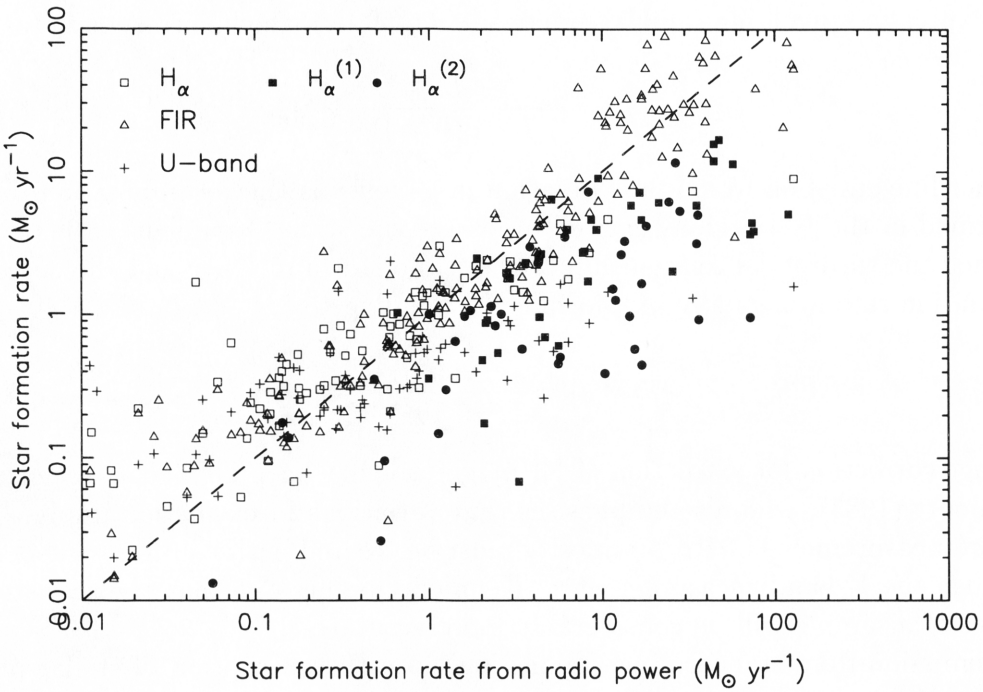

Figure 7.1 Comparison of star formation rates deduced from 1.4 GHz luminosities (horizontal axis) with the rates deduced using the other luminosities indicated. Solid symbols denote data from the high redshift samples of Benn et al. (1993) (squares), and this thesis (circles).

point is plotted in the Figure whenever a galaxy has a radio luminosity and at least one other luminosity – we do not require that *all* SFR indicators be available before plotting a galaxy.

Also plotted on Figure 7.1 as solid symbols are the radio/Hα data for two samples of distant star-forming galaxies, namely the objects classified as some variant of "*" in Table 3 of Benn et al. (1993) and the objects described as "Class A" in Chapter 5. It should be recognised that a radio-selected sample of galaxies will contain a significant number of objects in which the radio luminosity is not a measure of the SFR, although the proportion falls in samples restricted to sub-mJy flux densities. The original authors have identified these galaxies on the basis of their colour and/or spectral signature. They are excluded from consideration in this Chapter.

7.3 Radio luminosity as an SFR estimator

Firstly the "nearby" sample, in which several different estimators of SFR are often available for a single galaxy, is considered. Figure 7.1 indicates that SFR estimates based on the various indicators are in broad agreement with one another, but also points to the existence of systematic differences between different estimators of the

Table 7.1 Sources of data.

		Numbers of galaxies			
Authors	Selection criteria	1.4 GHz	Hα	60 μm	U-band
Kennicutt & Kent (1983)	optical mag limited, mostly spirals	78	69	73	58
Lehnert & Heckman (1996)	IR-selected starbursts (edge on)	28	13	27	19
Eales et al. (1988)	representative sample of IRAS galaxies	63		59	
Condon et al. (1991)	complete sample of ultra-luminous IRAS galaxies	40		40	
Benn et al. (1993)	VLA & WRST 1.4 GHz, 3 deep surveys	50	39		
This thesis	ATCA 1.4 GHz, deep survey	24	24		

SFR, as well as several objects in which at least one indicator is discordant.

The tightness of the relationship between $SFR_{1.4}$ and $SFR_{\rm FIR}$ reflects the well-studied radio/FIR correlation. A line of best fit to these points would imply that values of SFR deduced from 1.4 GHz luminosities using the equations presented above are about a factor of 2 lower than those deduced from 60 μm luminosities. This level of disagreement is consistent with the uncertainties in the theory underlying Equations 7.1 and 7.4. Apart from this systematic discrepancy there is a tight correlation between the two estimates, with the exception of a small number of galaxies in which the radio prediction is too high. These objects are NGC 4374 (M83) and NGC 4486 (M87) from Kennicutt & Kent (1983) and IRAS 0421+040 from Eales et al. (1988). In each of these sources there is evidence that some of the radio emission is not related to star formation.

Estimates of SFR based on Hα luminosities follow the trend of those predicted by $L_{1.4}$ or $L_{\rm FIR}$, but tend to lie above the trend at low SFR and below the trend at high SFR. A similar conclusion could have been drawn from Figure 1 of Devereaux & Young (1990). As noted by these authors, the general correlation supports the view that both the Hα and the FIR luminosity are produced mainly by massive stars. The systematic deviations at low radio luminosity could be related to the difficulty of correcting for possible underlying Hα absorption in the presence of weak Hα emission. The deviations at high radio luminosities could result from a relatively larger amount of extinction in those objects undergoing the most vigorous star formation, or from the loss of Lyα photons by free escape or grain opacity as

an alternative to recombination, or from an IMF which weights differently the high-mass stars mainly responsible for Hα and the lower mass stars which dominate the supernova numbers (or to a combination of these factors).

Estimates of SFR based on U-band observations exhibit the greatest scatter with respect to the radio estimates. Like the estimates based on Hα they tend to lie above the trend line at low SFR and below it at high SFR. Since even old stellar populations emit *some* U-band light (e.g., Bruzual & Charlot 1993, Figure 1) we would expect to see the former trend; the latter could reflect enhanced extinction in vigorous starbursts.

The filled symbols in Figure 7.1 correspond to galaxies selected from very deep radio surveys. At present, only the radio luminosities and the Hα luminosities are available. The Hα values have sometimes been derived from quite noisy spectra which were obtained to determine redshifts rather than line fluxes, and hence they are expected to show significant scatter. The expedient of rejecting radio-selected objects that are red and/or show absorption line spectra has led to a sample which follows a trend in Figure 7.1 that is similar to the "local" sample. It is reasonable to hypothesise that the radio luminosities of these type of galaxies provide estimates of their current star formation rates according to Equation 7.1. One corollary of this is that the faint radio-selected galaxies have star formation rates comparable with those of the intrinsically luminous IRAS galaxies.

While the SFR of a galaxy is a property of interest in its own right, the ratio of the current SFR to the total number of stars that have been formed in a galaxy offers additional insight the potency of the bursts. The total mass of stars being formed in the faint radio galaxies, M, can be estimated by using the R-band luminosities in the relation

$$M = \frac{L_R}{3.4 \times 10^{11}\,\mathrm{WHz^{-1}}}\,\mathrm{M_\odot\,yr^{-1}}. \tag{7.5}$$

Here, we have used the approximation (deduced from Bruzual & Charlot 1993) that steady star formation, with a standard IMF and occurring over a period of many Gyr, will produce an R-band absolute magnitude R$\sim 5\,\mathrm{M_\odot^{-1}}$. Since this approach fails to account for the contribution of the *current* star burst on the R-band luminosity it underestimates the significance of the burst.

Figure 7.2 exhibits the relationship between the SFR deduced from the radio luminosity and the total mass of stars deduced from Equation 7.5. There is a tendency for galaxies that have already formed many stars to support a higher rate of current star formation. There is also a wide scatter in the ratio of SFR to total mass at any chosen size, not all of which is due to errors of observation. There are about a dozen galaxies with a stellar mass $M \sim 10^{10}\,\mathrm{M_\odot}$ and a star formation rate $\mathrm{SFR} \geq 10\,\mathrm{M_\odot yr^{-1}}$. For such galaxies, the current burst of star formation is likely to increase the stellar mass by at least 10%, implying that the event is of considerable significance in the development of the system. These objects are reminiscent of the IRAS galaxies having high ratio of L_{FIR}/L_B (e.g., Sanders & Mirabel 1996, their Section 2.2).

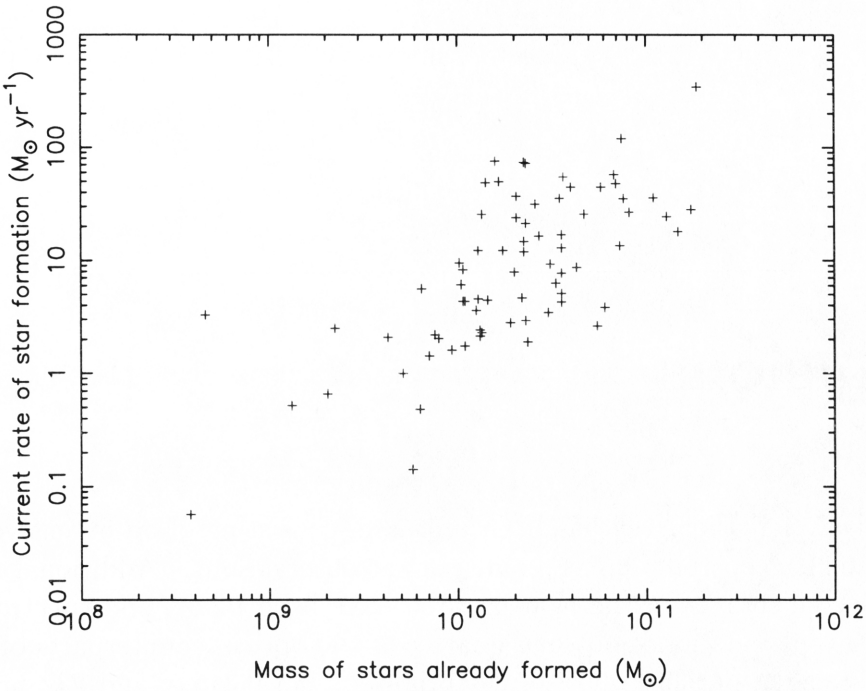

Figure 7.2 The current star formation rate inferred from the 1.4 GHz luminosity versus the total mass of stars inferred from the R-band luminosity for the objects contained in the radio-selected samples of Benn et al. (1993) and this thesis.

7.4 Prospects

The utility of decimetric radio luminosity as a measure of the star formation rate in a galaxy relies on observations that can be interpreted as showing that the luminosity is directly proportional to the supernova rate. Given the potential applications of this relation, it is desirable that the astrophysical interpretation of the phenomenon be explored further. Armed with the capacity to determine star formation rates from radio luminosities, we are in a position to probe the current star formation rates of galaxies to redshifts well beyond $z = 0.1$, provided that we can obtain optical identifications and thence redshifts. Optical photometric and spectroscopic observations also help to confirm that the galaxy is not host to a "monster" and to eliminate the possibility this it is radio loud. *Radio selection* of the candidates will preferentially reveal objects with high rates of current star formation.

The radio frequency sensitivity of the PDS is presently being extended using the Australia Telescope, and redshifts are being sought for all the optically identified radio sources using the 2dF fibre spectrograph on the Anglo-Australian Telescope. These data will provide a significant addition to the understanding of star formation in the regime $0.1 \lesssim z \lesssim 1$.

Chapter 8

Conclusions

A large multiwavelength survey has been initiated, consisting of an extensive (two degree diameter), deep radio survey and optical observations. Additional observations of selected sources in the near-infrared have been made, and spectroscopy has established redshifts for about one quarter of the optical counterparts of radio sources. A catalogue of 938 radio sources brighter than 0.3 mJy and 232 brighter than 0.1 mJy has been compiled. Of the 1079 radio sources detected in total, 541 have been identified optically.

It has been established through 2dF spectroscopy that a significant proportion of the PDS radio sources are identified with emission line galaxies, which are most likely to be exhibiting starburst activity. The implication is that deep radio surveys are certainly useful tools for the detection of these galaxies at moderate redshifts. Until more redshifts for the sources with fainter optical counterparts are measured, it is difficult to comment on whether this provides a good cosmological probe of the starburst phenomenon. However if the redshift distributions predicted from the model bivariate luminosity function are accurate, it would be expected that this is indeed the case.

Evolution of these phenomena can be investigated through less direct means by calling upon models of optical and radio luminosity functions. It has been established that to reproduce the observed source counts to a limiting flux density of 0.1 mJy in the radio, strong evolution of the starburst galaxy population is required, at a rate $(1+z)^Q$ where $Q = 3.3 \pm 0.8$, in addition to the already well established need for evolution of the AGN population. For the optical galaxies, however, to a limiting magnitude of $R = 22$, no evolution of the luminosity function needs to be invoked to reproduce the observed source counts.

The model BLF constructed in Chapter 4 has been used to make predictions of the BSC distribution, and redshift distributions. These compare qualitatively well with the observations, although it is clear that more work is required to produce a more accurate model. Establishing these refinements to the BLF model will form part of the continuing research on the PDS.

Through an analysis of the spectral observations, and in the absence of spectroscopy for a complete sample, it can be said that it appears the sub-mJy radio

population is comprised of an increasing fraction of starburst galaxies compared to the AGN sources. This agrees qualitatively with the distributions expected from the source count predictions of the luminosity evolution model of the radio luminosity functions. The model source counts predict the same surface density for the starburst and AGN populations at about 0.2 mJy, with the AGN being dominant at higher flux densities, and starbursts at lower. A quantitative comparison of this figure with observations will require a complete sample of redshifts. Another interesting observation is the small number of galaxies which are difficult to distinguish as either starbursts or AGN from emission line diagnostics. A few of the emission line galaxies would be classified differently from different diagnostic diagrams, and several more often appear on the border separating the distinct regions. It is possible that these objects are exhibiting both AGN and starburst characteristics, and this claim should be investigated more closely.

The Phoenix Multiwavelength Deep Survey is an ongoing project, which has obtained additional observational data since the drafting of this thesis. At the time of writing, a further set of spectroscopic observations with the 2dF have been made, as have CASPIR observations of additional sub-mJy radio sources. An additional $\sim$150 hours of observations using the ATCA have been made to extend the radio survey to fainter flux densities than have ever before been observed at 1.4 GHz, with an anticipated 5σ flux density limit of 60 μJy over a one degree diameter region within the PDF. The results established through the work contained in this thesis are an exciting first step in the analysis of PDS observations, and further observations and research will continue to expand our understanding of galaxy evolution, and the sub-millijansky and microjansky radio source population.

Bibliography

Baars, J. W. M., Genzel, R., Pauliney-Toth, I. I. K., & Witzel, A., 1977, A&A, 61, 99

Bailey, J. & Glazebrook, K., 1996, The 2dF User's Manual, (Anglo-Australian Observatory)

Baldwin, J. A., Phillips, M. M., & Terlevich, R., 1981, PASP, 93, 5

Balzano, V. A., 1983, ApJ, 268, 602

Barnes, J. E. & Hernquist, L., 1996, ApJ, 471, 115

Becker, R. H., White, R. L., & Helfand, D. J., 1995, ApJ, 450, 559

Benn, C. R., Rowan-Robinson, M., McMahon, R. G., Broadhurst, T. J., & Lawrence, A., 1993, MNRAS, 263, 98

Biermann, P., 1976, A&A, 53, 295

Brunner, R. J., Connolly, A. J., Szalay, A. S., & Bershady, M. A., 1997, ApJ, 482, L21

Bruzual, A. G. & Charlot, S., 1993, ApJ, 405, 538

Burkey, J. M., Keel, W. C., Windhorst, R. A., & Franklin, B. E., 1994, ApJ, 429, L13

Christiansen, W. N., 1963, ARA&A, 1, 1

Colina, L. & Pérez-Olea, D. E., 1995, MNRAS, 277, 845

Colina, L., Pérez-Olea, D., & Planesas, P., 1997, RevMexAA *(Serie de Conferencias),* 6, 84

Condon, J. J. & Mitchell, K. J., 1984, AJ, 89, 610

Condon, J. J. & Yin, Q. F., 1990, ApJ, 357, 97

Condon, J. J., Condon, M. A., Gisler, G., & Puschell, J. J., 1982a, ApJ, 252, 102

Condon, J. J., Condon, M. A., & Hazard, C., 1982b, AJ, 87, 739

Condon, J. J., Huang, Z.-P., Yin, Q. F., & Thuan, T. X., 1991, ApJ, 378, 65

Condon, J. J., Cotton, W. D., Greisen, E. W., Yin, Q. F., Perley, R. A., Taylor, G. B., & Broderick, J. J., 1997, preprint

Condon, J. J., 1984a, ApJ, 284, 44

Condon, J. J., 1984b, ApJ, 287, 461

Condon, J. J., 1989, ApJ, 338, 13

Condon, J. J., 1992, ARA&A, 30, 575

Connolly, A. J., Csabai, I., Szalay, A. S., Koo, D. C., & Munn, J. A., 1995, AJ, 110, 2655

Corbelli, E., Salpeter, E., & Dickey, J., 1991, ApJ, 370, 49

Cowie, L. L., Hu, E. M., Songaila, A., & Egami, E., 1997, ApJ, 481, L9

Crawford, C. H., Jauncey, T. P., & Murdoch, R. M., 1970, ApJ, 162, 405

Crawford, T., Marr, J., & Partridge, B., 1996, ApJ, 460, 225

Danese, L., DeZotti, G., Franceschini, A., & Toffolatti, L., 1987, ApJ, 318, L15

Devereux, N. A. & Eales, S. A., 1989, ApJ, 340, 708

Devereux, N. A. & Young, J. S., 1990, ApJ, 350, L25

Dickey, J. M. & Salpeter, E. E., 1984, ApJ, 284, 461

Dunlop, J. S. & Peacock, J. A., 1990, MNRAS, 247, 19

Eales, S. A., Wynn-Williams, C. G., & Beichman, C. A., 1988, ApJ, 328, 530

Elvis, M., Maccacaro, T., Wilson, A. S., & Ward, M. J., 1978, MNRAS, 183, 129

Fomalont, E. B., Windhorst, R. A., Kristian, J. A., & Kellerman, K. I., 1991, AJ, 102, 1258

Fomalont, E. B., Kellerman, K. I., Richards, E. A., Windhorst, R. A., & Partridge, R. B., 1997, ApJ, 298, L7

Franceschini, A., Danese, L., DeZotti, G., & Toffolatti, L., 1988, MNRAS, 233, 157

Gehrtz, R. D., Sramek, R. A., & Weedman, D. W., 1983, ApJ, 267, 551

Genzel, R., Lutz, D., Sturm, E., Egami, E., Kunze, D., Moorwood, A. F. M., Rigopoulou, D., Spoon, H. W. W., Sternberg, A., Tacconi-Garman, L. E., Tacconi, L., & Thatte, N., 1998, ApJ, 498, 579

Greenstein, J. L. & Matthews, T. A., 1963, Nature, 197, 1041

Griffith, M. R. & Wright, A. E., 1993, AJ, 105, 1666

Guiderdoni, B. & Rocca-Volmerange, B., 1991, A&A, 252, 435

Hammer, F., Crampton, D., Lilly, S. J., Fèvre, O. L., & Kenet, T., 1995, MNRAS, 276, 1085

Hanbury Brown, R., 1983, in Serendipitous Discoveries in Radio Astronomy, ed. K. Kellermann & B. Sheets, 133

Hazard, C., Mackey, M. B., & Shimmins, A. J., 1963, Nature, 197, 1037

Heckman, T. M., Balick, B., & Crane, P. C., 1980, A&AS, 40, 295

Heckman, T. M., 1980a, A&A, 88, 311

Heckman, T. M., 1980b, A&A, 88, 365

Helou, G., Soifer, B. T., & Rowan-Robinson, M., 1985, ApJ, 298, L7

Hopkins, A. M. & Cram, L. E., 1997, in IAU Symp. 186, Galaxy Interactions at Low and High Redshift, 79

Hunstead, R. W., 1972, ApJ, 12, L193

Katgert, J. K. & Spinrad, H., 1974, A&A, 35, 393

Katgert, P., Katgert-Merkelijn, J. K., Poole, R. S. L., & van der Laan, H., 1973, A&A, 23, 171

Katgert, P., Oort, M. J. A., & Windhorst, R. A., 1988, A&A, 195, 21

Katgert, P., 1975, A&A, 38, 87

Kennicutt, R. C. & Kent, S. M., 1983, AJ, 88, 1094

Kennicutt, R. C., 1983, ApJ, 272, 54

Kirk, J. G., 1994, in Plasma Astrophysics, ed. J. G. Kirk, D. B. Melrose, & E. R. Priest, 133

Knapp, G. R., Bies, W. E., & van Gorkom, J. H., 1990, AJ, 99, 476

Koo, D. C. & Kron, R. G., 1992, ARA&A, 30, 613

Kron, R. G., Koo, D. C., & Windhorst, R. A., 1985, A&A, 146, 38

Landolt, A. U., 1992, AJ, 104, 340

Large, M. I., Campbell-Wilson, D., Cram, L. E., Davison, R. G., & Robertson, J. G., 1994, PASA, 11, 44

Lehnert, M. D. & Heckman, T. M., 1996, ApJ, 472, 546

Maddox, S. J., Sutherland, W. J., Efstathiou, G., Loveday, J., & Peterson, B. A., 1990, MNRAS, 247, 1P

Mayer, C. H., McCullough, T. P., & Sloanaker, R. M., 1962, AJ, 67, 581

Metcalfe, N., Shanks, T., Fong, R., & Jones, L. R., 1991, MNRAS, 249, 498

Metcalfe, N., Shanks, T., Fong, R., & Roche, N., 1995, MNRAS, 273, 257

Meurs, E. J. A. & Wilson, A. S., 1984, A&A, 136, 206

Miller, S. J. & Mathews, W. C., 1972, ApJ, 172, 593

Mitchell, K. J. & Condon, J. J., 1985, AJ, 90, 1957

Mitchell, K. J., 1983, PhD thesis, Pennsylvania State University

Mobasher, B. & Mazzei, P., 1997, MNRAS, submitted

Norman, C. A. & Scoville, N. Z., 1988, ApJ, 332, 124

Oke, J. B., 1963, Nature, 197, 1040

Oort, M. J. A., 1987, A&AS, 71, 221

Oosterbaan, C. E., 1978, A&A, 69, 235

Partridge, R. B., Hilldrup, K. C., & Ratner, M. I., 1986, ApJ, 308, 46

Pearson, C. & Rowan-Robinson, M., 1996, MNRAS, 283, 174

Reynolds, J., 1994, in Australia Telescope Compact Array User's Guide, ed. S. Houghton, 118

Robertson, J. G., 1991, Aust. J. Phys., 46, 729

Rola, C. S., Terlevich, E., & Terlevich, R. J., 1997, MNRAS, 289, 419

Rowan-Robinson, M., Helou, G., & Walker, D., 1987, MNRAS, 227, 589

Rowan-Robinson, M., Benn, C. R., Lawrence, A., McMahon, R. G., & Broadhurst, T. J., 1993, MNRAS, 263, 123

Sadler, E. M., Jenkins, C. R., & Kotanyi, C. G., 1989, MNRAS, 240, 591

Sanders, D. B. & Mirabel, I. F., 1996, ARA&A, 34, 749

Sault, R. J., Staveley-Smith, L., & Brouw, W. N., 1996, A&AS, 120, 375

Saunders, W., Rowan-Robinson, M., Lawrence, A., Efstathiou, G., Kaiser, N., Ellis, R. S., & Frenk, C. S., 1990, MNRAS, 242, 318

Sawicki, M. J., Lin, H., & Yee, H. K. C., 1997, AJ, 113, 1

Schechter, P., 1976, ApJ, 203, 297

Schmidt, M., 1963, Nature, 197, 1040

Schmidt, M., 1968, ApJ, 151, 393

Scoville, N. Z. & Norman, C. A., 1988, ApJ, 332, 163

Searle, L., Sargent, W. L. W., & Bagnuolo, W. G., 1973, ApJ, 179, 427

Smith, D. A., Herter, T., & Haynes, M. P., 1998a, ApJ, 494, 150

Smith, D. A., Lonsdale, C. J., & Lonsdale, C. J., 1998b, ApJ, 492, 137

Sopp, H. M. & Alexander, P., 1991, MNRAS, 251, 112

Subbarao, M. U., Connolly, A. J., Szalay, A. S., & Koo, D. C., 1996, AJ, 112, 929

Sullivan, W. T., 1983, in Serendipitous Discoveries in Radio Astronomy, ed. K. Kellermann & B. Sheets, 39

Thronson, H. A. & Telesco, C. M., 1986, ApJ, 311, 98

Toffolatti, L., Franceschini, A., DeZotti, G., & Danese, L., 1987, A&A, 184, 7

Tresse, L., Rola, C., Hammer, F., Stasińska, G., Fèvre, O. L., Lilly, S. J., & Crampton, D., 1996, MNRAS, 281, 847

Ulrich, M.-H., 1978, ApJ, 219, 424

Valdes, F., 1982, The FOCAS User's Manual, (Tucson: NOAO)

Veilleux, S. & Osterbrock, D. E., 1987, ApJS, 63, 295

Wall, J. V. & Jackson, C. A., 1997, MNRAS, 290, L17

Wall, J. V., 1994, Aust. J. Phys., 47, 625

Weistrop, D., Wall, J. V., Fomalont, E. B., & Kellerman, K. I., 1987, AJ, 93, 805

Willis, A. G., Oosterbaan, C. E., & de Ruiter, H. R., 1976, A&AS, 25, 453

Windhorst, R. A., Kron, R. G., & Koo, D. C., 1984a, A&AS, 58, 39

Windhorst, R. A., van Heerde, G. M., & Katgert, P., 1984b, A&AS, 58, 1

Windhorst, R. A., Miley, G. K., Owen, F. N., Kron, R. G., & Koo, D. C., 1985, ApJ, 289, 494

Windhorst, R. A., Dressler, A., & Koo, D. C., 1987, in IAU Symp. 124, Observational Cosmology, ed. A. Hewitt, G. Burbidge, & L. Z. Fang, 573

Windhorst, R. A., Mathis, D. F., & Neuschaefer, L. W., 1990, in ASP Conf. Ser., Vol. 10, Evolution of the Universe of Galaxies, ed. R. G. Kron, 389

Windhorst, R. A., Fomalont, E. B., Partridge, R. B., & Lowenthal, J. D., 1993, ApJ, 405, 498

Windhorst, R. A., Fomalont, E. B., Kellermann, K. I., Partridge, R. B., Richards, E., Franklin, B. E., Pascarelle, S. M., & Griffiths, R. E., 1995, Nature, 375, 471

Appendix A

Radio source list

The source list presented here is a compilation of all the sources detected in both the PDF and the PDFS. Those objects which were detected in both samples have the data from the PDFS observations given below. See the notes at the foot of the table for column descriptions.

Table A.1 : Radio sources from the PDF and the PDFS.

	α			δ			bmaj $''$	bmin $''$	pa $^\circ$	$S_{1.4}$ mJy	sample
0001	1	08	33.013	-45	52	40.78	13.7	8.2	16.6	0.783	1
0002	1	08	33.157	-45	45	43.59	15.9	9.0	17.9	0.536	1
0003	1	08	33.456	-45	50	14.90	20.3	17.1	29.6	0.221	1
0004	1	08	37.161	-45	48	19.76	23.1	8.2	2.8	0.614	1
0005	1	08	37.530	-45	52	57.37	10.3	6.3	-1.2	0.571	1
0006	1	08	38.916	-45	52	45.56	11.9	7.2	13.5	1.342	1
0007	1	08	39.064	-45	58	18.98	11.7	7.5	10.8	1.913	1
0008	1	08	39.323	-45	56	56.18	11.9	8.3	45.8	0.517	1
0009	1	08	43.470	-45	38	51.14	13.2	7.9	19.6	0.582	1
0010	1	08	44.890	-46	02	56.30	15.7	8.1	-3.9	0.788	1
0011	1	08	46.352	-45	55	02.86	15.9	13.6	7.9	1.288	1
0012	1	08	49.719	-45	39	02.82	9.7	8.5	-56.0	0.316	1
0013	1	08	50.067	-45	40	03.32	10.7	7.2	37.0	0.402	1
0014	1	08	51.180	-45	33	07.24	12.4	8.0	9.7	1.379	1
0015	1	08	52.337	-45	25	57.17	10.7	7.1	-8.6	0.951	1
0016	1	08	53.935	-45	58	40.16	13.5	10.2	-3.2	1.093	1
0017	1	08	54.312	-45	21	58.60	15.6	8.1	-12.3	1.416	1
0018	1	08	56.493	-45	42	15.86	18.6	10.3	6.3	0.726	1
0019	1	09	00.005	-45	20	54.32	14.2	9.3	-11.3	1.050	1
0020	1	09	03.891	-45	22	33.91	10.9	7.9	7.9	8.852	1
0021	1	09	04.523	-46	10	52.12	20.0	8.6	59.7	1.059	1
0022	1	09	04.599	-45	46	24.70	11.8	7.3	5.5	4.791	1

continued from previous page

	α			δ			bmaj	bmin	pa	$S_{1.4}$	sample
0023	1	09	05.364	-46	08	18.00	10.0	6.6	36.3	0.459	1
0024	1	09	07.413	-45	41	43.19	28.5	7.5	-3.2	0.185	1
0025	1	09	08.333	-46	11	49.33	13.0	8.6	5.4	2.375	1
0026	1	09	09.458	-45	59	43.17	11.1	7.8	13.6	1.889	1
0027	1	09	09.619	-46	12	47.08	23.9	10.6	-10.1	10.793	1
0028	1	09	09.739	-45	58	05.57	14.0	7.3	5.2	0.328	1
0029	1	09	10.107	-46	12	59.12	15.3	10.2	-9.6	8.828	1
0030	1	09	11.772	-46	02	08.89	16.9	10.3	43.6	0.622	1
0031	1	09	13.282	-45	34	16.69	11.1	7.2	10.9	2.394	1
0032	1	09	13.287	-45	44	01.98	15.3	8.0	1.9	0.365	1
0033	1	09	13.479	-45	53	23.53	11.0	7.1	4.7	3.947	1
0034	1	09	14.668	-45	40	02.59	10.2	8.8	-0.1	0.259	1
0035	1	09	15.778	-45	47	03.46	13.6	6.7	6.2	0.269	1
0036	1	09	19.103	-45	59	22.38	13.3	10.6	68.2	0.472	1
0037	1	09	20.368	-46	02	08.97	14.9	7.0	-3.4	0.306	1
0038	1	09	25.119	-45	33	55.00	11.5	7.2	10.0	1.976	1
0039	1	09	27.144	-45	28	15.99	7.8	6.0	22.4	0.354	1
0040	1	09	28.577	-46	02	14.33	11.5	8.6	14.9	0.332	1
0041	1	09	29.090	-45	25	51.63	11.7	7.8	42.4	0.519	1
0042	1	09	31.170	-46	15	11.48	22.7	10.4	19.6	0.379	1
0043	1	09	31.334	-45	14	06.66	16.9	8.5	-1.7	11.950	1
0044	1	09	33.069	-45	48	23.86	16.3	11.0	43.7	0.519	1
0045	1	09	33.729	-45	31	12.45	19.0	10.9	-16.4	1.337	1
0046	1	09	33.860	-45	31	15.39	21.8	10.3	-17.2	1.481	1
0047	1	09	38.951	-45	39	26.04	8.8	6.7	88.9	0.291	2
0048	1	09	39.310	-45	51	13.75	15.9	8.6	11.3	0.522	1
0049	1	09	39.740	-45	15	01.17	10.4	8.2	5.5	2.050	1
0050	1	09	44.925	-45	55	15.58	12.0	6.3	16.2	0.261	1
0051	1	09	46.433	-45	50	01.36	13.9	7.1	68.1	1.779	3
0052	1	09	46.568	-45	46	57.15	8.3	6.4	42.6	0.985	3
0053	1	09	46.698	-45	32	52.13	11.4	7.3	14.7	0.453	1
0054	1	09	47.965	-45	51	24.07	9.2	6.6	52.7	0.599	3
0055	1	09	49.137	-45	40	31.19	14.5	7.5	-19.0	1.742	3
0056	1	09	49.796	-45	27	37.49	11.2	6.6	20.5	0.726	1
0057	1	09	49.958	-46	09	34.60	13.1	7.2	11.1	1.325	1
0058	1	09	49.998	-45	46	27.69	10.4	7.4	-52.8	0.419	2
0059	1	09	51.176	-45	56	24.17	13.8	7.4	16.2	0.929	1
0060	1	09	51.779	-45	10	45.10	11.2	8.4	-38.3	0.988	1
0061	1	09	53.425	-45	44	12.76	9.9	5.4	-16.1	0.145	2
0062	1	09	55.542	-45	55	51.46	9.0	6.6	36.3	1.208	3
0063	1	09	55.568	-45	50	20.08	5.6	5.0	-20.4	0.167	2

continued from previous page

	α			δ			bmaj	bmin	pa	$S_{1.4}$	sample
0064	1	09	55.738	-45	48	18.36	7.1	6.3	46.1	0.993	3
0065	1	09	55.799	-45	18	44.45	19.6	10.8	-0.3	0.588	1
0066	1	09	56.495	-45	44	07.30	15.0	8.0	-3.6	0.302	1
0067	1	09	56.840	-45	53	04.95	11.2	6.7	-89.4	0.238	2
0068	1	09	56.943	-46	21	56.58	9.4	6.0	29.8	0.443	1
0069	1	09	57.561	-45	46	08.82	7.1	5.1	31.9	0.135	2
0070	1	09	57.563	-45	34	57.18	12.3	7.4	-44.4	0.393	3
0071	1	09	57.653	-45	36	22.49	8.5	4.9	-22.7	0.190	2
0072	1	09	57.781	-45	40	48.11	8.4	7.0	25.5	0.387	3
0073	1	09	58.314	-45	46	36.16	11.6	9.2	1.8	0.269	1
0074	1	09	59.248	-45	20	02.77	10.3	7.5	9.9	0.285	1
0075	1	10	00.084	-45	56	43.51	8.5	5.0	-12.4	0.175	1
0076	1	10	00.691	-45	47	25.48	8.8	6.2	-53.0	0.281	3
0077	1	10	01.568	-45	38	54.66	8.4	5.8	-31.8	0.466	3
0078	1	10	01.858	-45	16	03.37	23.0	11.4	77.2	0.211	1
0079	1	10	02.168	-45	09	42.99	17.1	12.7	36.2	1.849	1
0080	1	10	04.681	-45	12	33.26	10.4	7.4	83.7	0.295	1
0081	1	10	05.607	-45	23	08.26	11.1	8.7	24.7	0.357	1
0082	1	10	05.847	-45	45	21.20	9.3	5.6	-9.6	0.409	3
0083	1	10	06.172	-45	21	56.31	22.4	8.4	-2.4	0.600	1
0084	1	10	06.366	-46	21	12.50	14.4	9.2	31.9	0.939	1
0085	1	10	07.210	-45	42	41.72	7.8	4.2	-14.4	0.111	2
0086	1	10	07.592	-45	13	17.03	12.2	6.7	16.8	0.757	1
0087	1	10	08.377	-45	40	22.04	6.5	5.7	18.5	0.166	3
0088	1	10	08.641	-45	35	29.58	12.3	8.7	57.5	0.248	1
0089	1	10	08.954	-45	30	19.44	12.4	7.6	4.0	0.297	1
0090	1	10	09.750	-45	30	59.91	11.4	8.8	72.3	3.279	3
0091	1	10	11.656	-45	52	51.03	11.4	8.7	21.3	0.340	2
0092	1	10	11.694	-46	21	59.07	20.3	12.8	-85.2	0.230	1
0093	1	10	11.717	-46	21	25.26	14.1	6.7	18.8	0.357	1
0094	1	10	13.232	-45	29	01.21	16.6	13.4	-1.7	0.546	1
0095	1	10	13.339	-45	58	59.24	16.1	10.1	46.2	0.564	1
0096	1	10	13.386	-45	54	34.35	8.3	5.6	17.5	0.190	2
0097	1	10	13.449	-45	33	59.34	8.8	7.2	51.7	0.236	2
0098	1	10	14.084	-46	01	45.26	13.0	8.8	4.2	0.616	1
0099	1	10	15.229	-46	15	08.31	0.0	0.0	0.0	26.512	1
0100	1	10	15.389	-46	14	14.45	10.9	7.4	13.1	6.938	1
0101	1	10	15.408	-45	13	38.70	15.1	7.8	-4.0	0.452	1
0102	1	10	15.550	-46	11	05.83	12.3	8.1	9.8	1.256	1
0103	1	10	15.927	-45	52	40.34	10.5	7.4	51.0	0.366	2
0104	1	10	16.268	-45	47	32.54	8.6	7.3	83.2	0.231	2

continued from previous page

	α			δ			bmaj	bmin	pa	$S_{1.4}$	sample
0105	1	10	17.108	-45	10	03.20	15.9	10.6	39.2	0.738	1
0106	1	10	17.842	-45	45	31.09	7.6	5.8	-26.5	0.122	2
0107	1	10	18.082	-45	49	05.24	10.6	8.0	82.8	0.333	2
0108	1	10	19.410	-45	51	13.35	7.4	6.1	23.4	10.654	3
0109	1	10	19.626	-45	55	24.39	8.1	6.3	22.5	0.886	3
0110	1	10	20.962	-46	14	33.02	18.6	9.8	18.1	0.885	1
0111	1	10	21.153	-45	11	44.21	12.2	7.3	-21.4	0.506	1
0112	1	10	21.259	-45	46	25.96	8.6	7.2	-80.0	0.302	2
0113	1	10	21.718	-46	20	36.73	19.5	16.4	-8.3	1.882	1
0114	1	10	22.439	-45	32	15.60	12.4	5.7	2.1	0.350	3
0115	1	10	22.873	-45	20	36.76	11.1	7.1	9.9	1.051	1
0116	1	10	23.449	-45	03	38.12	12.0	9.1	8.0	2.533	1
0117	1	10	25.237	-45	42	30.74	6.3	5.3	10.7	0.109	2
0118	1	10	25.725	-45	44	30.47	6.9	6.4	-3.4	3.405	3
0119	1	10	25.902	-45	56	45.64	6.1	4.9	-5.1	0.151	2
0120	1	10	26.110	-45	52	04.77	11.7	8.3	56.0	0.935	3
0121	1	10	27.625	-45	47	01.91	7.0	6.2	7.6	5.491	3
0122	1	10	27.776	-45	22	55.96	10.6	7.4	13.2	0.983	1
0123	1	10	27.844	-45	48	36.42	11.3	5.6	-9.8	0.225	2
0124	1	10	28.318	-45	34	13.54	7.8	5.9	-17.7	4.262	3
0125	1	10	29.437	-46	10	27.63	15.9	12.9	-22.2	4.687	1
0126	1	10	29.737	-45	48	58.05	7.6	6.3	-30.0	0.452	3
0127	1	10	30.194	-45	31	14.07	7.6	5.7	-15.6	0.972	3
0128	1	10	30.462	-46	07	55.31	14.2	8.7	13.9	0.521	1
0129	1	10	30.647	-46	19	29.57	10.4	7.4	37.0	0.369	1
0130	1	10	32.114	-45	48	26.95	7.2	6.9	76.2	1.776	3
0131	1	10	32.401	-45	42	48.30	8.7	6.0	-45.5	0.294	3
0132	1	10	32.432	-45	57	43.76	8.3	5.5	-53.4	0.221	3
0133	1	10	32.455	-45	46	53.07	6.7	5.8	-42.6	0.143	2
0134	1	10	32.551	-45	40	04.12	7.6	6.1	-13.6	0.618	3
0135	1	10	32.556	-45	54	04.61	11.7	6.1	-3.1	1.920	3
0136	1	10	33.299	-45	42	06.89	7.5	6.7	42.1	0.234	2
0137	1	10	33.361	-44	59	59.08	11.2	10.5	49.4	1.319	1
0138	1	10	33.646	-45	40	21.21	7.1	5.6	-8.1	0.306	3
0139	1	10	33.777	-45	50	09.32	7.6	5.4	7.8	0.497	3
0140	1	10	34.398	-45	51	20.74	9.0	5.3	43.8	0.248	2
0141	1	10	34.760	-45	40	26.38	9.1	6.4	-31.3	0.258	2
0142	1	10	35.625	-44	58	39.79	12.2	9.1	26.9	2.044	1
0143	1	10	36.590	-45	45	58.26	8.1	4.4	-44.5	0.096	2
0144	1	10	37.233	-45	32	59.07	8.3	5.9	-8.6	6.441	3
0145	1	10	38.208	-45	38	19.19	7.2	6.9	-65.3	0.257	3

continued from previous page

	α			δ			bmaj	bmin	pa	$S_{1.4}$	sample
0146	1	10	38.386	-45	50	40.12	8.6	6.0	84.5	0.144	2
0147	1	10	40.678	-45	47	24.96	10.2	6.4	40.9	0.168	2
0148	1	10	41.143	-45	54	20.54	7.9	5.7	12.7	1.386	3
0149	1	10	41.223	-46	20	31.84	11.3	6.6	21.1	0.234	1
0150	1	10	42.410	-45	16	13.88	13.2	7.9	17.0	0.658	1
0151	1	10	42.790	-45	31	20.65	7.5	5.8	-23.4	0.169	2
0152	1	10	43.142	-46	00	43.54	8.5	5.5	18.0	1.120	3
0153	1	10	43.888	-45	51	01.57	7.0	6.0	-63.8	0.129	2
0154	1	10	44.087	-45	51	23.74	8.1	6.5	47.3	0.198	2
0155	1	10	45.138	-45	06	46.85	10.3	7.4	12.3	2.311	1
0156	1	10	45.724	-45	53	24.49	9.1	6.2	1.0	0.195	2
0157	1	10	46.572	-45	41	40.77	11.2	7.3	-35.4	0.404	3
0158	1	10	47.181	-45	47	02.54	7.7	5.7	-27.4	0.192	2
0159	1	10	47.282	-45	32	56.18	11.9	7.5	57.8	0.329	2
0160	1	10	47.601	-45	16	16.70	10.9	8.7	32.3	1.259	1
0161	1	10	47.790	-45	46	37.85	8.6	6.9	3.7	0.269	3
0162	1	10	48.208	-46	20	38.83	9.8	9.4	1.5	0.501	1
0163	1	10	48.270	-46	24	53.60	8.8	7.4	-47.1	0.284	1
0164	1	10	49.218	-45	04	09.70	11.9	9.7	16.5	1.396	1
0165	1	10	49.933	-45	48	18.34	7.7	6.2	9.9	0.263	2
0166	1	10	50.443	-46	20	22.86	15.8	11.2	20.8	0.750	1
0167	1	10	52.139	-45	43	39.16	9.9	7.5	-13.6	0.182	2
0168	1	10	52.157	-45	33	53.32	8.6	6.5	-1.6	0.425	2
0169	1	10	52.308	-45	33	58.35	23.8	7.5	-5.4	0.464	1
0170	1	10	53.175	-46	07	00.95	10.8	7.4	8.8	8.740	1
0171	1	10	53.790	-46	15	57.23	12.0	11.1	-83.0	0.533	1
0172	1	10	53.813	-45	43	39.12	8.7	5.9	24.3	0.184	2
0173	1	10	54.647	-45	06	35.82	22.0	12.8	-80.0	1.045	1
0174	1	10	54.744	-45	57	32.74	9.8	6.0	26.7	0.213	2
0175	1	10	55.578	-45	46	26.08	10.1	8.2	15.9	0.181	2
0176	1	10	55.736	-45	39	19.28	11.4	7.1	72.5	0.315	2
0177	1	10	56.218	-46	09	46.01	15.8	11.6	60.9	0.665	1
0178	1	10	56.762	-45	32	33.30	6.9	4.7	10.3	0.141	2
0179	1	10	57.156	-45	52	10.79	8.0	5.2	12.1	0.840	3
0180	1	10	57.442	-45	04	36.28	12.6	8.9	88.8	0.453	1
0181	1	10	57.766	-46	15	54.66	11.6	6.9	35.9	0.342	1
0182	1	10	58.172	-45	57	36.54	6.2	5.3	11.5	0.133	2
0183	1	10	58.940	-45	38	12.33	8.1	5.8	-1.7	0.674	3
0184	1	10	59.525	-45	46	04.46	8.3	5.0	29.5	0.108	2
0185	1	10	59.738	-45	57	23.98	10.2	5.7	-7.8	0.178	2
0186	1	10	59.770	-45	54	42.58	7.9	5.4	0.2	0.541	3

continued from previous page

	α			δ			bmaj	bmin	pa	$S_{1.4}$	sample
0187	1	10	59.866	-45	28	07.63	8.6	6.3	0.0	2.512	3
0188	1	11	00.359	-46	19	09.60	15.0	7.7	5.8	0.795	1
0189	1	11	00.982	-45	49	39.47	7.0	6.0	49.1	0.143	2
0190	1	11	01.607	-46	04	48.53	13.9	11.7	-51.0	0.442	1
0191	1	11	01.672	-46	00	19.39	8.8	5.7	4.9	0.331	2
0192	1	11	01.793	-45	41	56.88	15.0	7.3	-88.0	0.246	2
0193	1	11	02.134	-46	01	18.75	9.3	6.0	33.3	0.320	2
0194	1	11	02.322	-46	18	22.56	11.8	8.2	9.7	0.712	1
0195	1	11	02.676	-45	51	34.72	7.6	5.7	-5.4	0.282	3
0196	1	11	02.733	-45	47	29.95	7.0	5.7	7.0	0.435	3
0197	1	11	02.842	-46	27	44.78	15.5	9.4	14.4	0.773	1
0198	1	11	03.146	-45	53	55.29	7.4	5.3	0.1	0.244	2
0199	1	11	03.780	-45	51	17.78	10.8	7.9	-21.3	0.248	2
0200	1	11	05.085	-45	59	50.39	8.1	5.2	-55.1	0.187	2
0201	1	11	05.189	-45	38	49.75	6.7	5.6	20.8	0.124	2
0202	1	11	05.887	-45	58	10.92	15.4	10.8	54.3	0.375	1
0203	1	11	06.077	-45	49	18.41	7.0	5.6	-1.1	0.303	3
0204	1	11	06.373	-45	14	34.51	11.1	7.5	21.6	2.291	1
0205	1	11	06.696	-46	34	26.59	11.8	9.5	-76.9	0.626	1
0206	1	11	07.228	-46	07	12.48	21.5	10.5	-4.7	0.795	1
0207	1	11	07.335	-46	12	09.27	16.0	12.5	-24.2	0.623	1
0208	1	11	07.797	-45	52	10.46	13.4	6.5	-19.6	0.207	2
0209	1	11	07.849	-45	40	26.09	8.7	5.2	-17.1	0.191	2
0210	1	11	07.933	-45	32	46.68	7.1	5.5	4.2	0.161	2
0211	1	11	08.085	-46	04	25.59	9.5	6.7	54.9	0.164	1
0212	1	11	08.729	-45	36	22.56	10.0	6.3	26.1	0.226	1
0213	1	11	08.757	-45	51	28.36	8.7	6.7	24.2	0.298	3
0214	1	11	09.009	-45	56	33.89	7.2	6.8	43.7	0.158	2
0215	1	11	09.508	-45	48	19.44	7.4	5.9	60.0	0.108	2
0216	1	11	10.048	-46	10	15.58	18.8	8.2	7.7	0.410	1
0217	1	11	10.789	-46	09	00.81	12.3	7.2	13.9	1.278	1
0218	1	11	12.224	-46	14	07.28	19.0	13.1	7.1	0.195	1
0219	1	11	12.271	-45	02	59.18	11.2	9.1	20.7	0.955	1
0220	1	11	12.588	-45	51	12.12	10.0	6.0	-27.4	0.154	2
0221	1	11	13.102	-45	14	08.94	16.4	11.0	0.6	0.549	1
0222	1	11	13.823	-46	00	17.36	8.1	4.6	43.0	0.159	2
0223	1	11	13.824	-45	51	51.78	7.0	5.5	0.9	1.037	3
0224	1	11	13.939	-45	57	23.33	7.6	5.6	2.2	0.854	3
0225	1	11	14.007	-45	36	01.65	7.8	5.6	2.1	6.967	3
0226	1	11	15.101	-45	32	14.26	8.8	6.2	-55.4	0.219	2
0227	1	11	15.788	-45	54	38.50	20.8	12.8	79.4	0.171	1

continued from previous page

	α			δ			bmaj	bmin	pa	$S_{1.4}$	sample
0228	1	11	15.829	-46	09	37.31	14.6	11.1	88.2	3.202	1
0229	1	11	15.902	-45	48	06.24	6.7	4.5	-1.7	0.107	2
0230	1	11	16.067	-45	43	43.36	9.0	6.4	-46.6	0.222	2
0231	1	11	16.304	-46	06	45.84	8.4	7.0	2.9	0.239	1
0232	1	11	17.142	-45	04	02.26	27.2	17.3	10.1	15.609	1
0233	1	11	18.468	-45	28	47.04	13.3	7.9	5.3	0.263	1
0234	1	11	19.046	-45	44	01.98	8.2	7.2	27.4	0.136	2
0235	1	11	19.198	-45	55	53.16	25.1	14.5	29.4	3.957	3
0236	1	11	19.899	-45	53	44.90	8.6	4.5	5.9	0.168	2
0237	1	11	20.618	-46	19	15.41	9.5	6.9	-6.0	0.285	1
0238	1	11	21.102	-45	42	49.76	10.2	6.3	-44.0	0.167	2
0239	1	11	21.289	-45	44	30.46	10.4	5.4	16.4	0.144	2
0240	1	11	21.699	-44	52	21.94	10.7	7.6	7.3	6.587	1
0241	1	11	21.872	-45	54	30.68	7.5	5.3	4.4	0.250	3
0242	1	11	21.934	-45	04	25.28	32.6	21.3	-42.0	18.194	1
0243	1	11	22.076	-45	58	17.37	8.1	6.2	2.6	0.284	3
0244	1	11	22.236	-46	10	13.06	11.5	7.7	0.2	1.128	1
0245	1	11	22.580	-45	40	00.08	7.5	5.0	-22.6	0.226	2
0246	1	11	23.111	-46	04	30.71	10.7	7.1	-20.1	0.326	1
0247	1	11	23.456	-45	35	18.04	7.5	6.1	-33.2	0.216	2
0248	1	11	23.652	-45	43	43.22	14.7	11.3	-69.3	0.351	1
0249	1	11	24.063	-45	47	37.97	7.3	5.9	-17.6	0.250	3
0250	1	11	24.285	-45	00	56.09	16.7	9.5	6.6	0.918	1
0251	1	11	24.413	-45	07	39.99	9.8	7.5	4.9	0.308	1
0252	1	11	24.496	-45	54	01.69	8.6	5.6	5.9	0.291	3
0253	1	11	24.668	-45	56	29.59	12.3	6.6	29.9	1.870	3
0254	1	11	25.669	-46	27	29.34	12.7	8.7	16.5	0.670	1
0255	1	11	25.758	-46	23	49.28	10.9	8.3	85.1	0.539	1
0256	1	11	26.293	-45	38	14.51	8.1	5.7	-7.3	0.419	3
0257	1	11	26.317	-45	30	17.48	10.8	8.1	71.4	0.323	2
0258	1	11	26.925	-45	34	14.64	7.5	6.4	-26.2	0.141	2
0259	1	11	27.218	-46	31	02.27	13.7	8.2	-13.1	0.334	1
0260	1	11	27.264	-45	41	52.21	7.3	5.4	3.4	1.084	3
0261	1	11	27.377	-45	32	30.16	8.8	5.1	34.0	0.134	2
0262	1	11	27.516	-45	49	45.79	6.9	5.7	-13.1	0.225	3
0263	1	11	27.595	-45	48	15.44	8.0	5.8	-9.0	0.438	3
0264	1	11	28.577	-45	54	10.75	6.5	5.6	-14.9	0.144	2
0265	1	11	29.062	-45	30	53.36	8.7	5.6	24.8	1.104	3
0266	1	11	29.671	-45	52	41.74	6.7	5.7	11.0	0.171	2
0267	1	11	30.072	-45	50	27.39	14.8	8.4	77.9	1.952	3
0268	1	11	30.408	-45	58	05.06	7.3	5.0	15.1	0.178	2

continued from previous page

	α			δ			bmaj	bmin	pa	$S_{1.4}$	sample
0269	1	11	30.500	-46	01	45.62	12.0	6.6	-70.9	0.295	2
0270	1	11	30.675	-45	37	23.98	8.6	7.6	81.3	0.202	2
0271	1	11	31.354	-46	26	20.66	10.7	7.9	9.8	0.689	1
0272	1	11	31.362	-45	40	02.31	8.0	4.9	6.6	0.197	2
0273	1	11	31.394	-45	50	14.98	7.3	7.2	48.0	2.616	3
0274	1	11	31.874	-45	43	30.00	8.5	6.1	43.4	0.147	2
0275	1	11	32.358	-45	52	56.83	13.5	7.8	16.9	0.251	2
0276	1	11	32.368	-46	24	21.50	11.5	8.2	-51.0	0.403	1
0277	1	11	32.422	-45	49	37.72	9.0	8.0	-22.1	0.205	2
0278	1	11	32.466	-45	48	13.55	14.0	9.3	88.6	0.306	1
0279	1	11	32.780	-45	17	57.98	12.1	9.3	61.7	0.333	1
0280	1	11	33.071	-45	08	10.44	12.6	7.3	-70.0	0.270	1
0281	1	11	33.178	-45	59	50.61	8.7	5.6	-12.8	0.491	3
0282	1	11	33.267	-45	31	28.56	7.6	5.2	8.8	0.347	3
0283	1	11	33.350	-46	13	35.91	11.3	8.2	24.6	4.182	1
0284	1	11	33.707	-45	07	32.59	10.8	6.8	-14.2	0.319	1
0285	1	11	34.173	-45	46	08.63	8.5	5.9	24.2	0.199	2
0286	1	11	35.138	-45	32	44.92	7.2	6.0	-67.2	0.172	2
0287	1	11	36.153	-45	34	24.36	8.2	5.7	16.2	0.331	3
0288	1	11	36.193	-45	42	48.44	7.2	6.1	-3.3	0.266	3
0289	1	11	36.230	-46	33	06.61	16.4	9.4	21.6	0.561	1
0290	1	11	36.383	-46	05	02.83	12.5	8.0	27.6	0.314	1
0291	1	11	36.796	-45	38	02.75	10.0	6.5	79.1	0.120	2
0292	1	11	36.883	-44	54	56.98	11.4	7.9	-7.4	0.525	1
0293	1	11	37.034	-45	40	36.51	10.7	8.1	20.7	0.295	2
0294	1	11	37.580	-45	47	04.82	7.8	5.0	1.0	0.119	2
0295	1	11	37.709	-45	45	23.95	10.6	6.0	47.9	0.193	2
0296	1	11	37.836	-45	36	29.57	8.3	5.8	55.2	0.098	2
0297	1	11	37.895	-46	33	40.95	10.5	7.2	30.0	0.846	1
0298	1	11	38.122	-45	32	49.94	6.5	4.7	25.5	0.223	2
0299	1	11	38.318	-45	33	57.00	7.8	6.2	20.1	0.163	1
0300	1	11	38.592	-45	52	58.87	13.6	8.1	-3.9	0.266	2
0301	1	11	38.687	-45	38	54.98	7.6	5.8	56.1	0.262	2
0302	1	11	38.774	-45	10	17.40	9.4	7.7	30.1	0.626	1
0303	1	11	39.206	-45	16	20.87	0.0	0.0	00.0	4.294	1
0304	1	11	40.000	-45	56	43.42	7.2	5.4	-10.2	0.119	2
0305	1	11	40.243	-45	39	06.83	7.7	6.0	5.8	1.031	3
0306	1	11	40.319	-45	47	12.81	7.3	6.4	-29.8	0.549	3
0307	1	11	40.331	-45	22	52.23	12.8	9.1	-2.9	0.675	1
0308	1	11	41.181	-45	53	16.21	8.1	5.2	22.0	0.206	2
0309	1	11	41.703	-45	35	32.05	7.8	5.1	-30.9	0.127	2

continued from previous page

	α			δ			bmaj	bmin	pa	$S_{1.4}$	sample
0310	1	11	42.145	-45	40	19.54	8.1	4.9	27.7	0.116	2
0311	1	11	42.758	-46	28	35.55	12.3	8.3	3.7	0.953	1
0312	1	11	42.854	-45	41	55.30	7.2	6.0	8.7	0.377	2
0313	1	11	43.955	-45	37	02.61	10.7	7.4	-21.2	0.256	2
0314	1	11	44.239	-46	20	23.45	11.4	7.6	26.6	0.270	1
0315	1	11	44.349	-45	27	56.63	12.5	8.4	18.3	0.246	1
0316	1	11	44.655	-45	52	11.02	8.9	6.7	-22.5	0.458	3
0317	1	11	46.212	-46	21	10.46	12.4	8.1	10.0	0.871	1
0318	1	11	46.389	-45	40	18.67	7.5	5.6	-19.2	0.144	2
0319	1	11	46.445	-45	33	16.71	7.9	4.8	-37.6	0.125	2
0320	1	11	47.250	-45	40	28.62	9.1	6.9	35.5	0.299	3
0321	1	11	47.443	-45	40	01.35	6.2	4.3	-2.7	0.110	2
0322	1	11	48.014	-45	34	02.72	9.7	4.4	38.1	0.115	2
0323	1	11	48.157	-46	21	59.42	16.0	8.3	-12.3	0.322	1
0324	1	11	48.299	-45	06	26.21	17.3	8.5	-11.2	0.437	1
0325	1	11	48.509	-45	57	56.50	8.8	4.9	-17.4	0.295	3
0326	1	11	48.582	-45	58	30.76	15.2	13.5	18.6	0.472	1
0327	1	11	49.609	-45	42	06.86	8.8	6.1	2.5	0.224	2
0328	1	11	49.623	-45	54	15.34	9.3	6.1	-52.6	0.140	2
0329	1	11	50.210	-45	37	26.80	8.6	5.1	26.5	0.255	3
0330	1	11	50.388	-45	26	20.41	13.3	8.5	4.5	0.595	1
0331	1	11	50.736	-46	00	13.01	9.0	5.8	-25.5	0.415	3
0332	1	11	51.127	-45	02	16.63	15.7	8.3	35.5	2.553	1
0333	1	11	51.226	-45	35	18.86	13.9	11.5	-10.2	0.362	1
0334	1	11	51.451	-45	44	44.89	9.1	6.8	-21.7	0.154	2
0335	1	11	51.473	-45	56	44.43	13.1	7.3	-11.9	0.471	3
0336	1	11	51.775	-46	25	25.63	16.8	13.7	14.1	0.206	1
0337	1	11	51.807	-45	41	01.73	7.8	5.6	5.0	0.367	3
0338	1	11	52.328	-46	20	44.86	10.6	7.9	14.9	1.359	1
0339	1	11	52.452	-45	37	00.10	7.7	6.8	-34.9	0.154	2
0340	1	11	52.863	-45	40	24.02	8.7	5.2	33.0	0.221	2
0341	1	11	53.049	-45	54	27.45	10.8	8.2	15.4	0.237	1
0342	1	11	53.059	-45	04	31.01	10.0	6.2	13.5	0.255	1
0343	1	11	53.320	-45	58	46.94	18.7	16.1	-49.2	0.181	1
0344	1	11	54.110	-45	30	39.62	8.4	6.4	15.2	0.295	2
0345	1	11	54.236	-45	54	08.51	8.6	6.1	-23.2	0.225	3
0346	1	11	54.697	-45	46	39.67	9.5	8.1	47.9	0.210	3
0347	1	11	54.920	-45	27	30.02	18.7	7.5	-10.1	0.428	1
0348	1	11	55.196	-45	42	12.67	9.9	6.2	-16.4	0.260	2
0349	1	11	55.295	-45	01	35.96	15.5	12.8	37.4	1.642	1
0350	1	11	56.395	-45	58	34.23	10.0	5.7	6.8	0.395	3

continued from previous page

	α			δ			bmaj	bmin	pa	$S_{1.4}$	sample
0351	1	11	56.710	-44	54	50.62	9.5	6.7	-4.9	0.734	1
0352	1	11	56.711	-45	47	54.29	7.4	5.3	14.2	0.152	2
0353	1	11	56.725	-46	05	22.73	14.4	9.0	75.6	0.568	1
0354	1	11	56.917	-45	05	54.20	13.2	8.8	21.0	0.841	1
0355	1	11	57.163	-46	25	17.23	23.4	14.5	-62.3	0.204	1
0356	1	11	58.086	-46	08	58.28	17.8	8.4	-74.8	0.371	1
0357	1	11	58.437	-45	40	27.88	7.2	6.1	41.5	0.136	2
0358	1	11	58.771	-45	52	10.16	10.3	6.1	61.7	0.182	2
0359	1	11	58.849	-45	08	40.15	20.9	9.9	-79.5	0.591	1
0360	1	11	59.099	-45	09	40.74	11.9	8.3	-3.1	0.524	1
0361	1	12	00.089	-45	33	55.72	9.5	5.3	-1.0	0.378	3
0362	1	12	00.663	-45	39	41.18	10.7	6.2	-45.8	0.157	2
0363	1	12	01.952	-45	39	48.17	8.1	6.5	-43.4	0.133	2
0364	1	12	03.421	-46	01	17.49	11.6	7.0	-1.0	0.529	1
0365	1	12	03.669	-45	56	52.75	7.7	5.0	-52.5	0.140	2
0366	1	12	03.979	-45	58	48.52	9.0	6.2	-35.6	0.386	3
0367	1	12	04.038	-45	59	15.36	7.4	7.3	54.5	0.418	3
0368	1	12	04.438	-45	40	56.37	8.4	4.8	25.7	0.120	2
0369	1	12	04.663	-45	44	48.12	9.4	6.0	4.7	0.346	2
0370	1	12	05.130	-46	36	52.77	11.4	7.7	13.4	3.057	1
0371	1	12	05.183	-45	52	16.15	9.4	6.0	39.6	0.176	2
0372	1	12	05.798	-44	54	42.66	22.6	7.9	6.7	0.541	1
0373	1	12	05.861	-45	46	23.78	8.8	5.7	-64.3	0.236	2
0374	1	12	06.365	-44	49	44.22	15.5	9.8	-2.7	0.885	1
0375	1	12	06.404	-45	25	38.75	11.2	8.8	48.5	0.295	1
0376	1	12	07.955	-45	48	38.24	7.3	6.7	5.5	0.444	3
0377	1	12	08.027	-45	49	33.73	8.6	7.2	46.9	1.882	3
0378	1	12	08.394	-45	54	00.39	12.6	6.5	-66.7	0.280	3
0379	1	12	08.574	-45	34	22.57	19.9	16.3	-12.3	0.155	1
0380	1	12	08.984	-45	43	24.94	11.4	7.4	87.8	0.234	2
0381	1	12	10.116	-45	49	24.50	9.4	7.2	77.1	0.769	3
0382	1	12	10.611	-46	34	54.78	11.1	7.2	5.3	0.934	1
0383	1	12	10.880	-45	39	30.91	6.6	4.9	-39.2	0.131	2
0384	1	12	11.124	-46	07	18.05	10.7	8.3	13.1	1.582	1
0385	1	12	11.238	-46	15	04.47	10.2	7.7	18.9	2.913	1
0386	1	12	11.279	-45	37	44.15	5.9	4.7	20.6	0.132	2
0387	1	12	12.044	-45	40	51.24	8.0	6.1	10.1	0.154	2
0388	1	12	12.208	-46	10	02.88	10.6	9.3	9.7	1.519	1
0389	1	12	12.282	-45	59	05.20	9.5	8.1	22.2	0.249	1
0390	1	12	12.359	-46	05	52.97	9.3	5.9	-11.2	0.223	1
0391	1	12	12.924	-46	10	05.34	22.5	9.4	-89.7	2.331	1

continued from previous page

	α			δ			bmaj	bmin	pa	$S_{1.4}$	sample
0392	1	12	13.069	-45	40	17.25	8.8	6.3	39.1	0.207	2
0393	1	12	13.082	-44	59	05.67	14.6	10.2	20.9	0.676	1
0394	1	12	14.089	-45	08	45.24	20.3	12.7	-43.6	0.654	1
0395	1	12	15.169	-46	23	40.31	12.1	10.8	18.3	0.420	1
0396	1	12	15.477	-45	36	13.79	7.8	5.8	9.5	0.250	2
0397	1	12	16.438	-45	48	10.12	5.8	5.4	31.1	0.123	2
0398	1	12	16.521	-45	45	20.63	7.4	5.4	-3.7	0.160	3
0399	1	12	16.998	-44	49	42.80	10.1	6.8	70.2	0.365	1
0400	1	12	17.030	-45	43	06.49	10.1	7.5	-5.2	0.260	2
0401	1	12	17.563	-46	29	32.44	11.9	7.7	18.1	6.975	1
0402	1	12	17.604	-44	58	36.82	10.4	7.9	15.3	1.727	1
0403	1	12	17.804	-46	39	37.38	8.9	5.9	-20.1	0.290	1
0404	1	12	17.909	-45	51	22.32	14.5	9.9	68.3	0.402	2
0405	1	12	19.012	-45	37	53.65	12.2	8.8	2.6	0.360	2
0406	1	12	19.077	-46	36	24.32	10.7	7.6	14.0	3.612	1
0407	1	12	19.681	-45	35	03.07	15.6	11.3	-58.9	0.353	1
0408	1	12	19.761	-45	53	19.81	22.3	13.7	12.2	0.868	1
0409	1	12	20.138	-46	37	17.57	12.5	8.6	11.5	0.375	1
0410	1	12	20.583	-45	39	51.05	13.9	8.9	11.0	0.252	1
0411	1	12	22.133	-45	21	01.92	14.6	7.6	2.2	0.603	1
0412	1	12	22.221	-46	17	40.04	10.8	6.9	23.6	0.260	1
0413	1	12	22.536	-46	06	28.98	21.9	10.0	-3.2	0.184	1
0414	1	12	23.004	-45	31	25.13	11.5	8.2	8.8	16.008	1
0415	1	12	24.103	-45	32	55.03	8.8	5.1	28.7	0.245	2
0416	1	12	24.262	-46	03	15.24	10.8	8.4	25.7	8.445	1
0417	1	12	24.323	-44	55	34.00	17.8	10.6	-76.9	0.934	1
0418	1	12	24.442	-44	54	27.06	10.8	7.6	19.7	1.448	1
0419	1	12	24.955	-45	52	32.55	12.5	9.0	74.9	0.424	2
0420	1	12	25.141	-45	47	00.18	7.1	5.6	17.6	0.225	2
0421	1	12	25.181	-46	28	38.89	20.4	10.9	0.4	0.178	1
0422	1	12	25.978	-45	50	08.53	6.2	4.4	10.1	0.138	2
0423	1	12	27.058	-45	32	10.41	11.4	7.9	4.2	3.165	1
0424	1	12	27.251	-45	48	01.81	7.4	7.1	-1.3	0.423	3
0425	1	12	27.407	-45	53	18.83	8.7	5.5	25.8	0.171	2
0426	1	12	27.486	-45	58	51.26	11.7	6.8	30.7	0.324	1
0427	1	12	27.530	-46	17	16.28	11.5	9.9	31.2	1.346	1
0428	1	12	27.738	-45	44	50.06	9.7	4.9	69.1	0.185	2
0429	1	12	28.243	-45	33	49.66	6.2	5.6	41.8	0.169	2
0430	1	12	28.343	-46	25	17.67	9.8	6.3	27.2	0.219	1
0431	1	12	28.657	-45	49	59.55	8.7	6.9	-48.7	0.236	2
0432	1	12	28.919	-46	19	25.67	18.3	10.2	25.0	0.409	1

continued from previous page

	α			δ			bmaj	bmin	pa	$S_{1.4}$	sample
0433	1	12	28.957	-46	16	29.23	13.2	10.3	8.0	4.057	1
0434	1	12	29.067	-46	23	51.19	12.2	8.2	8.0	0.295	1
0435	1	12	29.141	-45	53	49.13	9.7	6.7	11.0	0.383	3
0436	1	12	29.386	-45	57	05.87	8.7	5.6	-25.7	0.249	2
0437	1	12	29.803	-44	53	37.66	12.0	7.1	18.0	1.076	1
0438	1	12	31.568	-44	58	35.47	10.4	7.7	-4.3	0.685	1
0439	1	12	31.848	-45	27	20.28	16.1	11.2	82.7	0.492	1
0440	1	12	31.991	-45	45	22.95	7.1	7.0	63.3	3.785	3
0441	1	12	32.000	-46	05	57.19	10.6	7.9	15.3	4.707	1
0442	1	12	32.098	-44	56	10.12	12.5	8.4	15.8	2.475	1
0443	1	12	32.245	-45	08	30.66	13.4	8.8	-33.3	0.285	1
0444	1	12	32.579	-45	19	34.44	11.3	8.7	40.6	0.238	1
0445	1	12	32.695	-45	47	59.71	10.6	5.1	68.4	0.174	2
0446	1	12	32.893	-45	51	36.50	8.5	5.3	-20.8	0.196	2
0447	1	12	32.947	-45	22	38.63	19.6	11.5	20.5	0.674	1
0448	1	12	34.800	-45	24	16.52	19.5	12.1	25.6	0.519	1
0449	1	12	35.085	-44	47	54.18	16.5	13.6	27.6	1.794	1
0450	1	12	35.997	-44	55	03.54	19.2	15.2	-60.9	0.203	1
0451	1	12	36.455	-45	05	15.86	14.4	7.9	29.6	0.299	1
0452	1	12	36.478	-45	18	41.79	11.9	7.6	13.9	2.064	1
0453	1	12	37.614	-44	48	51.31	13.7	7.8	9.7	1.582	1
0454	1	12	37.732	-44	49	07.18	48.4	15.8	-2.9	5.073	1
0455	1	12	38.610	-46	26	48.46	12.2	10.6	4.3	0.542	1
0456	1	12	38.849	-45	37	49.19	7.5	5.1	-72.8	0.155	2
0457	1	12	39.317	-45	24	33.79	18.5	9.6	19.8	0.437	1
0458	1	12	39.339	-45	01	11.78	12.4	10.6	80.0	0.937	1
0459	1	12	39.408	-45	50	56.97	13.7	9.1	-7.6	0.323	1
0460	1	12	40.055	-45	12	46.88	19.3	17.2	71.1	0.170	1
0461	1	12	40.551	-45	07	52.83	12.3	8.2	44.8	0.252	1
0462	1	12	40.617	-45	10	39.82	14.5	8.5	10.4	0.324	1
0463	1	12	40.676	-45	38	41.63	6.7	4.0	2.6	0.224	3
0464	1	12	40.789	-45	25	49.88	12.0	8.6	72.7	0.260	1
0465	1	12	40.940	-45	05	57.51	19.3	11.4	-0.5	0.449	1
0466	1	12	41.151	-46	03	24.23	15.0	8.8	13.5	0.351	1
0467	1	12	41.172	-45	25	26.94	13.3	6.5	25.1	0.236	1
0468	1	12	41.189	-45	52	25.87	8.8	7.6	-66.1	0.591	3
0469	1	12	41.431	-46	04	02.96	15.9	10.4	-1.2	0.390	1
0470	1	12	42.000	-45	37	05.50	14.8	7.3	66.6	0.862	3
0471	1	12	43.155	-46	30	54.23	10.6	6.9	5.4	1.280	1
0472	1	12	43.661	-45	37	42.98	8.7	6.9	37.4	0.401	3
0473	1	12	44.135	-45	00	33.74	0.0	0.0	0.0	6.408	1

continued from previous page

	α			δ			bmaj	bmin	pa	$S_{1.4}$	sample
0474	1	12	44.226	-45	33	14.81	9.4	6.3	62.6	0.399	1
0475	1	12	45.088	-46	24	14.39	11.6	8.3	7.2	0.366	1
0476	1	12	45.140	-46	27	12.58	22.4	17.0	17.8	0.174	1
0477	1	12	45.526	-46	28	55.31	11.5	7.6	11.0	1.557	1
0478	1	12	45.599	-45	55	59.68	18.0	10.1	16.3	0.462	1
0479	1	12	46.646	-44	46	12.77	11.3	8.4	14.8	12.480	1
0480	1	12	46.919	-46	18	30.44	20.9	14.2	16.0	0.171	1
0481	1	12	47.318	-46	13	24.75	10.0	8.3	83.8	0.464	1
0482	1	12	47.884	-45	44	50.04	7.5	6.8	55.8	0.860	3
0483	1	12	47.987	-45	50	58.52	9.6	4.3	-17.3	0.142	2
0484	1	12	47.992	-46	22	46.25	13.5	10.8	6.7	0.358	1
0485	1	12	47.997	-45	49	19.07	8.6	6.1	80.9	0.205	2
0486	1	12	48.796	-45	36	14.30	9.6	7.7	7.8	0.218	1
0487	1	12	49.231	-46	17	02.10	10.6	8.4	23.6	0.822	1
0488	1	12	49.311	-46	24	38.75	9.8	7.8	-26.0	0.301	1
0489	1	12	49.809	-45	06	34.53	10.5	7.6	11.8	3.421	1
0490	1	12	49.839	-44	55	27.59	11.8	9.4	24.7	0.537	1
0491	1	12	49.872	-44	48	36.54	12.1	7.8	9.4	2.114	1
0492	1	12	51.563	-46	23	37.83	15.1	11.7	35.5	0.863	1
0493	1	12	52.028	-45	16	52.08	11.4	5.7	-11.2	0.283	1
0494	1	12	52.197	-46	13	46.61	11.7	8.6	-7.0	0.289	1
0495	1	12	52.664	-45	43	44.77	7.8	7.5	-55.5	1.584	3
0496	1	12	52.936	-45	50	13.20	12.4	8.3	13.6	1.278	1
0497	1	12	52.944	-44	48	41.20	16.5	8.1	-6.8	0.660	1
0498	1	12	53.110	-46	37	50.12	12.0	6.9	-22.1	0.383	1
0499	1	12	53.723	-46	27	19.64	22.2	13.9	-10.4	0.959	1
0500	1	12	53.913	-46	24	28.97	12.6	6.9	14.6	0.370	1
0501	1	12	54.557	-45	58	38.02	10.5	9.3	0.0	0.600	1
0502	1	12	54.972	-45	47	22.47	15.5	10.8	69.2	0.482	1
0503	1	12	55.030	-45	17	30.09	13.9	12.7	-44.2	0.436	1
0504	1	12	55.052	-45	33	53.58	16.0	8.3	-26.3	0.550	1
0505	1	12	55.498	-45	59	04.98	9.5	8.3	-20.3	0.373	1
0506	1	12	55.514	-44	51	34.34	8.0	7.2	1.2	0.235	1
0507	1	12	55.908	-45	55	24.86	10.7	6.9	34.2	0.213	1
0508	1	12	56.802	-45	44	11.70	16.6	11.5	16.5	0.434	1
0509	1	12	57.023	-45	34	22.27	14.9	12.8	53.7	0.527	1
0510	1	12	59.459	-46	27	40.98	10.1	9.6	-73.6	0.268	1
0511	1	13	00.298	-45	45	19.32	10.4	6.7	35.1	0.231	1
0512	1	13	01.554	-46	24	35.89	9.2	6.8	25.2	0.798	1
0513	1	13	01.674	-46	02	32.53	10.7	7.8	12.9	6.018	1
0514	1	13	02.336	-45	22	38.70	13.5	8.2	-8.1	0.746	1

continued from previous page

	α			δ			bmaj	bmin	pa	$S_{1.4}$	sample
0515	1	13	02.629	-45	17	47.20	19.7	8.1	3.6	0.467	1
0516	1	13	03.145	-45	14	15.78	11.6	8.9	9.4	7.100	1
0517	1	13	03.887	-45	30	09.76	12.2	7.0	2.3	0.305	1
0518	1	13	04.229	-46	21	03.53	13.6	9.4	-29.4	0.333	1
0519	1	13	04.450	-46	08	56.68	12.8	7.5	10.8	0.922	1
0520	1	13	04.837	-46	27	20.41	10.6	8.3	77.0	0.244	1
0521	1	13	04.938	-46	29	25.70	24.5	13.2	33.8	0.193	1
0522	1	13	06.019	-46	26	03.85	11.7	10.4	52.5	0.736	1
0523	1	13	06.049	-46	10	00.01	11.4	8.2	23.6	0.626	1
0524	1	13	06.246	-45	14	22.52	11.0	7.6	29.5	1.045	1
0525	1	13	06.452	-45	34	35.24	14.5	11.0	4.0	0.379	1
0526	1	13	06.730	-45	13	01.44	16.4	6.4	6.7	0.477	1
0527	1	13	07.091	-45	30	02.89	9.0	7.4	26.5	0.215	1
0528	1	13	07.770	-45	06	04.01	16.9	8.9	-8.0	0.893	1
0529	1	13	08.191	-45	57	48.02	15.8	9.8	-5.5	0.497	1
0530	1	13	10.424	-45	07	05.78	11.1	6.9	8.5	0.339	1
0531	1	13	10.710	-45	14	36.58	12.8	11.0	-1.8	1.329	1
0532	1	13	10.786	-44	50	14.73	14.7	6.5	4.5	0.489	1
0533	1	13	11.075	-45	01	43.61	13.1	10.1	11.5	0.643	1
0534	1	13	11.557	-45	42	59.82	21.8	14.9	15.9	0.166	1
0535	1	13	12.485	-46	14	04.30	16.6	9.6	21.3	0.507	1
0536	1	13	12.515	-44	47	40.29	16.8	7.3	7.0	0.926	1
0537	1	13	13.727	-46	01	57.85	14.8	10.4	17.1	0.578	1
0538	1	13	14.593	-45	37	00.47	13.7	10.3	-32.8	0.400	1
0539	1	13	14.609	-46	06	01.22	20.3	14.9	46.5	0.221	1
0540	1	13	14.772	-45	40	50.80	14.1	12.3	-2.3	1.229	1
0541	1	13	15.179	-45	45	22.04	11.4	9.6	-13.1	0.242	1
0542	1	13	15.207	-44	55	00.52	11.2	8.1	8.4	1.255	1
0543	1	13	15.766	-45	21	58.51	11.1	9.2	61.2	0.350	1
0544	1	13	15.894	-44	59	19.16	10.2	7.6	81.2	0.444	1
0545	1	13	16.103	-44	52	58.27	12.7	9.0	-52.9	0.504	1
0546	1	13	16.777	-46	02	08.71	12.7	7.0	-8.2	0.282	1
0547	1	13	17.904	-45	33	21.49	13.0	10.5	6.7	0.308	1
0548	1	13	19.117	-46	28	14.54	15.8	8.2	-0.4	0.375	1
0549	1	13	19.246	-45	45	31.03	11.9	8.7	10.5	3.005	1
0550	1	13	19.422	-45	26	11.84	10.5	6.0	31.2	0.243	1
0551	1	13	19.827	-45	24	06.07	10.3	7.2	-8.3	0.334	1
0552	1	13	20.951	-44	51	05.90	11.7	7.5	5.4	0.639	1
0553	1	13	21.104	-46	12	41.99	15.8	6.7	-11.0	0.403	1
0554	1	13	21.337	-45	44	42.14	13.8	7.6	10.6	0.290	1
0555	1	13	21.655	-45	38	05.59	12.3	7.7	-22.0	0.235	1

continued from previous page

	α			δ			bmaj	bmin	pa	$S_{1.4}$	sample
0556	1	13	21.779	-46	40	09.24	11.4	6.4	13.2	0.339	1
0557	1	13	22.001	-45	49	17.82	12.2	8.5	72.0	0.240	1
0558	1	13	23.156	-46	11	30.21	12.7	9.2	-2.2	0.442	1
0559	1	13	24.249	-45	32	47.10	15.8	9.8	-3.7	0.491	1
0560	1	13	25.168	-46	15	32.39	12.9	7.6	8.8	0.858	1
0561	1	13	25.353	-46	39	55.80	12.1	9.9	53.2	0.552	1
0562	1	13	25.917	-45	49	07.30	17.3	10.8	-6.6	0.508	1
0563	1	13	26.681	-45	15	13.57	11.8	8.7	13.0	0.274	1
0564	1	13	26.915	-46	24	23.27	11.2	8.3	3.5	0.902	1
0565	1	13	27.309	-45	01	05.24	15.9	6.1	15.3	0.267	1
0566	1	13	28.138	-46	31	04.27	15.6	10.6	88.9	0.671	1
0567	1	13	28.469	-46	31	00.43	18.0	9.1	6.9	0.662	1
0568	1	13	28.492	-45	58	49.77	11.3	7.9	6.6	6.499	1
0569	1	13	29.212	-46	43	05.82	14.7	10.6	51.0	0.881	1
0570	1	13	29.468	-45	37	21.55	17.8	9.9	20.1	0.546	1
0571	1	13	29.603	-45	56	34.20	13.2	8.7	-7.2	0.780	1
0572	1	13	29.656	-45	45	32.09	13.3	8.8	28.1	0.267	1
0573	1	13	30.655	-46	08	38.96	13.8	10.3	8.6	0.448	1
0574	1	13	30.929	-45	21	22.36	11.4	8.7	4.5	0.755	1
0575	1	13	31.822	-46	02	07.03	13.3	9.2	-8.4	0.484	1
0576	1	13	32.319	-46	11	27.35	12.8	8.2	3.9	0.921	1
0577	1	13	33.242	-46	10	34.50	15.0	7.8	10.1	0.293	1
0578	1	13	33.424	-45	38	41.54	11.6	8.7	-4.1	0.450	1
0579	1	13	33.734	-45	34	14.67	10.6	10.4	36.8	0.309	1
0580	1	13	33.807	-46	18	34.33	14.4	9.1	37.4	0.379	1
0581	1	13	33.971	-45	16	27.28	10.4	7.5	10.5	3.670	1
0582	1	13	35.410	-46	09	54.43	13.6	12.8	13.2	0.698	1
0583	1	13	36.891	-45	03	34.14	13.8	11.6	31.1	0.498	1
0584	1	13	38.486	-45	18	14.02	11.2	8.7	18.4	2.281	1
0585	1	13	38.604	-45	02	56.53	10.9	6.4	-6.8	0.236	1
0586	1	13	39.057	-46	02	49.52	13.9	12.7	34.5	0.794	1
0587	1	13	39.955	-45	04	45.67	9.8	8.9	81.2	0.370	1
0588	1	13	40.879	-46	03	47.72	13.9	9.1	38.1	16.256	1
0589	1	13	41.471	-45	16	23.76	12.2	10.1	-16.0	3.451	1
0590	1	13	41.729	-44	48	06.20	18.7	7.3	1.3	0.743	1
0591	1	13	41.821	-45	20	13.27	18.6	9.4	-82.0	0.465	1
0592	1	13	41.831	-46	35	41.28	10.9	10.0	80.3	1.235	1
0593	1	13	42.047	-45	49	25.42	9.4	6.5	63.5	0.258	1
0594	1	13	43.429	-45	06	59.49	12.4	8.2	20.0	0.311	1
0595	1	13	43.965	-45	56	16.51	14.0	10.0	-9.3	1.623	1
0596	1	13	44.611	-46	39	23.93	12.7	7.8	78.8	0.370	1

continued from previous page

	α			δ			bmaj	bmin	pa	$S_{1.4}$	sample
0597	1	13	44.656	-46	05	03.64	11.4	8.0	15.7	8.199	1
0598	1	13	45.796	-45	40	17.63	13.9	11.2	-23.7	0.339	1
0599	1	13	45.815	-46	15	55.41	13.0	9.4	-2.3	0.350	1
0600	1	13	46.150	-45	17	41.09	10.7	10.1	-27.5	38.226	1
0601	1	13	46.405	-46	04	48.05	12.9	8.9	17.5	4.061	1
0602	1	13	46.817	-45	26	49.58	11.3	10.2	-87.3	0.352	1
0603	1	13	48.573	-45	50	19.71	13.1	10.6	3.1	1.112	1
0604	1	13	49.180	-45	51	40.84	18.6	13.3	-22.6	0.157	1
0605	1	13	49.228	-45	40	51.69	13.4	8.3	-14.8	0.290	1
0606	1	13	49.522	-45	01	46.78	10.8	7.9	17.6	10.380	1
0607	1	13	50.468	-46	15	51.14	13.5	8.6	-17.9	0.520	1
0608	1	13	51.641	-46	22	12.18	10.3	8.8	5.3	0.826	1
0609	1	13	53.235	-45	04	36.46	13.9	7.0	-6.1	0.359	1
0610	1	13	53.351	-44	53	34.48	13.3	10.7	73.2	1.754	1
0611	1	13	55.063	-45	27	16.12	15.7	8.7	-24.8	2.428	1
0612	1	13	55.133	-46	10	21.47	10.3	7.0	35.2	0.229	1
0613	1	13	56.346	-45	16	50.90	10.6	8.2	12.9	0.402	1
0614	1	13	56.386	-45	47	13.48	12.1	9.7	-0.7	2.688	1
0615	1	13	57.599	-45	47	29.71	12.7	8.6	11.3	1.157	1
0616	1	13	57.710	-46	15	19.60	9.3	7.0	-70.7	0.226	1
0617	1	13	57.786	-46	11	05.51	10.9	8.9	0.5	1.345	1
0618	1	13	58.090	-45	04	05.26	20.6	7.8	22.9	1.331	1
0619	1	13	58.567	-45	03	53.59	12.4	8.2	4.9	1.910	1
0620	1	13	58.598	-45	04	50.07	17.1	8.0	81.1	0.435	1
0621	1	14	00.275	-45	47	52.64	30.8	13.6	-8.5	0.194	1
0622	1	14	00.673	-45	48	46.36	15.5	9.0	15.0	0.481	1
0623	1	14	01.297	-44	58	23.45	11.2	7.5	21.4	0.399	1
0624	1	14	02.372	-45	15	08.60	9.4	5.8	-24.0	0.322	1
0625	1	14	02.421	-46	23	06.26	12.4	9.0	29.8	0.303	1
0626	1	14	03.090	-45	52	28.01	19.3	10.5	-51.0	0.520	1
0627	1	14	03.188	-45	53	48.50	10.1	8.8	43.1	0.270	1
0628	1	14	04.049	-46	01	54.16	12.4	7.7	10.3	1.253	1
0629	1	14	04.240	-45	45	03.90	14.5	8.4	12.0	0.578	1
0630	1	14	04.494	-45	50	45.82	18.5	13.7	22.1	0.158	1
0631	1	14	04.579	-45	57	01.91	13.9	11.4	13.4	1.041	1
0632	1	14	04.804	-45	03	25.38	14.0	7.8	79.4	0.387	1
0633	1	14	05.026	-46	09	40.20	9.7	7.5	62.4	0.205	1
0634	1	14	05.276	-46	15	11.58	10.9	7.5	9.7	1.249	1
0635	1	14	05.968	-45	06	46.87	23.3	8.0	10.1	0.489	1
0636	1	14	06.229	-46	13	27.46	11.9	7.7	11.9	1.502	1
0637	1	14	06.253	-45	54	22.11	14.6	8.9	-3.2	1.496	1

continued from previous page

	α			δ			bmaj	bmin	pa	$S_{1.4}$	sample
0638	1	14	06.551	-45	20	46.55	10.7	9.4	84.1	0.285	1
0639	1	14	07.552	-46	28	53.70	20.5	17.2	73.6	0.226	1
0640	1	14	07.602	-45	14	48.13	31.8	7.9	17.4	20.318	1
0641	1	14	08.382	-44	56	48.49	11.0	8.3	6.4	0.862	1
0642	1	14	08.514	-45	28	58.70	13.1	9.0	3.2	0.738	1
0643	1	14	08.800	-44	48	49.45	10.7	7.1	11.2	1.555	1
0644	1	14	09.558	-45	32	44.85	18.2	8.0	-7.5	0.475	1
0645	1	14	09.571	-45	46	04.85	12.6	8.6	15.5	1.167	1
0646	1	14	09.595	-46	21	54.38	11.3	8.1	0.7	2.116	1
0647	1	14	10.797	-45	53	28.80	12.0	9.2	10.0	0.459	1
0648	1	14	10.831	-46	03	22.34	12.7	8.5	22.3	0.342	1
0649	1	14	10.897	-45	52	44.95	13.5	10.5	37.0	0.443	1
0650	1	14	10.952	-46	35	48.79	10.3	7.9	-5.2	51.250	1
0651	1	14	11.413	-46	26	30.76	11.1	7.8	55.0	0.191	1
0652	1	14	11.589	-46	17	32.68	9.9	9.1	40.0	0.537	1
0653	1	14	13.397	-46	07	49.88	11.7	9.8	16.1	0.771	1
0654	1	14	13.496	-45	23	34.13	18.7	10.8	-88.7	0.471	1
0655	1	14	14.071	-45	04	19.74	13.8	13.2	-55.3	0.232	1
0656	1	14	14.238	-45	09	11.22	13.7	5.8	-10.3	0.376	1
0657	1	14	14.486	-46	42	43.79	10.3	7.9	-11.0	8.517	1
0658	1	14	14.645	-45	19	51.68	12.4	8.0	-2.8	1.697	1
0659	1	14	14.874	-46	13	02.93	14.8	14.2	-31.1	0.382	1
0660	1	14	15.020	-45	48	24.62	15.5	11.4	5.6	1.531	1
0661	1	14	15.738	-45	31	48.35	11.1	9.4	-9.3	0.461	1
0662	1	14	16.188	-45	17	58.01	11.7	8.1	3.4	1.335	1
0663	1	14	17.370	-45	33	56.15	20.8	10.2	13.0	0.587	1
0664	1	14	18.968	-44	57	24.42	14.2	8.3	31.4	1.297	1
0665	1	14	18.968	-45	56	22.28	14.5	11.8	-28.3	0.453	1
0666	1	14	19.484	-45	31	55.19	10.9	6.7	-2.2	0.285	1
0667	1	14	20.301	-45	12	48.35	11.4	9.1	50.1	0.457	1
0668	1	14	20.494	-46	13	13.28	21.4	11.8	-2.0	0.701	1
0669	1	14	21.240	-45	00	55.44	12.5	7.6	18.8	1.469	1
0670	1	14	21.332	-45	50	37.87	17.9	13.5	10.3	0.478	1
0671	1	14	22.245	-46	15	55.25	11.4	9.4	14.0	0.729	1
0672	1	14	23.017	-45	34	29.78	12.2	8.7	3.7	1.675	1
0673	1	14	23.979	-44	57	29.03	12.3	7.3	21.2	0.950	1
0674	1	14	24.066	-45	10	40.15	10.2	7.5	8.8	11.485	1
0675	1	14	24.465	-46	13	07.79	30.1	11.6	-3.1	0.210	1
0676	1	14	25.134	-45	04	48.26	18.0	7.7	-5.1	1.317	1
0677	1	14	25.873	-46	26	16.22	10.7	8.5	-1.8	2.163	1
0678	1	14	26.190	-46	17	02.74	11.6	10.0	-2.3	0.459	1

continued from previous page

	α			δ			bmaj	bmin	pa	$S_{1.4}$	sample
0679	1	14	26.383	-45	52	24.10	12.3	8.7	45.1	0.331	1
0680	1	14	27.634	-45	24	27.98	17.7	15.1	67.4	0.739	1
0681	1	14	28.475	-45	36	37.55	13.9	10.4	9.0	0.929	1
0682	1	14	28.753	-45	54	01.41	14.0	8.6	2.2	0.738	1
0683	1	14	28.763	-46	27	05.80	9.6	8.5	13.8	1.552	1
0684	1	14	28.853	-45	28	21.40	13.8	10.7	-7.9	2.050	1
0685	1	14	29.125	-46	36	30.65	12.9	11.9	-67.3	0.546	1
0686	1	14	30.002	-46	33	15.15	9.4	7.0	-7.2	0.541	1
0687	1	14	30.206	-45	05	50.91	12.0	8.6	46.6	0.317	1
0688	1	14	30.645	-46	34	51.71	22.6	8.9	-2.8	0.679	1
0689	1	14	31.617	-45	54	45.03	16.5	9.6	1.0	0.588	1
0690	1	14	32.102	-45	25	25.19	13.1	9.0	20.1	0.327	1
0691	1	14	32.938	-45	24	00.86	12.7	9.7	75.5	0.375	1
0692	1	14	33.098	-46	18	29.74	10.1	8.7	5.4	2.133	1
0693	1	14	34.173	-45	32	00.27	17.6	13.1	-84.7	0.583	1
0694	1	14	34.428	-46	27	05.48	10.2	7.6	1.0	0.656	1
0695	1	14	34.854	-45	12	01.21	12.8	10.9	-0.2	0.383	1
0696	1	14	35.924	-44	58	53.49	9.0	7.0	45.8	0.790	1
0697	1	14	36.330	-45	20	56.62	14.1	9.0	84.9	0.386	1
0698	1	14	36.760	-46	24	06.22	19.9	7.4	-2.7	0.428	1
0699	1	14	36.773	-44	51	26.09	10.3	7.3	17.1	2.479	1
0700	1	14	37.192	-46	17	51.84	8.3	6.8	17.1	0.339	1
0701	1	14	38.377	-46	27	20.54	12.6	6.6	7.9	0.400	1
0702	1	14	38.894	-45	40	27.48	15.5	9.5	9.7	1.258	1
0703	1	14	40.480	-45	12	07.65	20.2	13.0	74.8	1.239	1
0704	1	14	41.785	-45	51	59.40	17.4	11.1	-6.9	0.351	1
0705	1	14	42.459	-45	29	17.82	14.0	11.3	8.8	0.598	1
0706	1	14	42.697	-45	24	22.47	12.8	11.1	59.5	1.318	1
0707	1	14	43.104	-45	54	16.74	13.7	11.2	-9.3	1.027	1
0708	1	14	43.420	-44	46	28.89	9.2	6.8	3.2	0.973	1
0709	1	14	44.009	-45	36	11.72	16.2	8.3	-1.3	0.404	1
0710	1	14	44.748	-46	19	52.46	12.3	8.8	13.8	1.724	1
0711	1	14	45.421	-45	31	29.03	12.7	11.9	17.5	0.784	1
0712	1	14	45.631	-45	02	19.03	24.2	9.9	89.8	2.263	1
0713	1	14	45.966	-45	02	19.31	26.6	10.5	87.3	2.383	1
0714	1	14	47.222	-46	14	38.28	12.7	8.4	6.4	0.307	1
0715	1	14	47.797	-45	30	46.82	9.1	8.6	27.5	0.296	1
0716	1	14	50.486	-46	30	34.09	10.2	8.0	1.9	1.537	1
0717	1	14	53.503	-45	39	05.13	18.0	12.4	-10.6	0.585	1
0718	1	14	53.554	-46	12	08.23	18.5	8.7	-4.4	0.368	1
0719	1	14	53.647	-46	39	17.26	14.9	10.2	56.2	3.921	1

continued from previous page

	α			δ			bmaj	bmin	pa	$S_{1.4}$	sample
0720	1	14	53.768	-45	58	20.79	24.7	9.0	7.2	0.670	1
0721	1	14	54.015	-44	56	03.25	11.5	8.1	11.4	1.242	1
0722	1	14	54.051	-45	47	06.66	18.0	8.4	-8.1	0.314	1
0723	1	14	54.649	-45	20	25.91	12.5	10.8	-27.4	0.901	1
0724	1	14	55.305	-46	42	19.47	15.1	8.3	1.7	0.610	1
0725	1	14	55.933	-46	18	00.10	11.3	8.8	46.8	0.207	1
0726	1	14	57.330	-44	59	23.65	20.1	9.1	42.1	5.212	1
0727	1	14	57.741	-45	49	49.30	15.4	6.9	8.0	0.275	1
0728	1	14	57.838	-45	06	16.17	9.2	7.0	-3.6	0.706	1
0729	1	14	59.921	-44	57	55.52	15.4	9.0	8.9	1.985	1
0730	1	15	01.951	-45	44	52.11	22.2	9.7	13.5	0.632	1
0731	1	15	02.047	-46	20	52.12	10.9	8.6	-18.5	0.483	1
0732	1	15	02.371	-45	36	04.80	25.2	12.0	-1.0	0.160	1
0733	1	15	02.740	-46	10	11.95	11.1	8.3	5.6	1.879	1
0734	1	15	03.619	-46	41	31.99	10.6	9.0	-1.3	5.368	1
0735	1	15	04.202	-46	15	08.29	10.5	8.6	13.3	0.324	1
0736	1	15	04.944	-45	49	43.20	13.1	10.4	22.1	0.467	1
0737	1	15	05.983	-46	02	36.69	13.7	10.2	17.5	0.884	1
0738	1	15	06.556	-46	16	12.58	12.4	8.6	-29.0	0.424	1
0739	1	15	06.584	-45	06	03.45	10.0	6.3	-88.8	0.336	1
0740	1	15	06.667	-46	15	33.85	9.4	7.8	-44.4	0.186	1
0741	1	15	07.339	-45	10	45.00	15.5	8.1	27.9	3.442	1
0742	1	15	07.811	-46	14	30.51	11.8	8.8	9.2	0.435	1
0743	1	15	07.957	-45	37	38.82	11.5	7.6	-3.3	0.643	1
0744	1	15	07.990	-45	42	19.71	13.7	8.5	26.3	0.755	1
0745	1	15	08.098	-46	15	30.57	23.8	7.6	-1.0	0.260	1
0746	1	15	09.905	-45	24	03.36	17.1	6.6	-9.9	0.345	1
0747	1	15	10.293	-45	50	20.00	19.0	9.8	-12.0	0.447	1
0748	1	15	10.443	-46	14	21.86	9.9	6.9	10.3	0.507	1
0749	1	15	10.481	-46	17	52.54	10.7	8.5	13.3	0.460	1
0750	1	15	10.638	-45	41	35.76	13.0	7.6	0.0	1.919	1
0751	1	15	10.732	-46	23	06.06	11.1	8.9	18.0	1.327	1
0752	1	15	10.744	-46	15	49.92	12.8	7.2	33.4	0.200	1
0753	1	15	12.876	-45	10	32.91	15.3	9.5	-10.5	0.620	1
0754	1	15	13.272	-46	15	28.19	16.9	8.3	-8.8	0.320	1
0755	1	15	14.555	-45	38	24.02	13.9	7.2	-46.7	0.220	1
0756	1	15	14.718	-46	07	44.51	11.5	8.5	14.0	0.265	1
0757	1	15	14.815	-45	04	15.82	10.0	8.4	21.8	10.467	1
0758	1	15	18.262	-44	52	04.92	21.7	11.0	-88.5	1.899	1
0759	1	15	18.842	-44	55	10.46	11.4	9.4	13.4	8.180	1
0760	1	15	20.762	-44	59	03.84	10.3	7.9	58.5	0.619	1

continued from previous page

	α			δ			bmaj	bmin	pa	$S_{1.4}$	sample
0761	1	15	21.856	-45	52	16.04	13.7	8.2	7.2	1.133	1
0762	1	15	23.526	-46	32	26.61	17.3	9.2	-89.3	0.405	1
0763	1	15	23.989	-45	47	32.91	17.0	8.3	3.5	0.723	1
0764	1	15	24.042	-46	06	36.23	16.0	7.8	77.6	0.220	1
0765	1	15	25.908	-45	02	50.86	12.9	9.9	18.6	1.615	1
0766	1	15	26.580	-44	50	58.87	9.8	7.7	23.0	5.829	1
0767	1	15	27.113	-45	31	01.41	11.3	9.6	-17.1	1.042	1
0768	1	15	27.171	-45	55	23.79	11.9	10.7	38.8	0.904	1
0769	1	15	27.220	-45	36	27.62	15.9	8.2	-84.6	0.343	1
0770	1	15	27.362	-45	15	04.07	16.0	7.0	-0.3	0.429	1
0771	1	15	27.507	-46	32	56.75	10.2	8.5	-3.8	1.348	1
0772	1	15	28.088	-46	34	45.57	10.0	8.0	-4.8	1.326	1
0773	1	15	29.619	-44	46	11.68	9.0	7.8	-88.1	0.692	1
0774	1	15	30.303	-44	47	45.49	15.2	8.2	40.0	0.801	1
0775	1	15	30.422	-44	48	54.01	8.8	6.5	-69.6	0.416	1
0776	1	15	30.737	-46	19	41.04	10.6	8.0	21.3	0.184	1
0777	1	15	33.083	-45	47	28.09	16.9	13.7	82.1	0.410	1
0778	1	15	35.089	-46	22	39.12	10.4	8.2	1.4	2.760	1
0779	1	15	36.645	-46	25	22.09	20.2	13.2	-1.0	0.158	1
0780	1	15	36.709	-45	38	32.21	14.8	9.2	76.5	0.427	1
0781	1	15	38.112	-45	00	23.51	13.4	9.9	-1.8	2.075	1
0782	1	15	38.770	-46	19	26.73	15.9	8.9	21.3	0.782	1
0783	1	15	38.786	-45	50	22.97	13.9	7.6	-9.7	0.575	1
0784	1	15	38.844	-45	47	41.47	14.0	8.4	-2.9	0.245	1
0785	1	15	39.093	-45	56	16.67	12.2	8.1	-3.7	4.530	1
0786	1	15	39.617	-45	53	43.97	13.0	8.0	-0.4	1.842	1
0787	1	15	40.113	-45	48	37.03	12.1	8.1	-2.0	8.787	1
0788	1	15	41.044	-46	28	44.69	10.3	8.2	-0.9	0.985	1
0789	1	15	41.291	-44	49	37.57	14.5	8.8	-64.8	0.952	1
0790	1	15	41.402	-46	27	21.56	13.8	10.0	27.8	0.364	1
0791	1	15	41.437	-46	29	33.39	16.9	10.5	-0.8	0.468	1
0792	1	15	41.959	-45	33	16.95	15.8	8.8	-87.1	0.374	1
0793	1	15	44.224	-46	21	03.77	9.9	8.1	2.9	2.717	1
0794	1	15	44.802	-45	55	50.18	11.9	7.8	-2.3	36.963	1
0795	1	15	45.313	-45	49	37.05	11.5	8.5	6.5	0.374	1
0796	1	15	45.603	-44	48	42.59	14.5	12.5	-11.1	1.895	1
0797	1	15	45.704	-45	47	34.50	13.5	9.2	-16.2	0.323	1
0798	1	15	45.746	-46	18	09.55	20.6	10.0	-22.1	0.336	1
0799	1	15	46.910	-46	40	00.45	16.3	10.4	4.2	1.177	1
0800	1	15	48.190	-46	09	48.20	12.8	8.8	24.1	7.490	1
0801	1	15	48.276	-45	50	40.39	13.2	9.6	-4.2	1.580	1

continued from previous page

	α			δ			bmaj	bmin	pa	$S_{1.4}$	sample
0802	1	15	48.660	-45	30	49.11	17.4	7.7	-89.7	0.663	1
0803	1	15	49.784	-45	13	11.23	12.3	7.6	-12.6	1.767	1
0804	1	15	50.727	-46	35	53.75	14.1	13.9	-65.6	0.686	1
0805	1	15	51.806	-45	45	07.32	10.6	9.4	-6.5	0.220	1
0806	1	15	51.818	-45	54	23.61	13.7	10.5	-13.9	1.114	1
0807	1	15	52.529	-46	30	02.79	12.6	9.2	53.9	0.296	1
0808	1	15	52.643	-45	56	19.21	10.7	7.1	-24.7	0.559	1
0809	1	15	52.958	-45	11	37.84	9.1	7.3	-7.3	27.976	1
0810	1	15	56.404	-45	04	13.81	9.5	7.6	5.2	5.609	1
0811	1	15	56.955	-45	36	09.89	15.6	8.5	-6.4	2.832	1
0812	1	15	57.937	-46	00	53.42	13.9	9.7	32.8	0.667	1
0813	1	15	57.984	-44	50	54.35	10.4	7.6	58.2	0.828	1
0814	1	15	58.299	-46	35	28.05	13.1	11.2	-20.0	0.627	1
0815	1	15	59.593	-46	38	36.89	15.4	12.0	-16.6	0.725	1
0816	1	16	00.359	-45	29	14.73	12.3	9.4	75.0	0.510	1
0817	1	16	00.978	-45	51	47.53	26.4	9.5	2.3	3.705	1
0818	1	16	01.463	-45	13	46.31	17.3	13.0	84.4	1.004	1
0819	1	16	02.486	-45	52	48.79	13.9	8.3	6.5	0.828	1
0820	1	16	03.532	-45	44	14.99	16.6	13.8	52.1	0.476	1
0821	1	16	03.801	-44	50	55.31	24.0	17.7	-12.4	0.274	1
0822	1	16	04.164	-45	50	17.11	11.1	8.3	-26.4	0.341	1
0823	1	16	04.818	-46	00	52.30	26.7	15.3	-0.1	1.356	1
0824	1	16	05.142	-45	24	00.20	11.0	7.4	-12.7	1.297	1
0825	1	16	05.167	-45	12	29.83	13.1	10.5	-14.7	1.213	1
0826	1	16	06.454	-45	34	39.75	19.1	9.0	20.2	0.827	1
0827	1	16	07.945	-46	27	45.98	10.9	7.7	27.1	0.346	1
0828	1	16	09.052	-45	40	10.73	11.6	8.1	11.6	0.414	1
0829	1	16	09.440	-46	01	47.46	15.3	11.9	1.6	0.337	1
0830	1	16	09.892	-44	56	49.20	13.6	5.8	14.9	0.682	1
0831	1	16	10.800	-45	58	22.56	20.0	15.7	-43.8	1.616	1
0832	1	16	11.101	-46	04	27.19	18.0	7.4	0.4	0.258	1
0833	1	16	11.235	-46	05	37.50	12.6	9.9	0.1	0.201	1
0834	1	16	12.834	-45	39	35.34	17.1	12.1	55.4	0.425	1
0835	1	16	14.404	-45	12	04.74	13.3	7.5	-11.9	3.771	1
0836	1	16	14.644	-46	20	28.56	12.1	8.7	23.4	2.995	1
0837	1	16	15.071	-45	42	56.17	20.5	13.0	38.6	0.165	1
0838	1	16	16.301	-45	23	41.08	14.5	8.7	-56.2	0.408	1
0839	1	16	16.828	-45	53	55.23	18.6	9.2	-4.4	0.498	1
0840	1	16	17.028	-46	03	02.92	14.2	8.2	-4.7	1.014	1
0841	1	16	19.926	-46	05	36.66	13.0	8.8	2.1	0.174	1
0842	1	16	19.934	-45	22	30.07	10.2	7.3	-13.6	2.020	1

continued from previous page

	α			δ			bmaj	bmin	pa	$S_{1.4}$	sample
0843	1	16	20.804	-46	02	23.25	12.5	10.0	0.2	0.336	1
0844	1	16	20.875	-45	00	20.27	15.3	7.7	0.1	0.783	1
0845	1	16	21.312	-45	58	21.33	14.0	9.5	-24.5	0.420	1
0846	1	16	21.872	-45	03	10.15	9.9	6.0	-89.8	0.372	1
0847	1	16	22.901	-46	11	07.12	12.4	9.3	76.4	0.236	1
0848	1	16	23.135	-46	33	48.42	9.6	8.1	-60.6	0.909	1
0849	1	16	23.723	-46	22	04.59	26.5	11.4	-3.1	0.191	1
0850	1	16	24.257	-45	49	24.86	13.9	8.1	8.7	0.667	1
0851	1	16	24.450	-45	24	02.43	8.9	6.3	-30.2	0.413	1
0852	1	16	24.597	-46	32	36.35	10.0	7.8	-3.8	61.536	1
0853	1	16	25.214	-45	53	45.84	11.2	8.2	-1.7	5.969	1
0854	1	16	25.616	-45	07	58.57	10.8	9.8	67.2	0.651	1
0855	1	16	25.859	-46	28	46.16	9.3	7.8	6.5	3.032	1
0856	1	16	25.906	-45	15	02.21	8.4	7.5	-12.5	1.188	1
0857	1	16	26.944	-44	51	16.63	11.0	6.6	70.8	0.630	1
0858	1	16	27.721	-45	59	03.20	13.9	7.1	-11.0	0.299	1
0859	1	16	28.642	-45	51	16.90	15.9	13.5	-45.9	0.506	1
0860	1	16	29.111	-46	31	26.27	21.1	17.9	17.6	0.339	1
0861	1	16	30.486	-45	51	58.86	17.9	12.7	42.1	0.461	1
0862	1	16	32.015	-45	06	52.97	8.9	7.3	-9.4	9.449	1
0863	1	16	32.101	-46	38	38.93	12.5	8.4	-89.1	0.495	1
0864	1	16	32.501	-46	19	58.71	11.6	8.1	-35.8	0.212	1
0865	1	16	32.714	-46	21	18.96	13.6	9.1	9.3	0.254	1
0866	1	16	33.484	-45	36	11.60	13.9	8.8	2.0	0.677	1
0867	1	16	33.756	-46	14	02.54	11.3	10.4	88.1	0.333	1
0868	1	16	34.580	-45	54	03.28	12.5	8.5	-22.3	0.268	1
0869	1	16	34.713	-46	17	42.84	11.9	9.0	7.1	0.927	1
0870	1	16	35.385	-45	41	01.82	16.9	10.8	-85.4	0.486	1
0871	1	16	35.533	-45	55	32.64	12.0	8.6	-3.3	1.665	1
0872	1	16	35.857	-46	16	42.84	9.8	8.0	15.9	0.371	1
0873	1	16	36.666	-45	46	17.90	12.3	8.6	3.6	0.217	1
0874	1	16	36.706	-45	30	10.67	16.7	11.0	-65.5	0.583	1
0875	1	16	36.870	-46	22	23.10	15.8	9.9	-50.5	0.435	1
0876	1	16	39.443	-45	01	45.86	14.8	11.2	17.0	0.906	1
0877	1	16	40.194	-46	37	02.52	10.8	7.5	-44.8	0.666	1
0878	1	16	40.313	-46	16	22.44	14.9	8.2	-10.4	0.308	1
0879	1	16	40.665	-45	40	54.95	15.0	9.7	16.0	1.299	1
0880	1	16	41.070	-46	19	52.72	11.1	8.6	10.9	0.190	1
0881	1	16	41.489	-45	40	43.74	12.8	9.5	12.6	2.150	1
0882	1	16	42.972	-46	37	28.17	10.4	7.7	-13.4	2.342	1
0883	1	16	44.571	-45	56	39.02	11.5	8.4	-17.4	1.141	1

continued from previous page

	α			δ			bmaj	bmin	pa	$S_{1.4}$	sample
0884	1	16	44.776	-45	01	53.74	11.4	7.9	-44.8	0.663	1
0885	1	16	45.008	-46	07	33.01	13.2	9.1	-4.7	0.255	1
0886	1	16	46.308	-45	38	02.12	18.6	10.1	8.6	0.443	1
0887	1	16	46.417	-46	27	15.24	10.5	7.9	-14.9	0.364	1
0888	1	16	47.757	-46	34	57.40	22.1	17.0	-1.7	1.828	1
0889	1	16	48.437	-45	50	37.54	13.3	11.6	19.7	0.491	1
0890	1	16	48.473	-45	07	36.60	14.7	10.7	-22.7	20.022	1
0891	1	16	51.905	-45	31	19.35	12.8	6.9	-21.9	0.384	1
0892	1	16	52.035	-45	56	11.00	13.8	10.3	-15.4	0.474	1
0893	1	16	53.841	-45	00	09.24	15.8	9.7	5.6	1.726	1
0894	1	16	54.115	-46	14	31.89	18.6	11.0	-12.8	0.340	1
0895	1	16	54.700	-44	58	36.52	11.8	9.8	2.6	2.186	1
0896	1	16	55.053	-46	28	45.52	10.8	7.8	-19.6	0.343	1
0897	1	16	55.560	-45	54	07.57	15.0	9.6	-5.3	0.646	1
0898	1	16	56.475	-45	08	26.87	11.1	8.7	-3.0	2.347	1
0899	1	16	57.378	-45	48	01.86	16.5	8.7	38.1	0.307	1
0900	1	16	57.470	-45	47	36.11	13.4	11.4	-48.9	0.237	1
0901	1	16	57.684	-44	54	46.58	8.5	7.7	22.6	37.168	1
0902	1	16	57.695	-45	31	11.29	12.0	9.7	-82.7	0.468	1
0903	1	16	57.758	-45	54	58.26	9.8	8.5	2.4	0.424	1
0904	1	16	59.300	-45	57	24.24	12.4	8.6	-4.2	1.210	1
0905	1	17	00.151	-46	05	01.51	12.0	9.4	5.0	0.677	1
0906	1	17	00.752	-45	58	10.72	11.0	8.0	-18.5	0.908	1
0907	1	17	01.699	-45	45	48.24	12.8	9.9	-12.9	0.244	1
0908	1	17	02.536	-45	25	24.74	15.3	13.7	53.2	0.693	1
0909	1	17	03.365	-46	24	32.36	17.7	10.0	-34.4	2.478	1
0910	1	17	03.539	-46	06	33.62	12.7	8.7	14.1	0.360	1
0911	1	17	03.726	-46	32	51.22	9.5	7.5	-16.5	1.323	1
0912	1	17	04.292	-45	39	22.63	10.2	8.3	-10.8	0.553	1
0913	1	17	05.987	-46	03	26.06	9.9	9.5	33.6	0.498	1
0914	1	17	06.051	-45	10	01.23	11.9	9.7	-2.8	0.577	1
0915	1	17	06.414	-46	12	22.79	12.5	10.4	45.8	0.420	1
0916	1	17	06.658	-46	35	28.47	13.5	9.9	-16.3	0.861	1
0917	1	17	06.963	-46	23	24.59	9.2	8.2	-19.1	1.189	1
0918	1	17	07.196	-45	16	07.26	12.4	6.4	41.3	0.350	1
0919	1	17	07.805	-46	04	16.18	13.1	10.7	-43.4	0.358	1
0920	1	17	08.663	-46	27	13.10	16.5	9.5	8.7	0.877	1
0921	1	17	10.530	-45	57	39.57	14.3	12.4	-21.5	2.709	1
0922	1	17	10.837	-45	24	27.71	10.0	7.6	-6.2	1.046	1
0923	1	17	11.366	-46	04	39.71	6.3	5.9	-15.0	0.189	1
0924	1	17	11.441	-45	32	46.03	8.7	7.4	58.1	0.372	1

continued from previous page

	α			δ			bmaj	bmin	pa	$S_{1.4}$	sample
0925	1	17	11.548	-45	57	46.96	13.2	10.4	-44.7	3.107	1
0926	1	17	13.894	-46	22	29.88	13.6	8.2	-11.0	0.350	1
0927	1	17	14.146	-45	58	09.95	18.2	11.9	-23.8	1.044	1
0928	1	17	15.754	-45	37	55.96	17.4	10.6	-7.7	0.552	1
0929	1	17	16.754	-44	55	55.34	8.9	7.8	-13.6	2.856	1
0930	1	17	17.083	-46	27	51.92	12.2	8.4	-9.6	0.606	1
0931	1	17	17.230	-45	02	58.45	10.9	7.7	87.6	0.854	1
0932	1	17	17.412	-46	25	17.31	11.0	6.4	14.8	0.261	1
0933	1	17	17.501	-45	37	54.83	12.2	7.5	-26.1	0.363	1
0934	1	17	18.424	-46	05	55.04	12.3	8.5	35.4	0.264	1
0935	1	17	19.433	-45	59	59.04	12.7	10.3	-25.1	0.728	1
0936	1	17	20.766	-44	59	24.45	15.2	8.9	-71.0	18.927	1
0937	1	17	22.207	-45	33	07.75	17.0	12.4	-26.3	0.722	1
0938	1	17	22.276	-45	46	48.37	11.1	8.6	1.4	0.607	1
0939	1	17	22.587	-45	50	22.38	12.0	8.1	-73.4	0.336	1
0940	1	17	23.278	-45	06	36.42	8.9	8.0	29.3	0.597	1
0941	1	17	24.322	-44	56	47.68	16.3	10.4	81.4	1.968	1
0942	1	17	24.492	-45	01	38.21	15.2	10.3	-86.9	2.177	1
0943	1	17	25.207	-46	05	48.90	14.5	10.4	57.2	0.951	1
0944	1	17	26.118	-45	16	45.22	9.6	7.2	-10.0	2.315	1
0945	1	17	26.947	-45	28	15.67	9.9	9.2	18.4	0.435	1
0946	1	17	30.556	-46	06	39.76	13.3	8.9	-12.5	1.012	1
0947	1	17	31.168	-45	38	20.37	10.2	8.2	-8.5	0.389	1
0948	1	17	32.444	-46	18	41.26	10.2	8.7	-4.9	0.597	1
0949	1	17	32.524	-46	21	33.55	11.8	9.1	-18.2	1.846	1
0950	1	17	32.882	-46	11	26.44	9.9	8.3	-11.8	0.350	1
0951	1	17	33.586	-46	14	48.36	16.0	8.0	-5.9	0.254	1
0952	1	17	34.732	-44	59	30.50	16.8	8.4	86.0	1.114	1
0953	1	17	34.880	-46	17	50.73	14.3	13.8	73.5	0.338	1
0954	1	17	35.375	-46	21	34.93	13.0	9.7	18.4	0.371	1
0955	1	17	35.558	-45	28	57.68	19.0	10.9	5.8	0.647	1
0956	1	17	36.031	-45	39	32.55	15.1	13.2	73.2	0.538	1
0957	1	17	37.560	-45	33	47.90	12.5	9.1	-30.5	9.460	1
0958	1	17	37.637	-46	21	32.90	11.9	10.3	-41.1	1.024	1
0959	1	17	37.674	-46	18	00.12	21.9	10.4	-21.0	0.429	1
0960	1	17	37.873	-46	10	56.34	8.2	6.9	25.5	0.198	1
0961	1	17	41.281	-45	50	55.67	12.3	10.6	16.5	0.336	1
0962	1	17	41.704	-46	11	03.58	9.8	7.2	-7.7	0.407	1
0963	1	17	41.747	-45	32	51.31	13.8	8.5	-7.9	0.600	1
0964	1	17	42.498	-46	24	15.56	14.2	7.4	68.6	0.377	1
0965	1	17	44.260	-45	53	34.97	12.0	10.5	-79.3	0.443	1

continued from previous page

	α			δ			bmaj	bmin	pa	$S_{1.4}$	sample
0966	1	17	45.280	-46	22	31.43	15.1	9.5	-19.5	0.810	1
0967	1	17	52.376	-46	14	42.76	11.0	8.1	11.3	0.679	1
0968	1	17	52.395	-45	45	13.28	13.7	12.3	59.9	2.222	1
0969	1	17	52.660	-45	31	03.51	14.4	12.8	-84.9	1.056	1
0970	1	17	53.414	-45	28	14.84	9.5	8.8	60.4	1.068	1
0971	1	17	54.528	-45	43	49.58	13.8	9.6	-82.9	1.594	1
0972	1	17	54.932	-45	32	09.42	0.0	0.0	0.0	17.477	1
0973	1	17	54.983	-45	51	24.62	11.0	9.3	-19.4	0.347	1
0974	1	17	55.158	-45	52	59.08	9.4	8.6	-17.5	0.651	1
0975	1	17	55.161	-45	42	07.30	13.4	12.8	11.6	1.477	1
0976	1	17	55.958	-45	42	09.23	32.3	12.2	-86.3	2.426	1
0977	1	17	56.518	-45	33	43.69	10.8	8.6	-31.1	0.554	1
0978	1	17	57.298	-45	14	28.23	9.6	8.6	-64.5	0.756	1
0979	1	17	57.631	-45	39	33.88	8.9	8.3	-29.3	0.984	1
0980	1	17	59.365	-45	17	50.25	16.3	13.3	-76.0	0.766	1
0981	1	18	00.904	-45	38	31.90	11.2	9.5	55.3	4.121	1
0982	1	18	00.942	-45	39	54.03	12.6	8.6	70.2	1.071	1
0983	1	18	01.898	-45	26	43.66	12.9	9.5	-13.1	0.672	1
0984	1	18	02.611	-45	46	12.80	10.2	8.7	18.7	0.561	1
0985	1	18	03.054	-45	39	49.94	27.0	11.9	-88.8	1.840	1
0986	1	18	04.130	-46	04	45.46	10.5	9.1	3.8	0.555	1
0987	1	18	04.612	-45	58	08.09	10.7	10.0	47.6	1.389	1
0988	1	18	05.128	-45	57	13.32	10.5	9.1	-44.4	9.544	1
0989	1	18	06.788	-45	19	02.67	11.4	10.3	-63.5	1.097	1
0990	1	18	07.134	-46	09	06.28	13.2	10.1	41.9	0.306	1
0991	1	18	07.243	-45	16	51.14	20.7	8.8	-14.2	0.541	1
0992	1	18	07.314	-46	21	21.59	12.7	7.8	-64.2	0.420	1
0993	1	18	07.611	-45	34	46.09	12.1	10.5	66.0	0.368	1
0994	1	18	08.349	-45	45	41.65	0.0	0.0	0.0	7.495	1
0995	1	18	10.132	-46	14	31.37	10.9	8.6	-17.9	1.947	1
0996	1	18	10.333	-45	16	49.25	14.1	9.3	-70.1	0.461	1
0997	1	18	10.366	-45	34	22.23	25.1	13.1	76.6	1.500	1
0998	1	18	10.453	-45	28	34.55	13.2	9.5	25.0	0.529	1
0999	1	18	12.027	-46	10	00.19	12.9	12.3	37.3	2.008	1
1000	1	18	12.166	-45	45	15.28	28.5	16.6	-4.6	2.574	1
1001	1	18	12.196	-45	45	21.02	32.8	13.9	8.1	2.894	1
1002	1	18	12.875	-45	56	08.80	17.5	11.6	-35.5	0.573	1
1003	1	18	13.522	-46	15	06.73	14.4	8.9	-6.6	2.548	1
1004	1	18	13.829	-46	15	32.67	59.5	10.2	-4.6	6.695	1
1005	1	18	13.896	-46	15	38.22	45.5	9.6	-3.9	5.638	1
1006	1	18	13.957	-46	23	37.98	10.0	8.1	-23.0	0.385	1

continued from previous page

	α			δ			bmaj	bmin	pa	$S_{1.4}$	sample
1007	1	18	14.132	-45	28	37.42	17.5	14.7	56.1	0.213	1
1008	1	18	16.454	-45	19	47.42	10.3	8.8	-14.7	0.882	1
1009	1	18	16.534	-45	51	21.49	9.9	9.2	70.6	0.628	1
1010	1	18	17.251	-46	25	22.63	11.3	8.9	-27.6	0.865	1
1011	1	18	17.971	-46	17	10.73	10.6	7.7	-5.6	0.357	1
1012	1	18	19.279	-45	27	19.05	9.8	8.8	5.5	2.308	1
1013	1	18	20.226	-46	11	41.92	14.7	8.1	82.5	0.304	1
1014	1	18	20.708	-45	39	39.15	9.9	9.1	-27.5	23.760	1
1015	1	18	23.069	-45	27	39.55	12.8	10.0	10.0	3.821	1
1016	1	18	23.231	-45	28	05.32	11.5	8.8	-22.0	3.455	1
1017	1	18	23.422	-46	16	22.02	11.4	8.5	-16.0	1.217	1
1018	1	18	23.668	-45	33	39.32	16.2	9.4	-58.0	0.879	1
1019	1	18	27.887	-46	06	48.86	12.8	12.0	57.5	0.518	1
1020	1	18	28.459	-46	12	12.65	10.1	8.3	-15.4	1.137	1
1021	1	18	29.902	-46	04	42.88	14.7	8.5	86.5	0.432	1
1022	1	18	30.381	-45	31	21.57	15.3	10.7	-21.8	1.189	1
1023	1	18	31.157	-45	48	14.84	11.5	10.2	-45.5	1.390	1
1024	1	18	31.213	-45	35	04.27	9.7	8.7	-37.5	6.286	1
1025	1	18	34.206	-45	36	31.27	19.7	12.9	-66.5	3.342	1
1026	1	18	34.825	-46	05	29.93	15.5	8.8	-8.0	0.975	1
1027	1	18	34.979	-45	48	49.12	10.5	9.4	-32.8	122.569	1
1028	1	18	35.777	-45	12	16.41	13.1	9.0	-82.0	1.846	1
1029	1	18	36.603	-45	36	24.19	15.1	9.3	80.2	1.506	1
1030	1	18	36.681	-45	09	39.94	12.5	7.4	67.6	1.030	1
1031	1	18	37.639	-46	09	32.25	14.3	10.4	-11.5	0.669	1
1032	1	18	37.748	-46	20	45.92	11.2	9.0	-22.8	6.388	1
1033	1	18	38.316	-45	23	03.93	12.9	11.7	89.4	1.697	1
1034	1	18	38.548	-45	49	25.45	25.4	7.8	-88.2	7.228	1
1035	1	18	38.725	-45	49	22.78	10.2	9.3	55.9	9.051	1
1036	1	18	39.385	-45	26	58.09	9.6	8.8	-20.9	67.137	1
1037	1	18	39.414	-45	25	39.03	9.8	8.6	-34.8	0.385	1
1038	1	18	41.082	-46	01	15.37	14.2	9.4	-72.5	0.381	1
1039	1	18	41.138	-45	36	30.37	16.8	13.3	-53.9	3.345	1
1040	1	18	42.943	-45	46	43.31	13.0	10.3	-41.2	0.551	1
1041	1	18	45.679	-46	18	47.90	13.8	8.4	-37.3	1.329	1
1042	1	18	47.883	-45	59	52.08	18.9	9.3	-83.2	1.770	1
1043	1	18	49.241	-45	57	55.64	29.4	14.2	-11.8	3.388	1
1044	1	18	52.656	-45	35	53.19	13.7	10.0	47.2	80.533	1
1045	1	18	54.069	-45	45	05.78	9.9	9.5	-50.5	3.515	1
1046	1	18	56.161	-45	42	49.52	9.6	8.5	-31.3	2.882	1
1047	1	18	58.839	-45	56	11.89	9.0	8.8	-29.4	0.732	1

continued from previous page

	α			δ			bmaj	bmin	pa	$S_{1.4}$	sample
1048	1	19	00.527	-46	05	44.99	17.1	14.6	-89.0	0.343	1
1049	1	19	01.049	-46	03	14.20	11.4	10.4	-54.5	1.924	1
1050	1	19	03.858	-45	50	40.68	14.3	8.1	82.6	1.092	1
1051	1	19	06.267	-45	38	45.65	21.5	13.7	-8.8	0.283	1
1052	1	19	06.711	-45	30	03.64	13.0	10.0	-62.7	1.185	1
1053	1	19	09.229	-45	29	09.73	9.7	8.9	-16.7	5.525	1
1054	1	19	09.404	-46	01	36.01	9.8	9.1	-20.6	19.095	1
1055	1	19	09.852	-45	30	15.52	10.4	10.0	-42.7	1.279	1
1056	1	19	11.193	-45	39	51.98	15.8	10.5	10.0	0.678	1
1057	1	19	12.189	-45	43	33.46	16.2	11.3	-65.4	0.755	1
1058	1	19	13.780	-45	42	03.10	9.6	8.5	-17.8	3.938	1
1059	1	19	14.079	-46	10	40.99	36.2	9.6	-6.2	6.940	1
1060	1	19	17.626	-45	31	38.91	11.6	9.5	-27.9	1.073	1
1061	1	19	17.801	-45	50	19.24	10.2	8.4	-21.6	2.791	1
1062	1	19	19.597	-45	34	30.00	12.3	10.2	83.5	0.902	1
1063	1	19	19.831	-45	46	28.69	8.9	7.8	-7.0	1.084	1
1064	1	19	21.592	-45	50	18.07	10.2	8.2	-9.9	2.037	1
1065	1	19	25.463	-45	29	45.01	12.7	11.3	-13.2	13.817	1
1066	1	19	25.782	-45	43	39.08	12.2	9.3	40.9	3.154	1
1067	1	19	26.050	-45	49	39.01	17.3	13.8	1.8	1.418	1
1068	1	19	26.062	-45	52	37.45	9.8	8.5	-8.6	3.671	1
1069	1	19	30.555	-45	38	30.85	25.5	13.3	-72.1	1.746	1
1070	1	19	31.853	-45	23	20.88	13.0	9.5	-80.0	0.694	1
1071	1	19	32.113	-45	49	03.32	10.2	9.1	44.5	1.571	1
1072	1	19	32.465	-45	49	34.42	17.5	9.7	18.1	6.165	1
1073	1	19	34.634	-45	37	29.91	13.9	9.9	-64.0	0.882	1
1074	1	19	38.948	-45	30	30.53	17.1	11.2	-77.9	0.875	1
1075	1	19	40.908	-45	45	05.16	9.4	8.6	-28.7	9.051	1
1076	1	19	46.820	-45	30	55.83	10.7	8.1	-65.3	0.357	1
1077	1	19	52.164	-45	39	21.62	11.9	9.8	-87.3	0.743	1
1078	1	19	52.754	-45	40	20.88	11.1	8.4	-5.0	0.692	1
1079	1	19	54.934	-45	42	54.04	13.2	11.4	-58.4	0.766	1

Column descriptions:

1. Catalogue number
2–7. Radio source position
8–9. Major and minor axes convolved with beam
10. Position angle in degrees
11. Flux density in mJy
12. 1: Object detected in PDF only; 2: Object detected in PDFS only
    3: Object detected in both PDF and PDFS

Appendix B

Optical IDs

Table B.1 : Optical IDs for radio sources.

	α			δ			class	F	dist	m_R
0002	1	8	33.14	-45	45	43.6	g	0.000	0.178	19.994
0003	1	8	33.74	-45	50	18.6	g	0.039	4.743	20.685
0004	1	8	37.22	-45	48	21.2	g	0.000	1.567	15.865
0005	1	8	37.56	-45	52	57.0	g	0.000	0.485	19.726
0006	1	8	38.98	-45	52	45.1	g	0.001	0.811	21.097
0008	1	8	39.31	-45	56	56.0	g	0.000	0.225	17.169
0010	1	8	44.81	-46	2	58.6	g	0.007	2.446	19.991
0011	1	8	46.63	-45	55	1.9	g	0.003	3.056	17.767
0012	1	8	49.99	-45	38	58.9	g	9.999	4.861	21.394
0014	1	8	51.17	-45	33	6.8	g	0.001	0.452	21.869
0016	1	8	53.93	-45	58	39.4	g	0.000	0.762	18.195
0018	1	8	56.54	-45	42	16.2	g	0.001	0.598	20.539
0019	1	9	0.01	-45	20	53.0	g	0.000	1.321	
0022	1	9	4.56	-45	46	23.2	g	0.000	1.555	12.670
0024	1	9	7.32	-45	41	44.5	g	0.003	1.633	19.975
0025	1	9	8.45	-46	11	50.6	g	0.004	1.757	20.472
0029	1	9	10.01	-46	13	0.1	g	0.003	1.405	20.660
0030	1	9	11.69	-46	2	8.9	g	0.000	0.854	17.501
0031	1	9	13.42	-45	34	16.7	g	0.001	1.449	17.820
0032	1	9	13.73	-45	44	1.0	s	0.033	4.741	20.358
0033	1	9	13.56	-45	53	23.3	g	0.001	0.876	19.838
0036	1	9	18.86	-45	59	24.0	f	0.029	3.006	21.821
0039	1	9	27.22	-45	28	16.7	g	0.002	1.069	20.799
0041	1	9	29.26	-45	25	51.6	f	0.015	1.790	22.488
0044	1	9	33.19	-45	48	24.5	g	0.001	1.418	18.770
0045	1	9	33.84	-45	31	14.9	g	0.011	2.714	20.440
0046	1	9	33.84	-45	31	14.9	g	0.000	0.533	20.440

continued from previous page

	α			δ			class	F	dist	m_R
0047	1	9	38.90	-45	39	28.8	g	0.008	2.811	19.887
0048	1	9	39.36	-45	51	14.8	g	0.005	1.173	21.755
0051	1	9	46.37	-45	50	2.4	g	0.002	1.231	20.232
0052	1	9	46.78	-45	46	57.7	g	0.000	2.285	14.490
0053	1	9	46.75	-45	32	52.8	s	0.002	0.864	21.335
0054	1	9	47.95	-45	51	24.8	g	0.000	0.747	14.983
0055	1	9	49.15	-45	40	31.1	g	0.000	0.163	20.885
0056	1	9	49.85	-45	27	38.5	f	0.009	1.159	23.062
0058	1	9	50.16	-45	46	28.6	g	0.002	1.924	18.342
0059	1	9	50.83	-45	56	24.7	g	0.008	3.648	19.147
0062	1	9	55.51	-45	55	50.2	g	0.000	1.303	12.215
0066	1	9	56.30	-45	44	11.8	s	0.021	4.941	19.594
0068	1	9	56.95	-46	21	59.0	g	0.011	2.421	20.757
0070	1	9	57.60	-45	34	57.4	g	0.000	0.446	19.210
0083	1	10	6.24	-45	21	51.8	g	0.033	4.567	20.626
0084	1	10	6.26	-46	21	11.2	g	0.008	1.701	21.602
0086	1	10	7.66	-45	13	16.0	g	0.006	1.256	21.940
0089	1	10	8.90	-45	30	20.9	s	0.003	1.566	20.077
0090	1	10	9.79	-45	30	59.8	s	0.000	0.435	19.022
0099	1	10	15.19	-46	15	8.6	f	0.001	0.498	22.123
0100	1	10	15.41	-46	14	14.6	g	0.000	0.265	21.551
0101	1	10	15.50	-45	13	37.9	g	0.003	1.259	20.950
0104	1	10	16.15	-45	47	32.6	g	0.001	1.236	19.610
0107	1	10	18.05	-45	49	7.7	g	0.013	2.483	21.120
0111	1	10	20.98	-45	11	44.5	g	0.010	1.852	21.637
0112	1	10	21.31	-45	46	26.0	f	0.001	0.535	22.082
0113	1	10	21.12	-46	20	41.3	g	0.026	7.696	18.527
0116	1	10	23.66	-45	3	35.6	g	0.012	3.369	19.802
0122	1	10	27.79	-45	22	55.2	g	0.000	0.774	17.717
0125	1	10	29.52	-46	10	28.6	g	0.000	1.298	15.517
0126	1	10	30.34	-45	48	56.2	g	0.036	6.570	19.577
0127	1	10	30.19	-45	31	14.2	s	0.000	0.137	17.040
0129	1	10	31.20	-46	19	37.6	s	0.048	9.864	18.659
0131	1	10	32.09	-45	42	50.8	g	0.006	4.106	18.175
0134	1	10	32.50	-45	40	4.4	g	0.000	0.603	20.106
0135	1	10	32.54	-45	54	5.0	g	0.000	0.424	17.993
0138	1	10	33.62	-45	40	21.4	g	0.000	0.332	18.952
0139	1	10	33.48	-45	50	15.7	g	0.019	7.095	18.198
0140	1	10	34.22	-45	51	19.4	g	0.009	2.292	20.533
0145	1	10	38.16	-45	38	19.3	g	0.000	0.515	17.286
0146	1	10	38.45	-45	50	40.2	f	0.002	0.674	22.335

continued from previous page

	α			δ			class	F	dist	m_R
0149	1	10	42.12	-46	20	34.4	s	0.000	9.635	11.118
0150	1	10	42.05	-45	16	9.8	g	0.033	5.576	19.953
0154	1	10	44.18	-45	51	23.0	g	0.002	1.221	19.983
0155	1	10	45.19	-45	6	46.8	g	0.001	0.553	21.686
0157	1	10	46.61	-45	41	40.9	g	0.000	0.419	16.320
0160	1	10	47.09	-45	16	17.0	s	0.003	5.403	15.557
0162	1	10	48.02	-46	20	38.0	f	0.029	2.116	22.948
0164	1	10	49.44	-45	4	7.7	g	0.041	3.087	21.929
0166	1	10	50.59	-46	20	22.2	f	0.010	1.659	22.031
0167	1	10	51.98	-45	43	40.4	s	0.004	2.076	19.761
0168	1	10	52.18	-45	33	54.0	g	0.000	0.722	18.544
0169	1	10	52.18	-45	33	54.0	g	0.010	4.553	18.544
0170	1	10	53.14	-46	7	0.8	g	0.000	0.394	16.027
0172	1	10	53.83	-45	43	39.0	f	0.000	0.215	22.461
0173	1	10	55.08	-45	6	36.7	g	0.013	4.668	19.029
0176	1	10	55.85	-45	39	19.1	g	0.000	1.209	15.697
0177	1	10	56.38	-46	9	44.3	g	0.005	2.399	19.720
0179	1	10	57.10	-45	52	11.3	g	0.001	0.776	21.422
0180	1	10	57.22	-45	4	35.4	g	0.023	2.511	21.808
0183	1	10	58.92	-45	38	12.1	g	0.000	0.311	21.575
0188	1	11	0.46	-46	19	10.2	g	0.003	1.206	21.015
0191	1	11	1.54	-46	0	18.7	g	0.003	1.539	20.262
0192	1	11	1.73	-45	41	57.5	g	0.000	0.906	18.951
0194	1	11	2.88	-46	18	29.5	g	0.029	9.033	18.031
0197	1	11	2.95	-46	27	42.8	g	0.006	2.273	20.060
0201	1	11	5.28	-45	38	48.8	g	0.003	1.347	20.748
0203	1	11	6.07	-45	49	18.5	g	0.000	0.116	17.724
0208	1	11	7.78	-45	52	13.8	g	0.029	3.345	21.553
0212	1	11	8.83	-45	36	22.3	g	0.000	1.091	17.133
0216	1	11	10.13	-46	10	11.3	g	0.007	4.364	18.479
0220	1	11	12.65	-45	51	13.0	g	0.002	1.093	20.927
0226	1	11	14.98	-45	32	13.6	g	0.001	1.432	18.697
0228	1	11	16.08	-46	9	37.8	g	0.007	2.653	19.929
0230	1	11	15.79	-45	43	41.5	g	0.025	3.446	21.082
0232	1	11	17.14	-45	4	1.2	f	0.005	1.060	22.224
0235	1	11	19.30	-45	55	55.7	g	0.000	2.761	
0237	1	11	20.57	-46	19	14.5	g	0.002	1.037	20.775
0239	1	11	21.24	-45	44	30.5	g	0.000	0.515	19.901
0242	1	11	21.89	-45	4	25.3	f	0.001	0.467	22.287
0244	1	11	22.30	-46	10	13.4	g	0.001	0.747	20.684
0245	1	11	22.56	-45	39	59.4	g	0.001	0.712	21.318

continued from previous page

		α			δ		class	F	dist	m_R
0248	1	11	23.62	-45	43	43.3	g	0.000	0.344	20.127
0252	1	11	25.30	-45	54	1.6	s	0.026	8.528	
0256	1	11	26.33	-45	38	14.6	g	0.000	0.398	18.411
0257	1	11	26.30	-45	30	16.6	g	0.001	0.898	19.734
0258	1	11	26.90	-45	34	16.3	g	0.001	1.681	18.575
0260	1	11	27.12	-45	41	52.1	f	0.013	1.513	23.085
0262	1	11	27.55	-45	49	46.2	g	0.000	0.543	18.743
0263	1	11	27.58	-45	48	14.8	g	0.000	0.659	18.554
0264	1	11	28.58	-45	54	9.7	g	0.001	1.050	20.169
0266	1	11	29.59	-45	52	43.0	s	0.005	1.518	21.214
0267	1	11	30.72	-45	50	27.6	s	0.046	6.775	19.916
0270	1	11	30.34	-45	37	27.5	s	0.052	4.970	20.919
0273	1	11	31.44	-45	50	15.4	g	0.000	0.638	17.687
0276	1	11	32.28	-46	24	20.2	f	0.009	1.587	22.044
0279	1	11	33.00	-45	17	56.8	g	0.002	2.604	17.706
0280	1	11	32.74	-45	8	8.2	f	9.999	2.642	23.030
0281	1	11	33.31	-45	59	51.0	f	0.014	1.430	23.098
0284	1	11	33.70	-45	7	33.6	f	0.006	1.013	22.871
0285	1	11	34.08	-45	46	8.8	g	0.001	0.988	19.409
0286	1	11	35.11	-45	32	44.9	g	0.000	0.295	15.961
0287	1	11	36.19	-45	34	24.6	g	0.000	0.457	18.973
0288	1	11	36.41	-45	42	49.3	g	0.005	2.430	19.682
0289	1	11	36.58	-46	33	9.7	s	0.030	4.752	20.231
0295	1	11	37.63	-45	45	24.5	f	0.006	0.993	23.027
0297	1	11	37.73	-46	33	38.9	f	0.027	2.664	21.912
0298	1	11	38.18	-45	32	49.2	g	0.000	0.959	18.516
0299	1	11	38.35	-45	33	57.2	g	0.000	0.391	20.783
0301	1	11	38.66	-45	38	48.1	s	0.016	6.886	18.001
0303	1	11	39.50	-45	16	17.4	g	0.013	4.655	19.121
0305	1	11	40.01	-45	39	6.5	g	0.003	2.465	18.496
0306	1	11	40.27	-45	47	12.8	s	0.000	0.513	18.976
0310	1	11	42.43	-45	40	24.6	g	0.024	5.876	19.267
0313	1	11	44.38	-45	37	0.5	g	0.047	4.933	20.838
0316	1	11	44.69	-45	52	11.6	g	0.000	0.686	18.750
0317	1	11	46.27	-46	21	10.1	f	0.003	0.700	22.390
0318	1	11	47.30	-45	40	19.2	g	0.044	9.563	19.050
0320	1	11	47.09	-45	40	27.1	f	0.032	2.263	23.390
0326	1	11	48.36	-45	58	31.1	f	0.024	2.339	22.076
0327	1	11	49.63	-45	42	6.8	g	0.000	0.228	20.990
0328	1	11	49.63	-45	54	14.0	g	0.005	1.342	21.189
0329	1	11	50.14	-45	37	26.8	g	0.000	0.734	19.304

continued from previous page

	α			δ			class	F	dist	m_R
0332	1	11	51.24	-45	2	15.0	g	0.001	2.023	18.089
0333	1	11	51.48	-45	35	20.8	g	0.018	3.297	20.663
0334	1	11	51.50	-45	44	43.8	g	0.004	1.205	21.166
0340	1	11	52.66	-45	40	17.4	g	0.006	6.954	16.490
0341	1	11	52.78	-45	54	20.2	g	0.047	7.775	19.417
0342	1	11	53.33	-45	4	31.8	s	0.002	2.977	17.440
0343	1	11	53.42	-45	58	46.2	g	0.001	1.278	18.587
0344	1	11	54.14	-45	30	39.2	g	0.000	0.525	19.136
0345	1	11	54.26	-45	54	9.4	g	0.000	0.925	18.201
0346	1	11	54.62	-45	46	39.0	g	0.001	1.048	20.146
0347	1	11	54.82	-45	27	32.8	g	0.004	2.972	18.625
0348	1	11	55.27	-45	42	14.0	g	0.001	1.539	17.995
0351	1	11	56.88	-44	54	51.5	s	0.001	2.009	18.114
0352	1	11	56.69	-45	47	54.6	g	0.000	0.380	20.217
0355	1	11	57.38	-46	25	17.0	g	0.011	2.256	20.976
0356	1	11	58.01	-46	8	49.9	s	0.014	8.417	16.876
0358	1	11	58.70	-45	52	10.2	g	0.001	0.743	20.232
0360	1	11	59.04	-45	9	40.3	f	0.003	0.764	22.755
0361	1	12	0.02	-45	33	55.8	f	0.003	0.729	22.409
0363	1	12	2.04	-45	39	46.8	g	0.003	1.652	20.109
0366	1	12	4.18	-45	58	47.6	f	0.028	2.288	22.486
0367	1	12	4.20	-45	59	15.7	g	0.004	1.722	20.294
0369	1	12	4.61	-45	44	48.1	g	0.000	0.555	18.311
0373	1	12	6.00	-45	46	27.1	s	0.009	3.625	19.283
0374	1	12	6.67	-44	49	44.0	g	0.002	3.252	16.678
0376	1	12	7.94	-45	48	38.5	f	0.001	0.304	22.799
0378	1	12	8.40	-45	54	1.8	f	0.014	1.411	23.396
0379	1	12	8.35	-45	34	23.2	f	0.041	2.435	23.173
0382	1	12	10.70	-46	34	55.2	g	0.000	1.009	17.535
0384	1	12	10.32	-46	7	13.1	g	0.012	9.715	16.158
0386	1	12	11.30	-45	37	44.0	f	0.000	0.267	22.493
0387	1	12	12.14	-45	40	51.2	g	0.001	1.007	19.856
0390	1	12	12.79	-46	5	55.3	g	0.024	5.052	19.694
0392	1	12	13.06	-45	40	17.8	f	0.001	0.558	22.035
0394	1	12	14.42	-45	8	43.8	s	0.032	3.786	21.281
0395	1	12	15.17	-46	23	39.8	g	0.000	0.510	17.980
0396	1	12	15.43	-45	36	14.8	g	0.004	1.124	21.522
0398	1	12	16.46	-45	45	19.1	g	0.001	1.658	18.487
0400	1	12	17.06	-45	43	5.5	f	0.005	1.039	22.326
0401	1	12	17.45	-46	29	32.3	f	0.007	1.175	22.508
0402	1	12	17.64	-44	58	37.6	g	0.002	0.869	20.942

continued from previous page

	α			δ			class	F	dist	m_R
0403	1	12	17.90	-46	39	34.9	f	0.036	2.670	22.666
0404	1	12	17.90	-45	51	22.7	f	0.001	0.391	22.010
0405	1	12	19.01	-45	37	49.4	f	0.076	4.250	22.030
0408	1	12	19.75	-45	53	22.6	g	0.001	2.792	18.214
0409	1	12	20.21	-46	37	17.0	g	0.001	0.935	19.395
0410	1	12	20.66	-45	39	48.6	g	0.004	2.580	19.200
0412	1	12	22.37	-46	17	38.8	f	0.017	1.981	22.136
0414	1	12	22.94	-45	31	25.0	f	0.003	0.685	22.950
0417	1	12	24.24	-44	55	34.3	g	0.000	0.931	16.037
0418	1	12	24.41	-44	54	27.7	f	0.004	0.725	23.951
0419	1	12	24.84	-45	52	33.6	g	0.002	1.595	19.785
0420	1	12	25.15	-45	46	59.9	g	0.000	0.295	18.413
0423	1	12	27.65	-45	32	8.5	s	0.004	6.507	15.609
0426	1	12	27.62	-45	58	50.5	f	0.012	1.590	22.254
0427	1	12	27.53	-46	17	17.9	f	0.019	1.620	22.855
0431	1	12	28.70	-45	50	0.2	g	0.001	0.790	20.576
0434	1	12	29.02	-46	23	49.9	g	0.001	1.379	18.241
0435	1	12	29.47	-45	53	55.7	s	0.020	7.414	18.132
0437	1	12	29.74	-44	53	38.0	g	0.000	0.751	19.257
0438	1	12	31.58	-44	58	36.8	g	0.000	1.336	16.100
0441	1	12	32.04	-46	5	57.1	s	0.000	0.426	20.036
0443	1	12	32.09	-45	8	34.4	g	0.017	4.084	19.852
0445	1	12	32.78	-45	47	58.9	g	0.003	1.203	21.002
0446	1	12	32.71	-45	51	38.5	f	0.036	2.767	22.642
0450	1	12	35.69	-44	55	6.2	g	0.027	4.208	20.621
0452	1	12	36.46	-45	18	42.8	g	0.000	1.028	17.734
0455	1	12	38.54	-46	26	47.8	g	0.001	0.979	20.251
0466	1	12	41.23	-46	3	23.8	g	0.001	0.928	19.437
0467	1	12	41.33	-45	25	28.2	g	0.004	2.087	19.746
0468	1	12	41.18	-45	52	25.7	f	0.000	0.194	21.804
0469	1	12	41.42	-46	3	58.3	g	0.049	4.661	21.104
0470	1	12	41.81	-45	37	6.6	g	0.002	2.277	17.901
0471	1	12	43.10	-46	30	54.7	f	0.002	0.737	21.995
0472	1	12	43.73	-45	37	44.0	g	0.001	1.251	18.506
0473	1	12	44.11	-45	0	34.6	g	0.001	0.900	20.284
0474	1	12	44.26	-45	33	15.1	g	0.001	0.460	21.220
0477	1	12	45.53	-46	28	57.0	f	0.013	1.691	22.444
0481	1	12	47.50	-46	13	22.1	g	0.019	3.254	20.860
0482	1	12	47.90	-45	44	50.6	g	0.000	0.585	18.367
0490	1	12	49.87	-44	55	26.0	g	0.007	1.624	21.725
0492	1	12	51.72	-46	23	37.7	g	0.007	1.629	21.227

continued from previous page

	α			δ			class	F	dist	m_R
0495	1	12	52.68	-45	43	44.8	g	0.000	0.170	15.234
0499	1	12	53.81	-46	27	20.5	f	0.008	1.244	22.879
0501	1	12	54.74	-45	58	37.9	f	0.023	1.911	22.604
0504	1	12	55.08	-45	33	54.0	g	0.001	0.513	21.858
0505	1	12	55.42	-45	59	7.1	g	0.005	2.271	19.620
0508	1	12	56.86	-45	44	7.4	g	0.031	4.343	20.580
0510	1	12	59.23	-46	27	40.7	f	0.032	2.383	22.542
0512	1	13	1.54	-46	24	36.0	f	0.000	0.182	21.908
0514	1	13	2.35	-45	22	37.9	f	0.003	0.813	22.174
0517	1	13	3.86	-45	30	9.0	g	0.000	0.811	16.375
0518	1	13	4.30	-46	21	5.0	f	0.018	1.644	23.221
0522	1	13	5.95	-46	26	3.5	g	0.000	0.795	17.137
0523	1	13	6.12	-46	10	4.4	g	0.028	4.452	20.374
0525	1	13	6.38	-45	34	35.4	g	0.002	0.773	21.818
0526	1	13	6.53	-45	12	58.7	s	0.017	3.460	20.383
0528	1	13	7.75	-45	6	3.2	g	0.000	0.837	17.722
0529	1	13	8.11	-45	57	49.7	g	0.003	1.880	19.733
0531	1	13	11.16	-45	14	34.1	g	0.035	5.361	20.046
0532	1	13	10.46	-44	50	5.6	s	0.023	9.766	17.372
0533	1	13	10.90	-45	1	45.8	g	0.000	2.870	17.444
0534	1	13	11.59	-45	42	59.8	f	0.001	0.346	23.404
0537	1	13	13.70	-46	1	57.0	g	0.000	0.895	16.026
0538	1	13	14.66	-45	37	0.8	g	0.000	0.777	18.969
0539	1	13	14.98	-46	6	5.0	s	0.048	5.402	20.581
0540	1	13	14.76	-45	40	51.2	f	0.001	0.419	22.165
0541	1	13	15.29	-45	45	23.8	g	0.009	2.109	21.089
0542	1	13	15.14	-44	55	2.3	f	0.014	1.917	22.129
0543	1	13	15.74	-45	22	0.5	f	0.023	2.009	22.616
0544	1	13	15.74	-44	59	18.6	g	0.001	1.727	17.399
0547	1	13	17.88	-45	33	21.6	f	0.000	0.275	22.204
0549	1	13	19.30	-45	45	30.2	g	0.003	1.004	21.752
0550	1	13	19.42	-45	26	11.8	s	0.000	0.045	21.626
0552	1	13	20.78	-44	51	6.8	f	0.022	2.029	23.032
0553	1	13	21.82	-46	12	36.4	g	0.220	9.289	21.342
0554	1	13	21.74	-45	44	39.1	s	0.003	5.200	15.778
0555	1	13	21.91	-45	38	4.6	f	0.050	2.852	22.573
0556	1	13	21.50	-46	40	7.7	g	0.023	3.259	21.202
0558	1	13	24.05	-46	11	26.9	g	0.047	9.856	18.633
0560	1	13	25.54	-46	15	29.9	g	0.008	4.592	18.184
0562	1	13	25.92	-45	49	10.6	g	0.003	3.300	17.739
0564	1	13	26.98	-46	24	22.0	g	0.001	1.437	18.069

continued from previous page

	α			δ			class	F	dist	m_R
0569	1	13	29.42	-46	43	3.7	g	0.011	3.012	20.036
0570	1	13	29.62	-45	37	18.8	g	0.025	3.179	21.277
0571	1	13	29.69	-45	56	32.6	g	0.009	1.839	21.625
0572	1	13	29.76	-45	45	33.8	g	0.007	2.027	20.746
0574	1	13	30.96	-45	21	21.6	g	0.000	0.827	18.290
0575	1	13	31.73	-46	2	7.1	g	0.000	0.961	15.890
0578	1	13	33.50	-45	38	41.3	g	0.000	0.832	18.455
0580	1	13	33.82	-46	18	34.9	f	0.002	0.586	23.014
0585	1	13	38.86	-45	2	58.9	s	0.021	3.602	20.624
0587	1	13	39.91	-45	4	48.0	g	0.004	2.378	19.288
0590	1	13	41.64	-44	48	5.4	g	0.002	1.240	20.467
0594	1	13	43.51	-45	6	58.3	f	0.015	1.467	23.453
0595	1	13	43.70	-45	56	17.5	g	0.011	2.936	20.288
0598	1	13	46.06	-45	40	19.9	s	0.015	3.579	20.077
0601	1	13	46.56	-46	4	40.8	s	0.015	7.427	17.514
0603	1	13	48.70	-45	50	19.0	g	0.000	1.505	16.251
0605	1	13	49.32	-45	40	50.5	s	0.002	1.532	20.039
0607	1	13	49.75	-46	15	52.6	s	0.005	7.587	15.234
0610	1	13	53.30	-44	53	35.2	g	0.000	0.901	16.357
0611	1	13	55.13	-45	27	16.6	g	0.000	0.853	15.531
0615	1	13	57.02	-45	47	31.9	s	0.014	6.440	17.933
0618	1	13	58.63	-45	4	1.2	g	0.037	7.015	19.500
0621	1	14	0.50	-45	47	52.8	g	0.003	2.358	19.586
0622	1	14	0.79	-45	48	46.8	g	0.001	1.300	19.405
0626	1	14	3.26	-45	52	23.2	g	0.036	5.127	20.383
0629	1	14	4.32	-45	45	2.5	g	0.010	1.631	21.986
0630	1	14	4.58	-45	50	47.4	f	0.012	1.818	22.116
0631	1	14	4.63	-45	57	0.7	g	0.001	1.322	19.736
0634	1	14	5.35	-46	15	11.5	g	0.000	0.772	15.490
0635	1	14	5.93	-45	6	50.4	g	0.004	3.553	17.667
0637	1	14	6.79	-45	54	19.4	g	0.044	6.226	20.234
0638	1	14	6.38	-45	20	46.7	s	0.010	1.809	21.966
0640	1	14	7.66	-45	14	48.1	g	0.000	0.613	15.568
0641	1	14	8.45	-44	56	49.9	g	0.000	1.584	17.806
0642	1	14	8.64	-45	28	57.0	f	0.030	2.155	23.041
0643	1	14	8.83	-44	48	50.4	g	0.000	1.002	16.174
0644	1	14	9.46	-45	32	44.2	g	0.002	1.218	20.121
0645	1	14	9.74	-45	46	3.7	f	0.029	2.109	23.228
0648	1	14	11.11	-46	3	21.6	g	0.014	2.997	20.514
0652	1	14	11.66	-46	17	33.4	g	0.000	1.030	15.624
0655	1	14	13.51	-45	4	18.5	s	0.016	6.071	18.436

continued from previous page

	α			δ			class	F	dist	m_R
0657	1	14	14.54	-46	42	43.9	g	0.000	0.566	16.041
0658	1	14	15.00	-45	19	48.0	g	0.004	5.249	16.317
0660	1	14	15.05	-45	48	24.5	g	0.000	0.336	15.543
0661	1	14	15.70	-45	31	48.4	g	0.000	0.402	16.871
0665	1	14	19.03	-45	56	21.8	f	0.003	0.805	22.236
0666	1	14	19.44	-45	31	54.8	s	0.000	0.605	19.970
0668	1	14	20.78	-46	13	14.9	g	0.040	3.381	21.738
0669	1	14	21.26	-45	0	55.8	s	0.000	0.418	19.684
0672	1	14	23.09	-45	34	30.4	s	0.003	0.986	21.503
0675	1	14	24.19	-46	13	10.9	g	0.012	4.221	20.022
0676	1	14	25.22	-45	4	49.4	g	0.000	1.459	15.622
0677	1	14	25.87	-46	26	16.1	f	0.000	0.124	22.196
0678	1	14	26.21	-46	17	3.1	g	0.000	0.415	19.630
0679	1	14	26.62	-45	52	22.4	g	0.006	3.003	18.977
0681	1	14	28.49	-45	36	37.1	g	0.000	0.477	19.558
0688	1	14	30.60	-46	34	48.4	g	0.004	3.342	18.368
0691	1	14	33.02	-45	23	59.3	g	0.002	1.783	18.748
0694	1	14	34.51	-46	27	6.1	g	0.001	1.050	20.005
0698	1	14	36.67	-46	24	4.3	g	0.007	2.134	20.531
0699	1	14	36.82	-44	51	26.6	g	0.000	0.714	19.908
0700	1	14	37.27	-46	17	51.7	s	0.001	0.820	20.226
0701	1	14	38.40	-46	27	20.9	g	0.000	0.431	19.916
0702	1	14	38.90	-45	40	27.5	g	0.000	0.066	21.330
0703	1	14	40.63	-45	12	5.8	g	0.011	2.436	20.848
0706	1	14	42.94	-45	24	14.8	g	0.006	8.086	15.584
0707	1	14	43.08	-45	54	16.6	g	0.000	0.287	20.761
0708	1	14	43.34	-44	46	28.2	f	0.008	1.096	23.747
0709	1	14	44.09	-45	36	11.2	f	0.006	0.996	22.692
0711	1	14	45.74	-45	31	29.6	f	0.046	3.400	22.198
0714	1	14	46.73	-46	14	38.4	s	0.040	5.105	20.369
0715	1	14	48.67	-45	30	48.6	g	0.046	9.347	18.815
0718	1	14	53.45	-46	12	10.1	g	0.006	2.159	20.330
0720	1	14	53.76	-45	58	22.1	g	0.000	1.313	17.517
0722	1	14	54.22	-45	47	5.3	g	0.003	2.230	19.182
0725	1	14	55.97	-46	18	00.0	g	0.000	0.396	17.981
0727	1	14	57.84	-45	49	47.6	g	0.017	1.990	21.934
0728	1	14	57.86	-45	6	15.1	g	0.001	1.095	19.294
0729	1	14	59.98	-44	57	58.0	g	0.002	2.558	18.013
0730	1	15	2.02	-45	44	52.8	g	0.002	0.999	20.824
0732	1	15	2.52	-45	36	6.1	s	0.003	2.034	19.253
0734	1	15	3.58	-46	41	32.3	g	0.000	0.507	20.729

continued from previous page

	α			δ			class	F	dist	m_R
0736	1	15	4.94	-45	49	44.8	s	0.006	1.601	21.096
0740	1	15	6.62	-46	15	31.3	g	0.019	2.596	21.569
0741	1	15	7.39	-45	10	46.9	f	0.026	1.975	23.156
0742	1	15	8.11	-46	14	30.1	f	0.043	3.129	22.172
0744	1	15	7.92	-45	42	19.8	g	0.001	0.739	21.500
0746	1	15	9.84	-45	24	7.9	g	0.042	4.591	20.908
0751	1	15	10.73	-46	23	5.6	g	0.000	0.460	20.550
0752	1	15	10.44	-46	15	53.6	g	0.043	4.846	20.748
0754	1	15	13.34	-46	15	26.3	g	0.001	2.017	17.068
0755	1	15	15.05	-45	38	19.7	s	0.018	6.754	18.289
0757	1	15	14.83	-45	4	16.0	f	0.000	0.240	22.966
0758	1	15	18.67	-44	52	5.9	g	0.044	4.447	21.131
0759	1	15	18.82	-44	55	10.6	g	0.000	0.272	14.219
0761	1	15	21.86	-45	52	15.6	g	0.000	0.442	19.009
0765	1	15	25.80	-45	2	47.0	s	0.010	4.026	19.088
0767	1	15	27.60	-45	31	6.6	g	0.031	7.289	18.938
0768	1	15	27.24	-45	55	23.2	g	0.002	0.931	21.415
0769	1	15	27.22	-45	36	26.6	g	0.001	1.020	19.918
0770	1	15	27.36	-45	15	7.9	g	0.020	3.830	20.412
0773	1	15	29.95	-44	46	11.6	g	0.012	3.526	20.058
0776	1	15	30.79	-46	19	43.3	f	0.035	2.326	23.131
0778	1	15	35.09	-46	22	39.7	f	0.001	0.580	22.464
0779	1	15	35.93	-46	25	17.8	s	0.008	8.548	15.808
0780	1	15	37.01	-45	38	31.9	f	0.041	3.172	22.528
0781	1	15	37.80	-45	0	22.3	s	0.003	3.523	17.104
0782	1	15	38.66	-46	19	25.3	s	0.000	1.828	16.184
0785	1	15	39.17	-45	56	17.5	g	0.002	1.155	20.310
0786	1	15	39.60	-45	53	44.5	f	0.002	0.559	22.280
0787	1	15	40.01	-45	48	37.8	s	0.006	1.324	21.650
0794	1	15	44.83	-45	55	50.5	g	0.000	0.433	16.324
0795	1	15	45.34	-45	49	37.2	g	0.000	0.320	19.175
0798	1	15	45.70	-46	18	7.6	g	0.003	2.007	19.078
0799	1	15	46.92	-46	39	59.0	g	0.001	1.454	17.991
0800	1	15	48.22	-46	9	49.0	s	0.001	0.859	20.707
0801	1	15	48.19	-45	50	39.8	g	0.001	1.075	20.210
0803	1	15	49.75	-45	13	11.3	g	0.000	0.366	18.273
0806	1	15	51.91	-45	54	23.4	g	0.001	0.983	20.183
0809	1	15	53.02	-45	11	42.7	s	0.036	4.904	20.387
0815	1	15	59.88	-46	38	39.8	s	0.008	4.148	18.620
0816	1	16	0.19	-45	29	14.3	g	0.001	1.828	17.611
0817	1	16	0.96	-45	51	53.3	g	0.039	5.773	20.143

continued from previous page

	α			δ			class	F	dist	m_R
0822	1	16	4.10	-45	50	17.5	g	0.000	0.774	18.139
0823	1	16	4.85	-46	0	52.9	g	0.000	0.686	16.198
0828	1	16	9.14	-45	40	9.5	f	0.009	1.537	22.328
0831	1	16	10.63	-45	58	22.8	g	0.000	1.788	14.183
0832	1	16	11.02	-46	4	27.8	g	0.002	1.040	20.505
0834	1	16	12.98	-45	39	37.1	f	0.022	2.332	22.335
0835	1	16	14.42	-45	12	5.4	g	0.000	0.681	18.331
0836	1	16	14.74	-46	20	20.8	s	0.036	7.823	18.980
0839	1	16	16.87	-45	53	57.8	g	0.011	2.607	20.603
0840	1	16	17.06	-46	3	2.9	g	0.000	0.334	16.818
0842	1	16	19.85	-45	22	30.0	s	0.002	0.888	20.867
0843	1	16	20.90	-46	2	23.6	g	0.002	1.059	20.748
0844	1	16	20.93	-45	0	20.9	g	0.000	0.859	18.897
0847	1	16	22.78	-46	11	6.7	g	0.003	1.325	20.388
0848	1	16	23.14	-46	33	48.2	g	0.000	0.226	15.882
0850	1	16	24.29	-45	49	26.4	g	0.010	1.578	21.576
0851	1	16	24.38	-45	24	2.5	g	0.000	0.741	16.766
0852	1	16	24.67	-46	32	36.2	s	0.001	0.768	20.688
0854	1	16	25.58	-45	7	58.8	g	0.000	0.445	21.101
0856	1	16	25.87	-45	15	2.5	g	0.000	0.478	19.806
0860	1	16	29.26	-46	31	25.0	g	0.000	1.994	14.453
0861	1	16	29.81	-45	52	0.8	g	0.036	7.322	19.207
0862	1	16	31.99	-45	6	52.6	f	0.001	0.455	22.795
0864	1	16	32.45	-46	19	55.9	g	0.013	2.859	20.521
0866	1	16	33.62	-45	36	9.7	g	0.007	2.376	20.285
0867	1	16	33.89	-46	14	5.6	g	0.001	3.361	15.983
0868	1	16	34.56	-45	54	2.9	f	0.001	0.434	22.380
0869	1	16	34.75	-46	17	44.5	g	0.000	1.704	16.171
0870	1	16	35.21	-45	41	2.8	g	0.001	2.079	17.646
0872	1	16	35.93	-46	16	42.6	g	0.000	0.794	19.352
0874	1	16	36.48	-45	30	12.2	g	0.002	2.826	17.222
0875	1	16	36.82	-46	22	23.2	g	0.000	0.527	19.773
0876	1	16	39.36	-45	1	47.6	f	0.023	1.950	22.511
0880	1	16	41.04	-46	19	53.8	g	0.003	1.124	21.495
0881	1	16	42.10	-45	40	47.6	g	0.032	7.477	18.964
0882	1	16	42.96	-46	37	28.6	g	0.000	0.447	18.817
0884	1	16	44.90	-45	1	54.1	g	0.002	1.363	20.286
0885	1	16	45.12	-46	7	33.6	f	0.010	1.305	22.911
0886	1	16	46.63	-45	38	2.4	g	0.004	3.389	17.939
0888	1	16	47.69	-46	34	59.2	g	0.000	1.928	15.096
0889	1	16	48.46	-45	50	38.0	f	0.001	0.519	22.520

continued from previous page

	α			δ			class	F	dist	m_R
0890	1	16	48.43	-45	7	32.5	g	0.013	4.125	19.487
0891	1	16	51.74	-45	31	18.1	g	0.016	2.138	21.889
0892	1	16	52.18	-45	56	12.1	g	0.001	1.870	17.789
0893	1	16	53.62	-45	0	8.6	f	0.031	2.430	22.497
0895	1	16	54.70	-44	58	37.2	g	0.000	0.680	19.742
0896	1	16	55.03	-46	28	50.5	s	0.022	4.986	19.898
0897	1	16	55.58	-45	54	5.8	g	0.001	1.782	18.343
0899	1	16	57.17	-45	48	4.3	f	0.048	3.269	22.649
0902	1	16	57.79	-45	31	10.6	g	0.002	1.214	20.361
0903	1	16	57.72	-45	54	58.3	f	0.001	0.399	23.034
0905	1	17	0.14	-46	5	1.7	g	0.000	0.222	21.218
0906	1	17	0.82	-45	58	10.6	g	0.001	0.719	20.936
0907	1	17	1.63	-45	45	51.5	g	0.010	3.339	19.654
0908	1	17	2.47	-45	25	27.5	f	0.043	2.846	22.540
0909	1	17	3.31	-46	24	32.4	g	0.000	0.570	15.590
0910	1	17	3.55	-46	6	32.0	f	0.010	1.624	22.084
0914	1	17	6.10	-45	10	1.2	g	0.001	0.519	21.171
0917	1	17	7.13	-46	23	25.1	g	0.001	1.802	18.169
0919	1	17	7.46	-46	4	13.8	s	0.005	4.307	17.530
0920	1	17	8.69	-46	27	12.6	g	0.000	0.573	15.539
0924	1	17	11.57	-45	32	47.0	g	0.003	1.667	20.113
0925	1	17	11.64	-45	57	47.2	g	0.002	0.989	20.815
0926	1	17	13.92	-46	22	28.9	g	0.001	1.016	19.263
0930	1	17	16.99	-46	27	53.6	f	0.021	1.935	23.154
0932	1	17	17.42	-46	25	17.0	f	0.000	0.321	22.312
0933	1	17	17.54	-45	37	54.5	g	0.000	0.526	16.743
0935	1	17	19.46	-46	0	0.0	g	0.000	1.000	18.329
0936	1	17	20.93	-44	59	24.7	g	0.007	1.758	21.177
0937	1	17	22.39	-45	33	10.8	g	0.013	3.605	19.884
0938	1	17	22.54	-45	46	48.7	g	0.002	2.781	17.630
0939	1	17	22.58	-45	50	23.6	g	0.000	1.222	16.456
0941	1	17	24.38	-44	56	48.5	g	0.002	1.025	21.140
0943	1	17	25.39	-46	5	47.8	g	0.001	2.198	17.111
0944	1	17	26.14	-45	16	44.4	f	0.004	0.852	22.971
0945	1	17	27.07	-45	28	15.6	g	0.001	1.296	19.374
0946	1	17	30.60	-46	6	40.3	s	0.000	0.708	19.855
0947	1	17	31.18	-45	38	20.8	g	0.000	0.448	20.752
0950	1	17	32.95	-46	11	26.9	g	0.000	0.843	17.549
0951	1	17	33.36	-46	14	46.7	g	0.029	2.873	21.971
0955	1	17	35.66	-45	28	58.4	g	0.001	1.292	18.171
0956	1	17	36.14	-45	39	34.2	g	0.002	2.007	18.253

continued from previous page

	α			δ			class	F	dist	m_R
0962	1	17	41.71	-46	11	4.2	g	0.000	0.623	16.475
0963	1	17	41.78	-45	32	50.6	g	0.002	0.790	21.261
0964	1	17	42.29	-46	24	11.9	s	0.031	4.246	20.661
0965	1	17	44.45	-45	53	35.2	g	0.010	1.997	21.238
0966	1	17	45.36	-46	22	30.7	f	0.006	1.104	22.791
0967	1	17	52.37	-46	14	42.7	s	0.000	0.086	18.404
0969	1	17	52.73	-45	31	3.7	g	0.000	0.760	17.322
0970	1	17	53.50	-45	28	14.5	g	0.000	0.966	18.707
0971	1	17	54.34	-45	43	43.7	s	0.011	6.201	17.626
0972	1	17	54.02	-45	32	8.2	s	0.015	9.660	16.554
0973	1	17	55.39	-45	51	27.0	g	0.009	4.873	18.186
0975	1	17	54.98	-45	42	6.5	f	0.024	2.058	22.709
0981	1	18	1.06	-45	38	29.4	s	0.002	2.988	17.001
0982	1	18	1.01	-45	39	54.4	g	0.002	0.803	21.417
0987	1	18	4.68	-45	58	8.0	g	0.001	0.715	21.425
0988	1	18	5.18	-45	57	13.0	g	0.000	0.630	19.615
0989	1	18	6.74	-45	19	1.9	g	0.000	0.922	18.631
0990	1	18	7.22	-46	9	9.4	g	0.004	3.245	17.980
0991	1	18	7.25	-45	16	48.0	f	0.037	3.141	22.349
0992	1	18	7.22	-46	21	27.7	g	0.038	6.187	19.816
0994	1	18	7.94	-45	45	39.6	g	0.012	4.746	18.917
0995	1	18	10.18	-46	14	32.3	g	0.000	1.055	16.081
0996	1	18	10.56	-45	16	53.4	s	0.011	4.792	18.535
0997	1	18	10.13	-45	34	21.4	g	0.002	2.613	17.873
0998	1	18	10.44	-45	28	36.8	g	0.016	2.254	21.771
0999	1	18	11.88	-46	9	56.2	g	0.006	4.272	18.139
1001	1	18	12.29	-45	45	26.3	g	0.016	5.371	19.000
1003	1	18	13.99	-46	15	7.2	s	0.047	4.877	20.936
1007	1	18	13.92	-45	28	35.8	g	0.019	2.756	21.315
1011	1	18	17.90	-46	17	12.1	g	0.002	1.555	19.606
1012	1	18	19.32	-45	27	19.4	f	0.001	0.556	22.105
1014	1	18	20.88	-45	39	40.3	g	0.001	2.139	16.000
1016	1	18	23.02	-45	28	2.6	s	0.028	3.511	21.055
1017	1	18	23.26	-46	16	22.8	g	0.012	1.852	21.802
1018	1	18	23.88	-45	33	39.2	g	0.003	2.230	18.973
1019	1	18	28.25	-46	6	50.8	g	0.038	4.244	20.964
1021	1	18	30.38	-46	4	45.8	s	0.046	5.767	20.362
1022	1	18	30.48	-45	31	19.9	s	0.001	1.968	17.472
1024	1	18	31.30	-45	35	4.6	g	0.000	0.971	18.776
1025	1	18	34.27	-45	36	38.9	s	0.018	7.659	17.952
1026	1	18	34.78	-46	5	28.3	f	0.013	1.696	22.577

continued from previous page

	α			δ			class	F	dist	m_R
1029	1	18	36.55	-45	36	24.8	g	0.000	0.825	19.086
1031	1	18	37.90	-46	9	30.6	g	0.026	3.174	21.179
1039	1	18	40.92	-45	36	29.5	s	0.002	2.447	18.244
1042	1	18	47.83	-45	59	51.7	g	0.000	0.670	19.988
1045	1	18	54.19	-45	45	8.6	f	0.030	3.091	22.088
1046	1	18	56.26	-45	42	49.3	g	0.001	1.060	19.896
1049	1	19	0.67	-46	3	13.3	g	0.019	4.047	20.143
1050	1	19	3.91	-45	50	40.9	f	0.002	0.586	23.119
1052	1	19	6.79	-45	30	4.3	g	0.002	1.061	20.674
1055	1	19	9.86	-45	30	15.8	g	0.000	0.292	16.174
1058	1	19	14.42	-45	41	59.3	g	0.042	7.707	19.347
1060	1	19	17.64	-45	31	39.0	g	0.000	0.172	20.011
1061	1	19	17.78	-45	50	19.0	g	0.000	0.325	20.835
1062	1	19	19.66	-45	34	34.3	g	0.003	4.351	16.503
1063	1	19	19.82	-45	46	29.6	g	0.001	0.917	19.602
1064	1	19	21.58	-45	50	18.2	g	0.000	0.181	21.087
1065	1	19	25.58	-45	29	39.5	g	0.041	5.646	20.191
1066	1	19	25.82	-45	43	39.4	g	0.000	0.512	16.563
1070	1	19	31.79	-45	23	16.6	f	0.027	4.332	
1072	1	19	31.73	-45	49	29.3	g	0.022	9.232	17.432
1073	1	19	34.85	-45	37	29.7	s	0.000	2.300	
1079	1	19	54.86	-45	42	54.4	g	0.001	0.855	20.254

Column descriptions:

1. Catalogue number
2-7. R-band source position
8. FOCAS2 classifier: s=star, g=galaxy, f=too faint
9. Fractional chance of ID being a coincidence
10. Distance (in arcsec) between optical and radio positions
11. R-band magnitude. Blank entries are COSMOS IDs of radio sources not observed in R-band.

Table B.2 : Radio sources lying outside R-band observations.

COSMOS ID	APM ID	COSMOS ID	APM ID
0015		0241	
0017		0243	
0019	×	0252	×
0020		0253	
0021		0269	

continued from previous page

COSMOS ID	APM ID	COSMOS ID	APM ID
0023		0290	
0043		0331	
0049		0353	
0110		1010	
0174		1028	
0182		1030	
0185		1032	
0186		1041	
0198		1053	
0200		1059	
0202		1068	
0214		1069	×
0222		1072	×
0224		1073	
0227		1075	
0235	×	1076	
0236		1077	

Table B.3 : Additional data on the optically identified sources.

	m_R	m_V	m_{B_J}	m_H	m_K	class	z	Q	type
0002	19.994	21.289				g			
0003	20.685		22.05			g			
0004	15.865		16.95			g			
0005	19.726	21.152				g			
0006	21.097	22.776				g			
0008	17.169	17.655	18.31			g			
0010	19.991	20.810	21.82			g	0.258	1	AB
0011	17.767	18.338	19.30			g			
0012	21.394			20.2		g			
0014	21.869	22.744				g			
0016	18.195	18.964	20.23			g			
0018	20.539	20.989				g			
0019			15.34			g			
0022	12.670	13.362	13.82			g			
0024	19.975	21.120	21.61			g			
0025	20.472	21.881				g			
0029	20.660		21.08			g			
0030	17.501	17.984	18.78			g			
0031	17.820	18.300	19.35			g			

continued from previous page

	m_R	m_V	m_{B_J}	m_H	m_K	class	z	Q	type
0032	20.358	21.396				s			
0033	19.838	21.113				g			
0036	21.821	22.009	23.05			f			
0039	20.799	22.307				g			
0041	22.488					f			
0044	18.770	19.314	19.99			g	0.134	1	B
0045	20.440	21.795				g			
0046	20.440	21.795				g			
0047	19.887	20.403	14.62			g			
0048	21.755	23.015	18.76			g			
0051	20.232	21.514				g			
0052	14.490	15.124	16.04	15.4		g			
0053	21.335	22.002	22.68			s			
0054	14.983	15.514	16.14			g			
0055	20.885	22.504				g			
0056	23.062					f			
0058	18.342	19.408	20.24			g			
0059	19.147					g			
0062	12.215	11.785	12.63			g			
0066	19.594	19.939	19.52			s			
0068	20.757	21.622	21.80			g	0.277	2	A
0070	19.210	19.737	21.03			g	0.242	1	AB
0083	20.626	22.659				g			
0084	21.602	22.260				g			
0086	21.940	22.973		20.7		g			
0089	20.077	21.294				s			
0090	19.022	20.019	21.52			s	0.372	2	C
0099	22.123	22.923	16.43			f			
0100	21.551	23.224				g			
0101	20.950	23.113		20.8		g			
0104	19.610	20.437	21.70		16.576	g	0.372	1	AB
0107	21.120	21.163	20.66			g			
0111	21.637	22.774				g			
0112	22.082				18.701	f			
0113	18.527		20.26			g			
0116	19.802	20.826				g			
0122	17.717	18.519	19.92			g	0.235	1	C
0125	15.517	16.041	15.32			g			
0126	19.577		22.37			g			
0127	17.040	17.206	17.88			s			
0129	18.659	19.410				s			

continued from previous page

	m_R	m_V	m_{B_J}	m_H	m_K	class	z	Q	type
0131	18.175		19.85			g			
0134	20.106	21.290	20.65	18.0	15.143	g	0.409	1	
0135	17.993	18.923	20.02			g	0.254	1	C
0138	18.952	20.014	23.22	18.7	15.595	g	0.411	1	AB
0139	18.198		19.23			g			
0140	20.533		22.00			g			
0145	17.286	17.675	18.61			g			
0146	22.335	23.414			17.601	f			
0149	11.118					s			
0150	19.953					g			
0154	19.983	20.134	20.10			g	0.210	1	A
0155	21.686	22.541		20.5		g			
0157	16.320	16.705	15.06			g			
0160	15.557	15.935	17.31			s			
0162	22.948					f			
0164	21.929					g			
0166	22.031	23.234				f			
0167	19.761	20.221	23.01			s	0.372	2	A
0168	18.544	18.875	19.91			g			
0169	18.544	18.875	19.91			g			
0170	16.027	16.707	17.80			g	0.102	1	C
0172	22.461					f			
0173	19.029	20.353	22.07			g			
0176	15.697	16.095	13.72			g			
0177	19.720	21.279				g			
0179	21.422	22.830	19.93			g			
0180	21.808					g			
0183	21.575	22.767			16.735	g			
0188	21.015	22.490				g			
0191	20.262	21.608				g			
0192	18.951	19.533	20.60			g	0.285	1	B
0194	18.031	18.675	19.61			g			
0197	20.060	21.604				g			
0201	20.748	22.033				g			
0203	17.724	18.187	18.54			g			
0208	21.553	23.196				g			
0212	17.133	17.598	18.66			g			
0216	18.479	19.273	20.03			g			
0220	20.927	21.887			16.924	g	0.551	2	
0226	18.697	19.668	21.56			g			
0228	19.929	20.264	20.25			g			

continued from previous page

	m_R	m_V	m_{B_J}	m_H	m_K	class	z	Q	type
0230	21.082	22.039				g			
0232	22.224					f			
0235			14.39			g			
0237	20.775	22.535				g			
0239	19.901	20.310	21.58		17.378	g			
0242	22.287					f			
0244	20.684	21.958				g			
0245	21.318	21.807			17.042	g			
0248	20.127				16.793	g	0.332	1	A
0252			19.32			s			
0256	18.411	19.005	18.08			g	0.124	1	C
0257	19.734	20.628	22.77			g			
0258	18.575	18.928	19.87			g	0.190	1	A
0260	23.085					f			
0262	18.743		20.53			g	0.342	1	A
0263	18.554		20.36			g			
0264	20.169		22.74		16.555	g	0.298	1	C
0266	21.214					s			
0267	19.916		22.82			s			
0270	20.919		19.18			s	0.126	1	C
0273	17.687		19.81			g			
0276	22.044	23.253				f			
0279	17.706	18.064	19.39	18.5		g			
0280	23.030			22.4		f			
0281	23.098					f			
0284	22.871		20.41	20.7		f			
0285	19.409	20.529	21.63	18.9	16.116	g	0.421	1	AB
0286	15.961	16.425	17.41	16.4		g			
0287	18.973	19.790	20.89	18.9		g			
0288	19.682	20.987	21.72	20.6		g	0.270	2	A
0289	20.231	21.434	22.62			s			
0295	23.027	23.572			19.146	f			
0297	21.912					f			
0298	18.516	19.075	20.35	18.4		g	0.300	1	B
0299	20.783	21.675	22.39	20.6		g			
0301	18.001		20.30			s			
0303	19.121	20.386	22.38	19.7		g			
0305	18.496		20.24			g			
0306	18.976	19.678	19.74	19.5	16.347	s	2.336	1	D
0310	19.267		21.65			g			
0313	20.838					g			

continued from previous page

	m_R	m_V	m_{B_J}	m_H	m_K	class	z	Q	type
0316	18.750		20.08			g			
0317	22.390	23.837				f			
0318	19.050		21.08	18.4		g			
0320	23.390			19.3		f			
0326	22.076	22.762				f			
0327	20.990	21.581			17.357	g	0.743	2	
0328	21.189					g			
0329	19.304	20.341	20.85		15.984	g	0.493	1	C
0332	18.089	19.653	20.25			g			
0333	20.663	21.485				g			
0334	21.166	21.998			19.376	g			
0340	16.490	21.133	20.94	18.8		g	0.229	1	AB
0341	19.417	19.991	21.00			g			
0342	17.440	18.725	17.94			s			
0343	18.587	19.087	18.12			g	0.025	1	A
0344	19.136	20.567			15.843	g	0.449	1	
0345	18.201		19.79			g	0.135	1	
0346	20.146	21.052			16.741	g	0.329	1	
0347	18.625	20.551	20.56			g	0.253	2	C
0348	17.995	18.439	19.51			g			
0351	18.114	18.351	18.50			s	1.056	3	D
0352	20.217	20.941	22.12		16.390	g	0.721	1	D
0355	20.976					g			
0356	16.876					s			
0358	20.232	20.784	21.83		17.007	g	1.240	1	D
0360	22.755					f			
0361	22.409					f			
0363	20.109	21.246	21.89			g			
0366	22.486					f			
0367	20.294	21.324				g			
0369	18.311	19.022	19.84			g	0.255	1	AB
0373	19.283	20.441				s			
0374	16.678		18.51			g			
0376	22.799	23.199				f			
0378	23.396	23.643				f			
0379	23.173					f			
0382	17.535	18.225	19.33			g			
0384	16.158	16.978	17.32			g			
0386	22.493			21.7		f			
0387	19.856	20.973	22.06		16.516	g			
0390	19.694		21.05			g			

continued from previous page

	m_R	m_V	m_{B_J}	m_H	m_K	class	z	Q	type
0392	22.035	23.905			18.029	f			
0394	21.281	22.993				s			
0395	17.980		19.40			g	0.256	1	AB
0396	21.522	23.061		21.1	17.288	g			
0398	18.487	18.855	19.70			g	0.299	1	AB
0400	22.326	23.056	19.83			f			
0401	22.508					f			
0402	20.942	22.255				g			
0403	22.666	23.294				f			
0404	22.010	23.226				f			
0405	22.030			19.8		f			
0408	18.214	18.057	15.90			g			
0409	19.395	21.432	20.80			g	0.427	1	A
0410	19.200	20.217	21.48			g			
0412	22.136	22.558				f			
0414	22.950					f			
0417	16.037	16.335	17.38			g			
0418	23.951	23.353				f			
0419	19.785	20.977				g			
0420	18.413	18.893	19.94			g			
0423	15.609	16.249	16.81			s			
0426	22.254	22.880				f			
0427	22.855	23.473				f			
0431	20.576	21.282			16.335	g			
0434	18.241		20.15			g	0.210	1	C
0435	18.132	19.021	19.08			s			
0437	19.257	22.209	21.60			g			
0438	16.100	16.453	15.52	16.6		g			
0441	20.036	20.359	19.57			s	2.249	1	D
0443	19.852	21.580				g			
0445	21.002	21.657				g			
0446	22.642					f			
0450	20.621					g			
0452	17.734	18.128	19.58			g	0.235	1	C
0455	20.251	21.778				g			
0466	19.437	19.850	19.27			g			
0467	19.746		23.03			g	0.419	2	C
0468	21.804	23.168				f			
0469	21.104	22.741				g			
0470	17.901	18.601	19.87	17.6		g			
0471	21.995	23.593				f			

continued from previous page

	m_R	m_V	m_{B_J}	m_H	m_K	class	z	Q	type
0472	18.506	19.180	20.74	18.7		g	0.235	1	C
0473	20.284	22.023				g			
0474	21.220	23.274				g			
0477	22.444	23.452				f			
0481	20.860		22.59			g	0.815	1	D
0482	18.367	19.223	20.23			g	0.240	1	AB
0490	21.725	23.679				g			
0492	21.227	22.879				g			
0495	15.234	16.054	16.92			g			
0499	22.879	22.977				f			
0501	22.604	23.008				f			
0504	21.858	22.936				g			
0505	19.620	20.526	21.39			g	0.445	1	A
0508	20.580	23.093				g			
0510	22.542					f			
0512	21.908	22.734				f			
0514	22.174	24.333				f			
0517	16.375	16.897	18.03			g			
0518	23.221					f			
0522	17.137	17.591	16.23			g	0.066	1	A
0523	20.374					g			
0525	21.818		22.20			g			
0526	20.383					s			
0528	17.722		19.63			g	0.235	1	A
0529	19.733					g			
0531	20.046	20.313	20.54			g			
0532	17.372					s			
0533	17.444	16.842	17.32			g	0.082	1	A
0534	23.404					f			
0537	16.026	16.678	14.43			g	0.133	1	C
0538	18.969	19.830	21.43			g			
0539	20.581					s			
0540	22.165	22.440				f			
0541	21.089	22.331				g			
0542	22.129					f			
0543	22.616	22.565				f			
0544	17.399	17.947	19.00			g	0.236	1	A
0547	22.204	23.115				f			
0549	21.752	22.160				g			
0550	21.626					s			
0552	23.032					f			

continued from previous page

	m_R	m_V	m_{B_J}	m_H	m_K	class	z	Q	type
0553	21.342					g	0.032	2	AB
0554	15.778	16.328	16.48			s			
0555	22.573	23.779				f			
0556	21.202	21.893				g			
0558	18.633		20.39			g	0.157	2	AB
0560	18.184		20.46			g			
0562	17.739	18.229	18.90			g	0.253	1	A
0564	18.069	18.931	20.33			g	0.254	1	C
0569	20.036	20.427	20.97			g			
0570	21.277	22.478				g			
0571	21.625	23.637				g			
0572	20.746	22.031	17.23			g			
0574	18.290	19.165	20.01			g	0.326	1	C
0575	15.890	16.672	16.99			g			
0578	18.455	19.365	19.20			g	0.276	1	A
0580	23.014	23.381				f			
0585	20.624	21.200	21.90			s			
0587	19.288	20.975				g			
0590	20.467	22.513	21.56			g			
0594	23.453					f			
0595	20.288	20.852	21.15			g			
0598	20.077	20.751	20.85			s			
0601	17.514		17.91			s			
0603	16.251		17.59	16.3		g			
0605	20.039	20.197	19.59			s	0.935	3	D
0607	15.234		15.89			s			
0610	16.357		18.60	15.3		g	0.147	1	C
0611	15.531	16.048	17.22	16.0		g			
0615	17.933	18.783	20.54			s			
0618	19.500					g			
0619	19.500					g			
0621	19.586		19.54			g	0.070	1	A
0622	19.405					g			
0626	20.383					g			
0629	21.986			20.5		g			
0630	22.116					f			
0631	19.736					g			
0634	15.490		17.48			g			
0635	17.667		18.82			g	0.077	1	A
0637	20.234		20.33			g			
0638	21.966					s			

continued from previous page

	m_R	m_V	m_{B_J}	m_H	m_K	class	z	Q	type
0640	15.568		17.40	15.8		g	0.089	1	C
0641	17.806		18.19			g	0.119	1	C
0642	23.041					f			
0643	16.174		18.35			g	0.146	1	C
0644	20.121	21.415				g			
0645	23.228			21.8		f			
0648	20.514					g			
0652	15.624		17.05			g			
0655	18.436					s			
0657	16.041		18.01			g			
0658	16.317		18.11	16.5		g	0.123	1	AB
0660	15.543		16.85	16.6		g	0.025	1	A
0661	16.871	17.107	18.57			g			
0665	22.236					f			
0666	19.970	20.431	21.56			s	0.827	2	D
0668	21.738		20.56			g			
0669	19.684		19.66			s			
0672	21.503	22.687	23.01			s	0.655	3	AB
0675	20.022		14.23			g			
0676	15.622		17.32	15.8		g			
0677	22.196					f			
0678	19.630		22.81			g			
0679	18.977		19.35			g	0.459	1	A
0681	19.558	20.363	22.22			g	0.047	3	C
0688	18.368		19.44			g			
0691	18.748		18.47			g			
0694	20.005					g			
0698	20.531		21.81			g			
0699	19.908					g			
0700	20.226					s			
0701	19.916		19.10			g			
0702	21.330	22.563	19.76			g			
0703	20.848					g			
0706	15.584		17.27	15.7		g			
0707	20.761					g			
0708	23.747					f			
0709	22.692					f			
0711	22.198					f			
0714	20.369					s			
0715	18.815		20.06			g			
0718	20.330					g			

continued from previous page

	m_R	m_V	m_{B_J}	m_H	m_K	class	z	Q	type
0720	17.517		19.01			g			
0722	19.182	19.597	19.76			g	0.216	2	B
0725	17.981		19.97			g	0.253	1	C
0727	21.934					g			
0728	19.294		19.96			g	0.333	1	A
0729	18.013		17.96			g	0.225	1	AB
0730	20.824	21.933				g			
0732	19.253		22.15			s	0.312	1	C
0734	20.729					g			
0736	21.096		19.57			s			
0740	21.569					g			
0741	23.156					f			
0742	22.172					f			
0744	21.500	22.998				g			
0746	20.908					g			
0751	20.550					g			
0752	20.748					g			
0754	17.068		18.82			g			
0755	18.289		20.30			s			
0757	22.966					f			
0758	21.131					g			
0759	14.219		16.14			g	0.032	1	A
0761	19.009		20.52			g	0.373	1	C
0765	19.088		21.80			s			
0767	18.938					g	0.379	1	C
0768	21.415					g			
0769	19.918		21.02			g			
0770	20.412		21.90			g			
0773	20.058					g			
0776	23.131					f			
0778	22.464					f			
0779	15.808		16.33			s			
0780	22.528	22.296				f			
0781	17.104		17.86			s	0.315	3	C
0782	16.184		16.91			s			
0785	20.310		22.27			g			
0786	22.280					f			
0787	21.650		22.79			s	0.373	1	
0794	16.324		17.71	16.5		g	0.104	1	C
0795	19.175		21.18			g	0.373	1	C
0798	19.078		19.74			g	0.335	1	AB

continued from previous page

	m_R	m_V	m_{B_J}	m_H	m_K	class	z	Q	type
0799	17.991		19.99			g	0.254	1	C
0800	20.707		21.94			s			
0801	20.210					g			
0803	18.273		20.51			g	0.325	1	C
0806	20.183					g			
0809	20.387					s			
0815	18.620		19.61			s			
0816	17.611	17.981	18.94			g	0.089	1	A
0817	20.143					g			
0822	18.139		20.01			g	0.371	1	C
0823	16.198		18.02	16.4		g	0.067	1	C
0828	22.328	22.675				f			
0831	14.183		15.65	15.4		g	0.026	1	B
0832	20.505					g			
0834	22.335	23.695				f			
0835	18.331		20.86			g	0.324	1	C
0836	18.980		20.39			s			
0839	20.603					g			
0840	16.818		18.42			g	0.201	1	A
0842	20.867					s			
0843	20.748					g			
0844	18.897		20.39			g			
0847	20.388		16.59			g	0.564	1	AB
0848	15.882		17.79			g	0.125	1	C
0850	21.576					g			
0851	16.766		18.34	17.7		g	0.124	1	A
0852	20.688		21.86			s			
0854	21.101					g			
0856	19.806		22.63			g	0.419	1	AB
0860	14.453		15.82			g	0.030	1	AB
0861	19.207					g			
0862	22.795					f			
0864	20.521					g			
0866	20.285	21.304				g			
0867	15.983		17.43			g	0.029	1	A
0868	22.380					f			
0869	16.171		17.13			g			
0870	17.646	18.071	19.31			g			
0872	19.352		22.34			g			
0874	17.222	17.669	18.97			g	0.178	1	B
0875	19.773					g			

continued from previous page

	m_R	m_V	m_{B_J}	m_H	m_K	class	z	Q	type
0876	22.511					f			
0880	21.495		20.67			g			
0881	18.964		19.88			g			
0882	18.817		21.88			g	0.387	3	C
0884	20.286					g			
0885	22.911					f			
0886	17.939		18.00			g	0.076	1	A
0888	15.096		16.26			g			
0889	22.520					f			
0890	19.487					g			
0891	21.889					g			
0892	17.789		19.54			g	0.203	1	A
0893	22.497					f			
0895	19.742					g	0.370	2	AB
0896	19.898		20.22			s			
0897	18.343		19.34			g	0.120	1	AB
0899	22.649	23.698				f			
0902	20.361	21.915				g			
0903	23.034					f			
0905	21.218					g			
0906	20.936					g			
0907	19.654	19.885	19.91			g	0.255	1	A
0908	22.540					f			
0909	15.590		16.13			g	0.030	1	AB
0910	22.084					f			
0914	21.171					g			
0917	18.169		19.23			g	0.273	1	C
0919	17.530		19.97			s	0.000	1	
0920	15.539		17.05			g	0.052	1	AB
0924	20.113	21.024				g			
0925	20.815					g			
0926	19.263		20.59			g	0.358	2	AB
0930	23.154					f			
0932	22.312					f			
0933	16.743	17.088	18.23			g	0.148	1	AB
0935	18.329		19.86			g	0.254	1	A
0936	21.177					g			
0937	19.884	20.479	21.05			g	0.180	2	A
0938	17.630	18.351	19.74			g			
0939	16.456		18.26			g	0.124	1	C
0941	21.140					g			

continued from previous page

	m_R	m_V	m_{B_J}	m_H	m_K	class	z	Q	type
0943	17.111		18.42			g			
0944	22.971					f			
0945	19.374	21.296	21.60			g	0.331	1	AB
0946	19.855		20.71			s	0.527	1	AB
0947	20.752	22.313				g			
0950	17.549		19.70			g	0.236	1	C
0951	21.971					g			
0955	18.171		18.15			g	0.174	1	A
0956	18.253	18.574	19.72			g	0.159	1	A
0962	16.475		18.35			g	0.105	1	A
0963	21.261	22.464				g			
0964	20.661		21.77			s			
0965	21.238					g			
0966	22.791					f			
0967	18.404		18.20			s	1.879	1	D
0969	17.322	17.626	18.58			g			
0970	18.707		21.80			g	0.378	1	C
0971	17.626		18.83			s			
0972	16.554	16.818				s			
0973	18.186		19.48			g	0.238	1	AB
0975	22.709					f			
0981	17.001	17.702	18.15			s	0.000	1	
0982	21.417					g			
0987	21.425					g			
0988	19.615					g			
0989	18.631		20.32			g	0.301	1	C
0990	17.980		19.46			g			
0991	22.349					f			
0992	19.816		21.94			g	0.374	1	C
0994	18.917		21.87			g			
0995	16.081		12.78			g	0.059	1	A
0996	18.535		18.64			s			
0997	17.873	18.506	19.25			g			
0998	21.771					g			
0999	18.139		19.82			g			
1001	19.000		20.74			g	0.371	1	A
1003	20.936		22.16			s			
1007	21.315					g			
1011	19.606		19.85			g			
1012	22.105					f			
1014	16.000	16.533	17.88	16.4		g	0.132	1	C

continued from previous page

	m_R	m_V	m_{B_J}	m_H	m_K	class	z	Q	type
1016	21.055					s			
1017	21.802					g			
1018	18.973	19.944	20.98			g	0.378	1	AB
1019	20.964		23.04			g	0.563	2	AB
1021	20.362		21.77			s			
1022	17.472	17.660	17.64			s			
1024	18.776	19.794	22.39	18.4		g			
1025	17.952	18.152	19.61			s			
1026	22.577					f			
1029	19.086	20.177	21.96	18.5		g	0.378	1	C
1031	21.179					g			
1039	18.244	19.086	20.38			s			
1042	19.988					g			
1045	22.088	23.536				f			
1046	19.896	21.077				g			
1049	20.143		23.03			g			
1050	23.119					f			
1052	20.674	21.463				g			
1055	16.174	16.640	17.68	16.5		g			
1058	19.347	19.510	20.19			g			
1060	20.011	20.838				g			
1061	20.835					g			
1062	16.503		18.35			g	0.104	1	AB
1063	19.602	20.744	22.33			g			
1064	21.087					g			
1065	20.191					g			
1066	16.563	17.168	18.46			g			
1070			22.75			f			
1072	17.432		19.65			g			
1073			19.59			s	0.174	1	AB
1079	20.254	21.699	23.07			g			

Column descriptions:

1. Catalogue number
2. R-band magnitude
3. V-band magnitude
4. B_J-band magnitude
5. H-band magnitude
6. K-band magnitude
7. FOCAS2 classifier
8. Redshift
9. Redshift qualifier: 1=certain, 2=less certain, 3=uncertain (see text)
10. Spectral type: see description in text

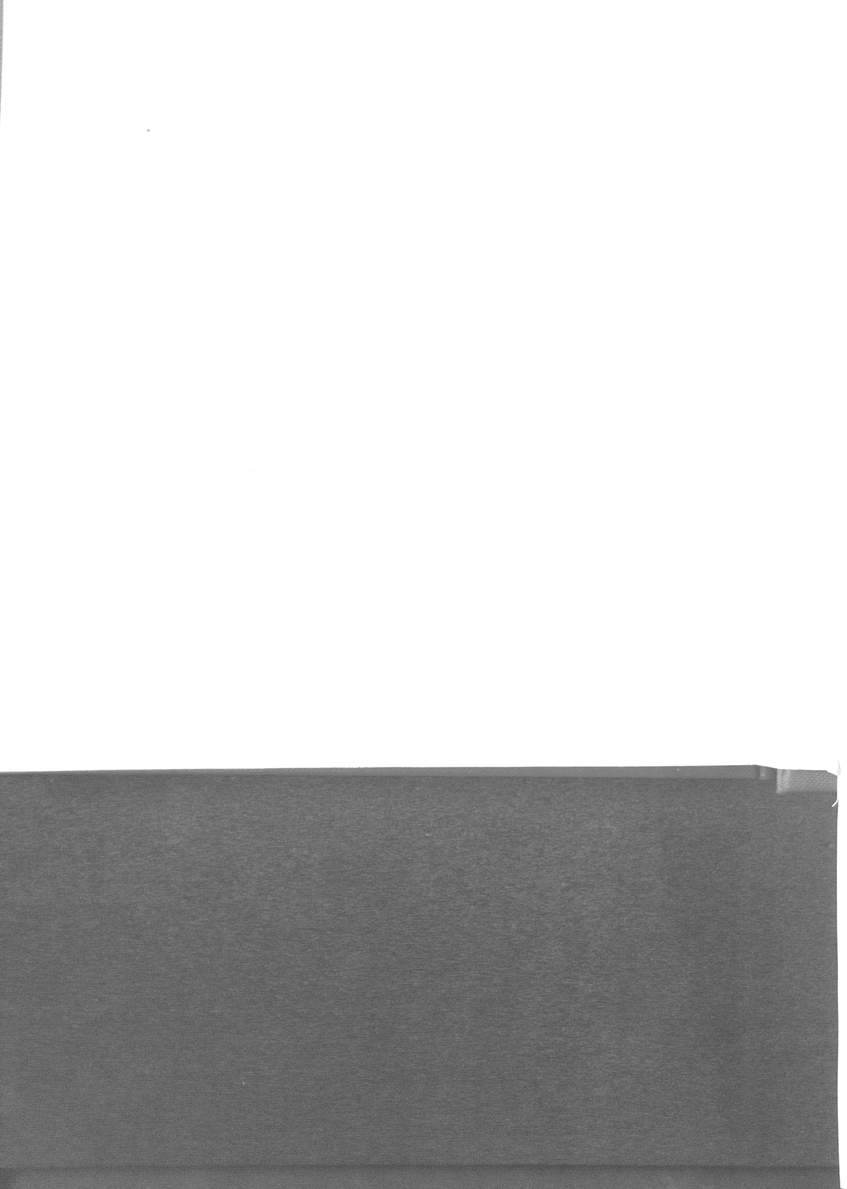

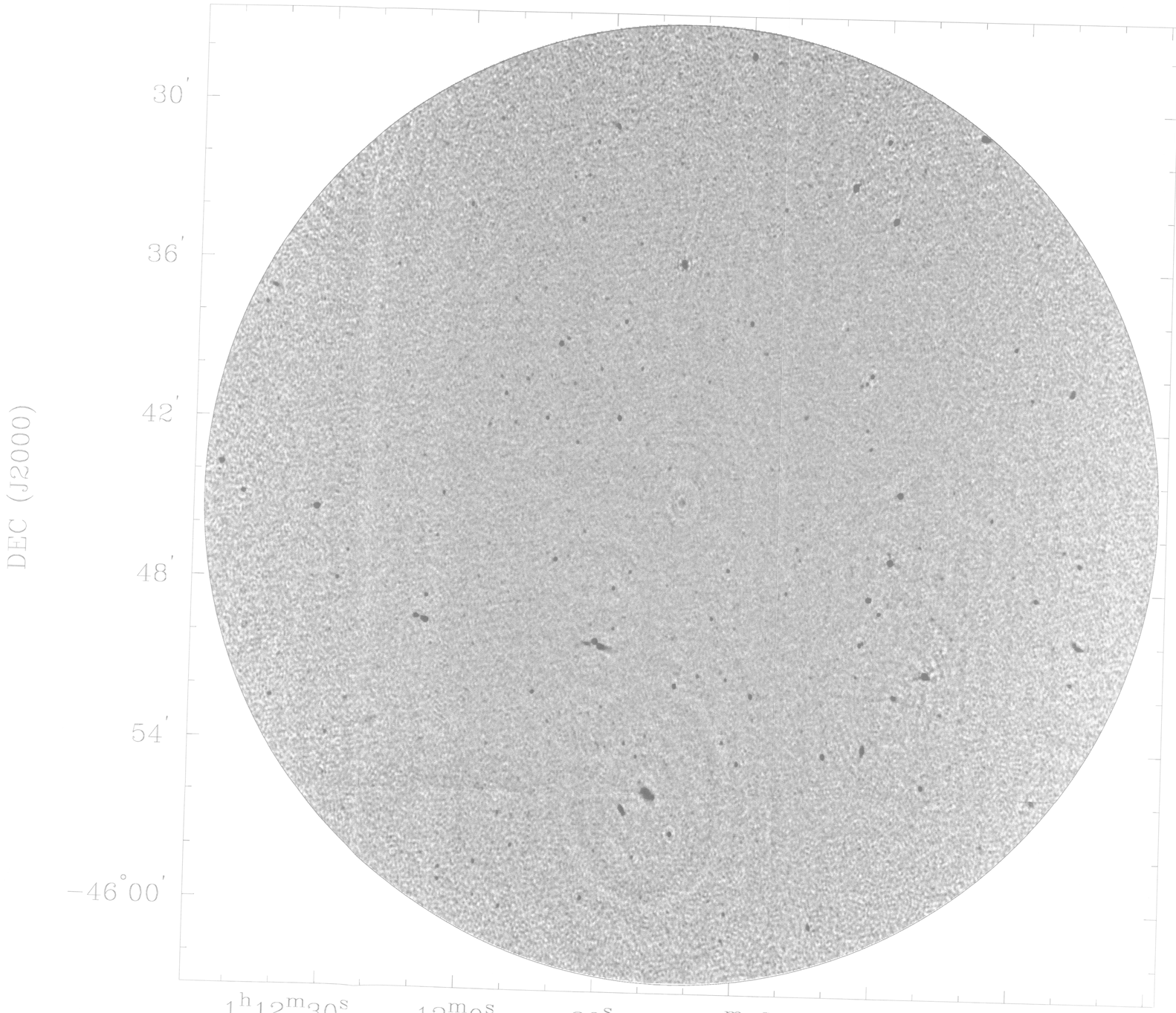
30′
36′
42′
48′
54′
−46°00′
DEC (J2000)
1h12m30s
12m0s
30s
11m0s
30s
10m0s
30s
RA (J2000)

−45°00′
20′
40′
−46°00′
20′
−46°40′
DEC (J2000)
1h20m
18m
16m
14m
12m
10m
RA (J2000)